

CR-TT2053

**CSDL-T-986**

**A DESIGN STUDY OF ONBOARD  
NAVIGATION AND GUIDANCE  
DURING AEROCAPTURE AT MARS**

by  
**Douglas Paul Fuhry**

**May 1988**

**Master of Science Thesis  
Massachusetts Institute of Technology**

(NASA-CR-172053) A DESIGN STUDY OF ONBOARD  
NAVIGATION AND GUIDANCE DURING AEROCAPTURE  
AT MARS M.S. Thesis (Draper (Charles Stark)  
Lab.) 200 p CSCI 22A

N88-24654

Unclas  
G3/12 0147010



**The Charles Stark Draper Laboratory, Inc.**

555 Technology Square  
Cambridge, Massachusetts 02139

A DESIGN STUDY OF  
ONBOARD NAVIGATION AND GUIDANCE  
DURING AEROCAPTURE AT MARS

by

Douglas Paul Fuhry

B.S.A.A.E., Purdue University  
(1986)

SUBMITTED IN PARTIAL FULFILLMENT  
OF THE REQUIREMENTS FOR THE DEGREE OF

MASTER OF SCIENCE IN  
AERONAUTICS AND ASTRONAUTICS

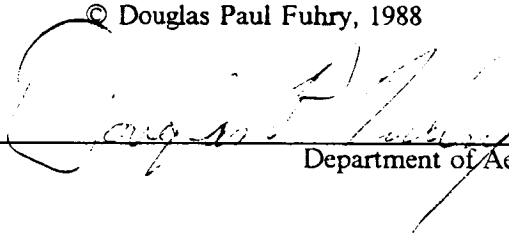
at the

MASSACHUSETTS INSTITUTE OF TECHNOLOGY

May 1988

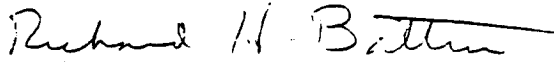
© Douglas Paul Fuhry, 1988

Signature of Author



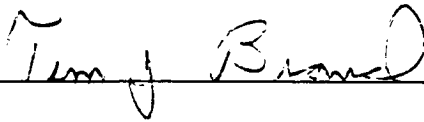
Department of Aeronautics and Astronautics  
May 6, 1988

Certified by



Professor Richard H. Battin  
Department of Aeronautics and Astronautics  
Thesis Supervisor

Certified by



Timothy J. Brand  
Technical Supervisor, CSDL

Accepted by

Professor Harold Y. Wachman  
Chairman, Departmental Graduate Committee

A DESIGN STUDY OF  
ONBOARD NAVIGATION AND GUIDANCE  
DURING AEROCAPTURE AT MARS

by

Douglas Paul Fuhry

Submitted to the Department of Aeronautics and Astronautics  
on May 6, 1988 in partial fulfillment of the  
requirements for the Degree of Master of Science  
in Aeronautics and Astronautics

**ABSTRACT**

The navigation and guidance of a high lift-to-drag ratio sample return vehicle during aerocapture at Mars are investigated. Emphasis is placed on integrated systems design, with guidance algorithm synthesis and analysis based on vehicle state and atmospheric density uncertainty estimates provided by the navigation system. The navigation system utilizes a Kalman filter for state vector estimation, with useful update information obtained through radar altimeter measurements and density altitude "measurements" based on IMU-measured drag acceleration. A three-phase guidance algorithm, featuring constant bank angle numeric predictor/corrector atmospheric capture and exit phases and an extended constant altitude cruise phase, is developed to provide controlled capture and depletion of orbital energy, orbital plane control, and exit apoapsis control.

Integrated navigation and guidance systems performance are analyzed using a four degree-of-freedom computer simulation. The simulation environment includes an atmospheric density model with spatially correlated perturbations to provide realistic variations over the vehicle trajectory. Navigation filter initial conditions for the analysis are based on planetary approach optical navigation study results. Results from a selection of test cases are presented to give insight into systems performance.

Thesis Supervisor: Dr. Richard H. Battin

Title: Adjunct Professor of Aeronautics and Astronautics

Technical Supervisor: Timothy J. Brand

Title: Division Leader, The Charles Stark Draper  
Laboratory, Inc.

## *ACKNOWLEDGEMENTS*

I would like to take this opportunity to express my gratitude to all those who have helped to make this thesis possible and my graduate studies at M.I.T. and Draper Laboratory so rewarding.

To my technical supervisor, Tim Brand, for providing the opportunity for graduate work at Draper and for his guidance of the research and writing of this thesis.

To my thesis advisor, Dr. Richard H. Battin, for his assistance in the preparation of this thesis and his teaching in the field of astrodynamics.

To Gene Muller, for his invaluable assistance in the design and interpretation of the navigation filter.

To the other members of the technical staff in the Guidance and Navigation Analysis Division, especially John Higgins, Frank Kreimendahl, Kevin Mahar, Bill Robertson, and Ken Spratlin, for their technical advice and support.

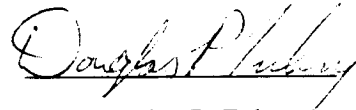
To my parents, whose unending love, support, and sacrifice have smoothed out many a bumpy road along the way.

Finally, to Cindy, for the love, encouragement, and faith which she has so freely shared.

This report was prepared at The Charles Stark Draper Laboratory, Inc. under NASA Contract NAS9-17560.

Publication of this report does not constitute approval by the Draper Laboratory or the sponsoring agency of the findings or conclusions contained herein. It is published for the exchange and stimulation of ideas.

I hereby assign my copyright of this thesis to The Charles Stark Draper Laboratory, Inc., Cambridge, Massachusetts.

  
Douglas P. Fuhry

Permission is hereby granted by The Charles Stark Draper Laboratory, Inc. to the Massachusetts Institute of Technology to reproduce any or all of this thesis.

## TABLE OF CONTENTS

Chapter	Page
<b>1. INTRODUCTION</b> .....	<b>23</b>
1.1 MARS ROVER SAMPLE RETURN MISSION .....	23
1.2 MOTIVATION .....	24
1.2.1 NAVIGATION .....	27
1.2.2 GUIDANCE .....	28
1.2.2.1 INTRODUCTION .....	28
1.2.2.2 PREVIOUS RESEARCH .....	29
1.2.2.3 PROPOSED ALGORITHM .....	30
1.3 THESIS OVERVIEW .....	33
<b>2. NAVIGATION SYSTEM DESIGN</b> .....	<b>35</b>
2.1 INTRODUCTION .....	35
2.2 INERTIAL MEASUREMENT UNIT .....	35
2.3 RADAR ALTIMETER .....	38
2.4 ESTIMATOR DESIGN .....	39
2.4.1 KALMAN FILTER EQUATIONS .....	39
2.4.2 DYNAMICS MODELS .....	42
2.4.2.1 STATE VECTOR PROPAGATION .....	42
2.4.2.2 COVARIANCE MATRIX PROPAGATION .....	44
2.4.3 MEASUREMENT MODELS .....	47
2.4.3.1 DENSITY ALTITUDE MEASUREMENT .....	47
2.4.3.2 RADAR ALTIMETER MEASUREMENT .....	49
<b>3. GUIDANCE DESIGN</b> .....	<b>51</b>
3.1 INTRODUCTION .....	51

3.2	ATMOSPHERIC CAPTURE PHASE .....	52
3.2.1	TARGET CRUISE ALTITUDE .....	52
3.2.2	GUIDANCE DESCRIPTION .....	53
3.2.2.1	PREDICTION ALGORITHM .....	55
3.2.2.2	CORRECTION ALGORITHM .....	57
3.3	CONSTANT ALTITUDE CRUISE PHASE .....	59
3.4	EXIT PHASE .....	61
3.4.1	GUIDANCE TARGET SELECTION .....	61
3.4.2	GUIDANCE DESCRIPTION .....	62
3.4.2.1	PREDICTION ALGORITHM .....	63
3.4.2.2	CORRECTION ALGORITHM .....	63
3.5	ORBIT PLANE CONTROL .....	65
<b>4.</b>	<b>COMPUTER SIMULATION PROGRAM .....</b>	<b>69</b>
4.1	INTRODUCTION .....	69
4.2	SIMULATOR PROGRAM FUNCTIONAL DESCRIPTION .....	69
4.3	ENVIRONMENT MODELS .....	72
4.3.1	PLANET MODEL .....	72
4.3.2	ATMOSPHERIC DENSITY MODEL .....	72
4.4	VEHICLE MODELS .....	76
4.4.1	EQUATIONS OF MOTION .....	76
4.4.2	AERODYNAMIC HEATING .....	77
<b>5.</b>	<b>PERFORMANCE RESULTS .....</b>	<b>79</b>
5.1	INTRODUCTION .....	79
5.2	NOMINAL AEROCAPTURE TRAJECTORY .....	79
5.3	NAVIGATION SYSTEM PERFORMANCE .....	81
5.3.1	ESTIMATOR INITIAL CONDITIONS .....	81

5.3.2	ERROR DEFINITION AND INITIALIZATION .....	90
5.3.3	NAVIGATION TEST CASES .....	91
5.3.3.1	+100% CONSTANT DENSITY BIAS CASES .....	91
5.3.3.2	DENSITY SHEAR CASES .....	113
5.4	COMBINED GUIDANCE AND NAVIGATION SYSTEMS PERFORM- ANCE .....	138
5.4.1	INTRODUCTION .....	138
5.4.2	PRESENTATION OF RESULTS .....	138
5.4.3	CONSTANT DENSITY BIAS CASES .....	140
5.4.3.1	DETAILED DESCRIPTION: CASE # 031000D, +100% DENSITY	141
5.4.4	DENSITY SHEAR CASES .....	158
5.4.4.1	DETAILED DESCRIPTION: CASE # 288500D .....	159
6.	CONCLUSION .....	193
Appendix		Page
A.	DERIVATION OF DENSITY ALTITUDE MEASUREMENT EQUATIONS .....	197
B.	DERIVATION OF ORBIT INSERTION $\Delta V$ EQUATIONS .....	199
List of References	.....	203

## LIST OF ILLUSTRATIONS

Figure	Page
1-1. MRSR Mission Scenario .....	25
1-2. Potential Biconic Aerocapture Vehicle Configuration .....	30
3-1. Bank Angle Control Definition .....	52
3-2. Aerocapture Altitude Corridor .....	54
3-3. Velocity Error Control Corridor .....	67
4-1. Simulator Program Functional Diagram .....	70
4-2. Nominal Density Model Comparison with Flight Data .....	75
5-1. Nominal Aerocapture: Altitude History .....	82
5-2. Nominal Aerocapture: Velocity History .....	83
5-3. Nominal Aerocapture: Flight Path Angle History .....	84
5-4. Nominal Aerocapture: Aerodynamic Load Factor Profile .....	85
5-5. Nominal Aerocapture: Bank Angle History .....	86
5-6. Nominal Aerocapture: Normalized In-Plane Lift .....	87
5-7. Nominal Aerocapture: Orbit Plane Errors .....	88
5-8. Case # 031000D, + 100% Density: Position Estimate Errors .....	95
5-9. Case # 031000D, + 100% Density: RMS Position Errors .....	96
5-10. Case # 031000D, + 100% Density: Velocity Estimate Errors .....	97
5-11. Case # 031000D, + 100% Density: RMS Velocity Errors .....	98
5-12. Case # 031000D, + 100% Density: Density Bias .....	99
5-13. Case # 031000D, + 100% Density: Density, Bias Estimate Errors .....	100
5-14. Case # 031000D, + 100% Density: Orbital $\hat{A}$ _ sis Estimate Errors .....	101
5-15. Case # 031000D, + 100% Density: $\theta_r, \theta_v$ Estimate Errors .....	102
5-16. Case # 031000RD, + 100% Density: Position Estimate Errors .....	105

5-17.	Case # 031000RD, + 100% Density: RMS Position Errors	106
5-18.	Case # 031000RD, + 100% Density: Velocity Estimate Errors	107
5-19.	Case # 031000RD, + 100% Density: RMS Velocity Errors	108
5-20.	Case # 031000RD, + 100% Density: Density Bias	109
5-21.	Case # 031000RD, + 100% Density: Density, Bias Estimate Errors	110
5-22.	Case # 031000RD, + 100% Density: Orbital Apsis Estimate Errors	111
5-23.	Case # 031000RD, + 100% Density: $\theta_r, \theta_v$ Estimate Errors	112
5-24.	Case # 288500D (Full Covariance): Position Estimate Errors	114
5-25.	Case # 288500D (Full Covariance): RMS Position Errors	115
5-26.	Case # 288500D (Full Covariance): Velocity Estimate Errors	116
5-27.	Case # 288500D (Full Covariance): RMS Velocity Errors	117
5-28.	Case # 288500D (Full Covariance): Density Bias	118
5-29.	Case # 288500D (Full Covariance): Orbital Apsis Est. Errors	119
5-30.	Case # 288500D (Full Covariance): $\theta_r, \theta_v$ Est. Errors	120
5-31.	Case # 288500RD (Full Covariance): Position Estimate Errors	122
5-32.	Case # 288500RD (Full Covariance): RMS Position Errors	123
5-33.	Case # 288500RD (Full Covariance): Velocity Estimate Errors	124
5-34.	Case # 288500RD (Full Covariance): RMS Velocity Errors	125
5-35.	Case # 288500RD (Full Covariance): Density Bias	126
5-36.	Case # 288500RD (Full Covariance): Orbital Apsis Est. Errors	127
5-37.	Case # 288500RD (Full Covariance): $\theta_r, \theta_v$ Est. Errors	128
5-38.	Case # 288500D (Diag. Covariance): Position Estimate Errors	131
5-39.	Case # 288500D (Diag. Covariance): RMS Position Errors	132
5-40.	Case # 288500D (Diag. Covariance): Velocity Estimate Errors	133
5-41.	Case # 288500D (Diag. Covariance): RMS Velocity Errors	134
5-42.	Case # 288500D (Diag. Covariance): Density Bias	135
5-43.	Case # 288500D (Diag. Covariance): Orbital Apsis Est. Errors	136

5-44.	Case # 288500D (Diag. Covariance): $\theta_r, \theta_v$ Est. Errors	137
5-45.	Case # 031000D, + 100% Density: Bank Angle Control Response	146
5-46.	Case # 031000D, + 100% Density: Normalized In-Plane Lift	147
5-47.	Case # 031000D, + 100% Density: Altitude History	147
5-48.	Case # 031000D, + 100% Density: Position Estimate Errors	148
5-49.	Case # 031000D, + 100% Density: Velocity Estimate Errors	148
5-50.	Case # 031000D, -50% Density: Bank Angle Control Response	149
5-51.	Case # 031000D, -50% Density: Normalized In-Plane Lift	150
5-52.	Case # 031000D, -50% Density: Altitude History	150
5-53.	Case # 031000D, -50% Density: Position Estimate Errors	151
5-54.	Case # 031000D, -50% Density: Velocity Estimate Errors	151
5-55.	Case # 281000D, + 100% Density: Bank Angle Control Response	152
5-56.	Case # 281000D, + 100% Density: Normalized In-Plane Lift	153
5-57.	Case # 281000D, + 100% Density: Altitude History	153
5-58.	Case # 281000D, + 100% Density: Position Estimate Errors	154
5-59.	Case # 281000D, + 100% Density: Velocity Estimate Errors	154
5-60.	Case # 281000D, -50% Density: Bank Angle Control Response	155
5-61.	Case # 281000D, -50% Density: Normalized In-Plane Lift	156
5-62.	Case # 281000D, -50% Density: Altitude History	156
5-63.	Case # 281000D, -50% Density: Position Estimate Errors	157
5-64.	Case # 281000D, -50% Density: Velocity Estimate Errors	157
5-65.	Case # 030500D: Bank Angle Control Response	163
5-66.	Case # 030500D: Normalized In-Plane Lift	164
5-67.	Case # 030500D: Altitude History	164
5-68.	Case # 030500D: Position Estimate Errors	165
5-69.	Case # 030500D: Velocity Estimate Errors	165
5-70.	Case # 031000D: Bank Angle Control Response	166

5-71.	Case # 031000D: Normalized In-Plane Lift .....	167
5-72.	Case # 031000D: Altitude History .....	167
5-73.	Case # 031000D: Position Estimate Errors .....	168
5-74.	Case # 031000D: Velocity Estimate Errors .....	168
5-75.	Case # 031500D: Bank Angle Control Response .....	169
5-76.	Case # 031500D: Normalized In-Plane Lift .....	170
5-77.	Case # 031500D: Altitude History .....	170
5-78.	Case # 031500D: Position Estimate Errors .....	171
5-79.	Case # 031500D: Velocity Estimate Errors .....	171
5-80.	Case # 035000D: Bank Angle Control Response .....	172
5-81.	Case # 035000D: Normalized In-Plane Lift .....	173
5-82.	Case # 035000D: Altitude History .....	173
5-83.	Case # 035000D: Position Estimate Errors .....	174
5-84.	Case # 035000D: Velocity Estimate Errors .....	174
5-85.	Case # 038500D: Bank Angle Control Response .....	175
5-86.	Case # 038500D: Normalized In-Plane Lift .....	176
5-87.	Case # 038500D: Altitude History .....	176
5-88.	Case # 038500D: Position Estimate Errors .....	177
5-89.	Case # 038500D: Velocity Estimate Errors .....	177
5-90.	Case # 280500D: Bank Angle Control Response .....	178
5-91.	Case # 280500D: Normalized In-Plane Lift .....	179
5-92.	Case # 280500D: Altitude History .....	179
5-93.	Case # 280500D: Position Estimate Errors .....	180
5-94.	Case # 280500D: Velocity Estimate Errors .....	180
5-95.	Case # 281000D: Bank Angle Control Response .....	181
5-96.	Case # 281000D: Normalized In-Plane Lift .....	182
5-97.	Case # 281000D: Altitude History .....	182

5-98.	Case # 281000D: Position Estimate Errors	183
5-99.	Case # 281000D: Velocity Estimate Errors	183
5-100.	Case # 281500D: Bank Angle Control Response	184
5-101.	Case # 281500D: Normalized In-Plane Lift	185
5-102.	Case # 281500D: Altitude History	185
5-103.	Case # 281500D: Position Estimate Errors	186
5-104.	Case # 281500D: Velocity Estimate Errors	186
5-105.	Case # 285000D: Bank Angle Control Response	187
5-106.	Case # 285000D: Normalized In-Plane Lift	188
5-107.	Case # 285000D: Altitude History	188
5-108.	Case # 285000D: Position Estimate Errors	189
5-109.	Case # 285000D: Velocity Estimate Errors	189
5-110.	Case # 288500D: Bank Angle Control Response	190
5-111.	Case # 288500D: Normalized In-Plane Lift	191
5-112.	Case # 288500D: Altitude History	191
5-113.	Case # 288500D: Position Estimate Errors	192
5-114.	Case # 288500D: Velocity Estimate Errors	192

## LIST OF TABLES

Table		Page
2-1.	H-750 LINS Error Parameters. ....	38
2-2.	Density Model Parameters. ....	48
4-1.	COSPAR Northern Summer Density Profile .....	74
5-1.	Nominal Entry State Definition .....	81
5-2.	Input Filter Error Covariance Matrix .....	90
5-3.	Aerocapture Performance Results (Constant Density Bias Cases) .....	144
5-4.	Guidance Errors (Constant Density Bias Cases) .....	144
5-5.	Estimation Errors (Constant Density Bias Cases) .....	145
5-6.	Vehicle and Trajectory Limits (Constant Density Bias Cases) .....	145
5-7.	Aerocapture Performance Results (Density Shear Cases) .....	161
5-8.	Guidance Errors (Density Shear Cases) .....	161
5-9.	Estimation Errors (Density Shear Cases) .....	162
5-10.	Vehicle and Trajectory Limits (Density Shear Cases) .....	162

PRECEDING PAGE BLANK NOT FILMED

## SYMBOLS

$\underline{a}$	non-gravitational specific force vector
$AFE$	Aeroassist Flight Experiment
$AOTV$	aeroassisted orbital transfer vehicle
$\underline{b}$	Kalman filter measurement sensitivity vector
$b_\rho$	percentage deviation of true atmospheric density from nominal
$C_B$	vehicle ballistic coefficient
$C_B^I$	body-to-inertial transformation matrix
$C_D$	vehicle drag coefficient
$C_0, C_1, C_2, C_3$	density model scale height polynomial coefficients
$\underline{D}$	vehicle aerodynamic drag vector
$e_a$	random acceleration error
$e_{K_\rho}$	filter model of $K_\rho$ estimate error
$e_r$	position error induced by random acceleration error
$e_v$	velocity error induced by random acceleration error
$E$	Kalman filter error covariance matrix
$F$	system dynamics matrix
$\underline{g}$	gravitational acceleration vector
$g_{aero}$	aerodynamic load factor
$G$	gravity gradient matrix
$h$	altitude
$h_a$	apoapsis altitude
$HS$	exponential density model scale height
$\underline{i}_h$	normal to current orbit plane

$\hat{i}_{hd}$	normal to desired orbit plane
<i>IMU</i>	inertial measurement unit
$I_n$	n x n identity matrix
$K_h$	constant altitude cruise guidance altitude gain
$K_{\dot{h}}$	constant altitude cruise guidance altitude rate gain
$K_\rho$	percentage error in filter density
$\underline{L}$	vehicle aerodynamic lift vector
<i>L/D</i>	vehicle lift-to-drag ratio
<i>LINS</i>	Laser Inertial Navigation System
<i>m</i>	vehicle mass
<i>MRSR</i>	Mars Rover Sample Return
<i>n</i>	number of Kalman filter states
<i>NASA</i>	National Aeronautics and Space Administration
<i>q</i>	measurement value
$\bar{q}$	dynamic pressure
<i>Q</i>	total aerodynamic heat load
$\dot{Q}$	aerodynamic convective heating rate
$\underline{r}$	vehicle position vector
$r_M$	Mars equatorial radius
$r_{Ml}$	local Mars surface radius
$R_n$	vehicle nose radius
<i>S</i>	Kalman filter process noise matrix
$S_{HOR}$	density perturbation horizontal scale distance
$S_{ref}$	vehicle aerodynamic reference area
$S_{VERT}$	density perturbation vertical scale distance
<i>t</i>	time
<i>u</i>	scalar control variable

$\underline{v}$	vehicle velocity vector
$v_h$	horizontal velocity
$\underline{w}$	Kalman filter optimal weighting vector
$\underline{x}$	Kalman state vector
$\alpha^2$	variance of measurement error
$\beta$	guidance prediction density scale factor
$\gamma$	flight path angle
$\underline{\gamma}_{ABI}$	accelerometer bias vector
$\underline{\gamma}_{ASF}$	accelerometer scale factor vector
$\underline{\gamma}_{GDR}$	gyro drift vector
$\delta$	wedge angle
$\Delta d$	horizontal distance covered between atmosphere subroutine calls
$\Delta h$	vertical distance covered between atmosphere subroutine calls
$\Delta t$	time increment
$\Delta V$	required propulsive velocity change
$\Delta\phi_p$	increment to current bank command in guidance prediction
$\Delta\phi_c$	correction to current bank angle command
$\epsilon_{ra}$	radar altimeter error
$\epsilon_{rM}$	terrain height deviation from reference
$\zeta$	constant altitude cruise guidance damping ratio
$\eta$	zero-mean normal random variable with unity standard deviation
$\theta_r$	out-of-plane angular position
$\theta_v$	out-of-plane angular velocity
$\Lambda$	environment acceleration cross-product matrix

$\mu$	Mars gravitational parameter
$\mu_{e_r, e_v}$	covariance between $e_r$ and $e_v$
$\rho$	atmospheric density
$\rho_{\text{exp}}$	atmospheric density from exponential filter model
$\sigma_{ABI}$	accelerometer bias standard deviation
$\sigma_{ASF}$	accelerometer scale factor standard deviation
$\sigma_{\delta\rho}$	standard deviation of atmospheric density perturbation
$\sigma_{e_a}$	standard deviation of $e_a$
$\sigma_{e_r}$	standard deviation of $e_r$
$\sigma_{e_v}$	standard deviation of $e_v$
$\sigma_{GDR}$	gyro drift standard deviation
$\sigma_M$	filter Markov process standard deviation
$\tau_M$	filter Markov process time constant
$\phi$	current vehicle bank angle
$\Phi$	Kalman filter state transition matrix
$\underline{\psi}$	IMU misalignment vector
$\Psi$	IMU misalignment matrix
$\omega_{IM}$	Mars angular rotation rate
$\omega_n$	constant altitude cruise guidance natural frequency

### ***SUPERSCRIPTS***

$B$	body-fixed coordinate frame
$I$	inertial coordinate frame

.	first total derivative
..	second total derivative
^	estimated quantity
~	error in estimated quantity
-	old value
+	new value

### ***SUBSCRIPTS***

<i>ave</i>	average
<i>c</i>	commanded
<i>cur</i>	current
<i>d</i>	drag
<i>earth</i>	Earth-related quantity
<i>env</i>	environment
<i>f</i>	filter or final
<i>h</i>	altitude
<i>m</i>	measured or miss
<i>nom</i>	nominal
<i>p</i>	predictor
<i>pole</i>	in the direction of the north pole
<i>ra</i>	radar altimeter
<i>rel</i>	planet-relative
<i>0</i>	reference or initial

$\rho$

atmospheric density

## CHAPTER 1

### INTRODUCTION

#### 1.1 MARS ROVER SAMPLE RETURN MISSION

The extraterrestrial study of the planet Mars has been of great interest to the scientific community for many years. The Mariner and Viking missions flown by NASA in the 1960's and 1970's were highly successful in facilitating our initial proximate observations of the planet and its satellites. Information returned by the various flyby and orbital probes and the robot landers Viking I and II has greatly increased our knowledge of the planet over that gained by Earth-based observation alone. It is widely accepted that the next step in our exploration of Mars should be the return of surface samples to space station or Earth-based laboratories for firsthand analysis. Such a mission would take us a step beyond the Viking missions, allowing the direct analysis of a variety of surface samples taken from diverse sample sites. The sample return mission, in addition to providing a wealth of scientific data on Martian surface composition, would also present technological challenges leading to advances in spacecraft and mission design and operations.

The Mars Rover Sample Return (MRSR) mission under preliminary study by NASA [1] would have as its main objective the return of diverse surface samples from Mars. This mission is also viewed as a precursor to a manned Mars mission, with science and technology returns providing valuable input for the planning of such a journey. One potential MRSR mission scenario is illustrated in Figure 1-1 on page 25, reproduced from [2]. In this scenario, a single launch vehicle/upper stage combination is used to inject the spacecraft into Mars transfer orbit. Orbit insertion at Mars is accomplished by an aerocapture maneuver. After final landing site selection and inspection from orbit, the ascent/rover/entry vehicle combination reenters the atmosphere for landing, leaving the Mars orbiter and Earth return vehicles in orbit. A single rover with signif-

icant ranging capabilities proceeds to collect, catalogue, and store samples for return to the ascent vehicle. After transfer of the samples from the rover, the ascent vehicle is launched to achieve rendezvous with the orbiter. The samples, once transferred from the ascent vehicle, are injected into Earth return orbit by the return vehicle for eventual retrieval by the Space Shuttle or space station in Earth orbit. For such a mission to be feasible, technological advancement would be required in many areas, including semi-autonomous rover operations, autonomous navigation, autonomous rendezvous, sample handling techniques, and planetary capture and landing techniques. Current plans call for mission launch somewhere in the 1996 to 2000 time frame.

## 1.2 MOTIVATION

Since the return of a payload of samples to Earth is the main objective of the MRSR mission, it is highly desirable to maximize the ratio of sample mass to spacecraft launch mass. The efficient design of the vehicles and their systems will provide obvious benefits in terms of mass reduction, but mission design will also play a significant role due to its effect on propellant load requirements. The potential of large fuel (and, hence, mass) savings lies in the choice of the method used to allow spacecraft capture by Mars on the outbound trajectory and by Earth on the return trajectory. Historically, retropropulsion has been used for such maneuvers to decrease orbital energy and allow capture by the planetary gravity field. Alternatively, studies have shown that the necessary energy depletion can be achieved by aerodynamic deceleration during a close pass through the planet's atmosphere. This process is called aerocapture. In addition to orbit insertion accuracies comparable to all-propulsive scenarios, aerocapture into Mars can result in mass savings exceeding 25% of the approach mass [3], thereby allowing a significant reduction in launch mass for a given sample size.

## COMBINED LAUNCH MARS ROVER/SAMPLE RETURN MISSION

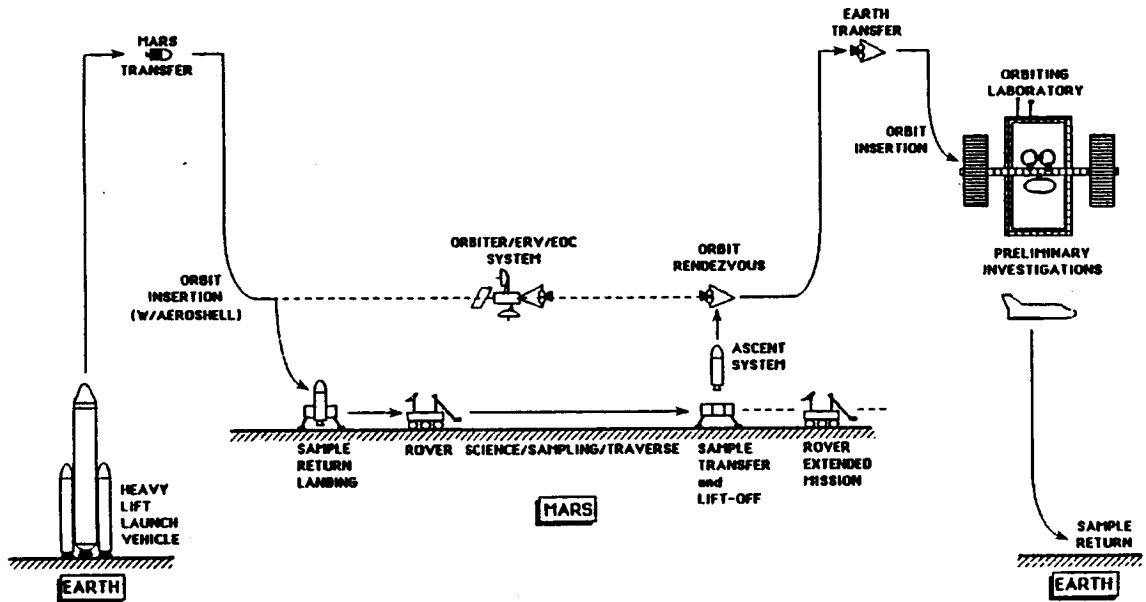


Figure 1-1. MRSR Mission Scenario

The aerocapture maneuver begins in much the same way as would a direct entry trajectory for landing. The planetary approach hyperbola is targeted so that the vehicle enters the atmosphere with desired flight path conditions. After atmospheric capture, the vehicle is aerodynamically controlled to deplete excess orbital energy. The major difference between entry and aerocapture is that the entry vehicle ultimately targets to a landing point on the surface of the planet, whereas the aerocapture vehicle targets to exit the atmosphere into a desired orbit. After

atmospheric exit, the propulsion system must be used to correct dispersions and insert the vehicle into its final parking orbit.

The success or failure of the aerocapture maneuver can be measured in terms of post-exit propulsive  $\Delta V$  required for orbit insertion. This  $\Delta V$  requirement is a function of the accuracy with which the vehicle can hit the desired exit orbit, which in turn is indirectly affected through the aerocapture guidance by uncertainties in vehicle mass and aerodynamic characteristics, errors in position and velocity estimates, and dispersions in atmospheric conditions. Sensitivity of target miss to these parameters requires a high degree of accuracy in onboard vehicle state estimates and a highly adaptive guidance system to respond to off-nominal conditions. The use of external navigation information and uplinked guidance commands during aerocapture is obviated by the possibility of blackout and the relatively short duration of the atmospheric pass, thereby requiring autonomous onboard guidance, navigation, and control of the vehicle to meet these requirements.

The purpose of the research leading to this thesis was to perform integrated design and analysis of the onboard navigation and guidance functions during aerocapture for a high lift-to-drag (L/D) ratio vehicle on a given nominal entry trajectory. During the actual aerocapture maneuver, guidance inputs, including current estimates of position and velocity and atmospheric dispersions, will be provided by the onboard navigation system. Therefore, the performance of the guidance system will be dependent to a certain extent on the performance of the navigation system. Previous aerocapture studies have focused almost entirely on either the navigation or the guidance aspect of the problem without examining the interactions between the two. The more balanced approach taken here was to base the guidance algorithm design and analysis on realistic inputs from a navigation system designed to take advantage of useful measurement information along the trajectory. This approach should increase confidence in guidance test results and provide a better overall picture of Mars aerocapture performance capabilities.

### *1.2.1 NAVIGATION*

As stated previously, the main function of the onboard navigation system during aerocapture is to provide accurate estimates of vehicle position, velocity and aerodynamic control capability to the guidance system for computation of trajectory control commands. This task is complicated by the presence of initial condition errors in position and velocity estimates, uncertainties in vehicle mass and aerodynamic characteristics, and unknown dispersions in atmospheric conditions. The heart of the onboard navigation system will be an inertial measurement unit (IMU). The IMU alone will provide accurate measurements of aerodynamic accelerations acting on the vehicle, allowing accurate propagation of position and velocity estimates. However, reduction of a priori state estimate errors and estimation of specific guidance parameters (e.g. atmospheric density, ballistic coefficient, or  $L/D$ ) requires further processing of IMU outputs and/or additional measurement information from other sources.

The approach taken here is to add an onboard Kalman filter to the navigation system for estimation of the vehicle position and velocity vectors and the deviation of the actual atmospheric density from the onboard model. The choice of density uncertainty as an estimated quantity was driven by the desire to provide the guidance with good knowledge of current aerodynamic control capability and the ability to predict future control capability. Two types of measurements have been examined to allow updating of initial state estimates and continuous estimation of density errors for the duration of atmospheric flight. After aerodynamic accelerations become large enough for measurement by the IMU, drag acceleration measurements are processed by the navigation filter. These measurements are actually incorporated by the filter as density altitude measurements by using an assumed atmospheric density model and estimated vehicle mass and aerodynamic parameters. Drag acceleration measurements are used during entry on the Space Shuttle [4], [5] for vertical channel stabilization and to improve knowledge of drag parameters used by the entry guidance. They have also been studied as an addition to the Aeroassist Flight

Experiment navigation system [6]. The density altitude measurement is useful for improving the accuracy of the altitude estimate to a level determined by the accuracy of the onboard density model and vehicle parameter estimates. In addition, errors in the knowledge of other position and velocity components may also be reduced due to correlations with vertical position contained in the initial filter covariance matrix. This measurement also allows continuous estimation of differences between the assumed density used by the guidance and the actual density observed through measured drag acceleration.

The addition of radar altimeter measurements prior to initiation of aerocapture control maneuvering has also been examined as a means to improve altitude knowledge before drag measurement processing begins. With accurate enough altitude determination, the entire drag measurement residual can be attributed to density model errors and corrections to the estimate made accordingly.

## **1.2.2 GUIDANCE**

### **1.2.2.1 INTRODUCTION**

The aerocapture vehicle used in this study is a biconic lifting body with a high lift-to-drag ratio ( $L/D=1.5$ ). A representative design configuration is shown in Figure 1-2 on page 30, reproduced from [7]. While the final design may have independent angle of attack control, it was assumed for this analysis that the vehicle will be designed to trim to a constant angle of attack. The only control in this case is the vehicle bank angle, which is the angle through which the lift vector is rotated about the atmosphere-relative velocity vector. Guidance becomes a question of determining what bank angle is required to meet target conditions for the current trajectory phase without violating vehicle or trajectory constraints. These constraints include terrain avoidance, aerodynamic heating limits, and structural load limits. The guidance must also be capable of

compensating for large trajectory dispersions due to entry navigation errors while maintaining control margin against future atmospheric density dispersions.

#### 1.2.2.2 PREVIOUS RESEARCH

Several approaches to aerocapture and aerobraking guidance for bank angle controlled vehicles have been suggested.

In [8] an atmospheric guidance algorithm for an aeroassisted orbital transfer vehicle (AOTV) is presented. This algorithm divides the aerobraking trajectory into an equilibrium glide phase and an exit phase. During the equilibrium glide phase, the guidance computes the bank angle required to satisfy a biased equilibrium glide (zero altitude acceleration) condition based on reference dynamic pressure and altitude rate profiles. Exit phase control is achieved by computing the altitude rate required to hit a target apoapsis altitude using an analytic predictor/corrector algorithm. The required bank angle is again computed to achieve a biased equilibrium glide condition, this time based only on reference altitude rate.

Another AOTV guidance concept is presented in [9]. This algorithm computes the sensitivity of exit apoapsis to current commanded bank angle using numerical integration of vehicle equations of motion to predict exit conditions. A correction algorithm utilizes this sensitivity to compute the increment to the current bank required to hit the apoapsis target.

Reference [10] presents an aeroassist guidance law which is based on an approximate analytic solution to the atmospheric flight equations of motion. This solution is used to find the bank angle control, based on the current  $L/D$  command, required to fly the vehicle from the current state to the final altitude achieving a given set of exit conditions. The algorithm is applied to the

ORIGINAL PAGE IS  
OF POOR QUALITY.

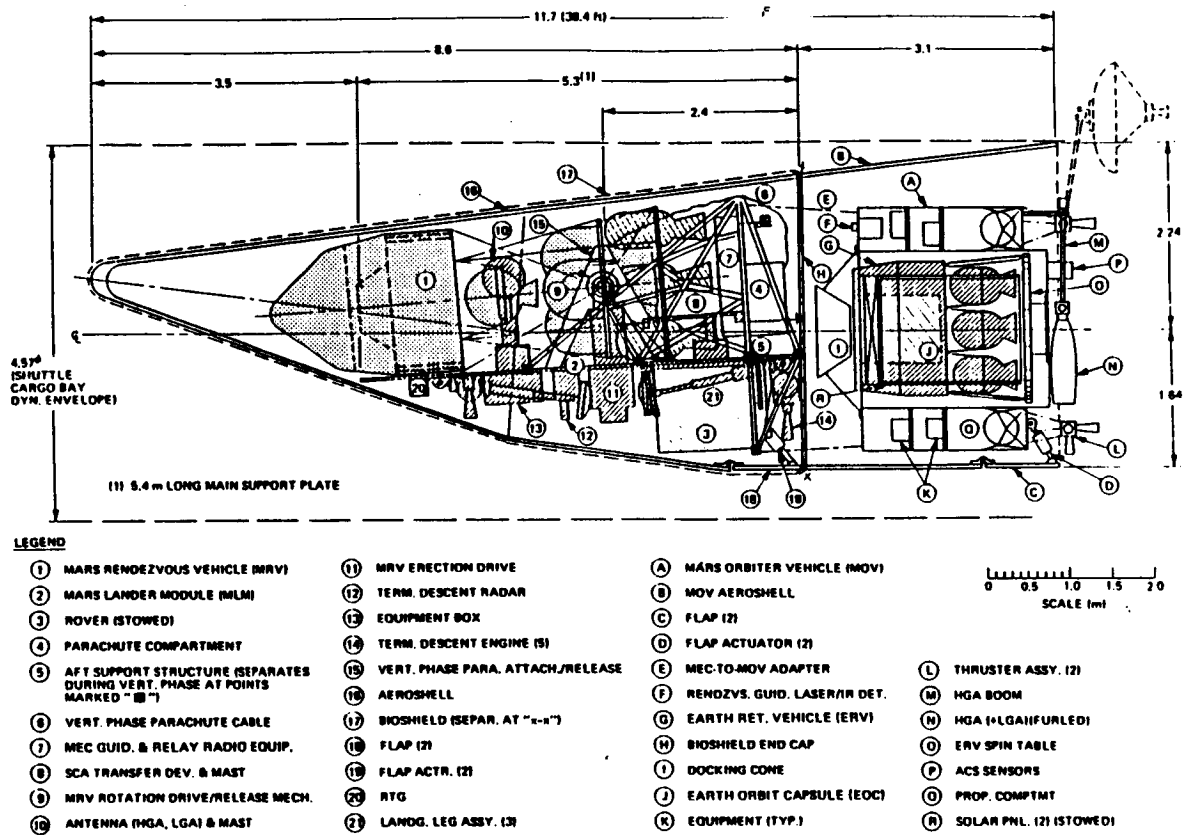


Figure 1-2. Potential Biconic Aerocapture Vehicle Configuration

MRSR aerocapture problem, commanding a constant altitude trajectory between unguided entry and exit phases.

### 1.2.2.3 PROPOSED ALGORITHM

The proposed approach is to fly a constant altitude trajectory at a given geometric altitude. Constant altitude flight is possible because of the control capability of the high L/D vehicle under

study, and is desirable for several reasons. Constraints on the allowable region of flight during aerocapture may easily be given in terms of an altitude corridor. The lower bound of the corridor is defined to satisfy terrain clearance constraints imposed due to large regions of high terrain present on Mars. The upper bound of the corridor is defined by the altitude above which vehicle control authority is insufficient to maintain constant altitude flight. Sustained constant altitude flight will be possible anywhere within this corridor. In addition, navigation results using IMU drag acceleration and radar altimeter measurements indicate that altitude errors should be small enough to prevent inadvertent flight outside the corridor. Flight at constant altitude is also desirable due to the trajectory uniformity provided. The effect is to desensitize the important atmospheric exit phase to entry trajectory dispersions. If the constant altitude cruise condition can be reached from the dispersed entry trajectory and flown until a given velocity has been reached, the exit trajectory will vary only due to errors in the knowledge of altitude and velocity and the effects of roll reversals.

The aerocapture trajectory has been divided into three phases:

1. atmospheric capture
2. constant-altitude cruise
3. exit

The three phases all have different targets and constraints and therefore can best be flown using different guidance schemes.

The atmospheric capture guidance phase extends from the initiation of guidance cycling after atmospheric entry until the vehicle reaches the target cruise altitude. The goal of this phase is to

determine the constant bank angle control required to reach the target cruise altitude with zero altitude rate. A numerical predictor/corrector guidance algorithm has been chosen for this phase. Control corrections are computed based on numerical prediction of final conditions given the current commanded control and estimated vehicle state vector. A key advantage of such an algorithm is its lack of dependence on knowledge of a reference trajectory. This makes it well-suited to handle the wide range of off-nominal entry trajectory dispersions possible due to approach navigation accuracy limits. If guidance cycling begins after navigation system cycling, state vector and density errors can be reduced to levels allowing very accurate numerical prediction of end conditions on the current trajectory, even if the initial state errors place it far off of the nominal trajectory.

A disadvantage of the numerical predictor/corrector is that it can be more computationally intensive than an analytic algorithm. Although the entire aerocapture maneuver can be quite long (500 to 1200 seconds), the capture phase is relatively short (less than 150 seconds). Therefore, if a reasonable integration step size can be chosen for the guidance prediction, the computational demands of numerical full-state prediction should not be overly excessive.

The constant altitude cruise phase is initiated when the vehicle reaches the target cruise altitude and is terminated when the inertial velocity has been decreased to a given value. The goal of this phase is simply to maintain level flight at the cruise altitude. This includes compensating for density dispersions and perturbations due to roll reversals. An analytic control law which results in altitude response analogous to a second-order spring/mass/damper system has been derived for this phase. Altitude response can be modelled as desired by the choice of two control gains.

The exit phase is initiated immediately at the end of the cruise phase and is terminated when measured aerodynamic acceleration drops below a set value. The goal of this phase is to compute the constant bank angle command required to hit the target apoapsis altitude at atmospheric exit.

Numerical predictor/corrector guidance has been chosen for this phase for essentially the same reasons as for the capture phase. The exit phase guidance can make use of the same prediction subroutine as the capture phase guidance, and the guidance similarity makes possible the use of the same correction equations modified simply for the different target quantity.

### 1.3 THESIS OVERVIEW

This thesis contains details and results of the design and testing of the navigation and guidance algorithms described above.

“Chapter 2. NAVIGATION SYSTEM DESIGN” on page 35 presents details of the navigation system design. The main components of the system are described, and computer models derived. The estimator design is discussed in detail, including the basic Kalman filter equations and measurement models used in the filter.

“Chapter 3. GUIDANCE DESIGN” on page 51 presents details of the guidance algorithm design and implementation. The three guidance phases and their respective guidance philosophies, targets, and constraints are discussed. The final section of the chapter addresses orbit plane control and presents the algorithm used for this study.

“Chapter 4. COMPUTER SIMULATION PROGRAM” on page 69 describes the computer simulation used in this research. Overall program flow is described, and environment and vehicle models presented.

Performance results are presented in “Chapter 5. PERFORMANCE RESULTS” on page 79. The performance of both the navigation and guidance algorithms is discussed for a number of

cases. Results are presented for nominal and dispersed entry trajectories flown with constant density bias and density shear profiles. The effects of adding radar altimeter measurements are illustrated and discussed.

"Chapter 6. CONCLUSION" on page 193 discusses conclusions of this study and suggestions for continuing analysis.

## CHAPTER 2

### NAVIGATION SYSTEM DESIGN

#### 2.1 INTRODUCTION

This chapter details the design and implementation of the proposed aerocapture navigation system described in general in "1.2.1 NAVIGATION" on page 27. The presentation is segmented to reflect the three main components of the system: the IMU, radar altimeter, and estimation algorithm. Descriptions of the IMU and radar altimeter models implemented in the simulation environment are presented. The estimation algorithm design is explained in detail, beginning with presentation of the Kalman filter equations which form the heart of the algorithm. The filter state vector is defined, and the filter models of the dynamics affecting its components are given. The filter error covariance matrix is defined, and the state transition and process noise matrices used for propagation of the covariance matrix are presented. Finally, models of the drag acceleration and radar altimeter measurements implemented in the estimator are derived.

#### 2.2 INERTIAL MEASUREMENT UNIT

The inertial measurement unit (IMU) provides a measure of the non-gravitational inertial specific force acting on the vehicle. It consists of three accelerometers, which measure the specific force components along orthogonal axes; three gyroscopes, which measure angular rates about these axes; and a computer for processing instrument outputs. It has been assumed for this analysis that the IMU outputs the three specific force components directly. It is also assumed that the IMU is a strapdown system, so that the components of the specific force and angular rate vectors are coordinatized in a body-fixed reference frame. The gyro outputs are used to maintain a trans-

formation matrix from the body-fixed IMU frame to the inertial frame, so that the specific force vector may be transformed for vehicle navigation in the inertial frame.

The sensed specific force components output by the IMU differ from the true specific force components due to the many error sources present. These error sources include accelerometer and gyro measurement inaccuracies and uncertain knowledge of the initial alignment of the IMU axes with respect to inertial space. In the simplified IMU model used for this study, the measured specific force is computed as

$$\underline{a}_m^I = \underline{a}_{env}^I - \Psi \underline{a}_{env}^I + C_b^I [\underline{\gamma}_{ABI}^B + \Lambda \underline{\gamma}_{ASF}^B] \quad (2-1)$$

where  $\underline{a}_m^I$  is the measured specific force,  $\underline{a}_{env}^I$  is the environment (true) specific force,  $C_b^I$  is the body to inertial transformation matrix, and  $\underline{\gamma}_{ABI}^B$  and  $\underline{\gamma}_{ASF}^B$  are vectors containing accelerometer bias and scale factor values, respectively. The superscript  $I$  indicates coordinatization in the inertial reference frame, and the superscript  $B$  indicates coordinatization in the body-fixed IMU frame, which is defined to have reference axes parallel to the accelerometer and gyro input axes. The "inertial" frame is defined to be Mars-centered with X and Y axes in the equatorial plane and the Z axis parallel to the planet spin axis. The accelerometer bias and scale factor components are assumed to be constants chosen from normal, zero-mean random distributions with standard deviations  $\sigma_{ABI}$  and  $\sigma_{ASF}$ , respectively. The matrix  $\Lambda$  is defined as

$$\Lambda = \begin{bmatrix} a_{env_x}^B & 0 & 0 \\ 0 & a_{env_y}^B & 0 \\ 0 & 0 & a_{env_z}^B \end{bmatrix} \quad (2-2)$$

where  $a_{env_x}^B$ ,  $a_{env_y}^B$ , and  $a_{env_z}^B$  are the components of  $\underline{a}_{env}$  in the body-fixed IMU reference frame. The misalignment matrix,  $\Psi$ , is defined as

$$\Psi = \begin{bmatrix} 0 & \psi_z & -\psi_y \\ -\psi_z & 0 & \psi_x \\ \psi_y & -\psi_x & 0 \end{bmatrix} \quad (2-3)$$

where  $\psi_x$ ,  $\psi_y$ , and  $\psi_z$  are the misalignment angles of the IMU frame about inertial axes. The platform misalignment is a function of both the initial misalignment and gyro drift rates. This functional relationship is expressed by the vector differential equation

$$\underline{\dot{\psi}}^I = C_B^I \underline{\gamma}_{GDR}^B \quad (2-4)$$

subject to the initial condition

$$\underline{\psi}^I(0) = \underline{\psi}_0$$

This equation is integrated numerically during the simulation to give the current platform misalignment. The components of the gyro drift rate vector  $\underline{\gamma}_{GDR}$  are assumed to be constants chosen from a normal, zero-mean random distribution with standard deviation  $\sigma_{GDR}$ .

The specific IMU chosen for this analysis is the Honeywell H-750 Laser Inertial Navigation System (LINS). The H-750 LINS is a space-qualified strapdown IMU which is currently a strong candidate for use as the primary navaid for the Aeroassist Flight Experiment (AFE) and the aeroassisted orbital transfer vehicle (AOTV). The error parameters used in the simulator model are listed in Table 2-1 on page 38 [11]. Random errors are computed using a random number generator which outputs one sample of a normally-distributed random variable with a mean of

Table 2-1. H-750 LINS Error Parameters.

Error Parameter	Symbol	1 $\sigma$ Value
Accelerometer Bias	$\gamma_{ABI}$	17 $\mu g$
Accelerometer Scale Factor	$\gamma_{ASF}$	70 ppm
Gyro Bias Drift	$\gamma_{GDR}$	0.01 deg/hr
Initial X-Axis Misalignment	$\psi_{x0}$	100 arcsec
Initial Y-Axis Misalignment	$\psi_{y0}$	100 arcsec
Initial Z-Axis Misalignment	$\psi_{z0}$	100 arcsec

zero and standard deviation equal to the input. The initial misalignment angles were chosen as conservative approximations of the accuracy obtained when aligning the space shuttle inertial platform using an onboard star tracker [15].

### 2.3 RADAR ALTIMETER

The radar altimeter is a device which provides information on the altitude of the vehicle above the local terrain. The measured altitude,  $h_m$ , can be expressed as

$$h_m = (r_{env} - r_{M_l}) + \varepsilon_{ra} \quad (2-5)$$

where  $r_{env}$  is the environment (true) distance from the center of Mars to the vehicle,  $r_{M_l}$  is the local distance from the center to the surface of Mars, and  $\varepsilon_{ra}$  is the error introduced by instrument inaccuracies. The local planet radius can be written as

$$r_{M_i} = r_M + \epsilon_{r_M} \quad (2-6)$$

where  $\epsilon_{r_M}$  represents the variation of local terrain height about the reference radius  $r_M$ . In this study, it was assumed that radar altimeter measurements will be possible in a narrow altitude band prior to commencement of vehicle bank maneuvers (see "2.4.3.2 RADAR ALTIMETER MEASUREMENT" on page 49). The elapsed time between these altitudes on the inbound trajectory is approximately 15 seconds. It is assumed that the terrain height variation over this interval is small and that  $\epsilon_{r_M}$  can be modelled for simplicity as a constant bias chosen from a normal random distribution with a mean of zero and a standard deviation of 1 km. For this study, it is assumed that  $\epsilon_{r_a}$  is an additive noise term modelled as a zero-mean normal random variable with a standard deviation of 1 km.

## 2.4 ESTIMATOR DESIGN

### 2.4.1 KALMAN FILTER EQUATIONS

The Kalman filter is a recursive algorithm designed to compute the minimum variance estimate of an  $n \times 1$  vector of system states, denoted  $\underline{x}$ , using noisy measurement data. The filter is derived under the assumption that the system is linear and that the system dynamics can be described by means of a set of linear differential equations. The two main functions of the Kalman filter are the incorporation of measurements to update the current filter estimate of the state vector and the propagation of the state vector estimate between measurement updates. The filter keeps track of its own performance during the estimation process by updating and propagating a covariance matrix whose elements provide a statistical measure of the error in the estimate of the state vector. The error covariance matrix is defined as

$$E(t) = \overline{[\tilde{\underline{x}}(t)\tilde{\underline{x}}^T(t)]} \quad (2-7)$$

where

$\tilde{\underline{x}}(t)$  = error in state vector estimate

$$= \hat{\underline{x}}(t) - \underline{x}(t)$$

$\underline{x}(t)$  = true state vector

$\hat{\underline{x}}(t)$  = estimated state vector

and the overbar denotes the expected value of the bracketed quantity. The "hat" symbol ( $\hat{\quad}$ ) will subsequently be used to denote an estimated quantity. It is seen that  $E$  is a symmetric matrix whose diagonal elements are the variances of the errors in the state vector elements and whose off-diagonal elements are a measure of the correlations between the errors in the state vector elements.

The dynamics of the system under analysis can be described by a nonlinear vector differential equation of the general form

$$\dot{\underline{x}}(t) = \underline{f}(\underline{x}(t), u(t), t) \quad (2-8)$$

where  $u$  is the scalar control. The filter state vector estimate is propagated between measurement updates by numerical integration of the differential equation

$$\dot{\hat{\underline{x}}}(t) = \underline{f}(\hat{\underline{x}}(t), u(t), t) \quad (2-9)$$

using a fourth-order Runge-Kutta algorithm. The covariance matrix is propagated between updates using

$$E(t + \Delta t) = \Phi(t) E(t) \Phi^T(t) + S(t) \quad (2-10)$$

where  $\Phi(t)$  is the state transition matrix,  $S(t)$  is the process noise matrix, and  $\Delta t$  is the propagation time step size. The state transition matrix satisfies the matrix differential equation

$$\dot{\Phi}(t) = F(t) \Phi(t) \quad (2-11)$$

where  $F(t)$  is the system dynamics matrix corresponding to the linearized form of (2-8), namely

$$\dot{\underline{x}}(t) = F(t) \underline{x}(t) \quad (2-12)$$

The process noise matrix is included to compensate for unmodelled effects in the covariance matrix propagation. These might include the effects of linearization, unmodelled accelerations, unmodelled IMU errors, and computer numerical inaccuracies. The elements of  $S(t)$  are functions of the assumed statistical properties of these effects. Specific values of  $\Phi$  and  $S$  used in the aerocapture navigation filter are given in "2.4.2.2 COVARIANCE MATRIX PROPAGATION" on page 44.

Given a measurement  $q$ , the state estimate is updated using

$$\hat{\underline{x}}^+ = \hat{\underline{x}}^- + \underline{w} (q - \hat{q}) \quad (2-13)$$

where

$$\underline{w} = \frac{E \underline{b}^T}{\underline{b} E \underline{b}^T + \alpha^2} \quad (2-14)$$

is the  $n \times 1$  optimal weighting vector,  $\hat{q}$  is the estimate of the measurement  $q$  given the information from all previously incorporated measurements,  $\underline{b}$  is a  $1 \times n$  matrix expressing the sensitivity of the measurement to the state vector,  $\alpha^2$  is the assumed variance of the measurement error, and

the superscript plus and minus signs refer to state vector estimates after and before incorporation of the measurement, respectively. The covariance matrix is updated using

$$E^+ = (I_n - \underline{w}\underline{b})E^- \quad (2-15)$$

where  $I_n$  is the  $n \times n$  identity matrix.

The basic Kalman filter equations used in the navigation system have been presented above for continuity and completeness. For more comprehensive discussions of recursive estimation and Kalman filtering, the reader is referred to References [12], [13], and [14].

## 2.4.2 DYNAMICS MODELS

### 2.4.2.1 STATE VECTOR PROPAGATION

The filter state vector is defined to be

$$\underline{x} = \begin{bmatrix} \underline{r}^I \\ \underline{v}^I \\ K_\rho \end{bmatrix} \quad (2-16)$$

where  $\underline{r}^I$  and  $\underline{v}^I$  are the  $3 \times 1$  inertial position and velocity vectors of the spacecraft.  $K_\rho$  is a bias term which indicates the percentage deviation of the current actual atmospheric density from the exponential filter model, so that

$$K_\rho = \frac{\rho_{env}}{\rho_{exp}} - 1 \quad (2-17)$$

where  $\rho_{env}$  is the true density at a given altitude and  $\rho_{exp}$  is the density at the same altitude computed using an exponential approximation to the nominal profile. The choice of  $K_\rho$  as an estimated quantity, along with the implicit estimate of altitude contained in the position vector estimate, allows very accurate determination of the current density in spite of the inability of the filter to differentiate between a density error and an altitude error. This result is discussed further in “5.3.3 NAVIGATION TEST CASES” on page 91.

Propagation of the state estimate requires determination of the function  $f$  in Eq. (2-9). The equations governing the dynamics of the position and velocity vector estimates during atmospheric flight are

$$\frac{d\hat{r}^I}{dt} = \hat{v}^I \quad (2-18)$$

$$\frac{d\hat{v}^I}{dt} = \underline{g}_f^I + \underline{a}_m^I \quad (2-19)$$

In Eq. (2-19),  $\underline{g}_f^I$  is the gravitational acceleration computed using the filter model and  $\underline{a}_m^I$  is the IMU-measured nongravitational specific force given by Eq. (2-1). Assuming a spherical planet, the gravitational acceleration can be modelled as

$$\underline{g}_f^I = -\frac{\mu}{\hat{r}^2} \frac{\hat{r}}{\hat{r}} \quad (2-20)$$

where  $\mu$  is the gravitational parameter of Mars and  $\hat{r}$  is the magnitude of the position vector estimate. The density bias estimate is propagated as a constant; that is

$$\frac{dK_\rho}{dt} = 0 \quad (2-21)$$

Modelling of the density bias estimate as a constant, when coupled with the modelling of the error in this estimate in the covariance matrix as a first-order Markov process, allows estimation of a wide range of density error profiles without modification of filter models.

### 2.4.2.2 COVARIANCE MATRIX PROPAGATION

Propagation of the error covariance matrix between measurement updates requires determination of the state transition and process noise matrices in Eq. (2-10). These matrices are derived here under the assumption that the dynamics of the error in  $\hat{K}_\rho$  are independent of the dynamics of the errors in  $\hat{r}^T$  and  $\hat{v}^T$ . In this case, the two matrices can be partitioned as

$$\Phi = \begin{bmatrix} \Phi_{rv} & \underline{0} \\ \underline{0}^T & \Phi_{K\rho} \end{bmatrix} \quad (2-22)$$

and

$$S = \begin{bmatrix} S_{rv} & \underline{0} \\ \underline{0}^T & S_{K\rho} \end{bmatrix} \quad (2-23)$$

and the nonzero partitions derived independently.

In the absence of aerodynamic forces, the system dynamics matrix  $F_v(t)$  of Eq. (2-12) corresponding to the linearized position and velocity is [12]

$$F_v(t) = \begin{bmatrix} 0_3 & I_3 \\ G(t) & 0_3 \end{bmatrix} \quad (2-24)$$

where

$$G = \frac{\mu}{r^3} (3r r^T - r^2 I_3) \quad (2-25)$$

is the 3 x 3 gravity gradient matrix, and  $I_3$  and  $0_3$  are the three-dimensional identity and zero matrices, respectively.  $\Phi_{rv}$  can now be found by solution of Eq. (2-11). An approximate solution is given in Reference [4] as

$$\Phi_{rv}(t) = \begin{bmatrix} I_3 + G_{ave}(\Delta t)^2/2 & I_3 \Delta t \\ G_{ave} \Delta t & I_3 + G_{ave}(\Delta t)^2/2 \end{bmatrix} \quad (2-26)$$

where

$$G_{ave} = \frac{1}{2} [ G(\hat{\mathcal{L}}(t)) + G(\hat{\mathcal{L}}(t + \Delta t)) ] \quad (2-27)$$

Thus,  $G_{ave}$  is the average gravity gradient matrix over the current propagation interval.

The process noise affecting propagation of position and velocity estimate errors is assumed to be due completely to a random acceleration error, denoted  $e_a$ . Inclusion of this noise term helps to compensate for covariance propagation errors due to the approximations made in deriving the state transition matrix of Eq. (2-26). The acceleration noise is assumed to be normal with zero mean and variance  $\sigma_{e_a}^2$ . The errors in position and velocity components induced by this acceleration over one propagation step are

$$e_v = e_a \Delta t \quad (2-28)$$

and

$$e_r = \frac{1}{2} e_a (\Delta t)^2 \quad (2-29)$$

The variances of  $e_r$  and  $e_v$ , and their covariance are therefore given by

$$\sigma_{e_v}^2 = \sigma_{e_a}^2 (\Delta t)^2 \quad (2-30)$$

$$\sigma_{e_r}^2 = \frac{1}{4} \sigma_{e_a}^2 (\Delta t)^4 \quad (2-31)$$

$$\mu_{e_r, e_v} = \frac{1}{2} \sigma_{e_a}^2 (\Delta t)^3 \quad (2-32)$$

Assuming that the variances of the errors in each component are the same, the partition of  $S$  corresponding to position and velocity is given by

$$S_{rv} = \begin{bmatrix} \sigma_{e_r}^2 I_3 & \mu_{e_r, e_v} I_3 \\ \mu_{e_r, e_v} I_3 & \sigma_{e_v}^2 I_3 \end{bmatrix} \quad (2-33)$$

A value of  $[10\mu g]^2$  ( $[9.8 \times 10^{-5} m/s^2]^2$ ) was chosen empirically for  $\sigma_{e_a}^2$  for this analysis.

The error in the estimate of  $K_\rho$  is modelled in the covariance matrix as a first-order Markov process. The error values are thus assumed to be exponentially correlated in time. In this model, the error at the current time is defined as

$$e_{K_\rho}(t) = a_M e_{K_\rho}(t - \Delta t) + \sigma_M \sqrt{1 - a_M^2} \eta \quad (2-34)$$

where

$$a_M = e^{-\Delta t / \tau_M}$$

and  $\sigma_M$  and  $\tau_M$  are the standard deviation and time constant defining the Markov process.  $\eta$  is a normal random variable with mean zero and standard deviation one. Given this model of the estimation error in  $K_\rho$ , the corresponding partition of  $\Phi$  is

$$\Phi_{K_\rho} = a_M \quad (2-35)$$

and the process noise is

$$S_{K_\rho} = \sigma_M^2 (1 - a_M^2) \quad (2-36)$$

The effect of the process noise in this case is to keep the filter actively estimating the continuously changing density bias by maintaining a high variance in the covariance matrix. A standard deviation of 1 and time constant of 100 seconds were found to provide good tracking of a variety of dynamic density bias fluctuations.

### 2.4.3 MEASUREMENT MODELS

#### 2.4.3.1 DENSITY ALTITUDE MEASUREMENT

The "measured" density altitude is actually computed using an IMU drag acceleration measurement and an assumed model of the atmospheric density profile. An exponential density model of the form

$$\rho_{\text{exp}} = \rho_0 e^{-(h - h_0)/HS} \quad (2-37)$$

is implemented in the estimator. The model scale height,  $HS$ , is computed using

$$HS = C_0 + C_1 h + C_2 h^2 + C_3 h^3 \quad (2-38)$$

where the coefficients  $C_0, \dots, C_3$  are chosen so that the exponential model closely matches the nominal Mars atmosphere data. Table 2-2 on page 48 lists the density model parameters corresponding to the simulator environment model (see Table 4-1 on page 74).

Using this model, the density altitude corresponding to the measured drag acceleration  $a_{d_m}$  is

$$q_{h\rho} = h_0 + HS \ln \left[ \frac{\rho_0 \hat{v}_{rel}^2}{2 C_B a_{d_m}} \right] \quad (2-39)$$

where

Table 2-2. Density Model Parameters.

Altitude Range	Model Parameter	Value
0 → 50 km	$h_0$	0 km
	$\rho_0$	0.0156 kg/m <sup>3</sup>
	$C_0$	10.8301848 km
	$C_1$	0.0790101
	$C_2$	-0.0036160 km <sup>-1</sup>
	$C_3$	0.0000347 km <sup>-2</sup>
50 → 100 km	$h_0$	50 km
	$\rho_0$	0.000108 kg/m <sup>3</sup>
	$C_0$	10.5642821 km
	$C_1$	-0.0506220
	$C_2$	0.0001290 km <sup>-1</sup>
	$C_3$	0.0000009 km <sup>-2</sup>

$$a_{d_m} = \underline{a}_m^I \cdot \left( -\frac{\hat{v}_{rel}^I}{|\hat{v}_{rel}^I|} \right) \quad (2-40)$$

$$\hat{v}_{rel}^I = \hat{v}^I - \omega_{IM} (\hat{i}_{pole} \times \hat{r}^I) \quad (2-41)$$

$$C_B = \frac{m}{C_D S_{ref}} \quad (2-42)$$

and  $\underline{a}_m^l$  is the IMU-measured specific force given by Eq. (2-1). The estimate of the density altitude measurement is given by

$$\hat{q}_{h\rho} = \hat{h} - HS \ln(1 + \hat{K}_\rho) \quad (2-43)$$

where  $\hat{h}$  is the current filter estimate of geometric altitude. Equations (2-39) and (2-43) are derived in detail in “Appendix A. DERIVATION OF DENSITY ALTITUDE MEASUREMENT EQUATIONS” on page 197. From Eq. (2-43), the measurement sensitivity vector is found to be

$$\underline{b}_{h\rho} = \left[ \text{UNIT}(\hat{r}), 0, 0, 0, -\frac{HS}{1 + \hat{K}_\rho} \right] \quad (2-44)$$

Density altitude measurements are incorporated by the estimator when the measured aerodynamic load factor exceeds 0.01 g's (0.098  $m/s^2$ ). When the radar altimeter is used, incorporation of density altitude measurements is delayed until altimeter measurements cease (see “2.4.3.2 RADAR ALTIMETER MEASUREMENT”). Estimator performance does not appear to be significantly impacted by the density altitude measurement update frequency, so a frequency of 0.1 Hz was used to decrease computational requirements. The filter measurement variance was chosen empirically to be (3 km)<sup>2</sup>.

#### 2.4.3.2 RADAR ALTIMETER MEASUREMENT

The radar altimeter measurement to be incorporated by the estimator is given by

$$q_{ra} = h_m \quad (2-45)$$

where  $h_m$  is given by Eq. (2-5). The estimate of this measurement is simply the filter altitude estimate, or

$$\hat{q}_{ra} = \hat{r} - r_M \quad (2-46)$$

The reference planet radius  $r_M$  is modelled as a constant equal to the equatorial radius (3397.2 km.). The corresponding sensitivity vector is

$$\underline{b}_{ra} = [ \text{UNIT}(\hat{r}), 0, 0, 0, 0 ] \quad (2-47)$$

Because of antenna pointing constraints, use of the altimeter is feasible only during the portions of atmospheric flight when the vehicle is not rolling to follow bank commands. This would include the segments immediately after entry and before exit when aerodynamic forces are too small for trajectory control to be possible. It is assumed that the altimeter will be used only prior to aerocapture, and that it is effective at altitudes below 100 km. Since vehicle maneuvering begins soon after passing through 80 km, this altitude is chosen as the minimum for altimeter measurements. Measurements are taken at a frequency of 0.5 Hz while the measured altitude is in this range. The filter measurement variance  $\alpha_a^2$  is set to a constant value of  $(2 \text{ km})^2$  for altimeter measurement incorporation.

## CHAPTER 3

### GUIDANCE DESIGN

#### 3.1 INTRODUCTION

The aerocapture vehicle used in this study utilizes lift vector modulation about the relative velocity vector for trajectory control. The direction of the lift vector is specified by the bank angle, denoted  $\phi$ , as shown in Figure 3-1 on page 52. By definition, positive bank implies a right hand rotation about the relative velocity vector. Bank angle values can range from  $-180^\circ$  to  $180^\circ$ , with  $\phi = 0^\circ$  implying lift vector "up" in the vertical plane. It has been assumed for this study that the orbital energy control problem can be treated as independent from the orbit plane orientation control problem. The choice of a bank angle command can thus be divided into two independent parts: determination of the angle magnitude required to achieve the desired energy control and choice of the sign of this angle to control the direction of rotation of the orbit plane. In order to maintain at least a small perpendicular lift component for plane control at all times, the magnitude of the bank angle command is constrained to lie between  $15^\circ$  and  $165^\circ$ .

This chapter contains details of the design of the guidance algorithm proposed for trajectory control during aerocapture. The three guidance phases - capture, constant-altitude cruise, and exit - are addressed. Discussions of guidance target selection and derivations of important guidance equations are presented for each phase. The final section of the chapter contains a discussion of the orbit plane control logic.

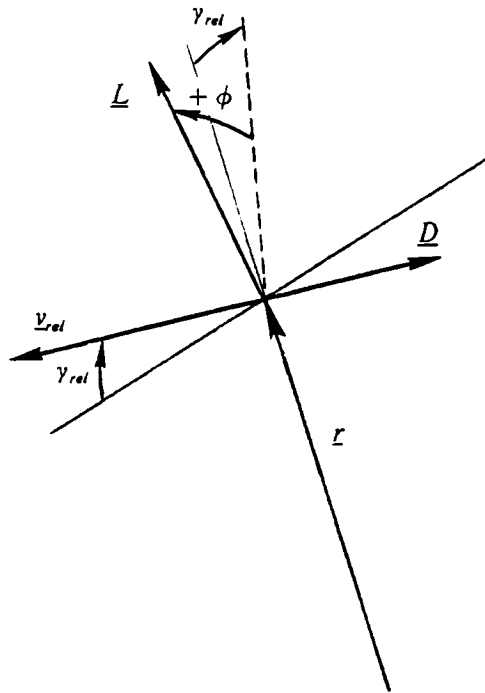


Figure 3-1. Bank Angle Control Definition

## 3.2 ATMOSPHERIC CAPTURE PHASE

### 3.2.1 TARGET CRUISE ALTITUDE

The choice of the nominal cruise altitude is by no means unique. Figure 3-2 on page 54 illustrates the flyable altitude corridor for the vehicle and nominal entry trajectory examined in this study. The minimum altitude of the corridor (27 km) is fixed by terrain clearance constraints. It is assumed that this altitude is set by the largest volcano, Olympus Mons, whose altitude above the reference surface is 27 km [16]; however, since the planet-relative location of the aerocapture trajectory will be known, this lower limit could be reduced if warranted. The maximum corridor altitude (44 km) is set by the limit of vehicle control capability, that is, this is the highest altitude

at which the vehicle, entering on the nominal trajectory and with nominal atmospheric density, can maintain constant altitude flight long enough for capture to occur. Constant altitude flight is possible anywhere within the corridor. The nominal cruise altitude is chosen to provide margin for hot days, when the actual atmospheric density is less than the nominal. For a 60% thin atmosphere, the maximum altitude at which constant altitude flight is possible drops to approximately 34 km. This is expected since the density at 34 km is now approximately equivalent to the nominal density at 44 km. Therefore, this is chosen as the cruise altitude to provide a large margin for thin atmospheric density dispersions. It should also be noted that a 7 km margin remains with respect to the minimum corridor altitude. This margin will help to compensate for possible undershoot of the target altitude in the capture phase and cruise altitude errors due to navigated altitude uncertainties.

### 3.2.2 GUIDANCE DESCRIPTION

The purpose of the capture guidance phase is to compute bank angle commands to drive the vehicle to reach the target cruising altitude ( $h_{cruise}$ ) with zero altitude rate. Numerical predictor/corrector guidance has been selected for this phase for the reasons stated in "Chapter 1. INTRODUCTION" on page 23. Basically, the guidance corrects the current commanded bank angle based on prediction of the target miss given the current command. The nominal guidance cycle is as follows:

1. Set predictor bank angle to current command ( $\phi_c$ )
2. Initialize predictor state vector to current navigation system estimated state
3. Predict final altitude ( $\dot{h} = 0$ )

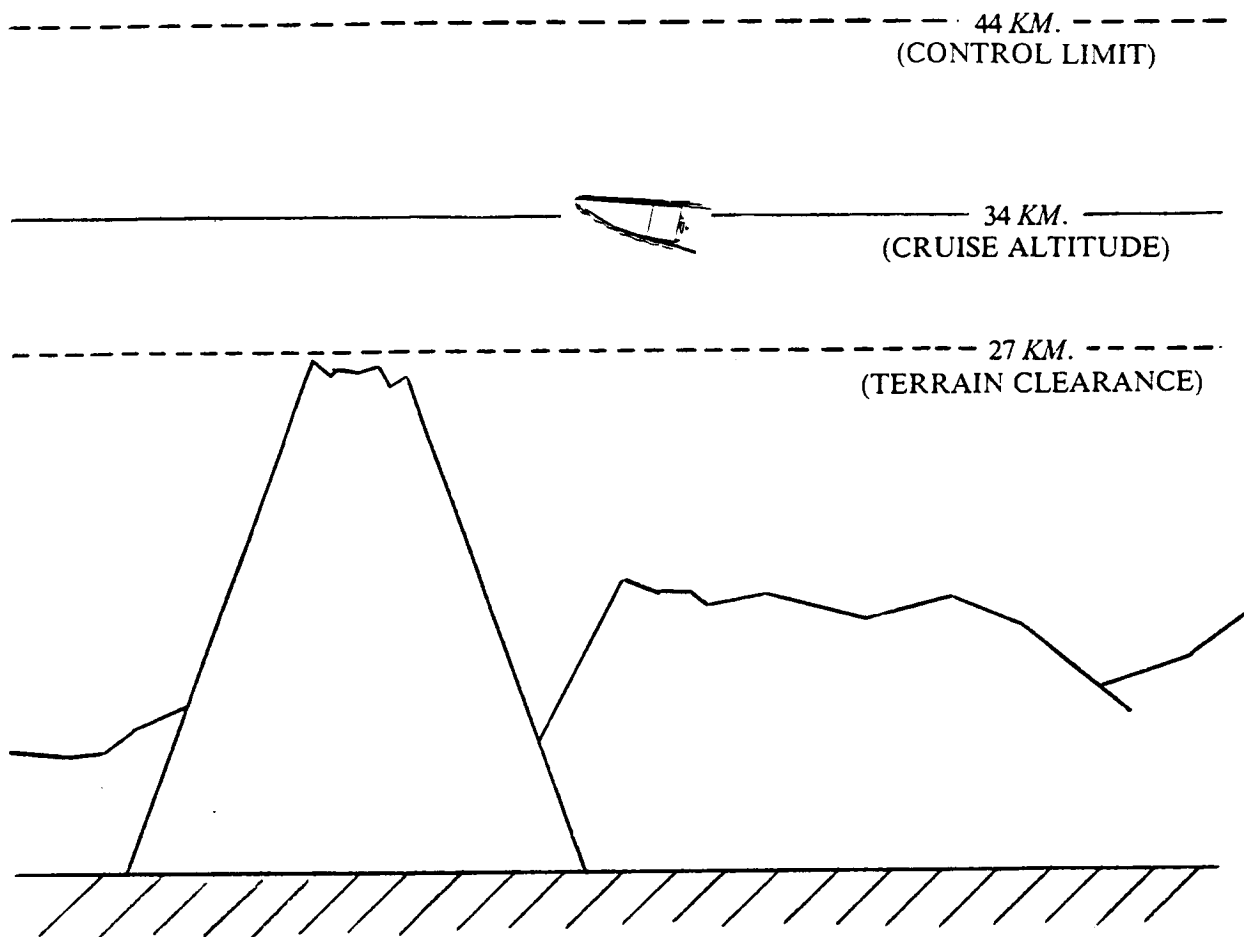


Figure 3-2. Aerocapture Altitude Corridor

4. Set predictor bank angle to  $\phi_c + \Delta\phi_p$
5. Repeat steps 2 and 3
6. Using results of steps 3 and 5, compute the sensitivity of minimum altitude to bank angle
7. Compute and limit correction to  $\phi_c$  to null target miss

This cycle is repeated until the guidance is converged.

Guidance cycling is initiated when the measured aerodynamic load factor,  $g_{aero}$ , exceeds 0.05 g's. The load factor is computed as

$$g_{aero} = \frac{|\underline{a}_m^l|}{g_{0_{earth}}} \quad (3-1)$$

where  $\underline{a}_m^l$  is the IMU-measured specific force vector and  $g_{0_{earth}}$  is the sea-level gravitational acceleration on Earth ( $9.81 \text{ m/s}^2$ ). The commanded bank angle is initialized to a value of  $90^\circ$ . Capture phase guidance cycling is terminated when either the estimated altitude rate increases above  $-50 \text{ m/s}$  or the estimated altitude drops below  $h_{cruise}$ .

Although there is no explicit control of aerodynamic heating rate or load factor, constraints can be satisfied by correct choice of the nominal entry trajectory to control maximum penetration depth.

### 3.2.2.1 PREDICTION ALGORITHM

The prediction process involves numerical integration of the vector equations of motion from the current time ( $t_{cur}$ ) to some given termination conditions given the current navigation system state estimate and a specified constant bank angle. The vector equations of motion to be integrated are

$$\frac{d\underline{r}^l}{dt} = \underline{v}^l \quad (3-2)$$

$$\frac{d\underline{v}^l}{dt} = \underline{g}^l + \underline{a}_{aero}^l \quad (3-3)$$

subject to the initial conditions

$$\underline{r}^I(t_{cur}) = \hat{r}^I(t_{cur})$$

$$\underline{v}^I(t_{cur}) = \hat{v}^I(t_{cur})$$

The gravitational acceleration is given by

$$\underline{g}^I = -\frac{\mu}{r^2} \frac{\underline{r}^I}{r} \quad (3-4)$$

The aerodynamic acceleration can be written in terms of the lift and drag components as

$$\underline{a}_{aero}^I = -D \underline{i}_x + L \underline{i}_y \quad (3-5)$$

where

$$D = \frac{\bar{q}}{C_D} \quad (3-6)$$

$$L = \left( \frac{L}{D} \right) D \quad (3-7)$$

$$\bar{q} = \frac{1}{2} \rho_p v_{rel}^2 \quad (3-8)$$

$$\rho_p = \beta \rho_0 e^{-(h-h_0)/HS} \quad (3-9)$$

$$\beta = \frac{\hat{\rho}(t_{cur})}{\rho_{exp}(t_{cur})} \quad (3-10)$$

$$\underline{i}_x = UNIT(\underline{v}_{rel}^I) \quad (3-11)$$

$$\underline{i}_z = UNIT(\underline{i}_x \times \underline{r}^I) \quad (3-12)$$

$$\underline{i}_y = \cos \phi_p (\underline{i}_z \times \underline{i}_x) + \sin \phi_p \underline{i}_z \quad (3-13)$$

and  $\phi_p$  is the bank angle used in the prediction. The factor  $\beta$  is used to scale the exponential density to reflect the current deviation of the estimated density from this model. The equations of motion are integrated numerically using a fourth-order Runge-Kutta algorithm with a time step of 2 seconds. The prediction is terminated when either the predicted altitude rate changes sign from negative to positive or the predicted altitude becomes negative. In the event of the latter, two courses of action are possible. If the bank angle used in the prediction was less than  $95^\circ$ , this angle is decremented until the predicted minimum altitude becomes greater than zero. If the bank angle used in the prediction was greater than  $95^\circ$ , the bank command is set to  $165^\circ$  and the guidance is exited. This action is warranted because a shallow entry is indicated and full lift-down will help the vehicle to "dig in" and build up control effectiveness. This command is held until the minimum predicted altitude achieved with  $90^\circ$  bank is less than  $h_{cruise}$ . This prevents guidance convergence problems which can occur due to the high sensitivity of minimum altitude to bank angle for bank angles greater than  $90^\circ$ .

### 3.2.2.2 CORRECTION ALGORITHM

The correction algorithm computes an increment to the current bank command to null the predicted target altitude miss ( $h_{m1}$ ). The altitude miss can be written in a Taylor series expansion of the bank angle control as

$$\Delta h_m = \frac{\partial h_m}{\partial \phi_c} \Delta \phi_c + \frac{\partial^2 h_m}{\partial \phi_c^2} \frac{(\Delta \phi_c)^2}{2!} + \dots \quad (3-14)$$

Neglecting all but the first-order term, the bank angle increment resulting in a specified altitude miss is given approximately by

$$\Delta \phi_c \cong \left[ \frac{\partial h_m}{\partial \phi_c} \right]^{-1} \Delta h_m \quad (3-15)$$

Thus, the increment to the current bank command required to null the target miss is

$$\Delta\phi_c = - \left[ \frac{\partial h_m}{\partial \phi_c} \right]^{-1} h_{m_1} \quad (3-16)$$

The sensitivity term in Eq. (3-16) is computed numerically from the results of the two predictions using control values  $\phi_c$  and  $\phi_c + \Delta\phi_p$ . If the resulting minimum altitudes are  $h_{f_1}$  and  $h_{f_2}$  respectively, then

$$\frac{\partial h_m}{\partial \phi_c} \cong \frac{h_{f_2} - h_{f_1}}{\Delta\phi_p} \quad (3-17)$$

and

$$h_{m_1} = h_{f_1} - h_{cruise} \quad (3-18)$$

The control is corrected by

$$\phi_c^+ = \phi_c^- + \Delta\phi_c \quad (3-19)$$

Care must be taken to account for the assumption of linearity made in the above solution. Because of the truncation of the series of Eq. (3-14) after the first-order term, it is assumed that the sensitivity of the target miss to the control is the same over the entire control range. Although the assumption of constant sensitivity is good in a small range about  $\phi_c^-$ , it breaks down for larger deviations. The control correction has been limited to  $\pm 15^\circ$  during the capture phase in an attempt to prevent overcorrection due to nonlinearities.

The guidance is considered to be converged when the correction  $\Delta\phi_c$  is less than 1 degree or the target altitude miss is less than 1 km. Typically, the guidance converges in one or two iterations after the initial cycle at the start of aerocapture.

### 3.3 CONSTANT ALTITUDE CRUISE PHASE

The purpose of the constant altitude cruise phase guidance is to continually compute bank angle commands to maintain flight at the target altitude,  $h_{cruise}$ , until the specified level of energy depletion has been achieved. This requires compensation for off-nominal atmospheric density fluctuations and damping of altitude rates induced by bank reversals. An analytic feedback control law which results in altitude response analogous to a second-order spring/mass/damper system has been developed for this phase. The commanded bank angle is computed by

$$\cos \phi_c = \cos \phi \Big|_{\ddot{h}=0} - K_h \frac{\dot{h}}{\bar{q}} - K_h \frac{(h - h_{cruise})}{\bar{q}} \quad (3-20)$$

where

$$\cos \phi \Big|_{\ddot{h}=0} = \frac{C_B}{\bar{q}} \frac{1}{L/D} \left[ g - \frac{v^2}{r} \right] \quad (3-21)$$

is the cosine of the bank angle required to maintain zero altitude acceleration. The linearized equation of motion for vehicle altitude can be written as

$$\ddot{h} = -g + \frac{v^2}{r} + \frac{\bar{q}}{C_B} \left( \frac{L}{D} \right) \cos \phi \quad (3-22)$$

Substituting the control of Eq. (3-20) into this equation shows the resulting linearized altitude response to be

$$\ddot{h} + \left( \frac{1}{C_B} \frac{L}{D} \right) K_h \dot{h} + \left( \frac{1}{C_B} \frac{L}{D} \right) K_h (h - h_{cruise}) = 0 \quad (3-23)$$

By analogy to a second-order spring/mass/damper system [17], expressions for the natural frequency and damping ratio are given by

$$2\zeta\omega_n = \frac{1}{C_B} \frac{L}{D} K_h \quad (3-24)$$

$$\omega_n^2 = \frac{1}{C_B} \frac{L}{D} K_h \quad (3-25)$$

Thus, for given vehicle characteristics ( $L/D$ ,  $C_B$ ) and desired damping and natural frequency, the appropriate control gains can be computed using

$$K_i = \frac{2 C_B}{L/D} \zeta \omega_n \quad (3-26)$$

$$K_h = \frac{C_B}{L/D} \omega_n^2 \quad (3-27)$$

Damping ratio and natural frequency values of

$$\zeta = 1.50$$

$$\omega_n = 0.06 \text{ radians/second}$$

were chosen empirically for this study. For the biconic vehicle examined, the resulting control gains are

$$K_h = 2.46$$

$$K_i = 123$$

These gains were found to provide good response to target altitude overshoot during the capture phase and quick damping of bank reversal-induced altitude rates.

Cycling of the constant altitude cruise guidance is initiated immediately after termination of capture guidance cycling and is terminated when the inertial velocity drops below 4400 m/s. The guidance is cycled at a frequency of 1.0 Hz.

## 3.4 EXIT PHASE

### 3.4.1 GUIDANCE TARGET SELECTION

The ultimate goal of the aerocapture maneuver is to control flight path conditions at atmospheric exit such that the fuel required for propulsive insertion into the target orbit is as small as possible. The target orbit is specified by its apoapsis and periapsis altitudes. Since only one control ( $\phi$ ) is available, the decision must be made as to whether apoapsis distance, periapsis distance, or some combination of both should be controlled during the exit phase. Several trade-offs can be examined in making this decision:

1. For the target orbit used in this study (2000 km by 350 km), approximately 50% more fuel is required to correct a periapsis error than an apoapsis error of the same magnitude.
2. Sensitivity of final apoapsis to bank angle is much greater than sensitivity of final periapsis to bank angle.
3. For a cruise altitude of 34 km, the maximum possible exit periapsis altitude achievable is approximately 56 km (with nominal atmospheric density conditions).
4. Lift-down ( $\phi > 90^\circ$ ) is required to raise periapsis altitude during the exit phase.

While the first item suggests that periapsis control is more desirable, the second indicates that the error in apoapsis induced by controlling only periapsis would overwhelm any potential fuel savings. The third item suggests that very limited improvement in periapsis altitude is possible, even with full lift-down commanded over the entire exit phase. Raising the periapsis by 22 km during

exit results in less than 5 m/s savings in required propulsive  $\Delta V$  for insertion, an amount which would be negated by an apoapsis miss of only 35 km.

Because of the possibility of unpredictable density fluctuations, it is desirable to fly the exit phase with a bank angle of approximately  $90^\circ$  to maintain control margin. This constraint would be violated by the fourth item if periapsis were controlled, since the tendency of the guidance would be to command lift-down to raise periapsis. Based on these considerations, it was decided to control only exit apoapsis altitude during the exit phase and to leave periapsis altitude unconstrained.

### *3.4.2 GUIDANCE DESCRIPTION*

The purpose of the exit phase guidance is to compute bank angle commands to control the vehicle to the desired target apoapsis at atmospheric exit. The exit guidance algorithm is very similar to the capture phase guidance, with a numerical predictor/corrector algorithm used to compute the constant bank angle required to hit the specified target. The nominal guidance cycle is as follows:

1. Set predictor bank angle to current command ( $\phi_c$ )
2. Initialize predictor state vector to current navigation system estimated state
3. Predict atmospheric exit apoapsis altitude
4. Set predictor bank angle to  $\phi_c + \Delta\phi_p$
5. Repeat steps 2 and 3

6. Using results of steps 3 and 5, compute the sensitivity of exit apoapsis altitude to bank angle
7. Compute and limit correction to  $\phi_c$  to null target miss

The predictor/corrector cycle is repeated until guidance convergence criteria are met.

The exit phase is initiated immediately after termination of the constant altitude cruise phase. Initially, full lift-up ( $|\phi_c| = 15^\circ$ ) is commanded and held until the predicted bank angle required to hit the apoapsis target becomes greater than  $80^\circ$ . This is done to assure that the exit phase is begun with nearly zero vertical lift to provide control margin for thick or thin density shifts which might occur in the future. Exit phase guidance cycling is terminated when the measured aerodynamic load factor drops below 0.05 g's.

#### 3.4.2.1 PREDICTION ALGORITHM

The exit phase predictor utilizes the same set of equations as the capture phase predictor (see "3.2.2.1 PREDICTION ALGORITHM" on page 55). The prediction time step during this phase has been increased to 8 seconds without affecting the accuracy of the solution. The prediction is terminated when the predicted aerodynamic load factor drops below 0.01 g's or the altitude becomes negative. In the latter event, the current predictor bank angle is decremented until the predicted trajectory exits the atmosphere.

#### 3.4.2.2 CORRECTION ALGORITHM

The exit phase correction logic is the same in principle as that of the capture phase; that is, the control correction is based on a truncated Taylor series expansion of the target miss in terms

of the control (see "3.2.2.2 CORRECTION ALGORITHM" on page 57). The Taylor series expansion of Eq. (3-14) can be modified for the exit phase simply by replacing the cruise altitude miss,  $h_m$ , by the target apoapsis miss,  $h_{a_m}$ . After truncation, the control correction to null the target miss is computed as

$$\Delta\phi_c = - \left[ \frac{\partial h_{a_m}}{\partial \phi_c} \right]^{-1} h_{a_{m1}} \quad (3-28)$$

The sensitivity term in Eq. (3-28) is found using the results of two predictions using the current control command and a perturbed control command. If the resulting exit apoapsis altitudes are  $h_{a_1}$  and  $h_{a_2}$  respectively, then

$$\frac{\partial h_{a_m}}{\partial \phi_c} \cong \frac{h_{a_2} - h_{a_1}}{\Delta\phi_p} \quad (3-29)$$

and

$$h_{a_{m1}} = h_{a_1} - h_{a_{target}} \quad (3-30)$$

The control is now corrected using Eq. (3-19).

As in the capture phase, care must be taken to account for the linear nature of the above solution. At the start of the exit phase, the control sensitivity is extremely high, but it rapidly falls off as the vehicle nears atmospheric exit. It has been observed that large overcorrections and convergence problems can result due to large control sensitivity early in the exit phase. This problem lessens as the sensitivity decreases. Therefore, the magnitude of the control correction is limited as follows:

$$|\Delta\phi_c| \leq 0.5^\circ \text{ for } \frac{\partial h_{a_m}}{\partial \phi_c} \geq 150 \text{ km/deg}$$

$$|\Delta\phi_c| \leq 15^\circ \text{ for } \frac{\partial h_{a_m}}{\partial \phi_c} \leq 150 \text{ km/deg}$$

The guidance convergence criteria also depend on the magnitude of the control sensitivity. The guidance is considered to be converged if

$$|\Delta\phi_c| \leq 0.1^\circ \text{ for } \frac{\partial h_{a_m}}{\partial \phi_c} \geq 150 \text{ km/deg}$$

$$|\Delta\phi_c| \leq 1.0^\circ \text{ for } \frac{\partial h_{a_m}}{\partial \phi_c} \leq 150 \text{ km/deg}$$

or if the predicted target miss is less than 1 km. The guidance typically converges in one or two iterations after the initial guidance cycle.

### 3.5 ORBIT PLANE CONTROL

Control of the final orbit plane orientation is achieved by commanding bank angle sign reversals in order to null the error between the current plane and the target plane. The target plane is defined by a unit vector in the direction of the angular momentum vector, denoted  $\underline{i}_{hd}^l$ . Since the position and velocity vectors will have no projections onto  $\underline{i}_{hd}^l$  if the vehicle is in the target plane, the current plane error can be viewed in terms of the projections of these vectors onto  $\underline{i}_{hd}^l$  and the plane control problem as one of driving these projections to zero. The position and velocity errors can be viewed as angular errors if written as

$$\theta_r = \frac{\underline{r}^l \cdot \underline{i}_{hd}^l}{r} \tag{3-31}$$

$$\theta_v = \frac{\underline{v}^l \cdot \underline{i}_{hd}^l}{v_h} \tag{3-32}$$

where  $v_h$  is the projection of the velocity vector onto the local horizontal plane.

Since the only plane control available is the sign of the bank angle, only one of the above errors or a combination of the two can be controlled at a time. It has been decided to control

only the velocity error  $\theta_v$  over the entire aerocapture maneuver. As discussed in Reference [9], little can be done to control the position error over the aerocapture trajectory. One particular danger in controlling  $\theta_v$  is that a large out-of-plane velocity may be commanded to null the position error, thereby resulting in a large final velocity error which will require much more fuel to correct than will have been saved by the decrease in  $\theta_v$ . On the other hand, if  $\theta_v$  is controlled, the amount and direction of growth in  $\theta_v$  are indirectly controlled since the position error is essentially the integral of the velocity error. Thus, it is seen that  $\theta_v$  can at least be bounded by attempting to "average out" the direction of  $\theta_v$  over the aerocapture trajectory.

Control of  $\theta_v$  is achieved by constructing an error corridor which defines the maximum allowable error at each point along the trajectory. When  $\theta_v$  becomes larger than the corridor width, a sign reversal is commanded to drive the error in the opposite direction. The width of the corridor decreases along the trajectory to reflect decreasing trajectory control authority. The  $\theta_v$  control corridor is illustrated in Figure 3-3 on page 67. During the capture phase, the corridor is held constant at a value of  $4.16^\circ$ . In the constant altitude cruise and exit phases, the corridor decreases linearly with velocity down to a minimum value of  $0.16^\circ$ . The shallow slope during cruise was chosen in an attempt to prevent unbalanced growth of  $\theta_v$  in either direction while still reflecting the decreasing control authority with time. The slope is increased during exit due to the more rapid decrease in control capability.

Although  $\theta_v$  is not explicitly controlled, the impact of an initial position error can be lessened by choosing the sign of the initial bank command during the capture phase such that  $\theta_v$  is decreased instead of increased. This implies that the sign of the initial bank command, which has a magnitude of  $90^\circ$ , should be chosen as

$$SIGN(\phi_{c_0}) = SIGN(\theta_{r_0})$$

where  $\theta_{r_0}$  is the plane position error at the start of aerocapture guidance cycling.

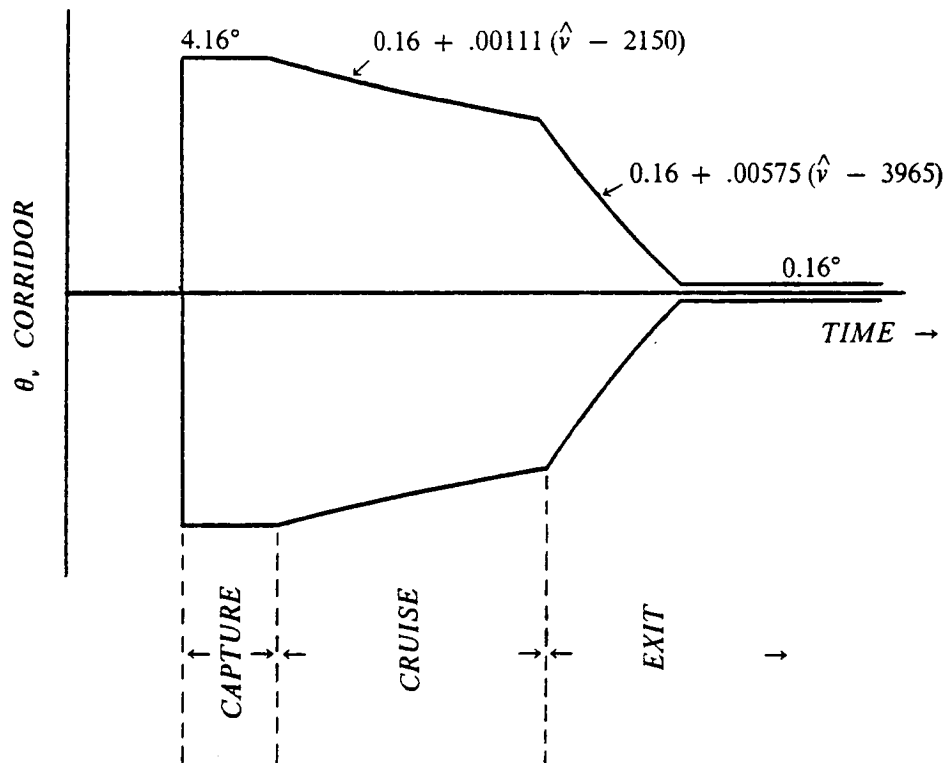


Figure 3-3. Velocity Error Control Corridor

The direction in which the vehicle rolls in executing a bank reversal is based on the magnitude of the current command. During the first two guidance phases, bank reversals are through the shortest distance; that is, if  $|\phi_c| \leq 90^\circ$ , the vehicle rolls over the top, and if  $|\phi_c| > 90^\circ$ , the vehicle rolls through lift-down. In the exit phase, the vehicle rolls over the top if  $|\phi_c| \leq 110^\circ$  in order to offset the tendency of rolling through lift-down to drive the commanded bank to lift-up, causing excessive periapsis altitude loss.

## CHAPTER 4

### COMPUTER SIMULATION PROGRAM

#### 4.1 INTRODUCTION

This chapter presents a description of the computer simulation program written for testing and evaluation of the proposed navigation and guidance algorithms. The simulator is coded in MAC, a computer language which allows straightforward programming of vector and matrix algebraic operations. (MAC was developed and is used exclusively at the Charles Stark Draper Laboratory, Inc.). Overall program functional flow is described, including major inputs, outputs, and functions of key subroutines. In addition, environment models of the planet Mars and the aerocapture vehicle are presented.

#### 4.2 SIMULATOR PROGRAM FUNCTIONAL DESCRIPTION

A functional diagram of the computer simulation program written for analysis and testing of the navigation and guidance systems is presented in Figure 4-1 on page 70. The simulator is constructed as an executive program calling five major subroutines at different rates. The principle subroutine inputs and outputs are also shown in Figure 4-1.

The executive program controls overall simulation cycling and sequencing. All data input and program initialization functions are performed here, along with principle simulation output and file data storage. This program also contains the simulation environment, wherein the vehicle state is propagated based on force inputs from the environment models. The environment state is considered to be "truth" against which the navigation system performance can be measured.

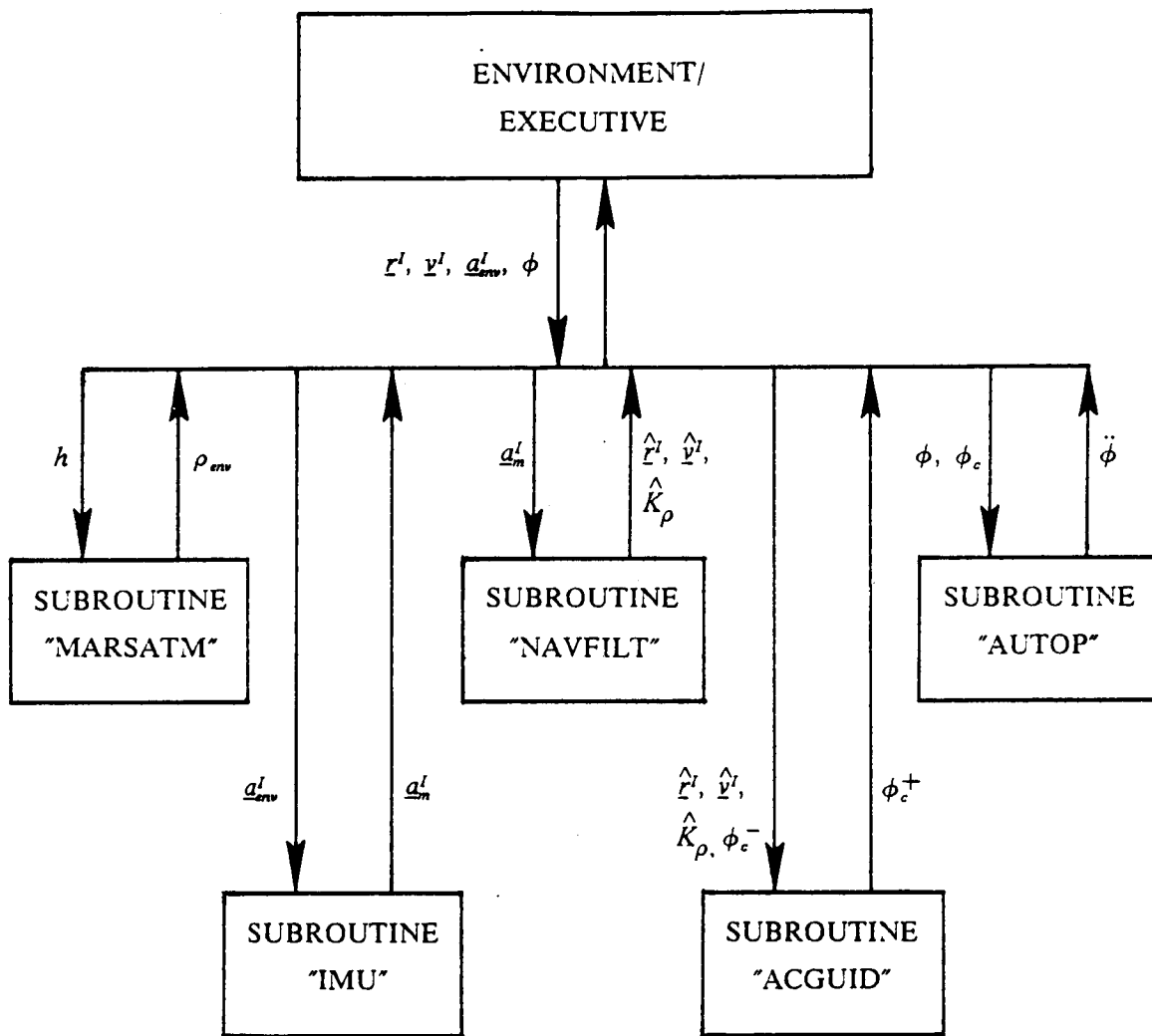


Figure 4-1. Simulator Program Functional Diagram

Subroutine MARSATM contains the atmosphere model described in “4.3.2 ATMOSPHERIC DENSITY MODEL” on page 72, including the density perturbation equations. Based on the input environment altitude, linear interpolation is used to determine the current nominal density. If desired, the new density perturbation is computed based on the old value and input values of the horizontal and vertical distances flown since the last subroutine call.

Subroutine IMU contains the IMU model described in “2.2 INERTIAL MEASUREMENT UNIT” on page 35. The erroneous output specific force,  $\underline{a}_m^I$ , is computed based on the true specific force  $\underline{a}_{env}^I$  from the environment. Also included in this subroutine is the calculation of the body-to-inertial transformation matrix,  $C_b^I$ .

Subroutine NAVFILT contains all of the navigation system functions described in “Chapter 2. NAVIGATION SYSTEM DESIGN” on page 35. The main input to the subroutine is the measured specific force vector, which is used for state vector estimate propagation and density altitude measurement incorporation. The main subroutine outputs are the estimated position, velocity, and density bias.

Subroutine ACGUID contains the aerocapture guidance algorithm equations as described in “Chapter 3. GUIDANCE DESIGN” on page 51. All guidance computations are based on the position, velocity, and density estimates from the navigation subroutine.

Subroutine AUTOP is a roll autopilot designed to execute bank maneuvers given finite roll rate and acceleration limits. Based on these limits, the autopilot computes the times of maximum acceleration and deceleration required to achieve the desired bank angle in minimum time. The direction in which the vehicle rolls is determined by the magnitudes of the current and desired bank angles and, in the case of bank reversals for plane control, on the command from the guid-

ance to roll through lift-up or lift-down. The maximum roll rate and roll acceleration have been set to 20 deg/s and 5 deg/s<sup>2</sup>, respectively, for this study.

### 4.3 ENVIRONMENT MODELS

#### 4.3.1 PLANET MODEL

The planet Mars has been modelled in the environment as a sphere of radius 3397.20 km. The gravitational attraction is thus given by

$$g_M = \frac{\mu}{r^2} \quad (4-1)$$

where

$$\mu = 42828.2804 \text{ km}^3/\text{sec}^2$$

is the gravitational parameter and  $r$  is the distance from the center of Mars to the center of mass of the spacecraft. The planet is assumed to rotate about its North polar axis at a constant rate of

$$\omega_{IM} = 7.088218127 \times 10^{-5} \text{ rad/sec}$$

The above physical constants were obtained from Reference [18].

#### 4.3.2 ATMOSPHERIC DENSITY MODEL

The COSPAR northern summer atmosphere model [19] was chosen as the nominal simulation atmosphere. Table 4-1 on page 74 lists the density profile values given by the model and Figure 4-2 on page 75 [19] shows a graphical comparison of this data with the density profiles computed from Viking I and II and Soviet Mars 6 entry trajectory data. The nominal density

profile is implemented in a table look-up subroutine with linear interpolation used to find density values at altitudes between the table data points.

In reality, the actual atmospheric conditions encountered by the spacecraft during aerocapture will never exactly match the nominal model. In order to include the effects of off-nominal density conditions, the environment density is modelled as

$$\rho_{env} = (1 + b_{\rho}) \rho_{nom} \quad (4-2)$$

where  $\rho_{nom}$  is the nominal density as described above and  $b_{\rho}$  represents a percentage deviation of the true density from the nominal. This perturbation has been modelled as a first-order Markov process followed by a low-pass filter for attenuation of high frequency variations. The density perturbation factor is computed as

$$b_{\rho}^{+} = b_{\rho}^{-} + 0.05(\zeta^{+} - b_{\rho}^{-}) \quad (4-3)$$

where

$$\zeta^{+} = a_{b_{\rho}} \zeta^{-} + \sigma_{b_{\rho}} \sqrt{1 - a_{b_{\rho}}^2} \eta \quad (4-4)$$

$$a_{b_{\rho}} = e^{-\xi} \quad (4-5)$$

$$\xi = \sqrt{\left(\frac{\Delta d}{S_{HOR}}\right)^2 + \left(\frac{\Delta h}{S_{VERT}}\right)^2} \quad (4-6)$$

In this model,  $\sigma_{b_{\rho}}$  is the standard deviation of the density perturbation and  $\eta$  is a normally distributed random variable with mean zero and standard deviation one. In the autocorrelation function  $a_{b_{\rho}}$ ,  $\Delta d$  and  $\Delta h$  are the horizontal and vertical distances traversed since the last subroutine call, and  $S_{HOR}$  and  $S_{VERT}$  are horizontal and vertical scale distances. The Markov process model for density perturbations is similar to that used in the Global Reference Atmosphere

Table 4-1. COSPAR Northern Summer Density Profile

Altitude (km)	Density (kg/m <sup>3</sup> )	Altitude (km)	Density (kg/m <sup>3</sup> )
0	1.56E-02	50	1.08E-04
2	1.30E-02	52	8.54E-05
4	1.08E-02	54	6.69E-05
6	9.07E-03	56	5.24E-05
8	7.65E-03	58	4.09E-05
10	6.47E-03	60	3.19E-05
12	5.45E-03	62	2.47E-05
14	4.57E-03	64	1.91E-05
16	3.81E-03	66	1.48E-05
18	3.17E-03	68	1.14E-05
20	2.63E-03	70	8.75E-06
22	2.18E-03	72	6.70E-06
24	1.79E-03	74	5.12E-06
26	1.47E-03	76	3.92E-06
28	1.20E-03	78	3.00E-06
30	9.81E-04	80	2.29E-06
32	7.98E-04	82	1.75E-06
34	6.48E-04	84	1.34E-06
36	5.24E-04	86	1.03E-06
38	4.23E-04	88	7.87E-07
40	3.40E-04	90	6.03E-07
42	2.72E-04	92	4.62E-07
44	2.17E-04	94	3.54E-07
46	1.73E-04	96	2.71E-07
48	1.37E-04	98	2.08E-07
		100	1.60E-07

(GRAM) [20]. A Markov process followed by low-pass filtering was used in [21] to generate density shear profiles for use in Earth aerobraking studies. This model is intuitively satisfying because it contains the decreasing correlations with distance moved which would be expected due to the continuous nature of the fluid atmosphere mass.

The choice of the density perturbation model parameters is difficult due to the lack of global Mars atmosphere data. The intention here is not to simulate a perfectly accurate model of the

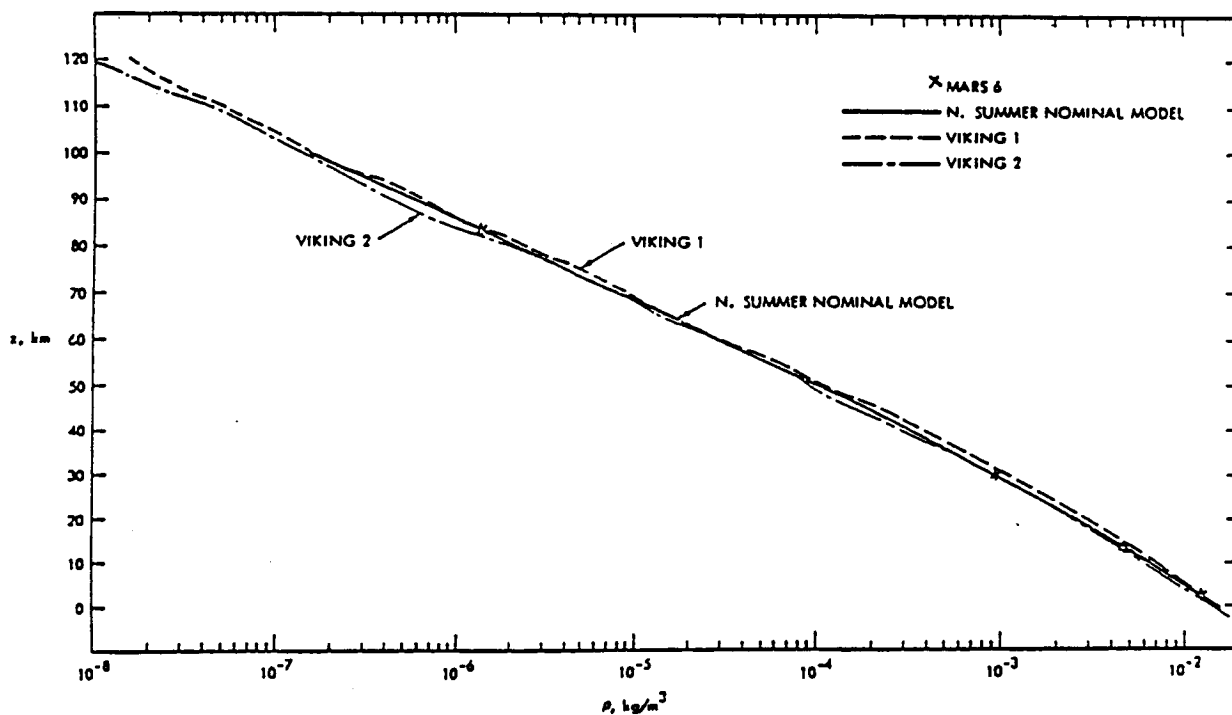


Figure 4-2. Nominal Density Model Comparison with Flight Data

Mars atmosphere, but to provide physically reasonable density variations to account for the dynamic nature of the atmosphere for testing of the navigation and guidance systems. Thus, parameter values were chosen to provide density variations of reasonable magnitude and duration. A value of 25% was chosen for  $\sigma_{\rho}$ , and it is assumed that this value is constant throughout the atmosphere. It was also assumed, for lack of better information, that the horizontal and vertical scale distances are the same as those used for the Earth atmosphere in the GRAM model. These are computed as [20]

$$S_{HOR} = 900 + 6h \quad (4-7)$$

$$S_{VERT} = 5 + 0.05h \quad (4-8)$$

where  $h$  is the current altitude.

#### 4.4 VEHICLE MODELS

##### 4.4.1 EQUATIONS OF MOTION

The aerocapture vehicle examined in this study is a biconic lifting body similar in design to the configuration shown in Figure 1-2 on page 30. For the purpose of preliminary guidance and navigation systems analysis, only the translational dynamics of the vehicle need be modelled in the simulation. Therefore, the motion of the spacecraft is found completely by solution of the equations of translational motion of the center of mass as given by

$$\frac{d\underline{r}^I}{dt} = \underline{v}^I \quad (4-9)$$

$$\frac{d\underline{v}^I}{dt} = \underline{g}^I + \underline{a}_{env}^I \quad (4-10)$$

where

$$\underline{g}^I = -\frac{\mu}{r^2} \frac{\underline{r}^I}{r} \quad (4-11)$$

$$\underline{a}_{env}^I = -D \underline{i}_x + L \underline{i}_y \quad (4-12)$$

$$D = \frac{\bar{q}}{C_B} \quad (4-13)$$

$$L = \frac{L}{D} D \quad (4-14)$$

$$\bar{q} = \frac{1}{2} \rho_{env} v_{rel}^2 \quad (4-15)$$

$$\hat{i}_x = UNIT(\underline{v}_{rel}^l) \quad (4-16)$$

$$\hat{i}_z = UNIT(\hat{i}_x \times \underline{r}^l) \quad (4-17)$$

$$\hat{i}_y = \cos \phi (\hat{i}_z \times \hat{i}_x) + \sin \phi \hat{i}_z \quad (4-18)$$

The vehicle lift-to-drag ratio and ballistic coefficient are assumed to be constant with values of

$$\frac{L}{D} = 1.5$$

$$C_B = 1025 \text{ kg/m}^2$$

for the vehicle examined. The environment equations of motion are integrated numerically using a fourth-order Runge-Kutta algorithm with a step size of one second.

#### 4.4.2 AERODYNAMIC HEATING

The convective heating rate during atmospheric flight can be computed from an empirical formula given in [22]. The heating rate is given by

$$\dot{Q} = \frac{865.0}{\sqrt{R_n}} \sqrt{\frac{\rho}{\rho_{SLE}}} \left( \frac{v_{rel}}{10000} \right)^{3.5} \quad (4-19)$$

in units of  $Btu/ft^2/s$ . In this equation,  $R_n$  is the vehicle nose radius in units of feet and  $\rho_{SLE}$  is the nominal sea-level atmospheric density on Earth. Values of

$$R_n = 1.640 \text{ ft}$$

$$\rho_{SL_E} = 1.226 \text{ kg/m}^3$$

were used for these parameters in the simulator. The integrated heat load due to aerodynamic heating is computed as

$$Q(t) = \int_0^t \dot{Q}(\tau) d\tau \quad (4-20)$$

## CHAPTER 5

### PERFORMANCE RESULTS

#### 5.1 INTRODUCTION

This chapter presents the results of a selection of cases illustrating the performance of the guidance and navigation algorithms described in this thesis. The intent here is not to provide exhaustive data covering all possible dispersions, but to examine a limited number of strenuous cases which lend insight into systems performance characteristics. The nominal aerocapture trajectory is first described and illustrated for reference. Next, the performance of the navigation system alone is examined. Finally, combined guidance and navigation performance for a number of cases of interest is discussed.

Individual test cases are identified by a six digit number followed by one or two letters. The first two digits identify a specific vector of initial position and velocity errors chosen from a set of 100 random samples. The final four digits are the initial seed for the random number generator which is used for computing density variations, radar altimeter errors, and IMU errors. The letters indicate which measurement types are incorporated by the navigation filter: "D" indicates density altitude measurements and "R" indicates radar altimeter measurements.

#### 5.2 NOMINAL AEROCAPTURE TRAJECTORY

The nominal aerocapture trajectory is defined to be the atmospheric path flown with initial conditions defined on the nominal Mars approach hyperbola and with no navigation errors or atmospheric density dispersions. The nominal initial vehicle position and velocity vectors are

constructed using altitude, speed, flight path angle, and azimuth angle values specified at a given latitude and longitude. Table 5-1 on page 81 lists the quantities which define the nominal vehicle state initial conditions used in this analysis. The initial velocity was chosen as a typical value in the range of possible Mars approach speeds [22]. The initial flight path angle corresponding to this speed was selected to center the nominal trajectory in a corridor defined by tolerable known trajectory dispersions; that is, with the given nominal flight path angle, equal levels of known positive and negative initial correlated altitude/flight path angle dispersions can be tolerated without violating minimum or maximum aerocapture altitude limitations.

Major trajectory and control parameters for the nominal aerocapture trajectory are plotted in Figures 5-1 through 5-7. Figures 5-1 through 5-3 are graphs of the nominal altitude, velocity, and inertial flight path angle time histories, respectively. Figure 5-4 shows the aerodynamic load factor experienced by the vehicle along the trajectory. The bank angle history for the nominal case is shown in Figure 5-5. Figure 5-6 is a plot of the cosine of the commanded bank angle versus time. This plot gives an indication of vehicle in-plane (vertical) lift capability required for trajectory control, with values of plus and minus one implying the utilization of all available control authority. Finally, Figure 5-7 on page 88 shows the time histories of  $\theta$ , and  $\dot{\theta}$ , the orbit plane position and velocity angular errors defined in Equations (3-31) and (3-32). The  $\dot{\theta}$  control corridor has also been plotted to illustrate the performance of the orbit plane control routine.

Table 5-1. Nominal Entry State Definition

Parameter	Value
Altitude	243.840 km
Velocity	5900 m/s
Inertial Flight Path Angle	-16.745°
Azimuth Angle	0°
Latitude	0°
Longitude	0°

### 5.3 NAVIGATION SYSTEM PERFORMANCE

#### 5.3.1 ESTIMATOR INITIAL CONDITIONS

Prior to initiation of navigation system cycling, the estimator state vector and error covariance matrix must be initialized. The seven-dimensional filter state vector is initialized as

$$\hat{\mathbf{x}}_0 = \begin{bmatrix} \hat{r}_I \\ \hat{r}_0 \\ \hat{v}_0 \\ \hat{K} \\ \hat{\rho}_0 \end{bmatrix} = \begin{bmatrix} 3641040 \text{ m} \\ 0 \text{ m} \\ 0 \text{ m} \\ -1699.86 \text{ m/s} \\ 0 \text{ m/s} \\ 5649.82 \text{ m/s} \\ 0 \end{bmatrix} \quad (5-1)$$

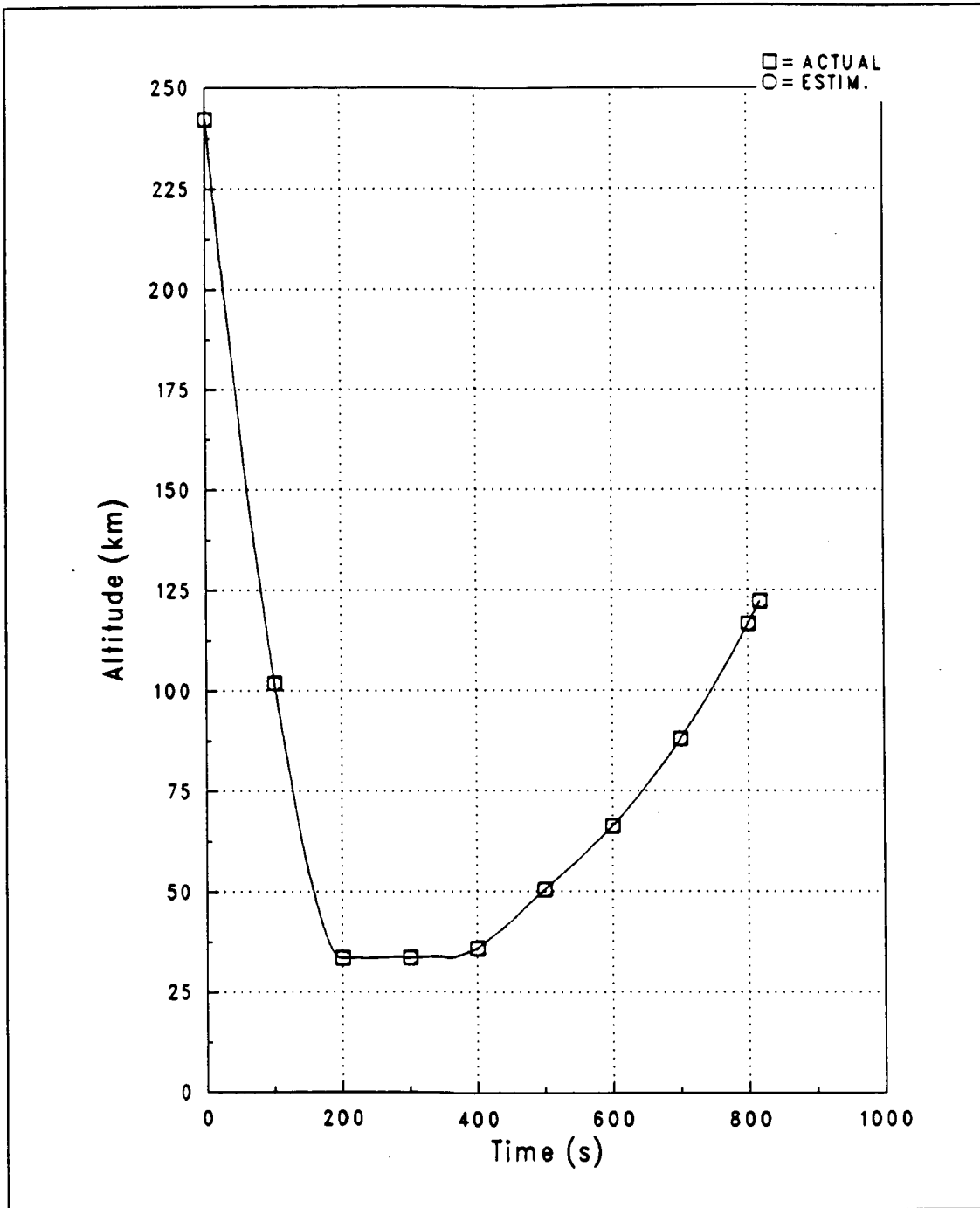


Figure 5-1. Nominal Aerocapture: Altitude History

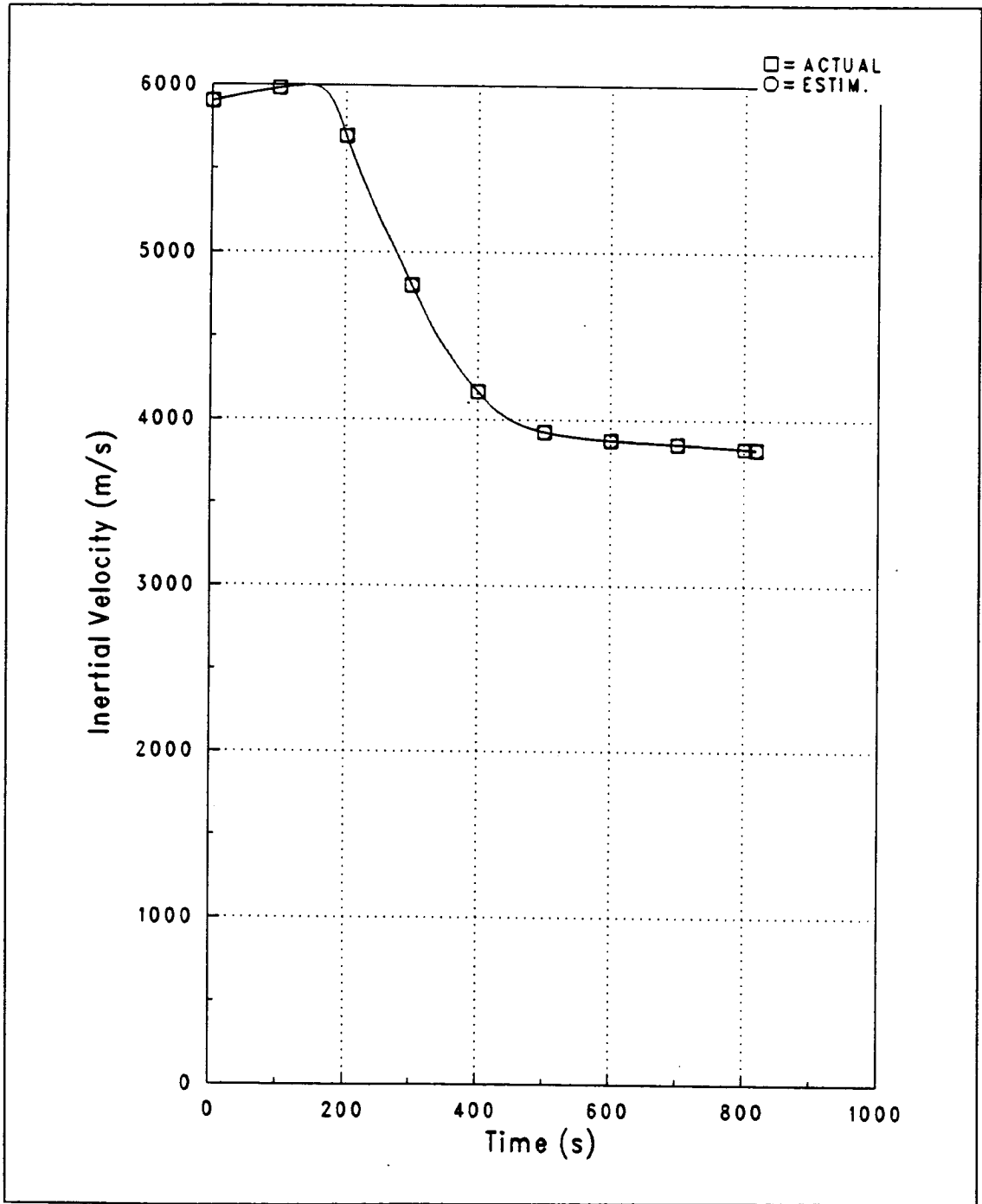


Figure 5-2. Nominal Aerocapture: Velocity History

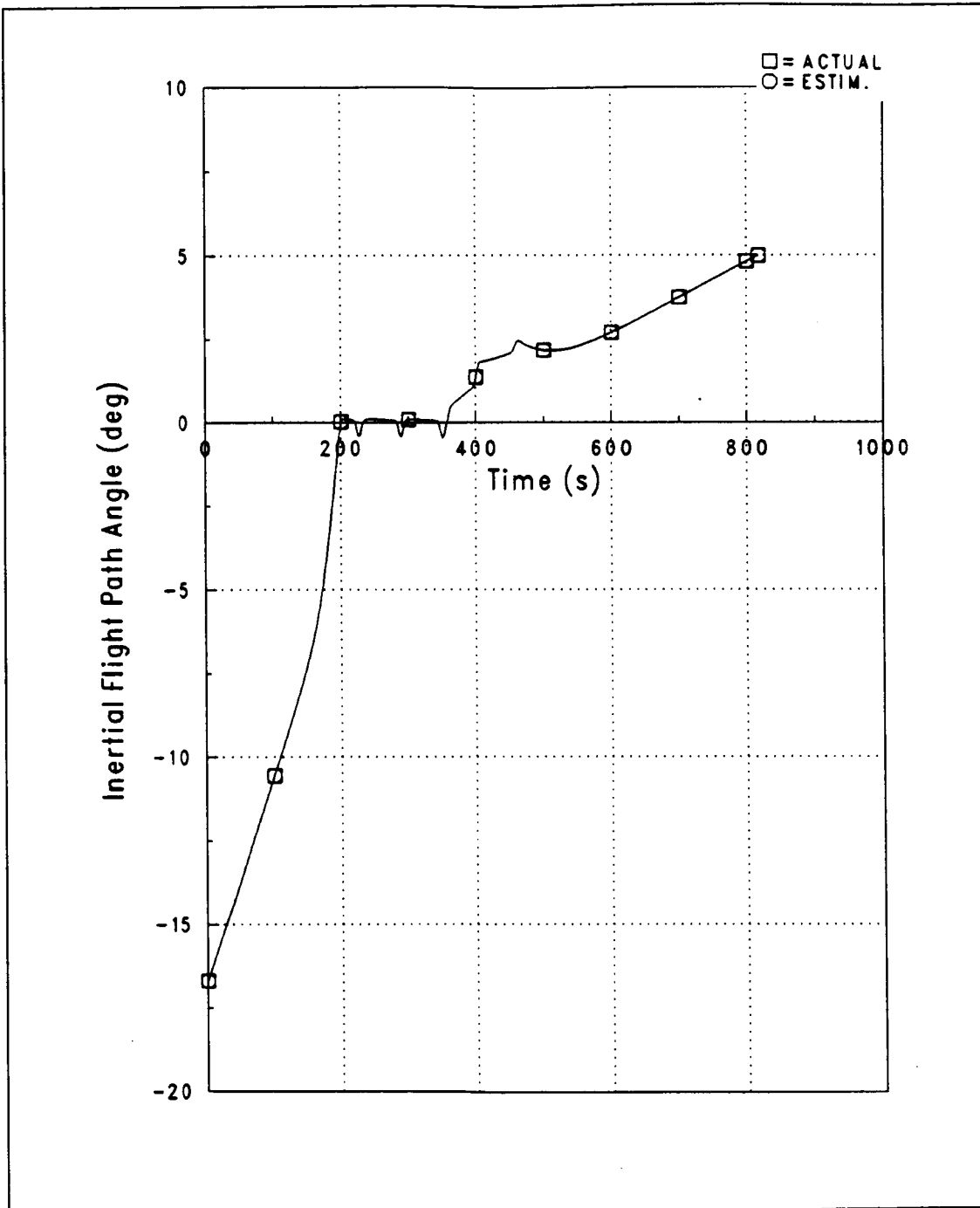


Figure 5-3. Nominal Aerocapture: Flight Path Angle History

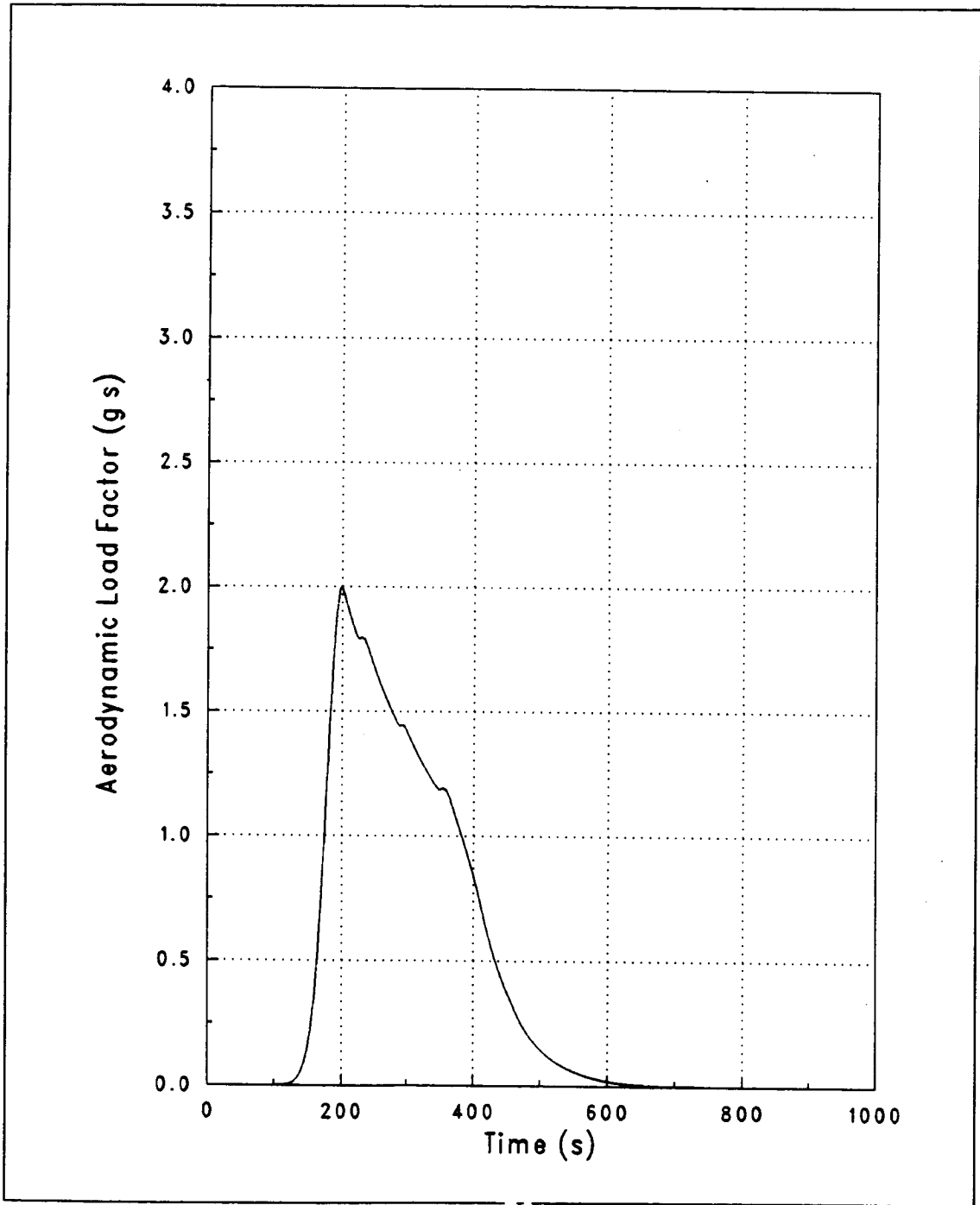


Figure 5-4. Nominal Aerocapture: Aerodynamic Load Factor Profile

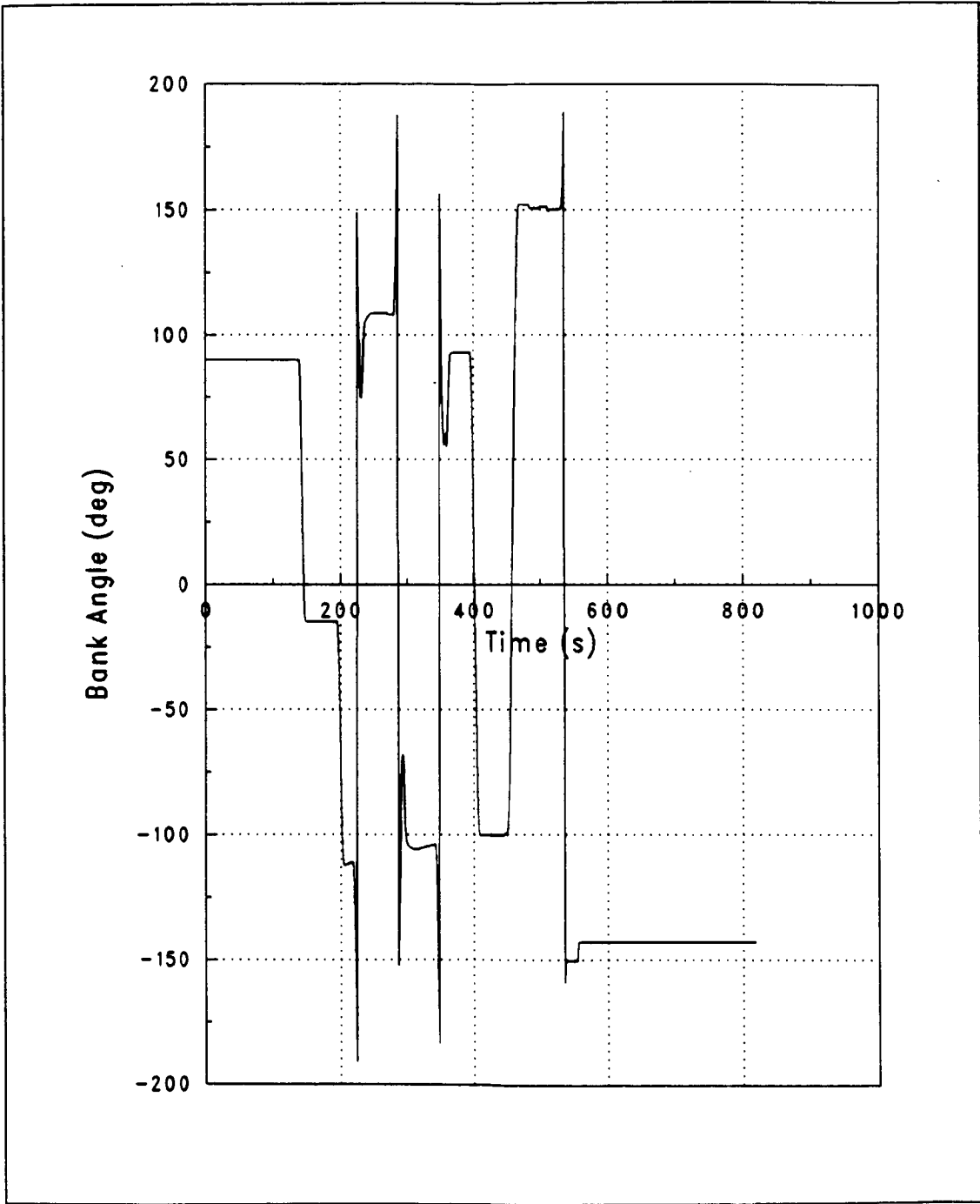


Figure 5-5. Nominal Aerocapture: Bank Angle History

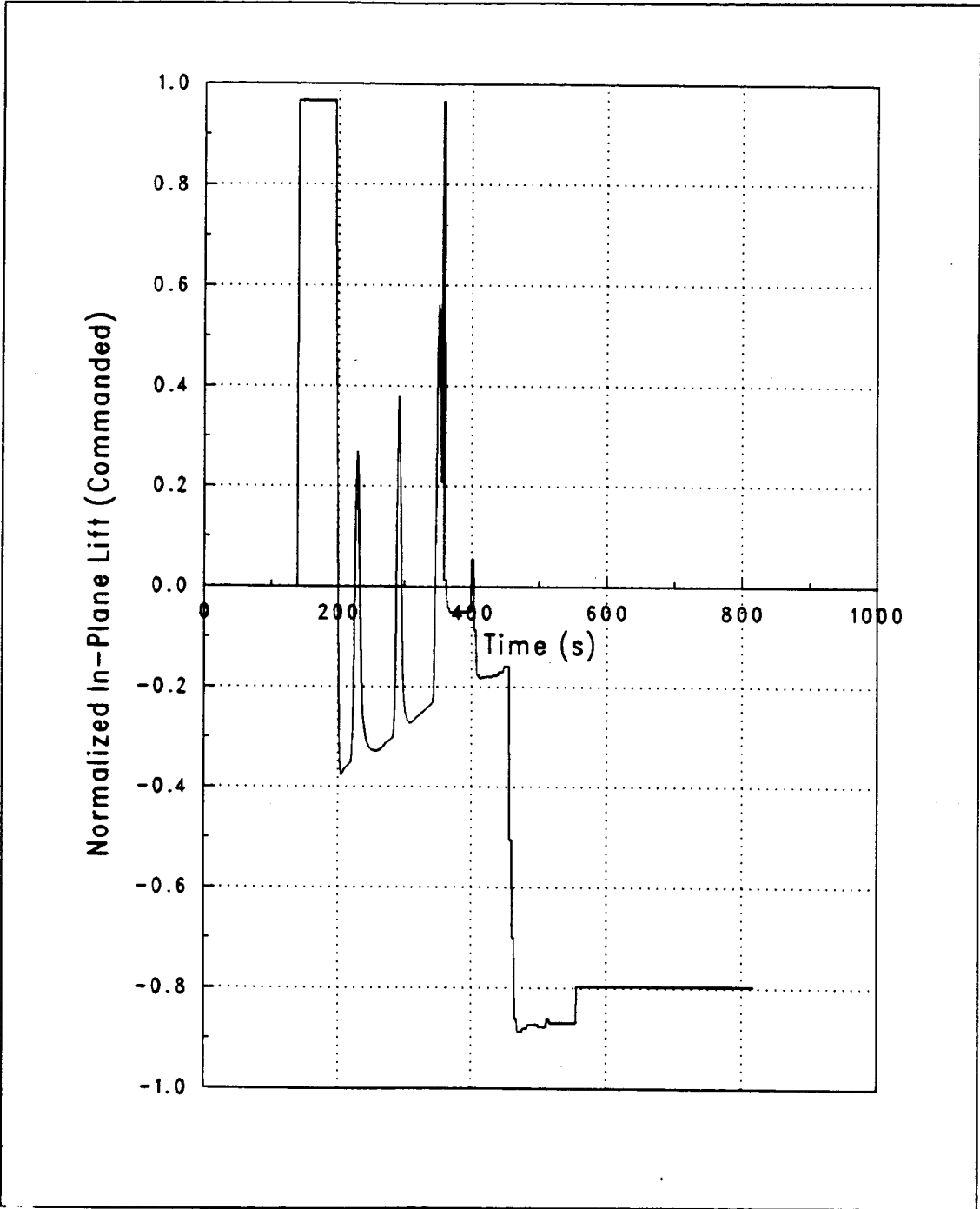


Figure 5-6. Nominal Aerocapture: Normalized In-Plane Lift

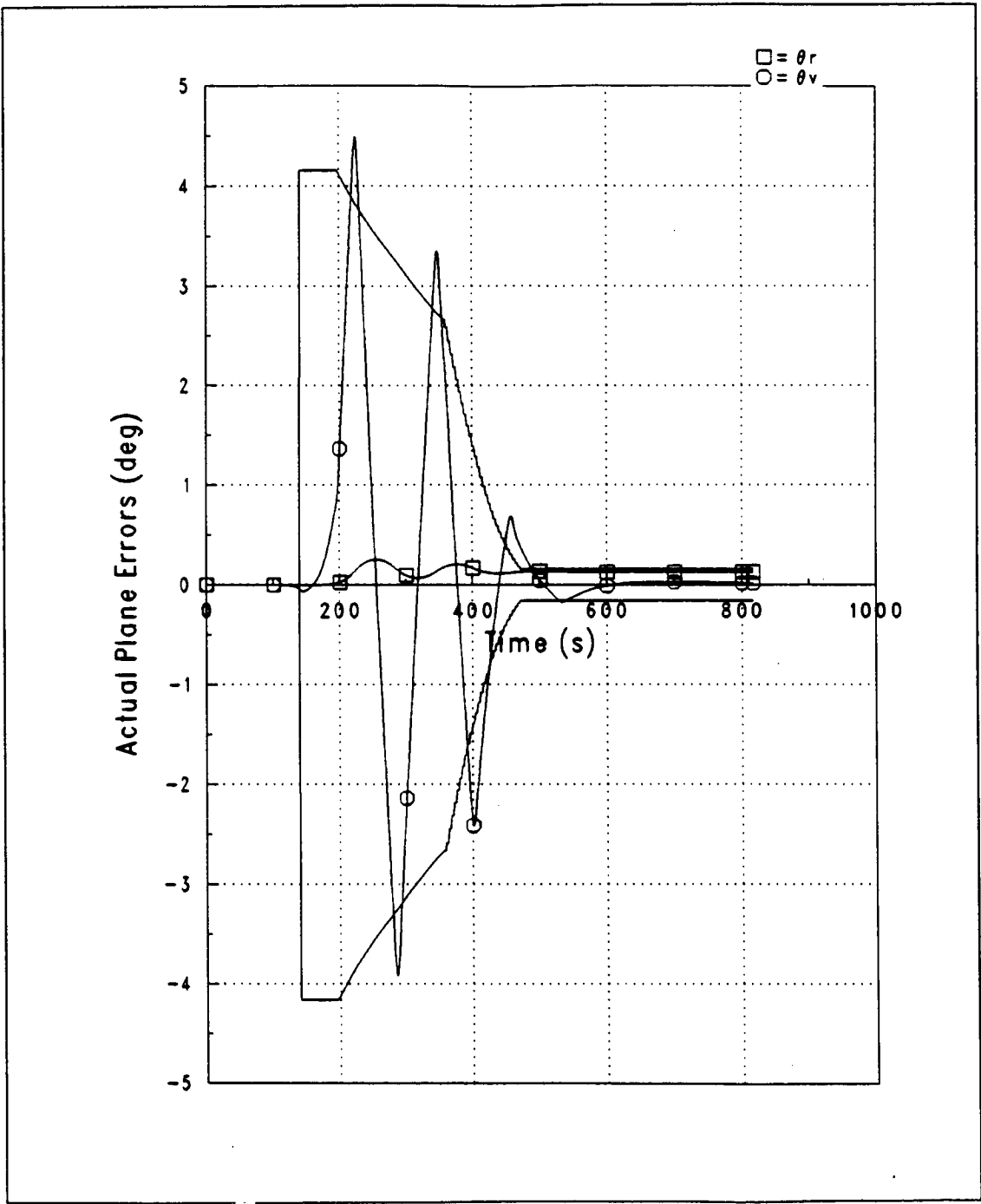


Figure 5-7. Nominal Aerocapture: Orbit Plane Errors

using the nominal approach state parameters defined in Table 5-1. The construction of the initial position and velocity estimates assumes that the Mars-centered inertial frame is initially aligned with the vertical/crosstrack/downrange (V/CT/DR) coordinate frame with axes defined as

$$\hat{i}_V = UNIT(r^I) \quad (5-2)$$

$$\hat{i}_{CT} = UNIT(\underline{v}^I \times r^I) \quad (5-3)$$

$$\hat{i}_{DR} = \hat{i}_V \times \hat{i}_{CT} \quad (5-4)$$

The filter error covariance matrix elements can be initialized based on Mars approach navigation results. Radiometric and optical navigation techniques allow the estimation of vehicle state parameters on the approach hyperbola, and the statistics of the state errors at the start of aerocapture are determined by the accuracy, frequency, and quantity of measurements taken. The initial error covariance matrix utilized in this study is given in Table 5-2 on page 90. The covariances between state elements are shown above the main diagonal, while the correlation coefficients are given below the main diagonal. The position and velocity terms in the matrix correspond to the vector components in the V/CT/DR frame defined in Equations (5-2), (5-3), and (5-4). The six-dimensional position and velocity submatrix was found by linear propagation of the error covariance matrix from 24 hours before periapsis on the inbound hyperbola until 1 hour before periapsis with optical star angle measurements incorporated every hour. Initial conditions for this propagation were taken from expected Deep Space Network (DSN) tracking accuracies on the interplanetary trajectory. It is seen that strong correlations exist between vertical position and most other position and velocity components. This indicates that both density altitude and radar altimeter measurements will cause updates to all state components even though they are essentially only measurements of vertical position.

Table 5-2. Input Filter Error Covariance Matrix

	<i>V Pos.</i>	<i>CT Pos.</i>	<i>DR Pos.</i>	<i>V Vel.</i>	<i>CT Vel.</i>	<i>DR Vel.</i>	$K_p$
<i>V Pos.</i>	7.746E8	6.148E8	5.143E7	3.022E5	-3.734E5	-3.499E5	0.0
<i>CT Pos.</i>	0.9871	5.010E8	3.587E7	2.422E5	-3.044E5	-2.770E5	0.0
<i>DR Pos.</i>	0.5835	0.5061	1.004E7	1.703E4	-2.163E4	-2.413E4	0.0
<i>V Vel.</i>	0.9942	0.9908	0.4923	1.193E2	-1.472E2	-1.361E2	0.0
<i>CT Vel.</i>	-0.9865	-1.0000	-0.5021	-0.9908	1.851E2	1.682E2	0.0
<i>DR Vel.</i>	-0.9996	-0.9840	-0.6058	-0.9907	0.9832	1.582E2	0.0
$K_p$	0.0	0.0	0.0	0.0	0.0	0.0	0.09

### 5.3.2 ERROR DEFINITION AND INITIALIZATION

Navigation system performance results can be expressed in terms of the differences between estimated quantities or parameters calculated using these quantities and the true values as contained in the simulation environment. The estimation errors presented here are formally defined as the difference between the estimated and true quantities, that is

$$\text{estimate error} = \text{estimated value} - \text{true value}$$

The initial values of filter state estimate errors are incorporated by offsetting the environment state from the estimator (nominal) state at the start of aerocapture. The initial errors in the six-dimensional position/velocity vector estimate are random samples generated statistically based on the input covariance matrix of Table 5-2. Thus, the initial position and velocity error components reflect the correlations contained in this matrix. The initial density bias error,  $b_{\rho_0}$ , is computed simply as a sample of a normal, zero mean random variable with standard deviation  $\sigma_{b_{\rho}}$ .

### 5.3.3 NAVIGATION TEST CASES

Two cases are discussed here in detail in order to illustrate basic concepts of navigation filter performance. The first case examines system performance in the presence of a 100% thick ( $3\sigma$ ) atmosphere ( $b_{\rho} = 1.0$ ), both with and without the inclusion of radar altimeter measurements. The initial position and velocity errors for this case place the vehicle on a trajectory which is lower and more steep than the nominal. The second case examines system performance in the presence of a variable density shear profile. The initial position and velocity errors for this case place the vehicle on a trajectory which is higher and more shallow than the nominal. Results using the full covariance matrix, with all covariance terms included, and a diagonal covariance matrix, with all of the off-diagonal covariance terms deleted, are presented. All navigation system performance runs were made with the orbit plane control logic inactive so that no bank reversals were executed.

#### 5.3.3.1 +100% CONSTANT DENSITY BIAS CASES

*5.3.3.1.1 FULL COVARIANCE (NO RADAR ALTIMETER):* Performance of the navigation algorithm with no radar altimeter measurements is shown in the graphs of Figures 5-8 on page 95 through 5-15 on page 102 for the 100% thick constant density bias case.

Figure 5-8 on page 95 shows the true position error components in the V/CT/DR coordinate frame. It is seen that corrections are made to all three position components at the initiation of density altitude measurement incorporation at approximately  $t=100$  s due to the initial correlations in the covariance matrix. One should note, however, that the vertical position error, which is essentially equivalent to the altitude error, is initially reduced from 22800 m to a level of only approximately -4000 m and that this error remains nearly constant throughout aerocapture. This constant altitude error can be explained by examining the problem of simultaneous estimation of altitude and density bias using density altitude measurements. The corrections to vertical position and density bias are a function of the measurement residual, which is the difference between the actual and estimated values of the density altitude measurement (see Eq. (2-13)). By reference to the density altitude measurement equations, Eq. (2-39) and (2-43), it is seen that either an altitude error or a density error will result in a nonzero residual, with the problem being that the two are indistinguishable given the nature of the measurement. In other words, a given residual could be the result of an altitude error, a density error, or a combination of both. The task becomes one of choosing how to weight the initial altitude and bias corrections given the uncertainty in the source of the residual. The amount of the residual attributed to each error source is essentially determined by the respective variance values in the covariance matrix prior to the update. For the case under examination, attributing the entire residual arising from an altitude error of 22800 m and density bias of +100% to just an altitude error would result in an overcorrection of 5300 m, or an altitude estimate error of approximately -5300 m (using the exponential density profile of Eq. (2-37) with an estimated altitude of 75 km at the time of the measurement). This maximum error will increase with decreasing measurement altitude due to increasing density model scale height. The covariance matrix loading used in this analysis was chosen to attribute most, but not all, of the initial residual to altitude error since this appears to be its main contributor. Figure 5-12 on page 99 shows the true and estimated values of the atmospheric density bias. It is seen that, with the given covariance matrix loading, the filter estimates the bias at only 22% after the first measurement. This means that an altitude error equiv-

alent to a + 78% density bias (approximately -4400 m) should result to account for the entire initial measurement residual. This agrees closely with the actual results in Figure 5-8.

Figure 5-9 on page 96 shows the rms values of the position error components for the + 100% density bias case. The rms error is simply the square root of the corresponding diagonal element of the current filter error covariance matrix, and can be thought of as the level of estimate accuracy the filter "thinks" it has achieved. The rms vertical and crosstrack position errors are very close to the actual error magnitudes, while the rms downrange error indicates that the filter is slightly optimistic in light of the actual error.

Figures 5-10 on page 97 and 5-11 on page 98 show the actual and rms velocity errors, respectively. The initial correlations with vertical position result in reduction of the error magnitudes in all three components below their initial values. The rms errors vary around approximately 4 m/s, which means that the filter is slightly optimistic since the actual vertical and downrange velocity errors approach -6 m/s and + 6 m/s, respectively, near atmospheric exit.

Figure 5-12 on page 99 shows the actual and estimated values of atmospheric density bias. It is seen that the density bias estimate never exceeds 32%, and that small variations in the estimate occur due to changing altitude. Again, this is due to the nature of the density altitude measurement error and the nearly constant vertical position error established by the first measurement update. An interesting phenomenon is illustrated in Figure 5-13 on page 100, which shows the percentage errors in estimated density bias and calculated density. Despite errors in excess of -70% in the estimated density bias, errors in the density (calculated using this estimate and the estimated altitude) remain near zero for the duration of measurement incorporation. This can be explained in light of the mechanics of the Kalman filter. Essentially, the filter is attempting to drive the measurement residual, or the difference between the measured and estimated density altitudes, to zero. This is equivalent to driving the difference between the the measured and esti-

mated densities to zero. Since the filter is estimating altitude and density bias, the two major error sources in the calculation of density, the estimates of these quantities will be correlated so that the residual is driven to zero. Thus, the corrections to vertical position and density bias, which are correlated through the components of the measurement sensitivity vector of Eq. (2-44), are made such that the resulting errors have a cancelling effect in the calculation of the estimated density by Eq. (A-5). It is therefore seen that the accuracy of the estimated density, which is the quantity of interest for calculation of aerodynamic control capability in the guidance, can be kept very high even in the presence of large errors in individual parameters used in its calculation, provided that these parameters are estimated together in the filter.

Figure 5-14 on page 101 is a plot of the errors in orbital apoapsis altitude, periapsis altitude, and semi-major axis. The error in apoapsis altitude is of concern because of its effect on exit phase guidance targeting. The spike at  $t = 200$  s indicates the point at which the orbital energy has been decreased to the level at which the Mars-relative orbit becomes elliptical. The errors in apoapsis and periapsis altitudes are reduced to approximately 17 km and -3 km, respectively, by the end of aerocapture. The error in semi-major axis results for the most part from the errors in vertical position and downrange velocity, which are nearly equivalent to the errors in altitude and velocity magnitude, respectively.

The errors in the estimates of the out-of-plane position and velocity angles,  $\theta$ , and  $\theta_v$ , are plotted in Figure 5-15 on page 102. Our main concern is with  $\theta_v$ , which is the variable used in orbit plane control. Accuracy in the estimate of  $\theta_v$  is important since fuel requirements for correction of plane errors after aerocapture are very high, and plane control performance, especially during the exit phase, is very sensitive to the estimate accuracy. The error in  $\theta_v$  is reduced from  $.12^\circ$  to  $-.02^\circ$  by the first measurement update and remains fairly constant. Without this correction, the error would have been unacceptably large since it was on the order of the  $\theta_v$  control corridor width during exit ( $0.16^\circ$ ).

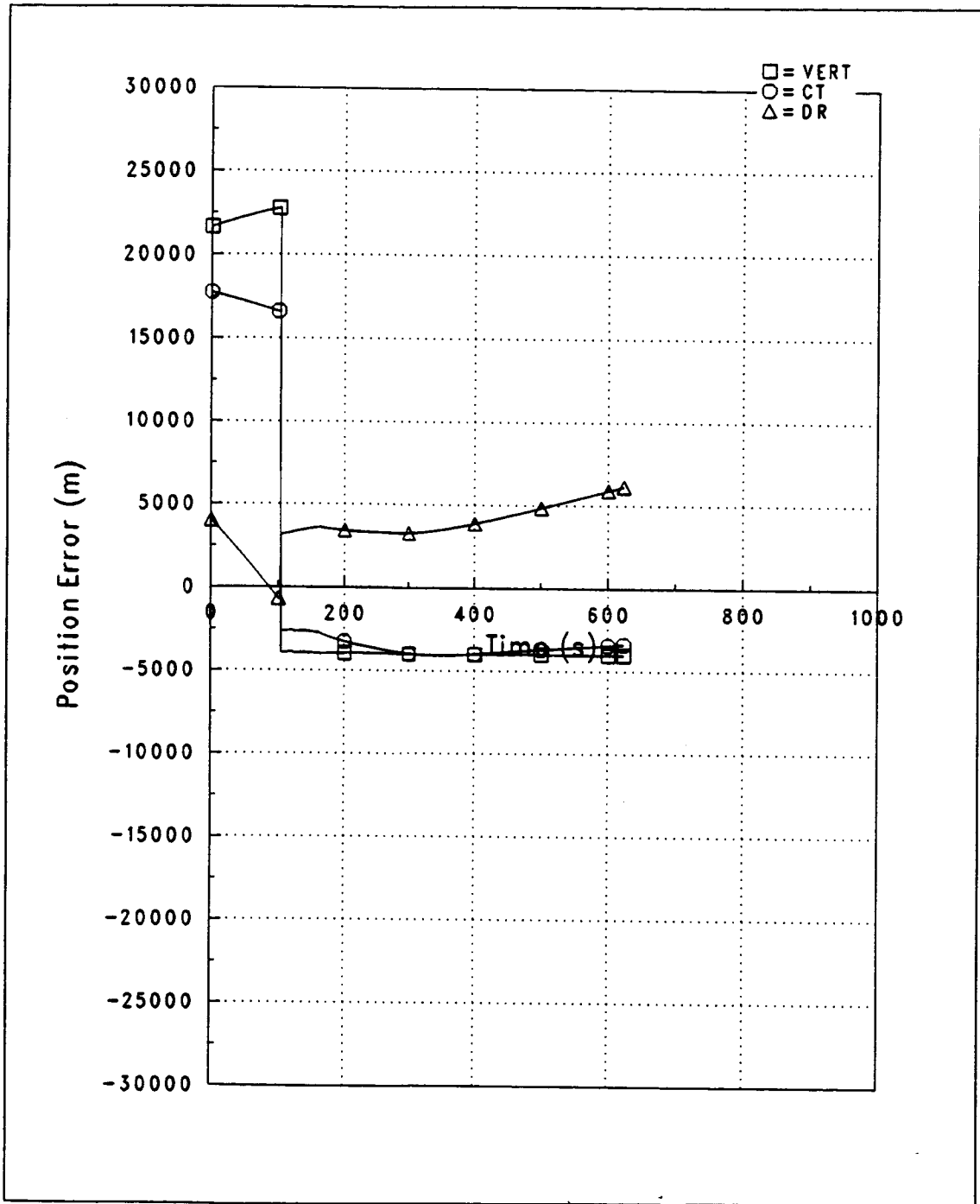


Figure 5-8. Case # 031000D, + 100% Density: Position Estimate Errors

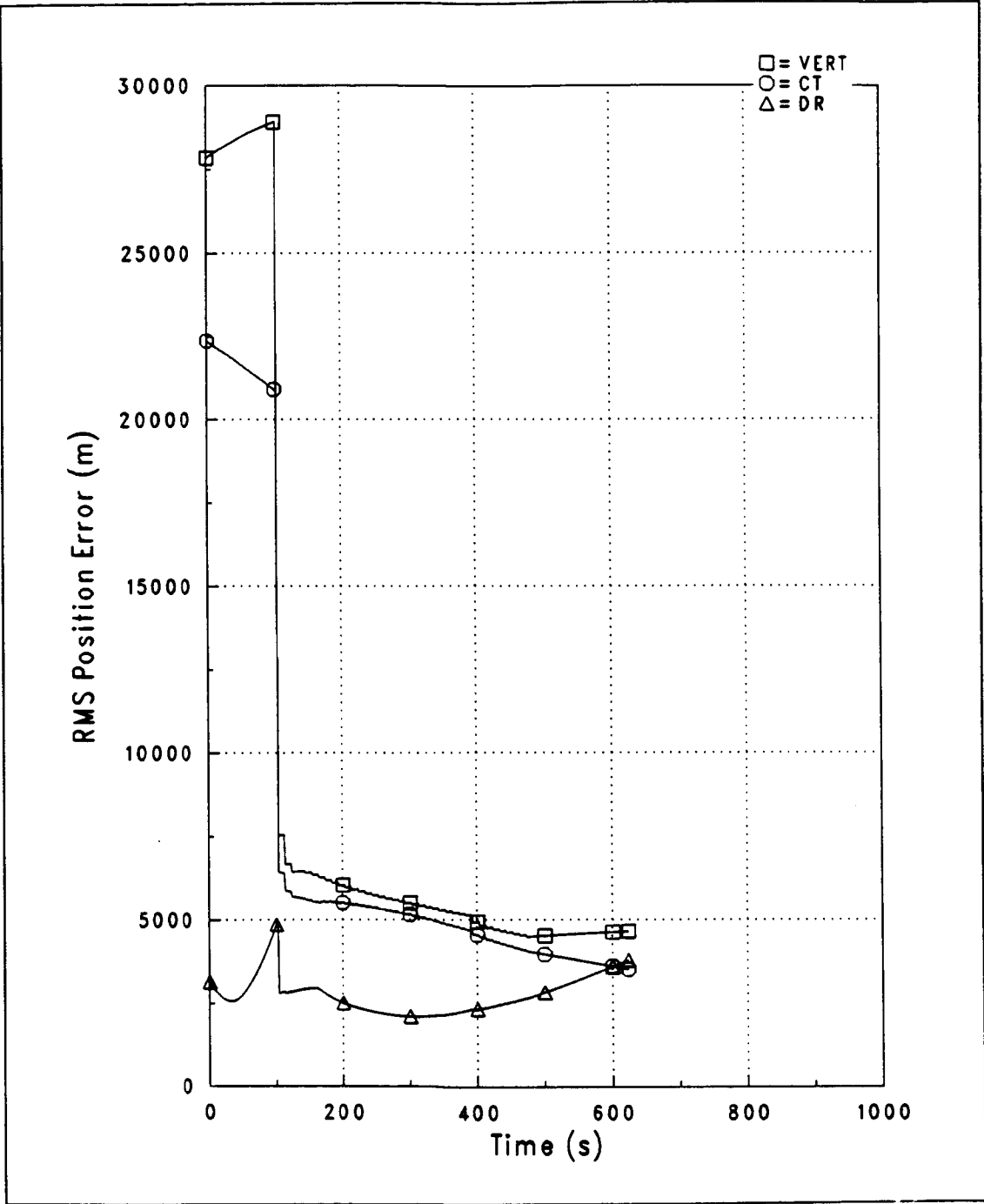


Figure 5-9. Case # 031000D, + 100% Density: RMS Position Errors

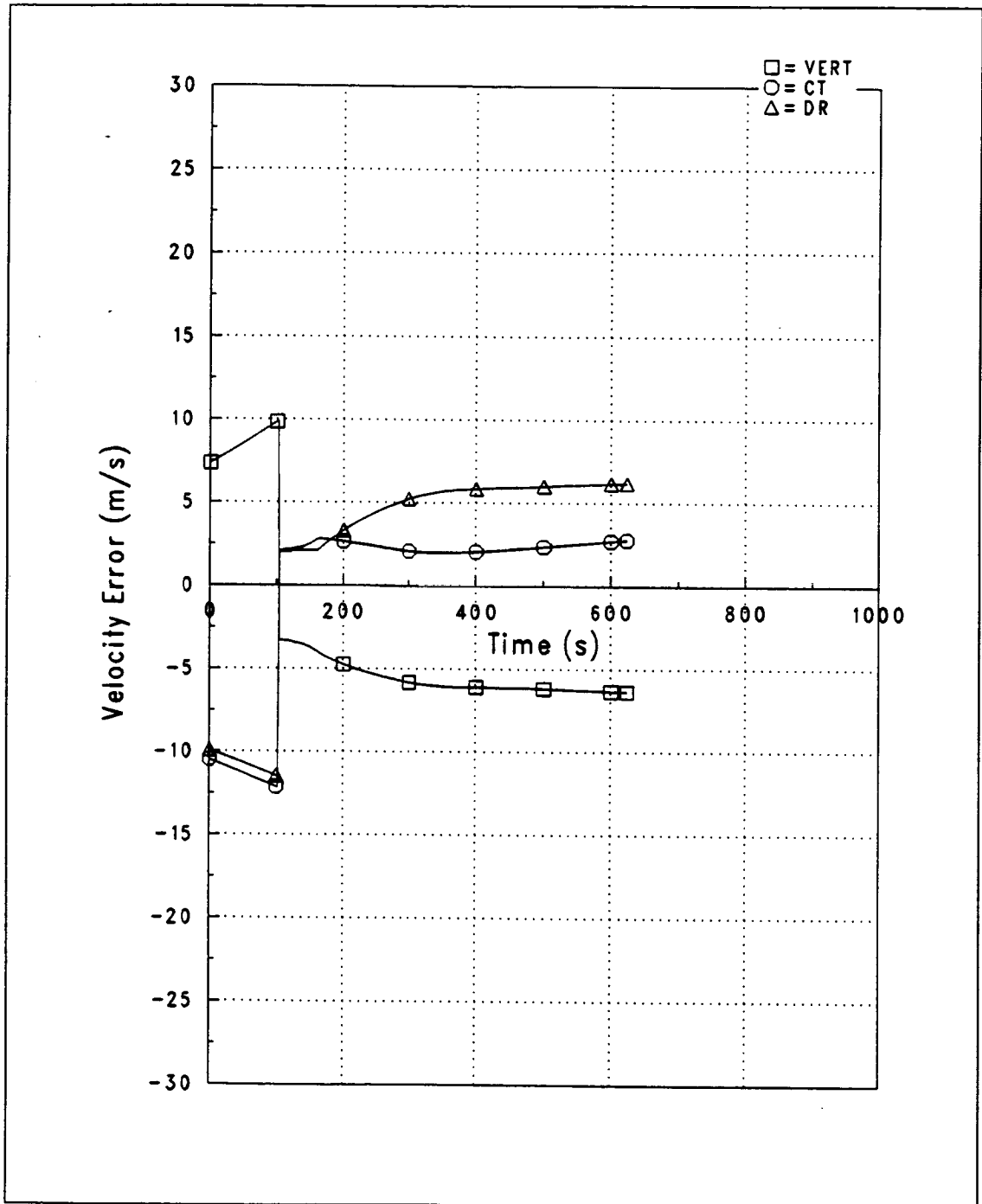


Figure 5-10. Case # 031000D, + 100% Density: Velocity Estimate Errors

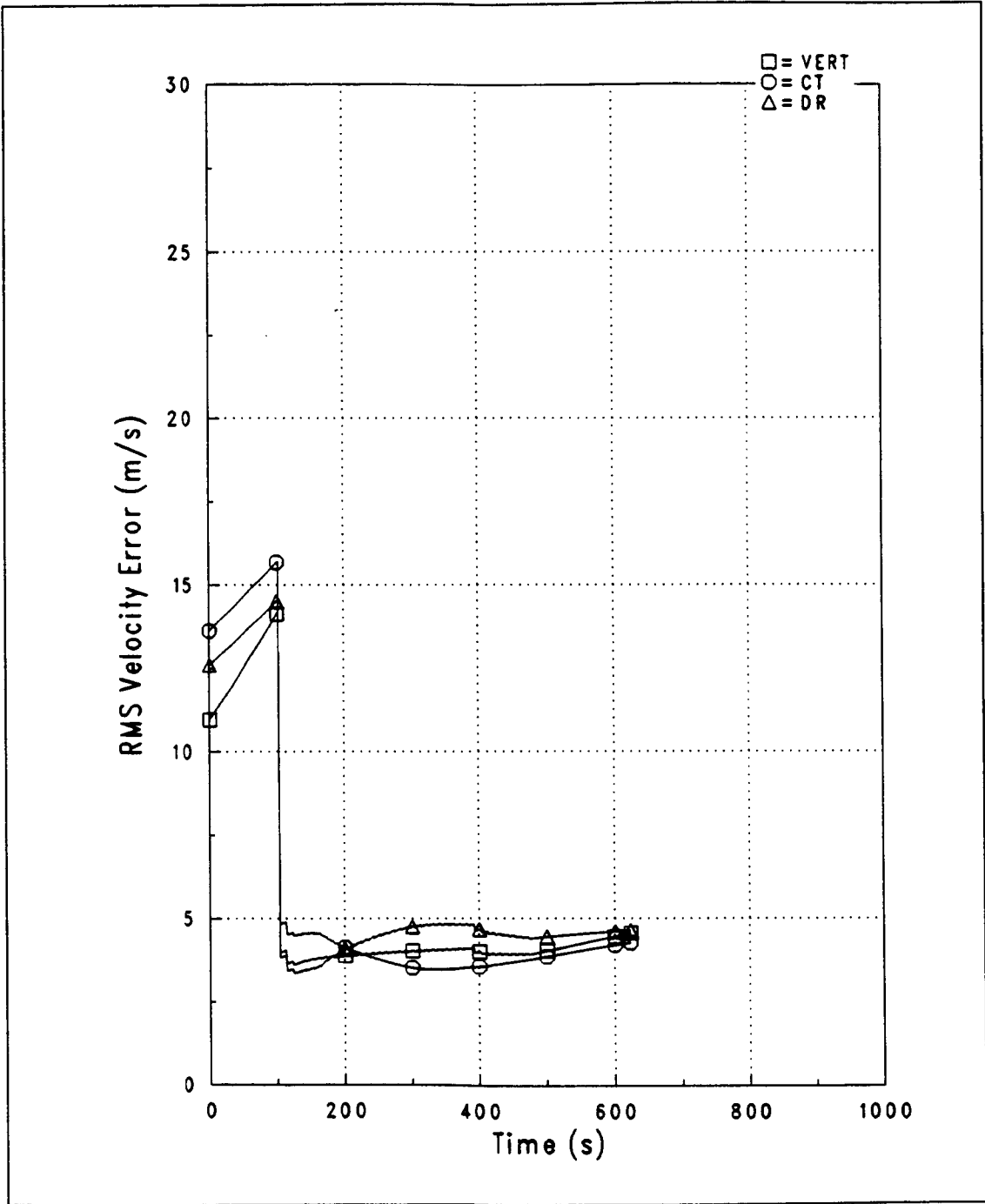


Figure 5-11. Case # 031000D, + 100% Density: RMS Velocity Errors

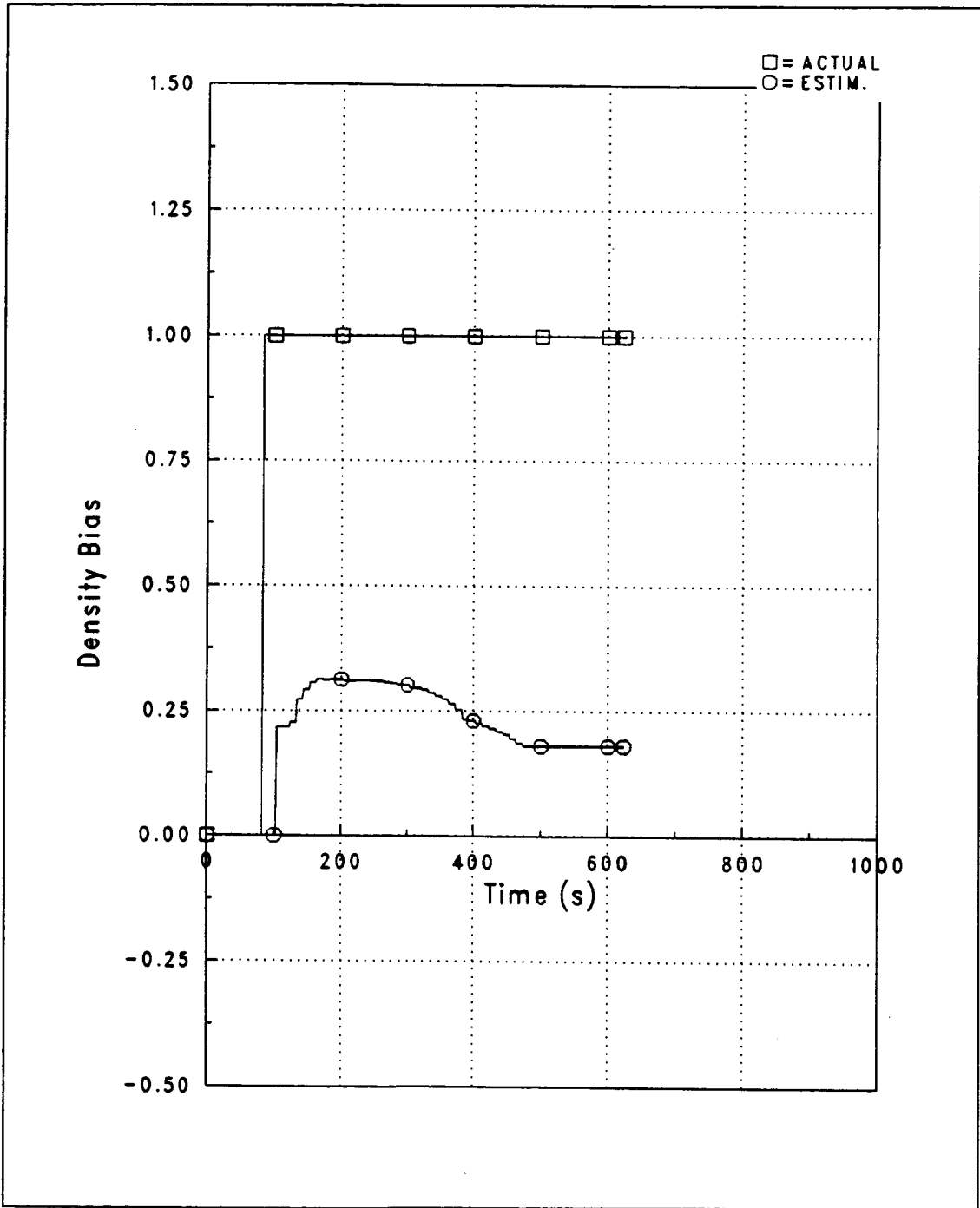


Figure 5-12. Case # 031000D, + 100% Density: Density Bias

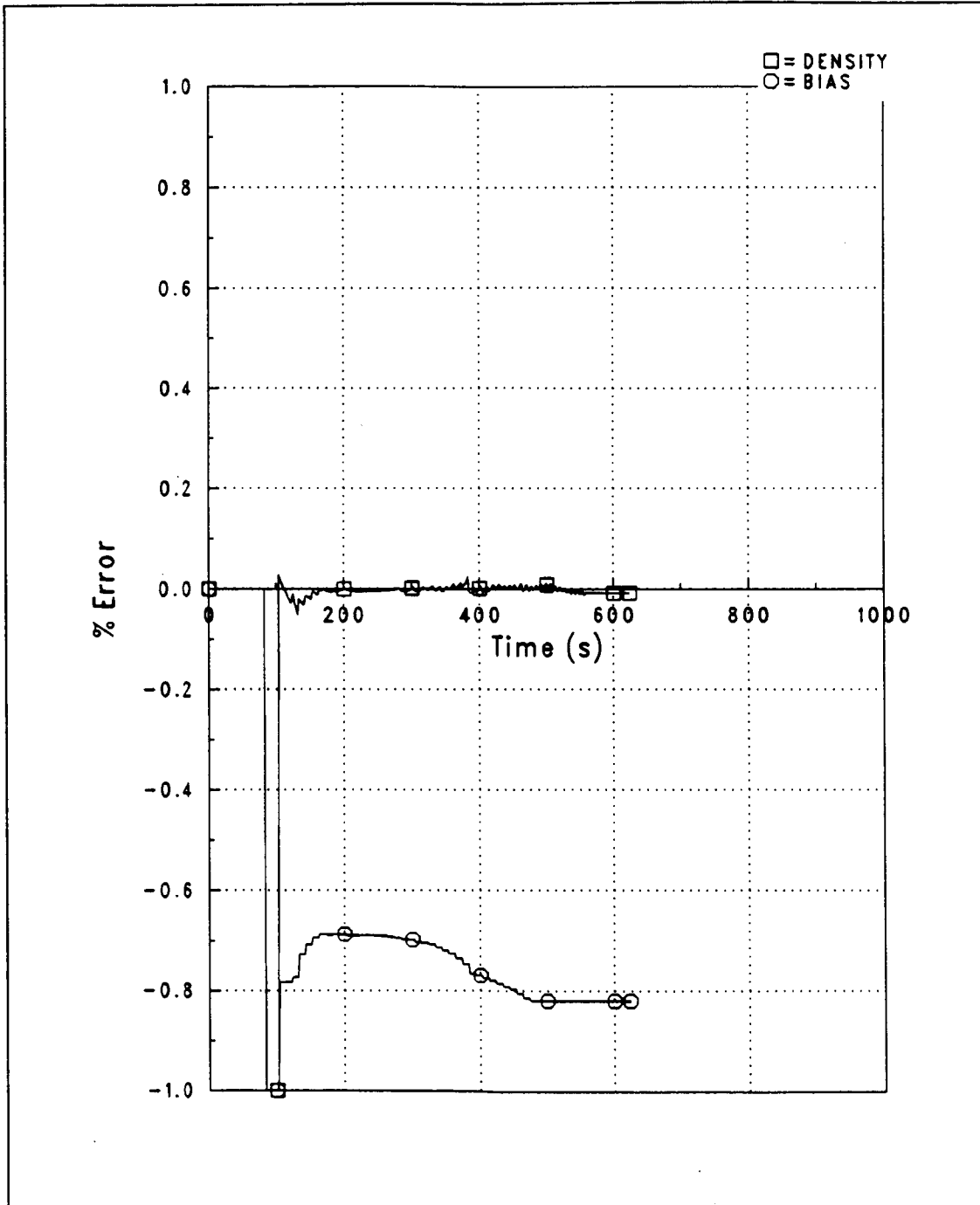


Figure 5-13. Case # 031000D, + 100% Density: Density, Bias Estimate Errors

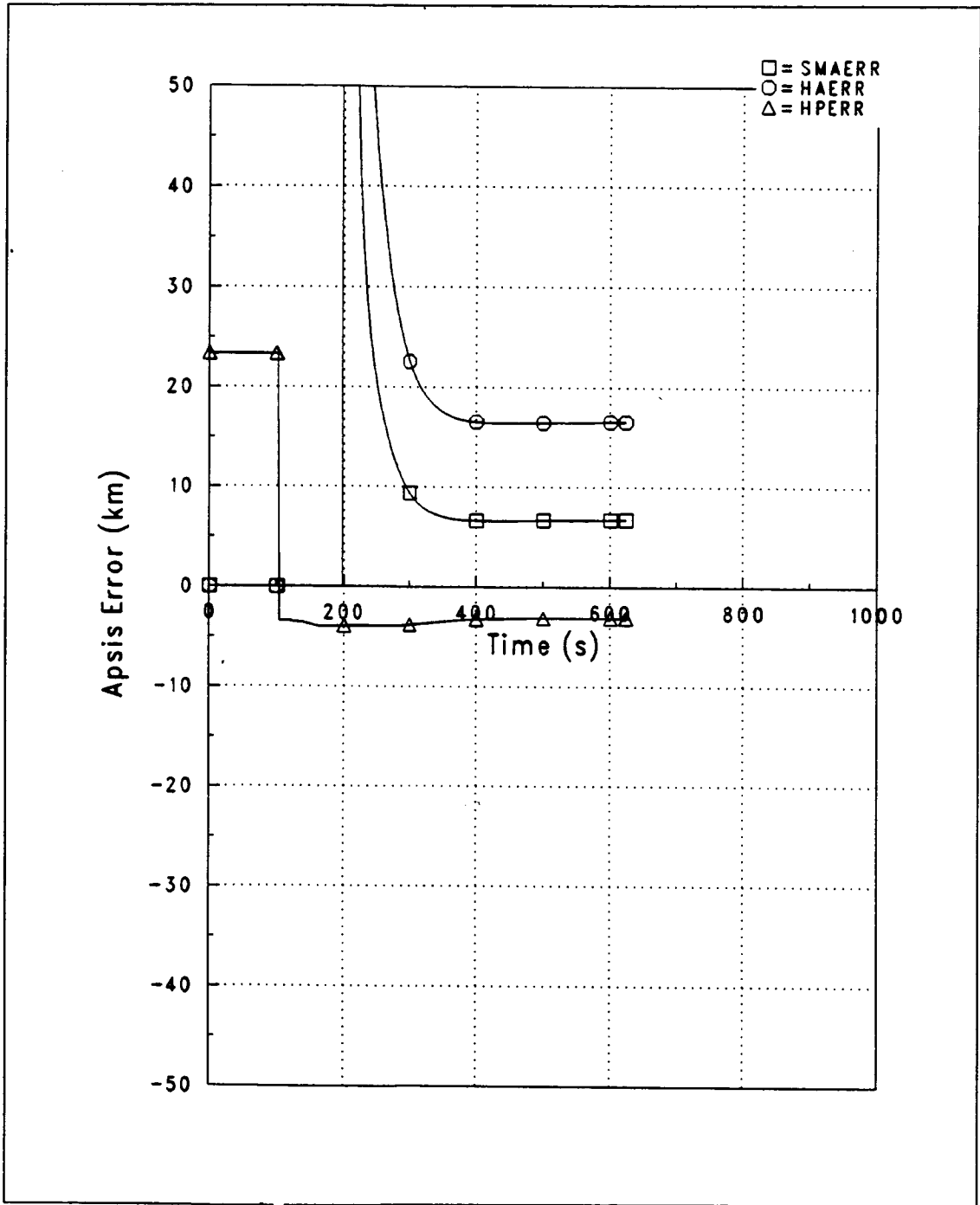


Figure 5-14. Case # 031000D, + 100% Density: Orbital Apis Estimate Errors

C - 2

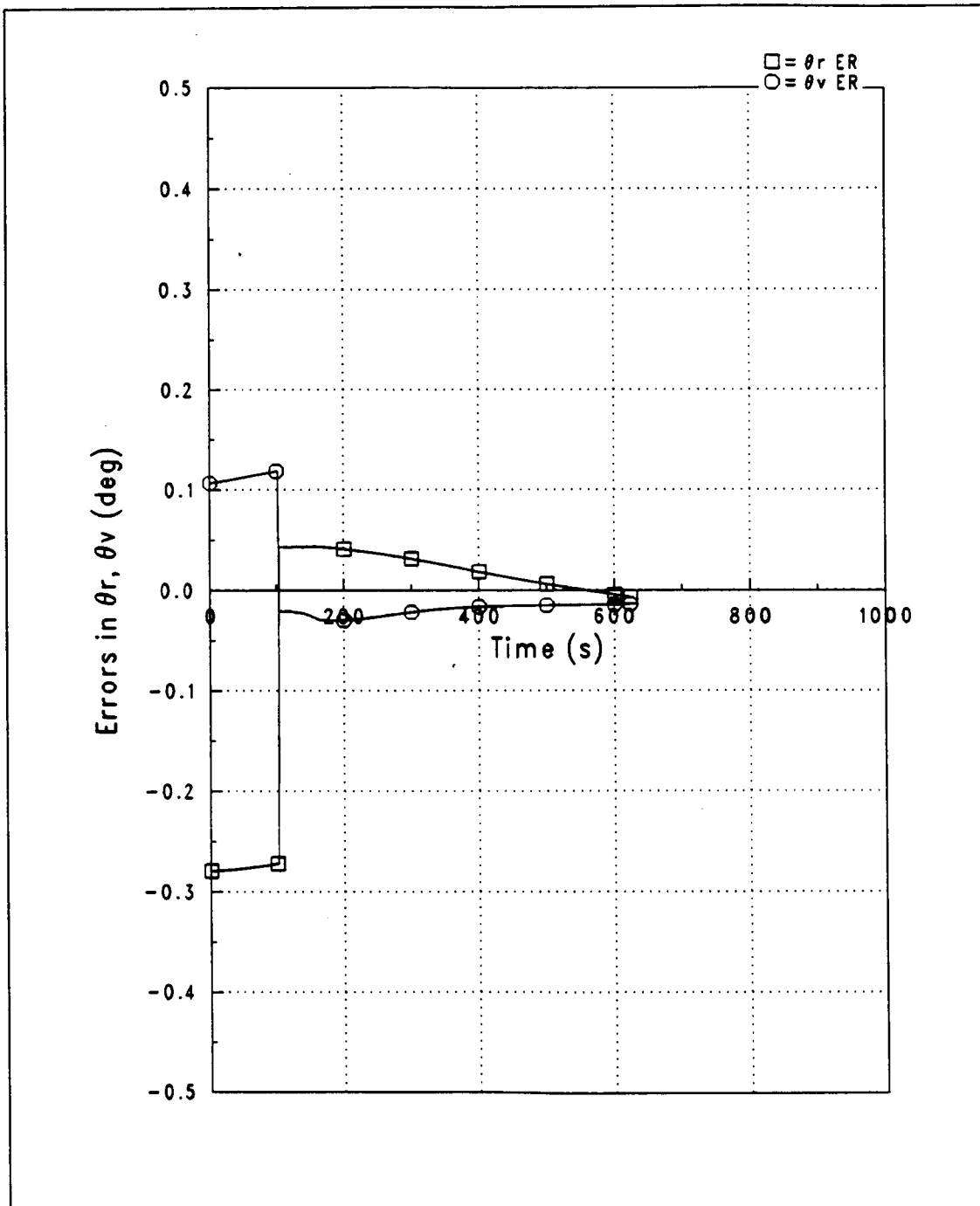


Figure 5-15. Case # 031000D, + 100% Density:  $\theta_r$ ,  $\theta_v$  Estimate Errors

5.3.3.1.2 *FULL COVARIANCE (WITH RADAR ALTIMETER)*: Figures 5-16 on page 105 through 5-23 on page 112 illustrate navigation performance for the +100% density bias case with radar altimeter measurements included prior to aerocapture.

The actual V/CT/DR position error components are shown in Figure 5-16 on page 105. The first radar altimeter measurement is incorporated at  $t = 86$  s, 17 s before the start of density altitude measurements. Using the altimeter measurements, the vertical position error is brought down to less than 500 m before density altitude measurements begin. The accuracy of the down-range and crosstrack components is also improved over the previous case, where only density altitude measurements were incorporated. The improved accuracy is realized due to the accuracy of the altimeter measurements and the fact that the entire measurement residual can be attributed to a vertical position error. The rms position errors are graphed in Figure 5-17 on page 106.

Figures 5-18 on page 107 and 5-19 on page 108 are plots of the actual and rms velocity error components, respectively. A general improvement in the accuracy of the estimates over the case with no altimeter measurements is seen.

The actual and estimated density bias values are shown in Figure 5-20 on page 109. Since the altitude error has been decreased to a small value by the time density altitude measurements are initiated (as is indicated by the actual and rms vertical position errors), it can be safely assumed that most of the measurement residual can now be attributed to density bias, and that the measurements should be used to correct the density bias estimate and not the vertical position estimate. It is seen in Figure 5-20 that the filter response is to do exactly this. The first few measurements bring the estimate within the range of the true bias, and the density bias estimate remains much closer to the actual than in the case where altimeter measurements were not used.

Comparison of the navigation performance for the cases with and without the inclusion of radar altimeter measurements shows that some improvement is realized through the use of the altimeter. However, it should be remembered that a + 100% constant density bias is a worst case scenario, and that relative improvement of navigation results using the radar altimeter will diminish with decreasing initial density bias. This will be seen in the density shear results in the next section. Also, the assumed error characteristics of the altimeter used in this study provide a measurement accuracy of better than 2 km. It is seen from the case just examined that the addition of altimeter measurements will provide little or no improvement in navigation performance over density altitude measurements alone if the altimeter measurement accuracy level is more than approximately 5 km.

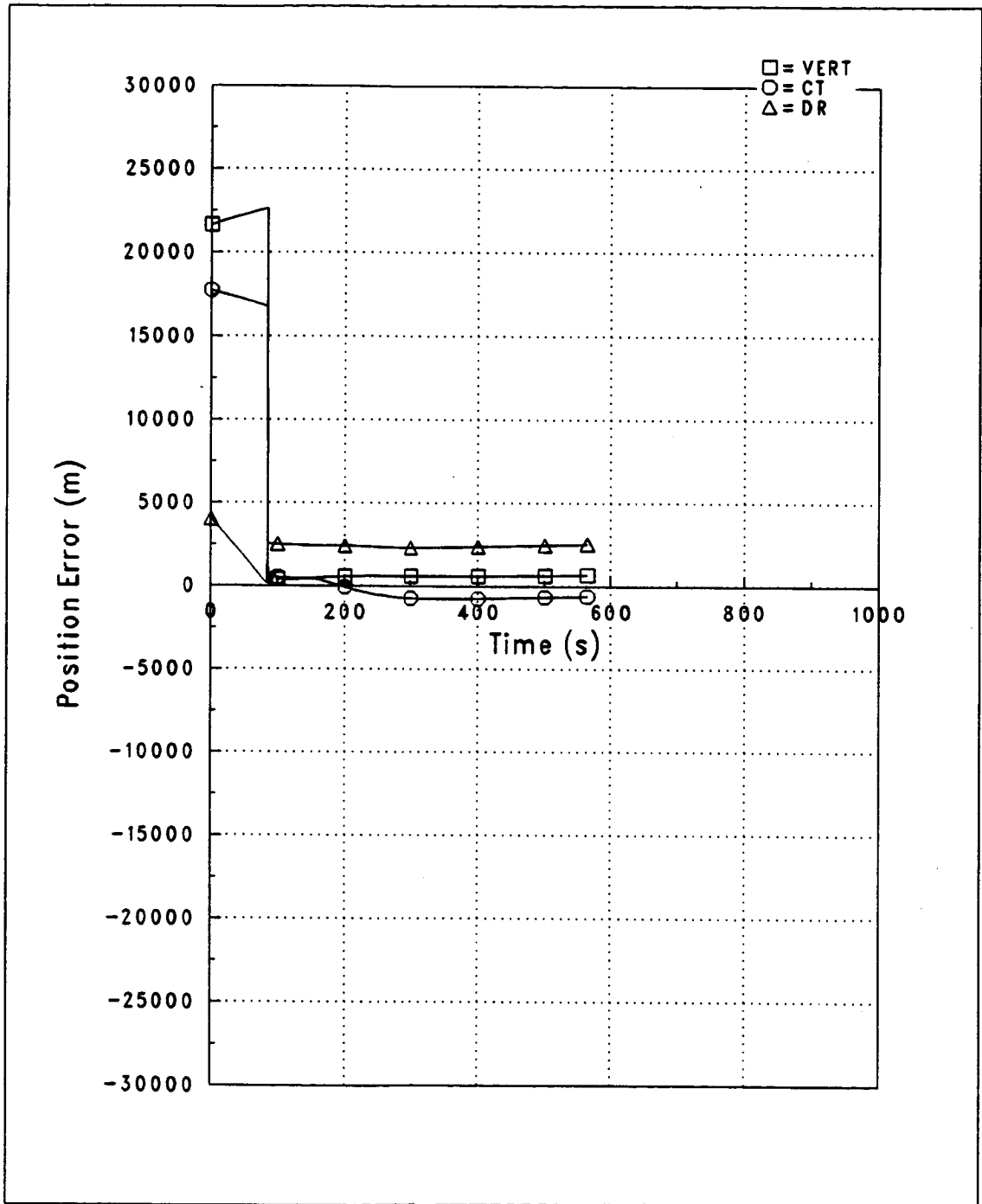


Figure 5-16. Case # 031000RD, + 100% Density: Position Estimate Errors

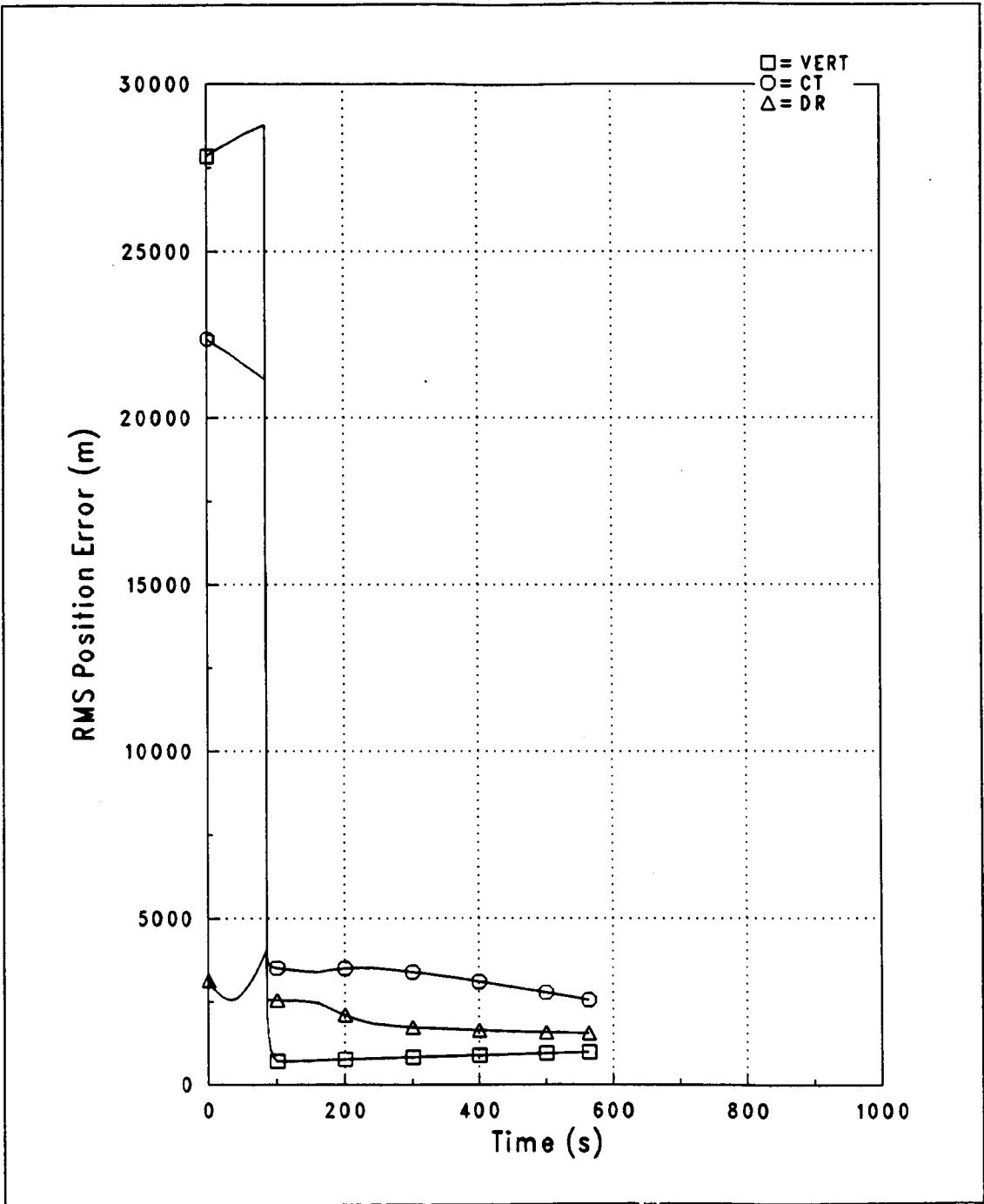


Figure 5-17. Case # 031000RD, + 100% Density: RMS Position Errors

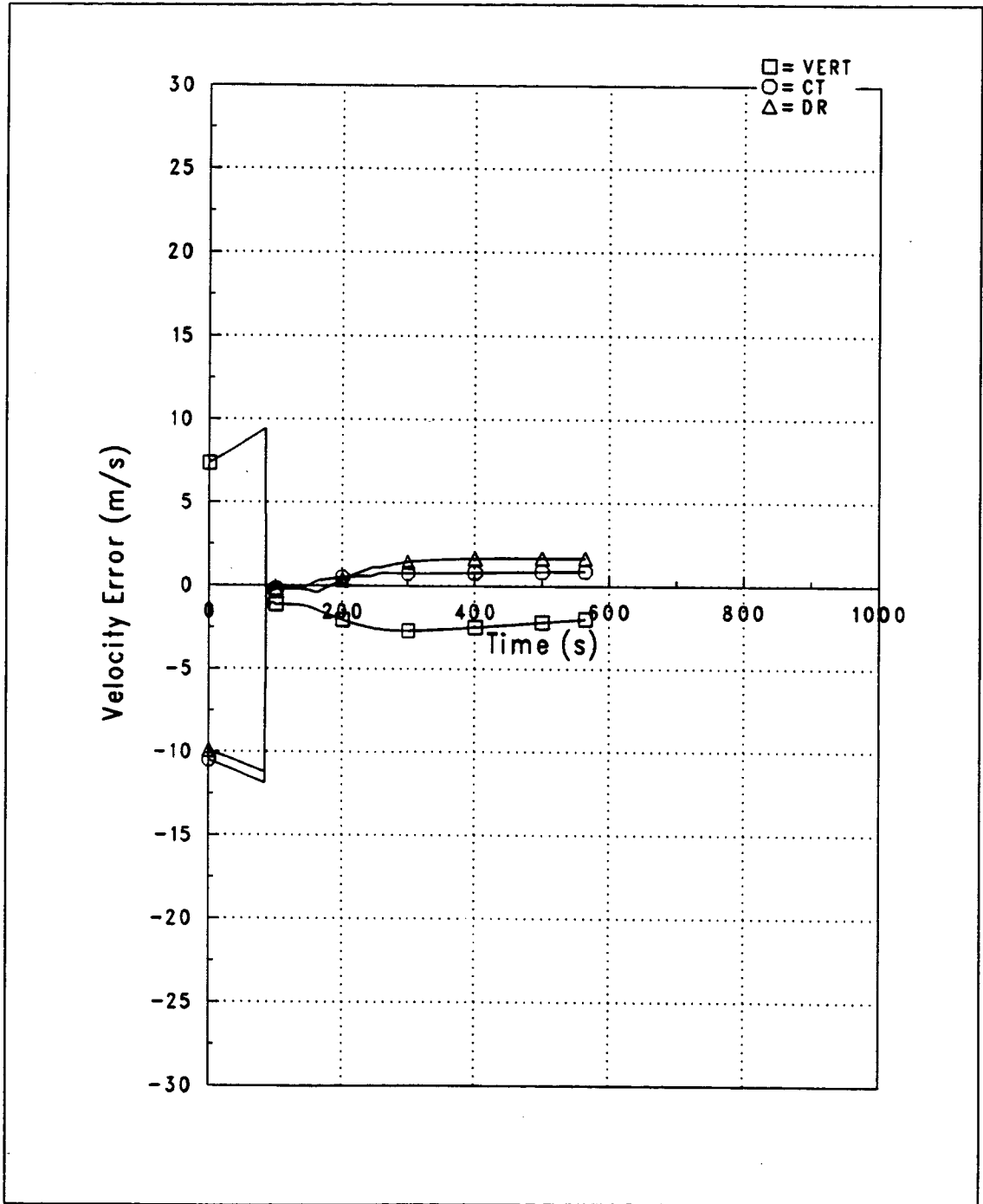


Figure 5-18. Case # 031000RD, + 100% Density: Velocity Estimate Errors

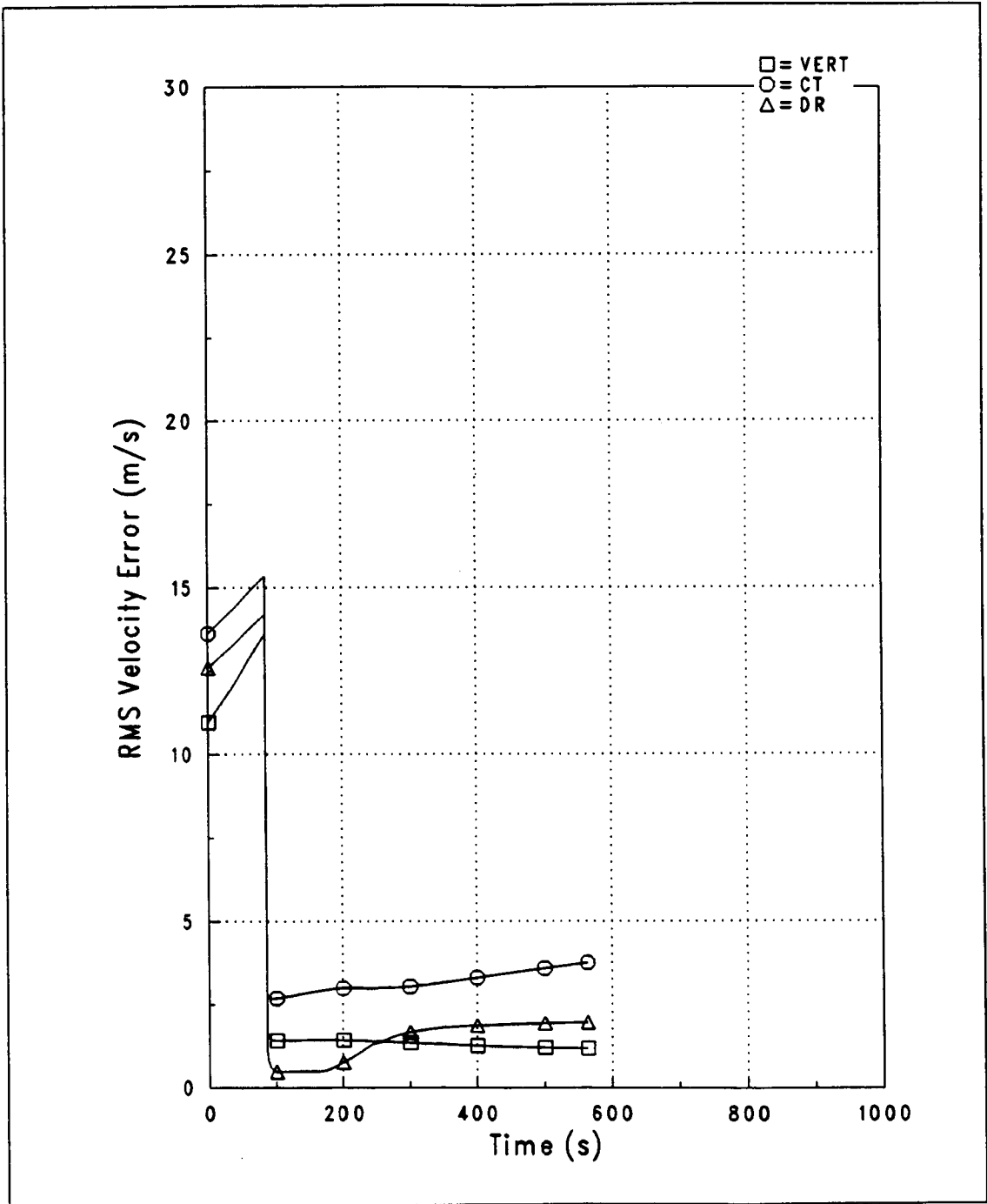


Figure 5-19. Case # 031000RD, +100% Density: RMS Velocity Errors

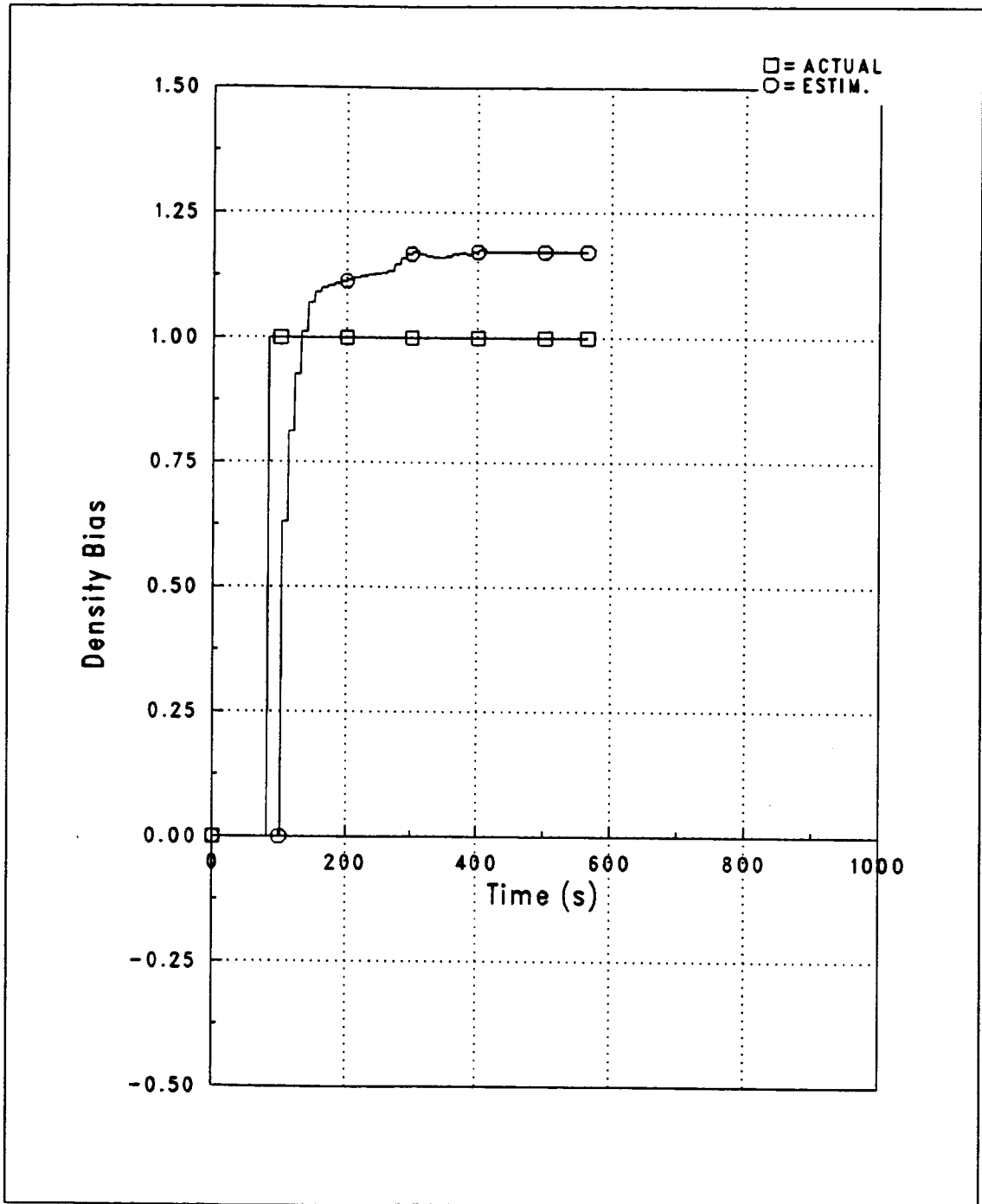


Figure 5-20. Case # 031000RD, + 100% Density: Density Bias

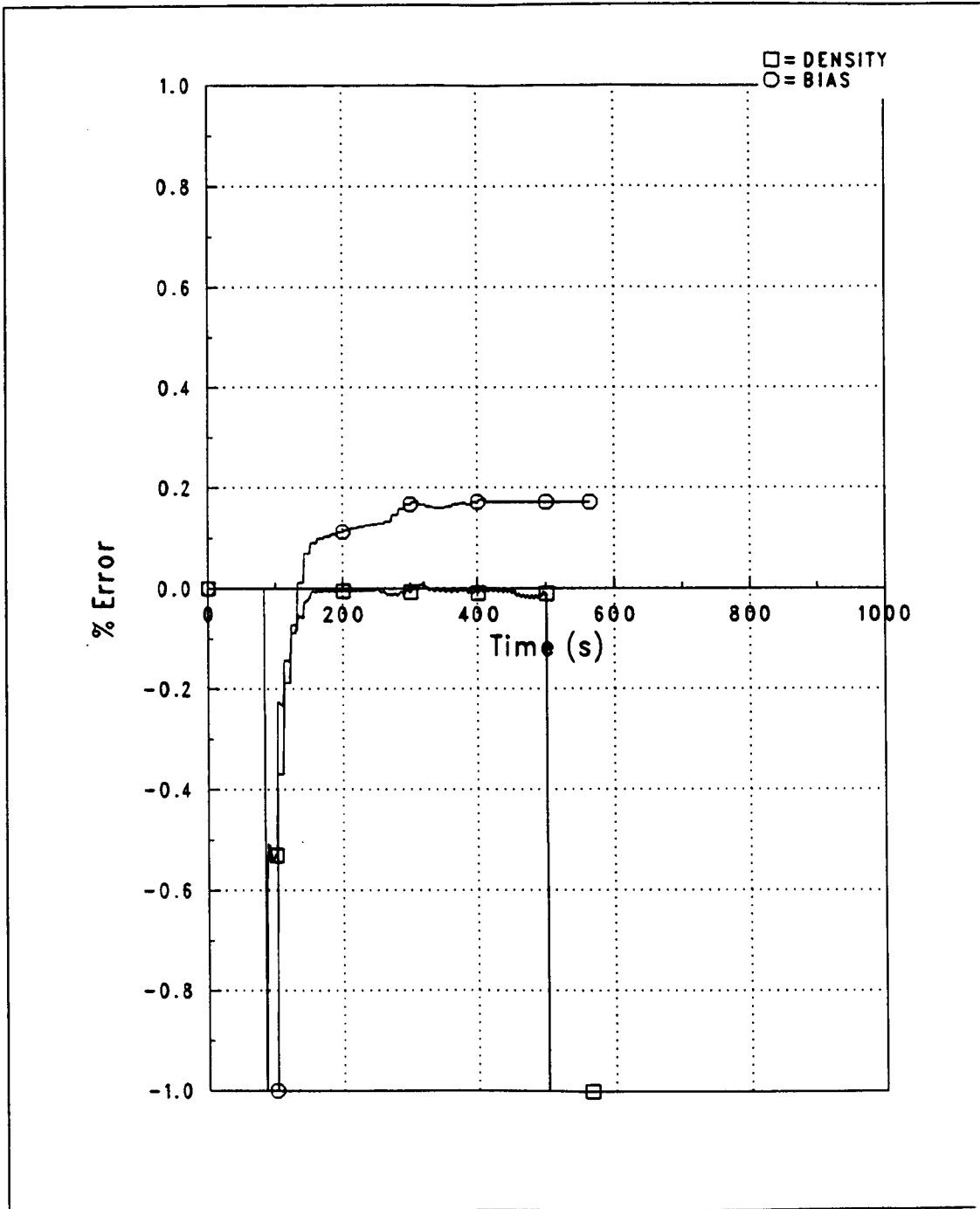


Figure 5-21. Case # 031000RD, + 100% Density: Density, Bias Estimate Errors

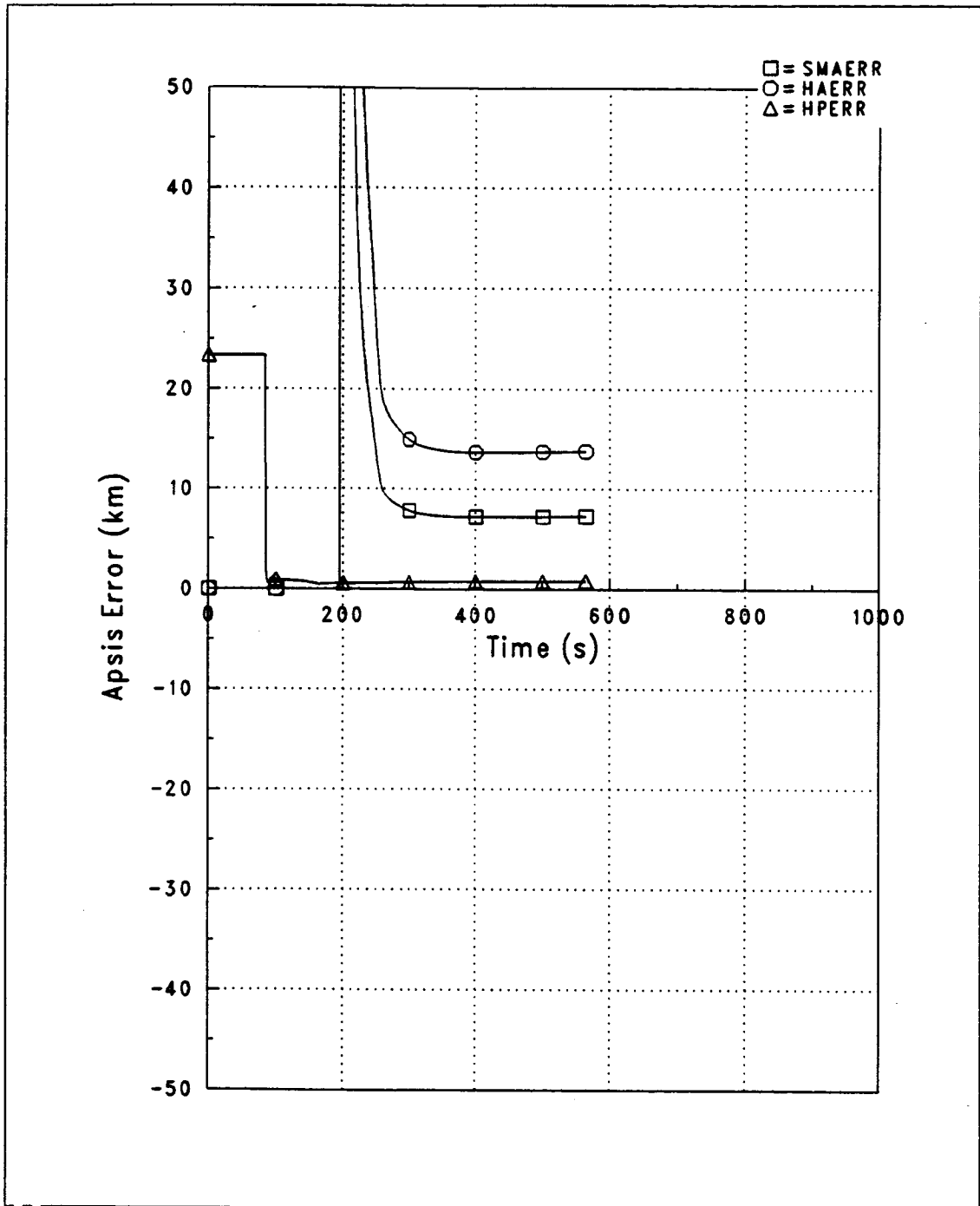


Figure 5-22. Case # 031000RD, + 100% Density: Orbital Apis Estimate Errors

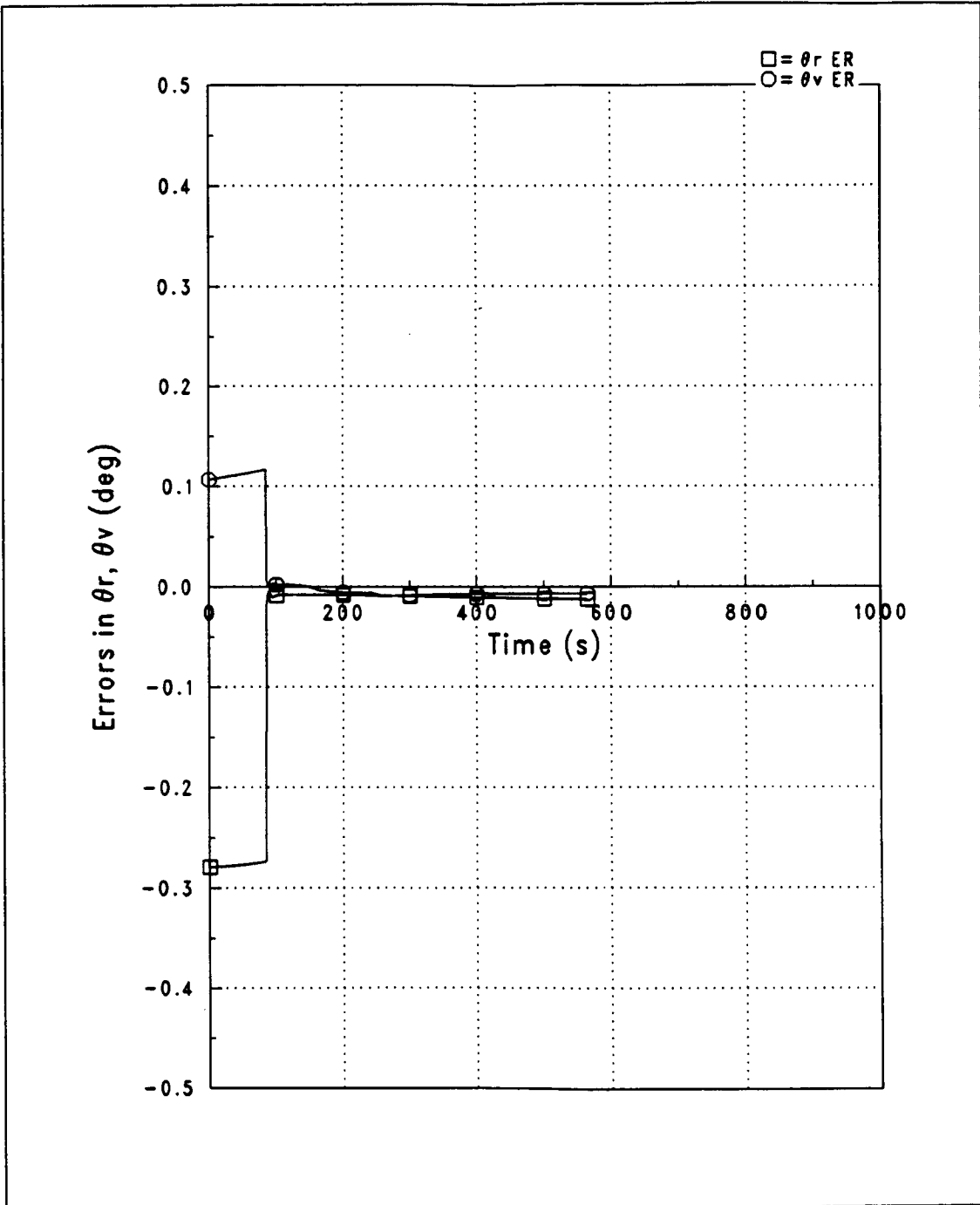


Figure 5-23. Case # 031000RD, + 100% Density:  $\theta_r$ ,  $\theta_v$  Estimate Errors

### 5.3.3.2 DENSITY SHEAR CASES

5.3.3.2.1 *FULL COVARIANCE (NO RADAR ALTIMETER)*: Figures 5-24 on page 114 through 5-30 on page 120 show navigation performance results for a case in which the atmospheric density bias is no longer constant, but varies dynamically with position.

The actual and estimated density bias profiles are shown in Figure 5-28 on page 118. The true density bias varies widely over the trajectory, with "shears" of up to 60% occurring. Density altitude measurement incorporation is initiated at approximately  $t = 150$  s. It is seen that the first density bias correction is very large and is applied in the wrong direction. While a portion of this miscorrection can be attributed directly to the vertical position error, it was found that most of it is due to the error in the density model scale height induced by the large negative vertical position error (see Eq. (2-38)). Figure 5-24 shows that the vertical position error is reduced to less than 1000 m by the first measurement, so that the error in the density model scale height will also be greatly reduced for the second measurement. Referring again to Figure 5-28, it is seen that the correction due to the second measurement is in the opposite direction of the first correction, effectively cancelling the scale height-induced error.

The density bias estimate plot shows that the filter actively tracks the dynamic density variations over the trajectory. It should be noted, however, that the estimated profile is offset from the actual profile. This offset is due primarily to the vertical position estimate error which remains after the first few measurement updates. It is also partially due to the filter model of the density bias. Although the filter noise level is kept high to keep it tracking the dynamic variations, tracking accuracy is affected by both the time constant of the Markov model and the measurement update rate.

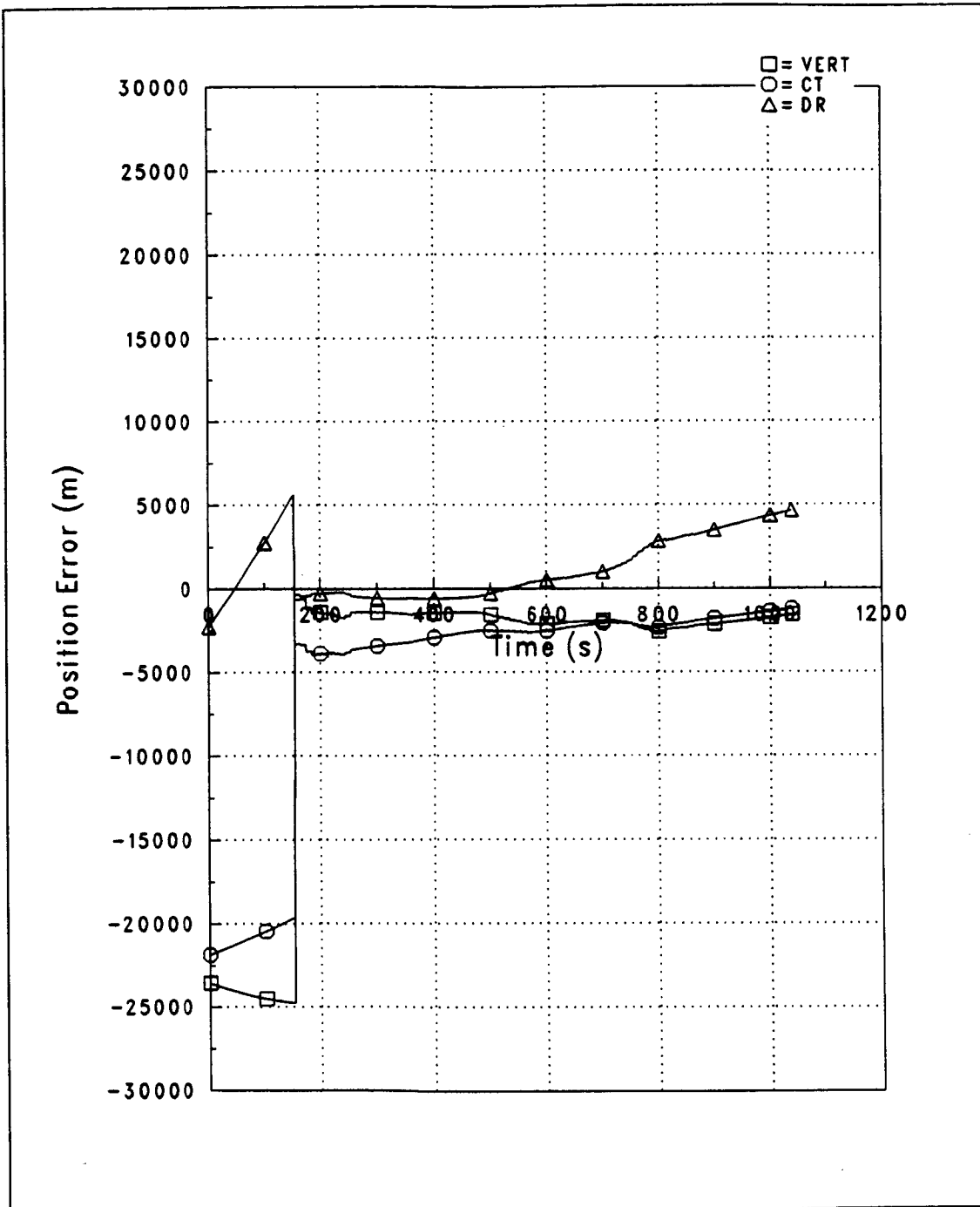


Figure 5-24. Case # 288500D (Full Covariance): Position Estimate Errors

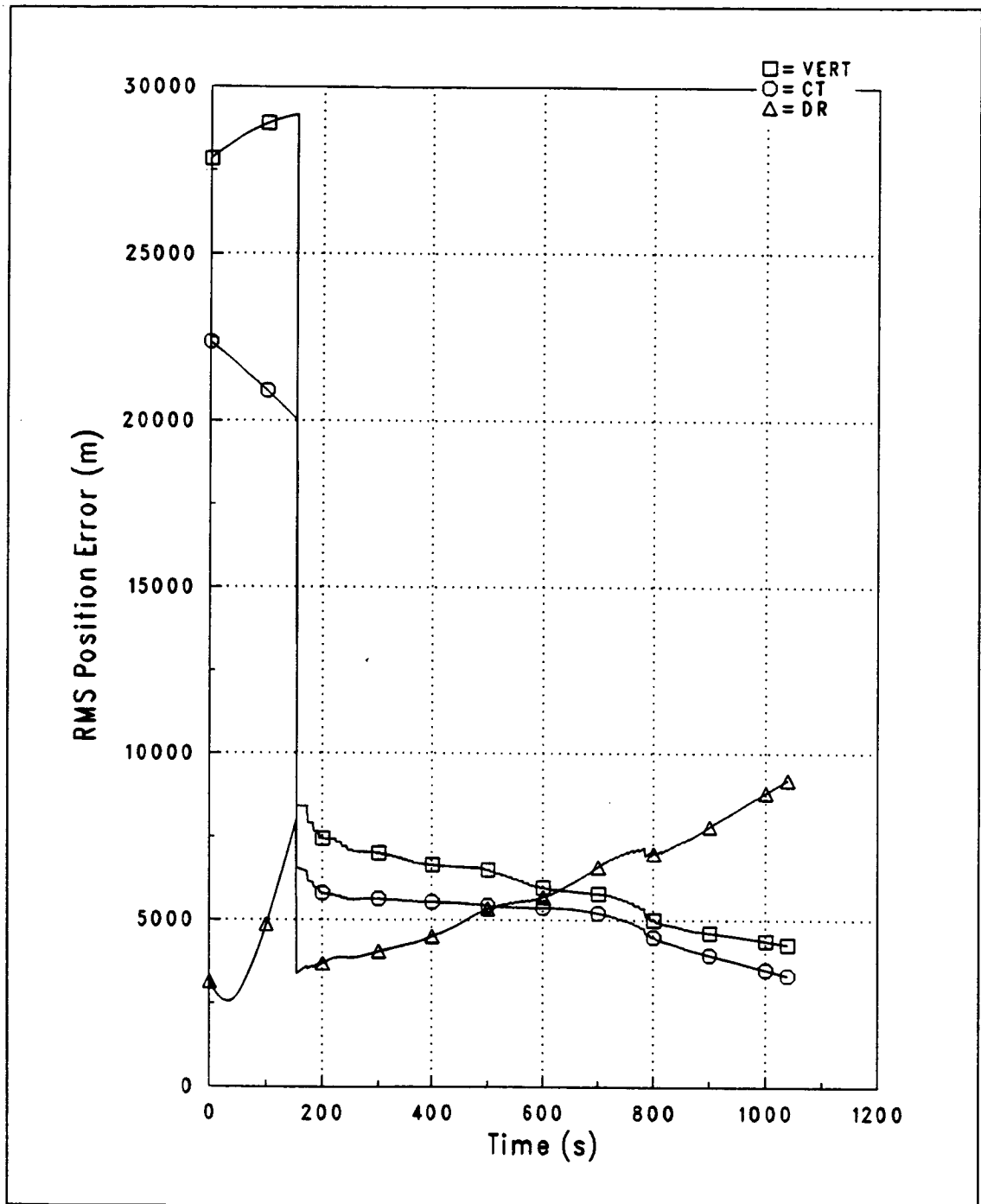


Figure 5-25. Case # 288500D (Full Covariance): RMS Position Errors

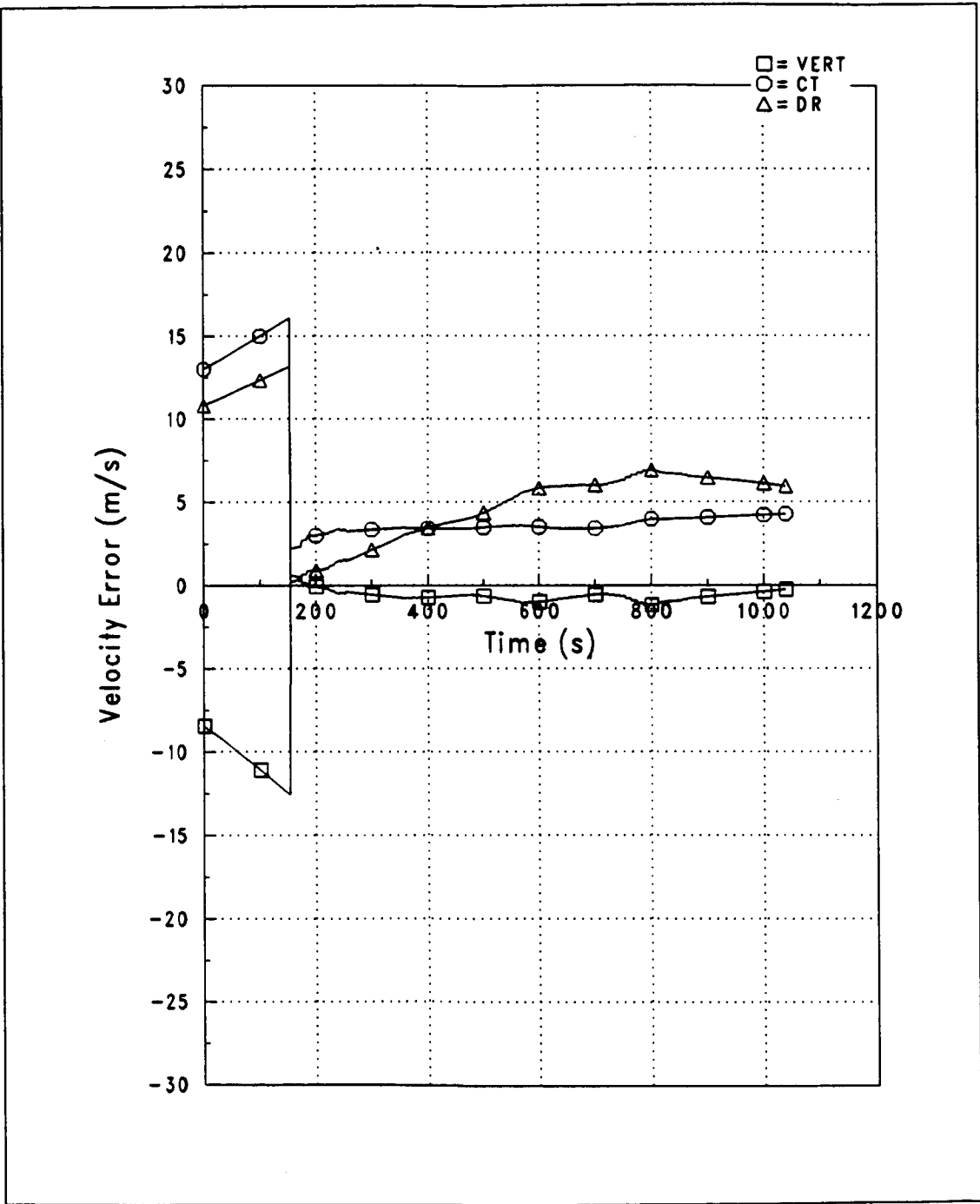


Figure 5-26. Case # 288500D (Full Covariance): Velocity Estimate Errors

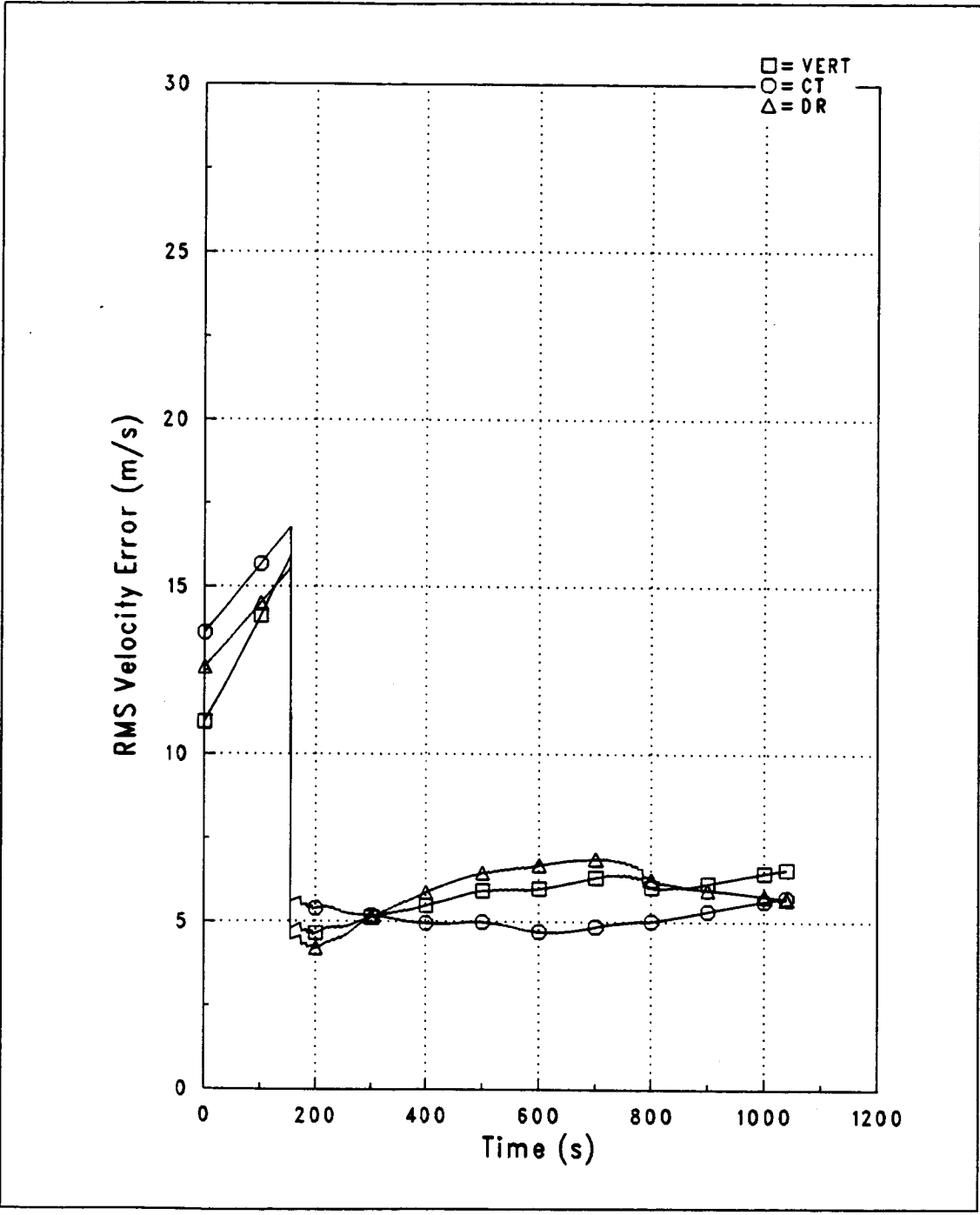


Figure 5-27. Case # 288500D (Full Covariance): RMS Velocity Errors

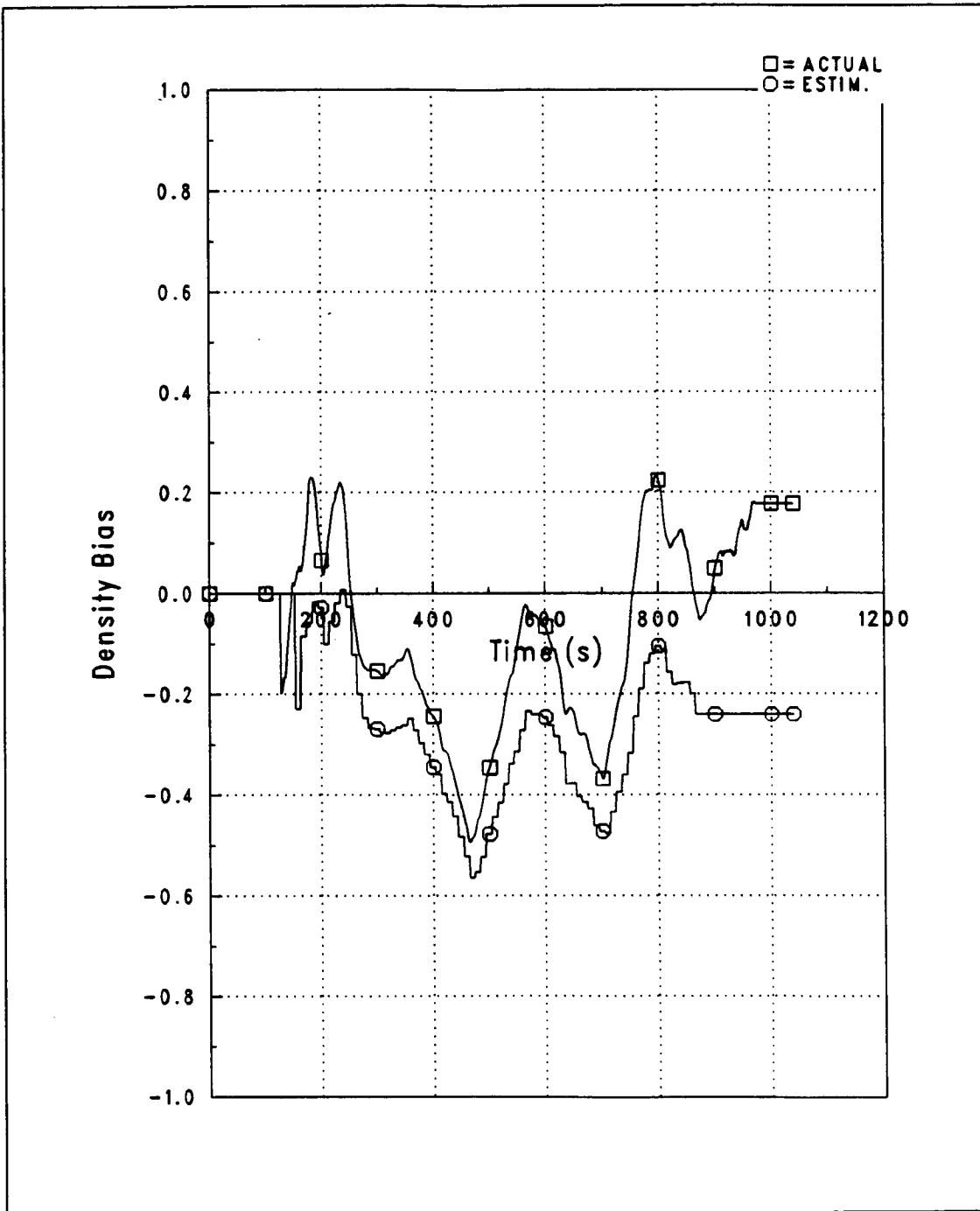


Figure 5-28. Case # 288500D (Full Covariance): Density Bias

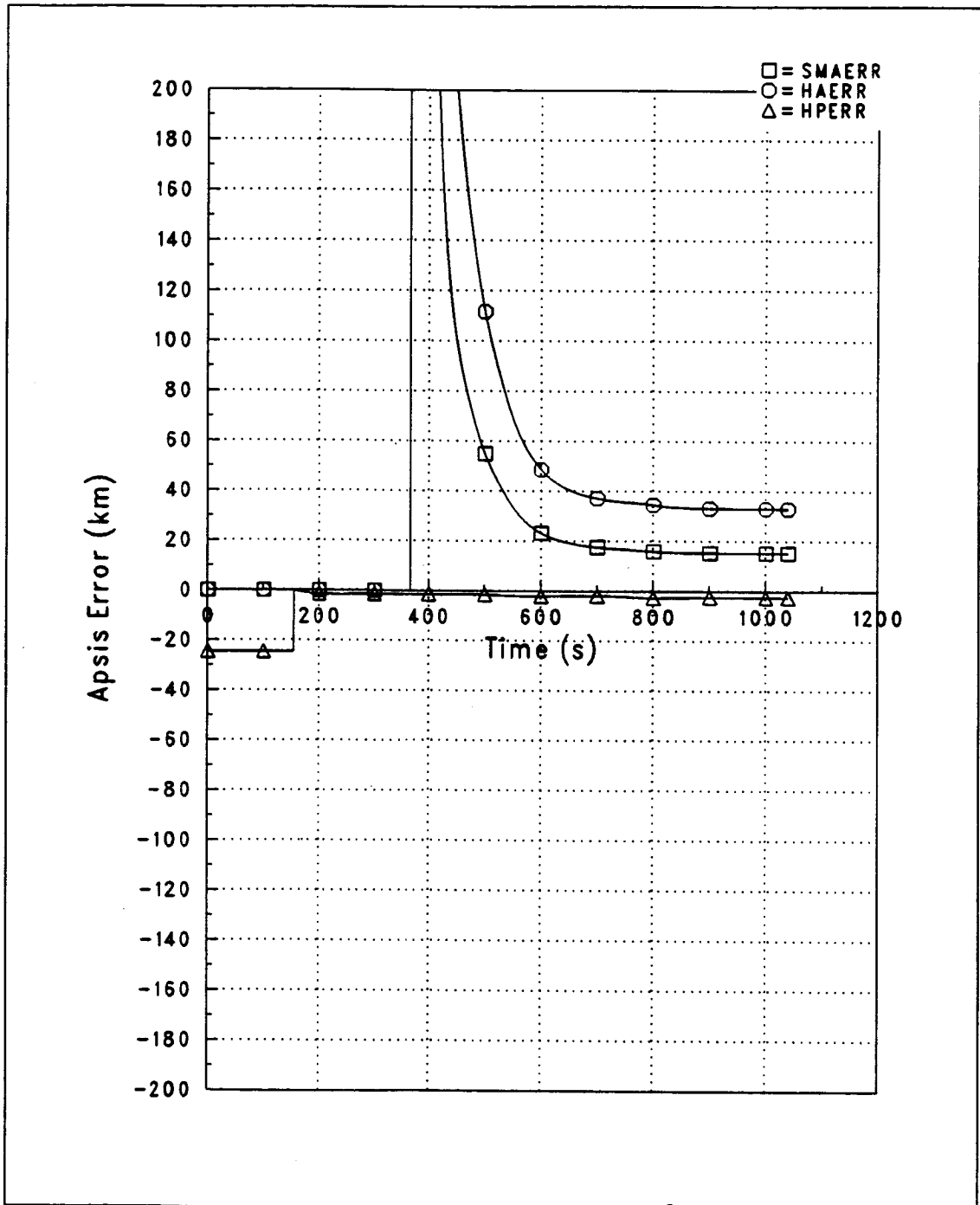


Figure 5-29. Case # 288500D (Full Covariance): Orbital Apis Est. Errors

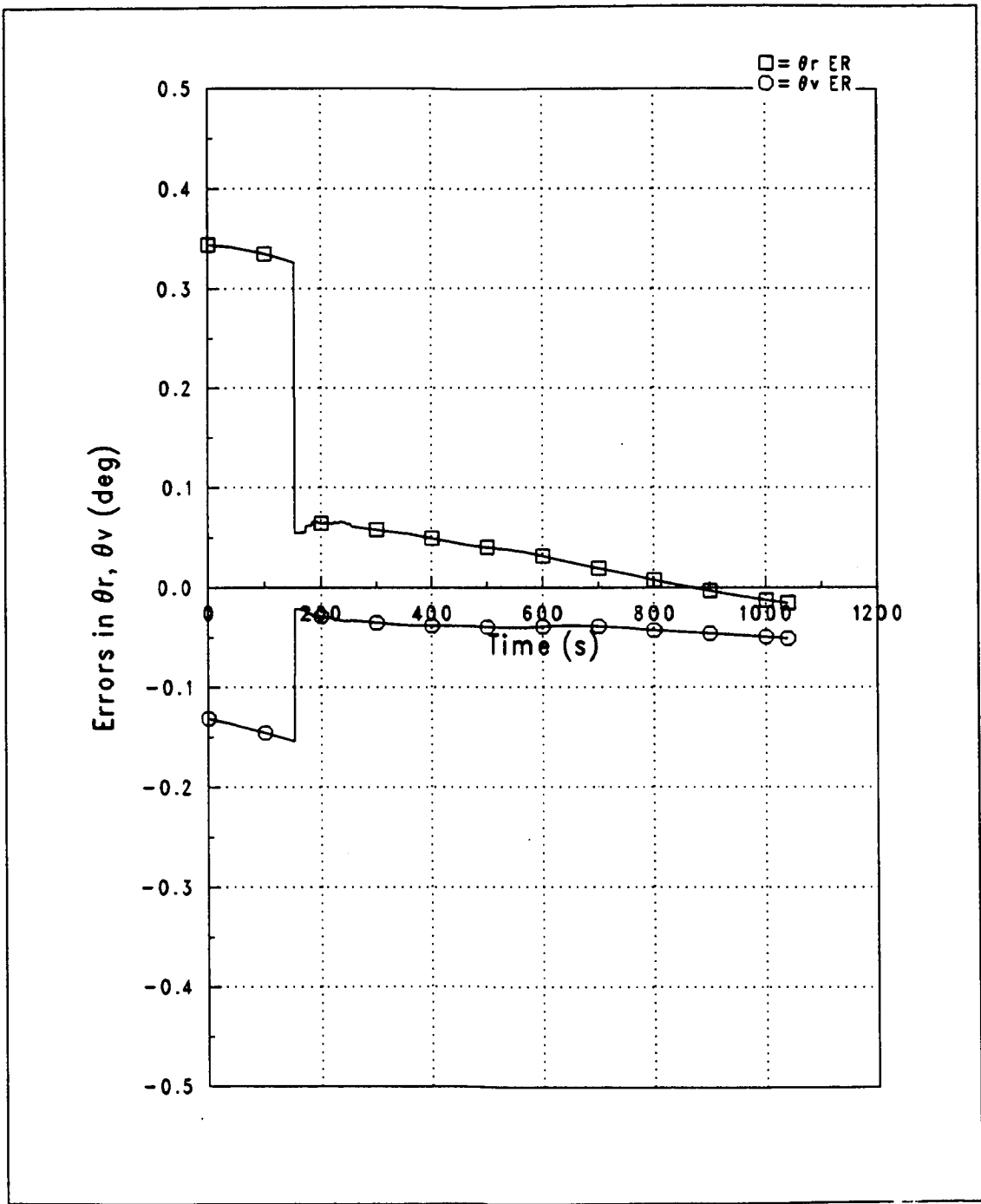


Figure 5-30. Case # 288500D (Full Covariance):  $\theta_r$ ,  $\theta_v$  Est. Errors

5.3.3.2.2 *FULL COVARIANCE (WITH RADAR ALTIMETER)*: Performance of the navigation system with radar altimeter measurements for the density shear case is illustrated by the plots of Figures 5-31 on page 122 through 5-37 on page 128.

Again, the main contribution of the radar altimeter measurements is to increase the accuracy of the vertical position estimate, thereby allowing better determination of the density bias. Since the vertical position error is decreased, the offset of the estimated bias profile from the actual profile in Figure 5-35 on page 126 is also decreased. The improvement seen with the addition of altimeter measurements in this case is not as dramatic as in the + 100% constant density bias case because the actual density bias at the time of the first density altitude measurement is very small and contributes little to the measurement residual.

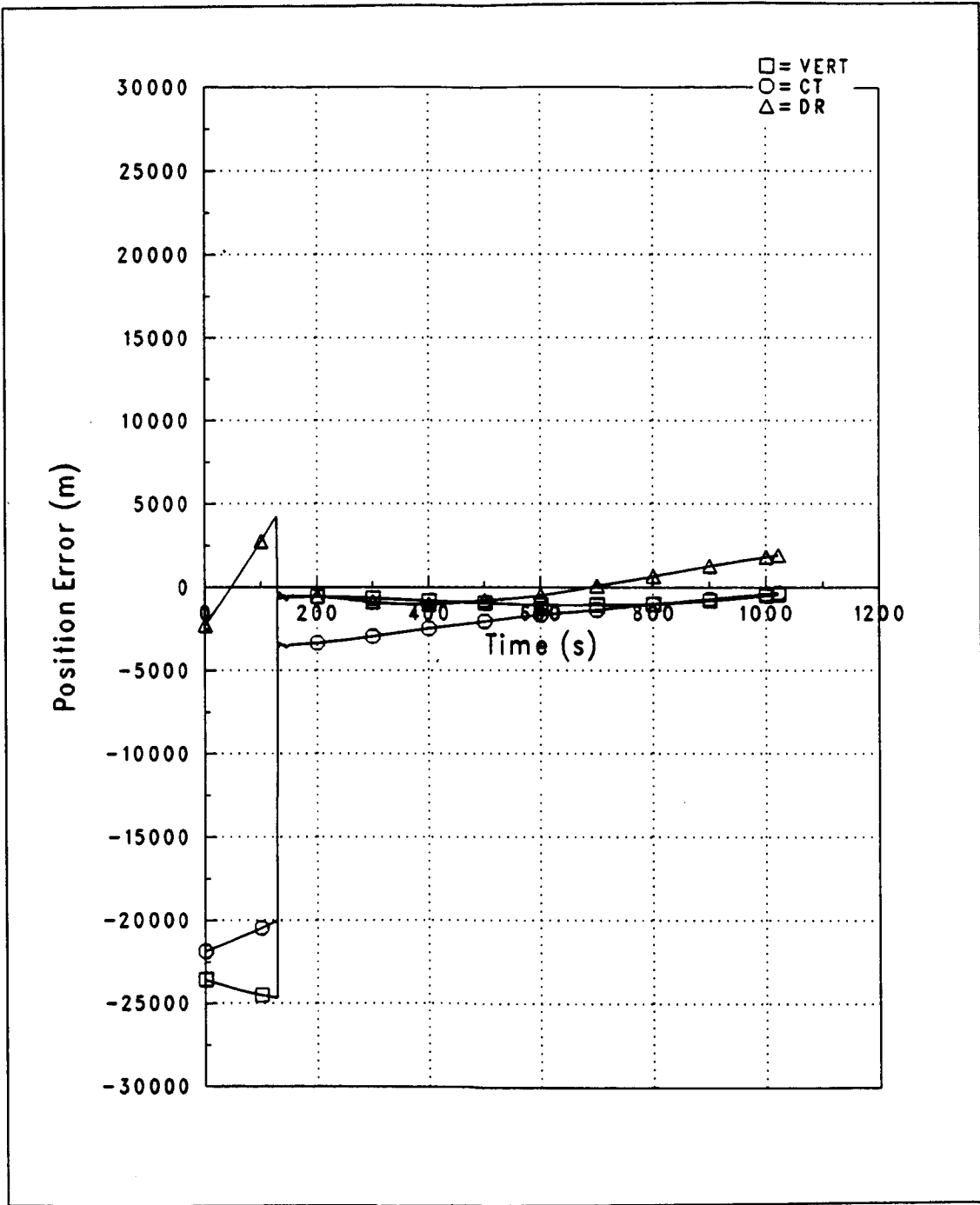


Figure 5-31. Case # 288500RD (Full Covariance): Position Estimate Errors

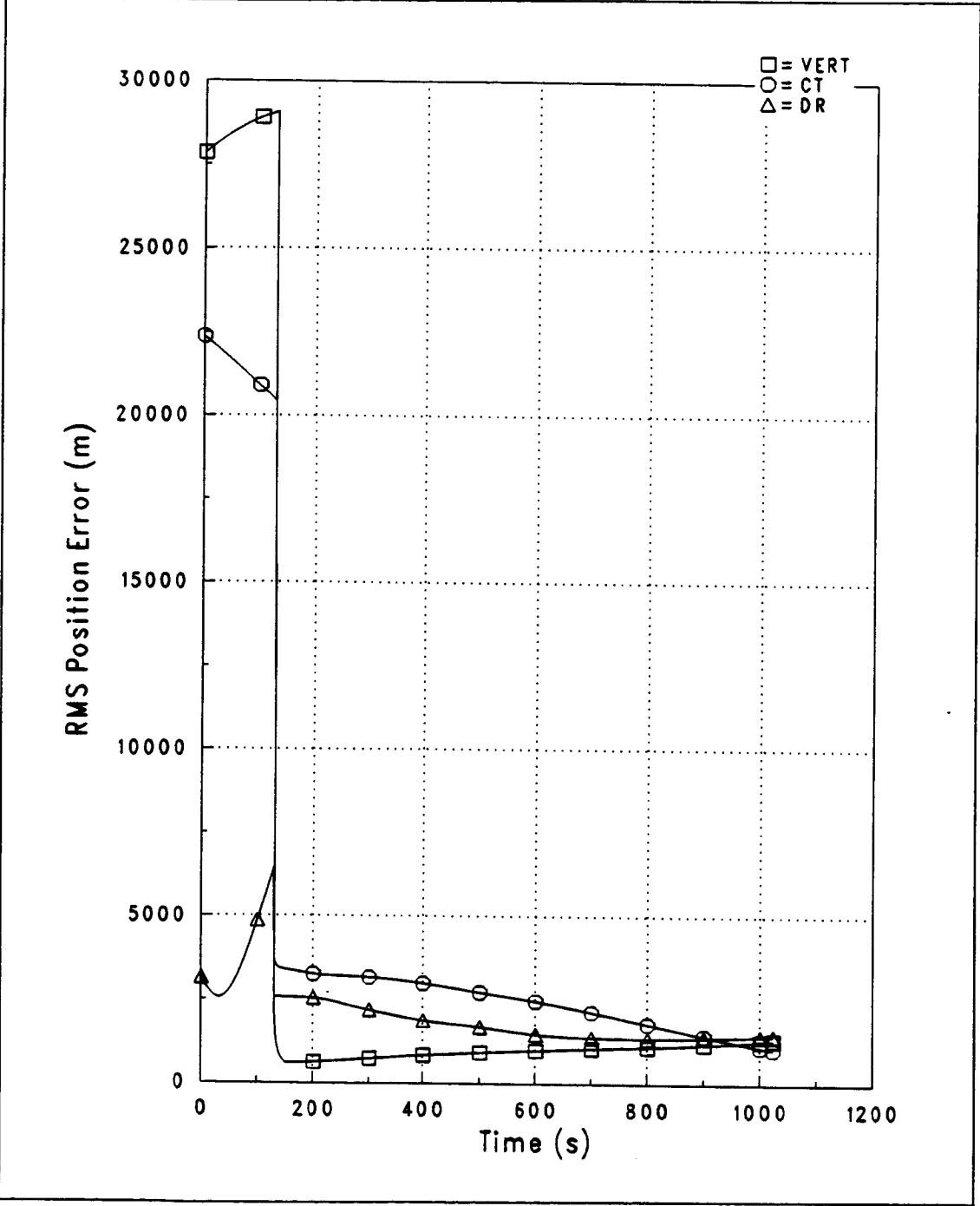


Figure 5-32. Case # 288500RD (Full Covariance): RMS Position Errors

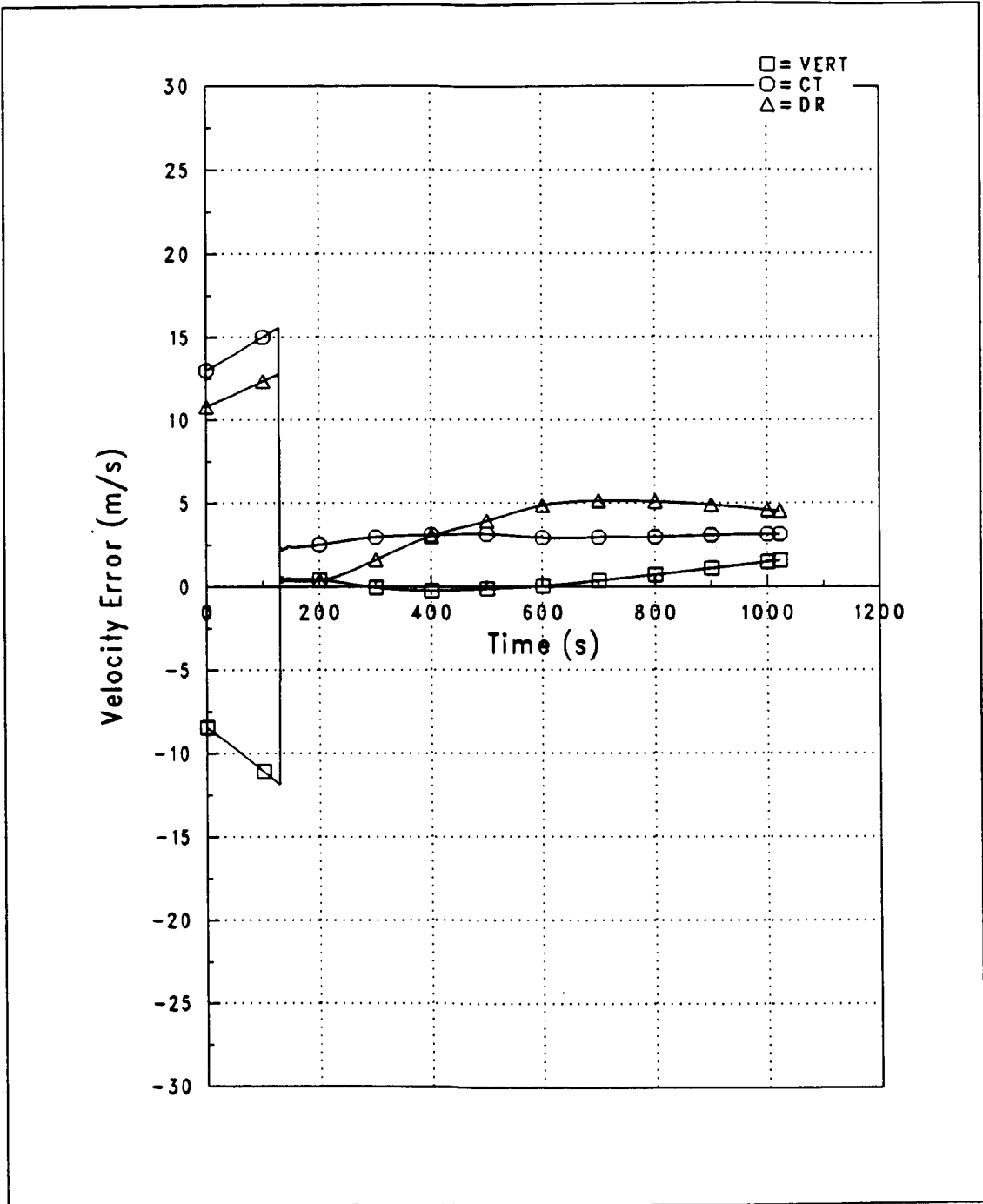


Figure 5-33. Case # 288500RD (Full Covariance): Velocity Estimate Errors

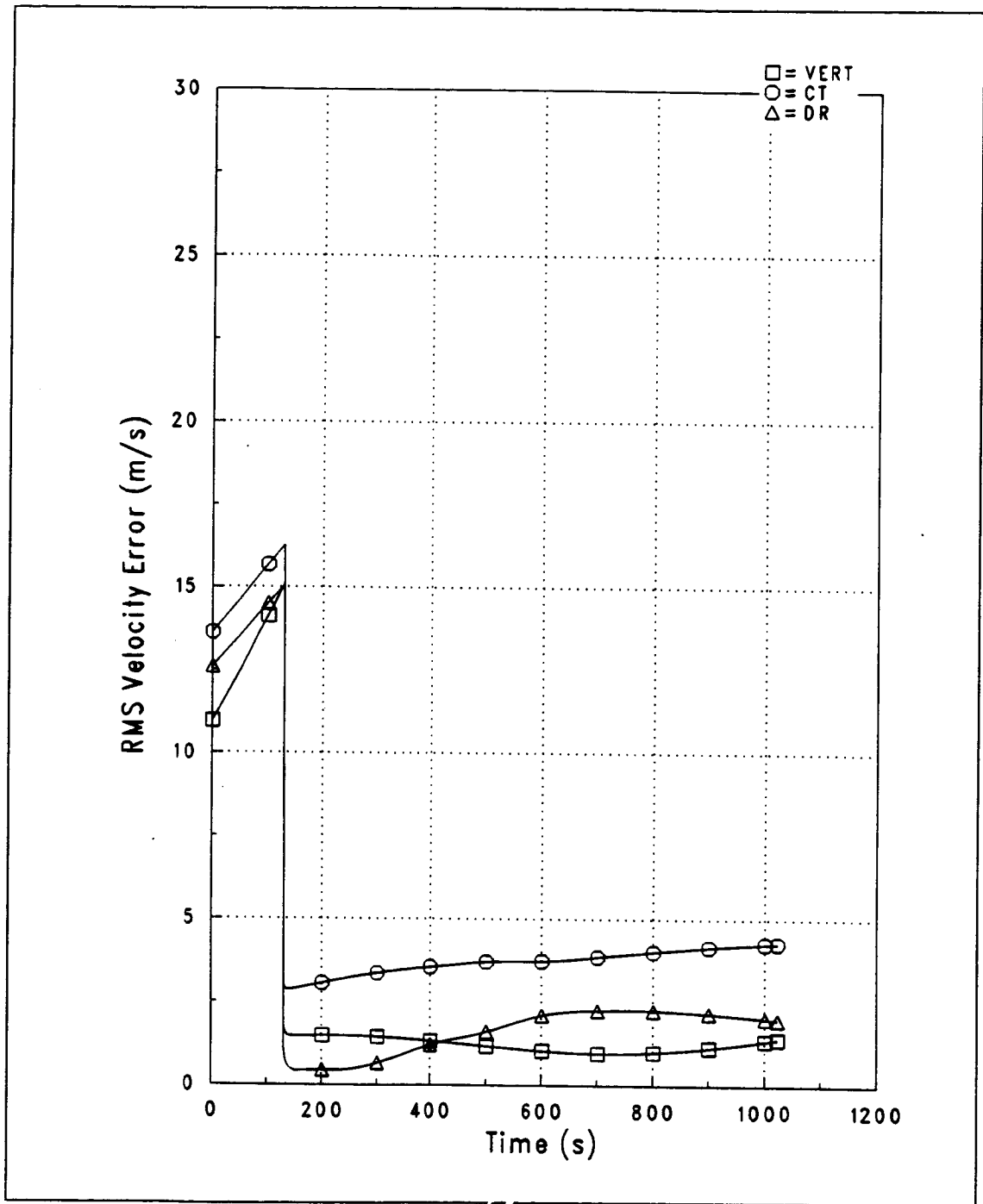


Figure 5-34. Case # 288500RD (Full Covariance): RMS Velocity Errors

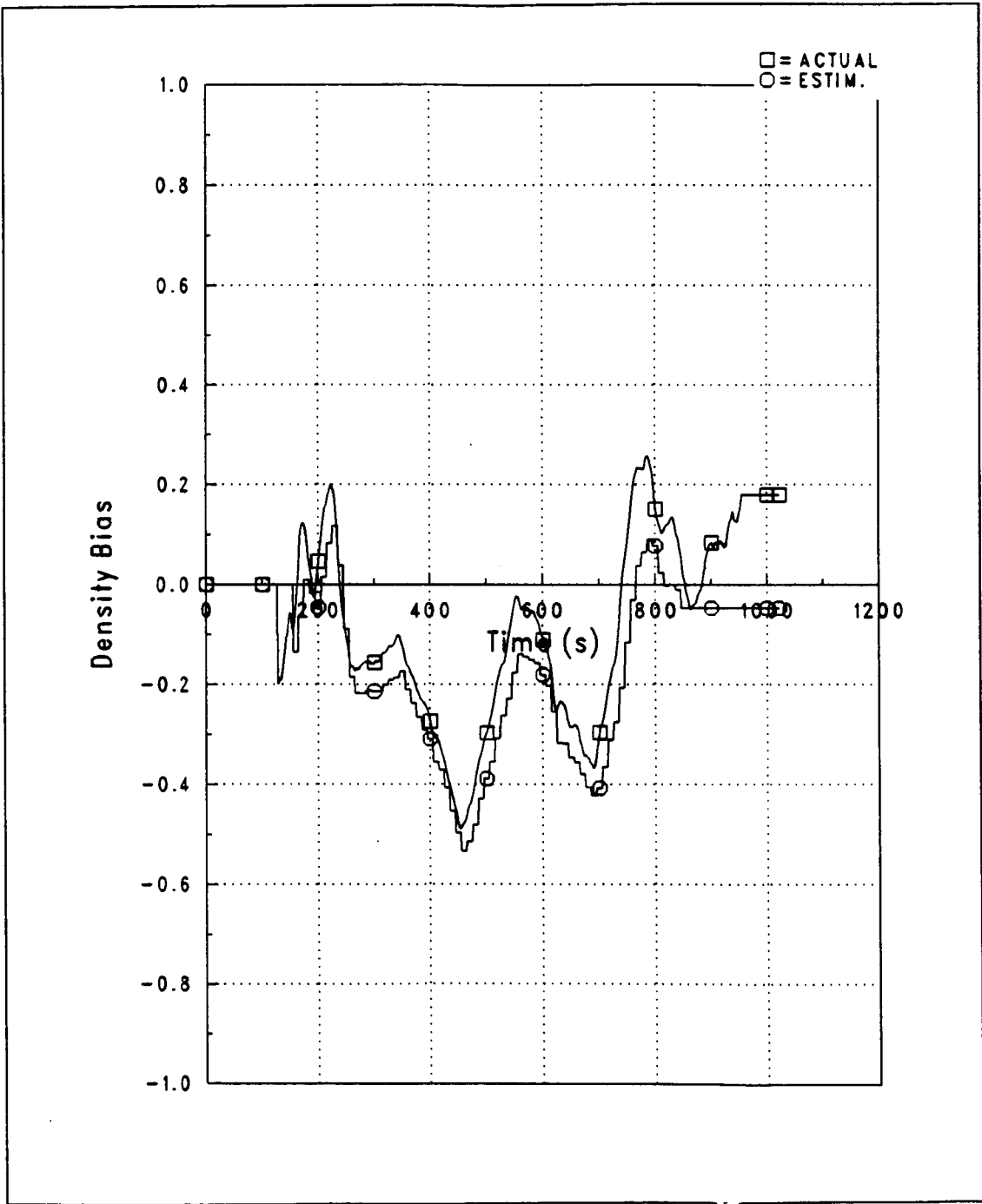


Figure 5-35. Case # 288500RD (Full Covariance): Density Bias

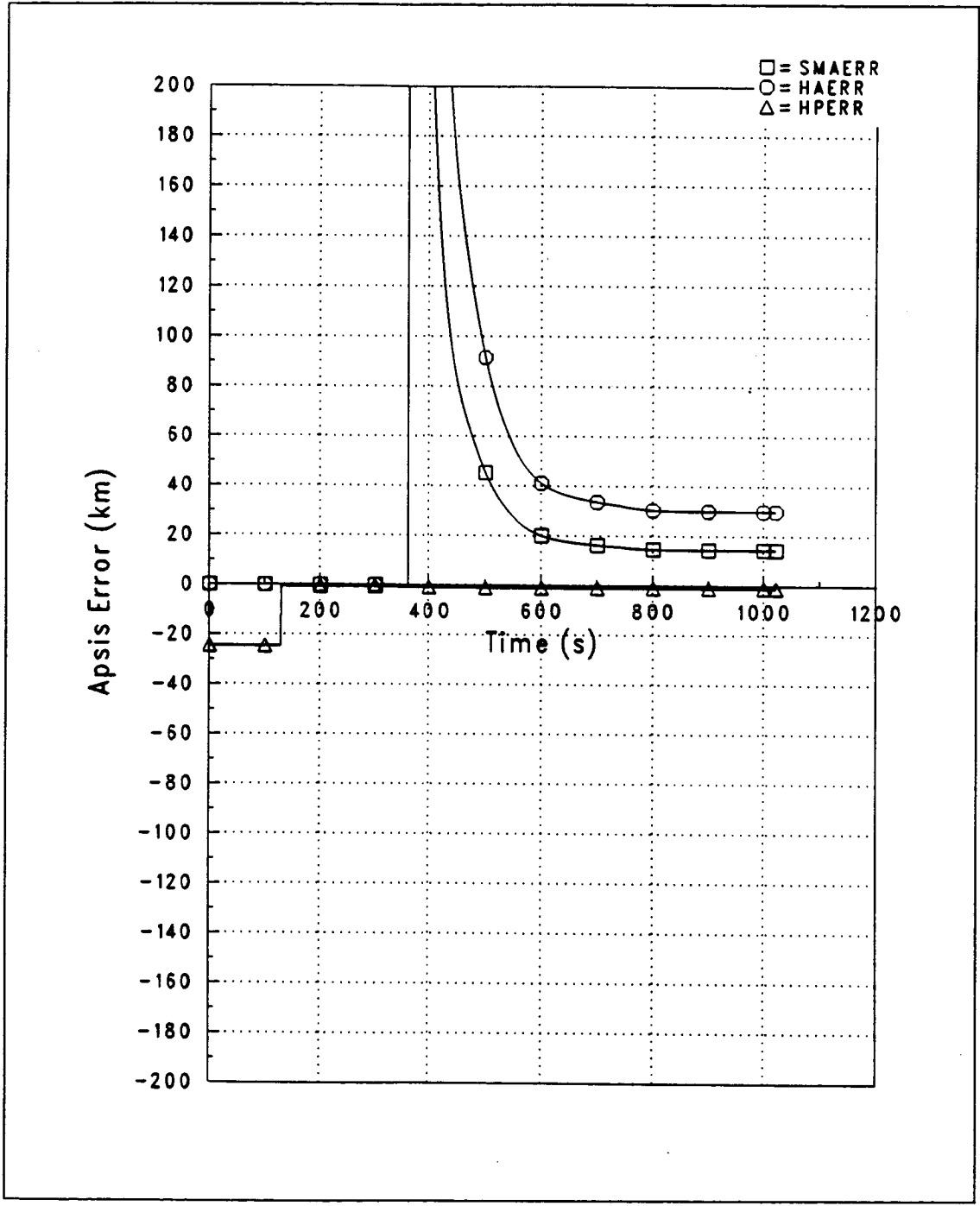


Figure 5-36. Case # 288500RD (Full Covariance): Orbital Apsis Est. Errors

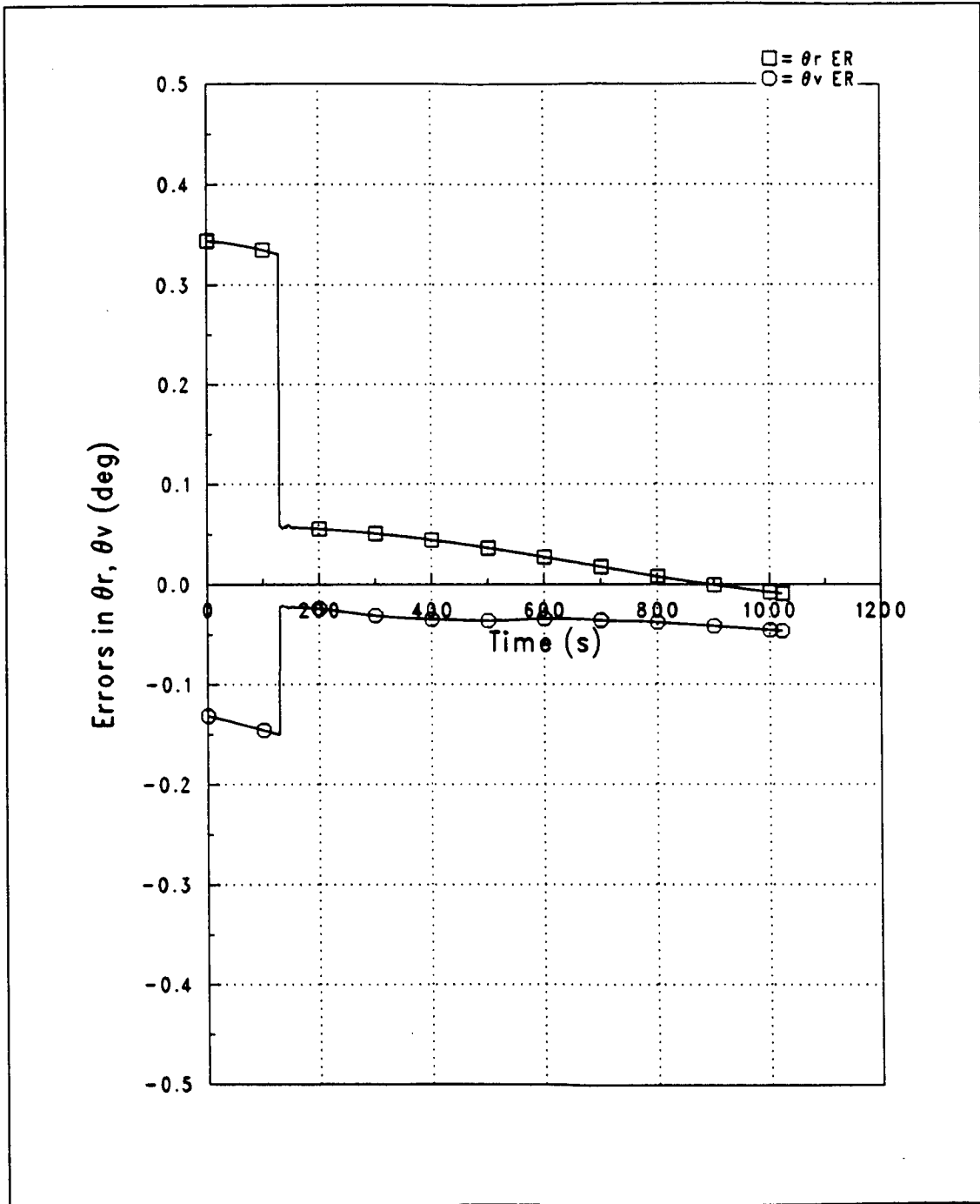


Figure 5-37. Case # 288500RD (Full Covariance):  $\theta_r$ ,  $\theta_v$  Est. Errors

5.3.3.2.3 *DIAGONAL COVARIANCE (NO RADAR ALTIMETER)*: The density shear case under examination is now run with all but the diagonal elements of the input covariance matrix of Table 5-2 on page 90 set equal to zero. The navigation performance results with no radar altimeter measurements are shown in Figures 5-38 on page 131 through 5-44 on page 137.

The deletion of the covariance terms in the input covariance matrix is a more conservative approach to navigation system performance determination. For the actual flight, these terms might not be available or their accuracy might be in question, so that it could be more harmful than helpful to include them. The safest course in this event would be to only load the diagonal variance terms and let the correlations build up with time. The obvious shortcoming to the deletion of the covariance terms is that little or no improvement in the knowledge of state components other than vertical position is provided by altitude measurements.

Figures 5-38 and 5-39 show the actual and rms position errors for this case. During the approximately 150 s between the start of the simulation and the first density altitude measurement, the correlation between vertical position and downrange position becomes nonzero so that the downrange error is decreased by the measurement. However, since no correlation between vertical and crosstrack position exists, there is no improvement in the crosstrack estimate. The velocity error plots of Figures 5-40 and 5-41 indicate that correlations built up between vertical position and vertical and downrange velocity allow small corrections of these two components, while the crosstrack velocity estimate remains unaffected.

The impact of the increased errors in position and velocity estimates on key guidance parameters is shown in Figures 5-43 and 5-44. In Figure 5-43, it is seen that the error in estimated apoapsis altitude, which is the guidance target parameter during the exit phase, is nearly 160 km. The increase in this error is due for the most part to the increased downrange velocity error, which is nearly five times as large as in the case run with the full initial covariance matrix. This

error is unacceptably high, and will cause a large target miss and, hence, fuel penalty. Figure 5-44 shows that no corrections are made to the estimates of  $\theta_r$  and  $\theta_v$ , again due to the lack of correlation between vertical position and crosstrack position and velocity. The estimation error in  $\theta_r$  remains unacceptably high, reaching almost twice the magnitude of the control corridor during exit.

The results presented here indicate that, for the levels of initial position and velocity errors examined, the estimation accuracy levels achieved using a diagonal initial filter covariance matrix are unacceptable. While the accuracy level of the vertical position estimate remains comparable to the full covariance matrix case, the lack of improvement in the estimates of other state components causes errors which will have a large negative impact on guidance performance and could conceivably result in mission failure.

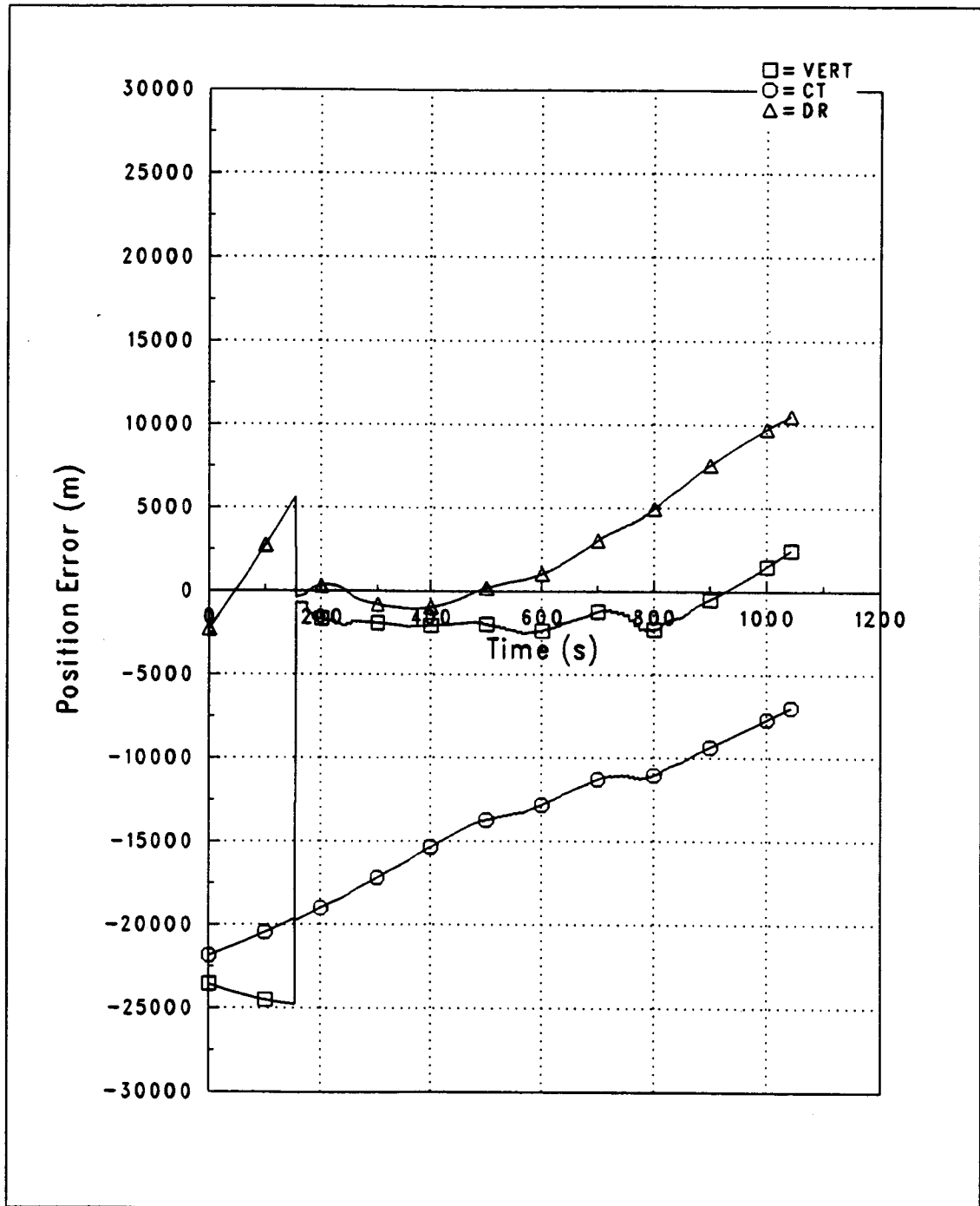


Figure 5-38. Case # 288500D (Diag. Covariance): Position Estimate Errors

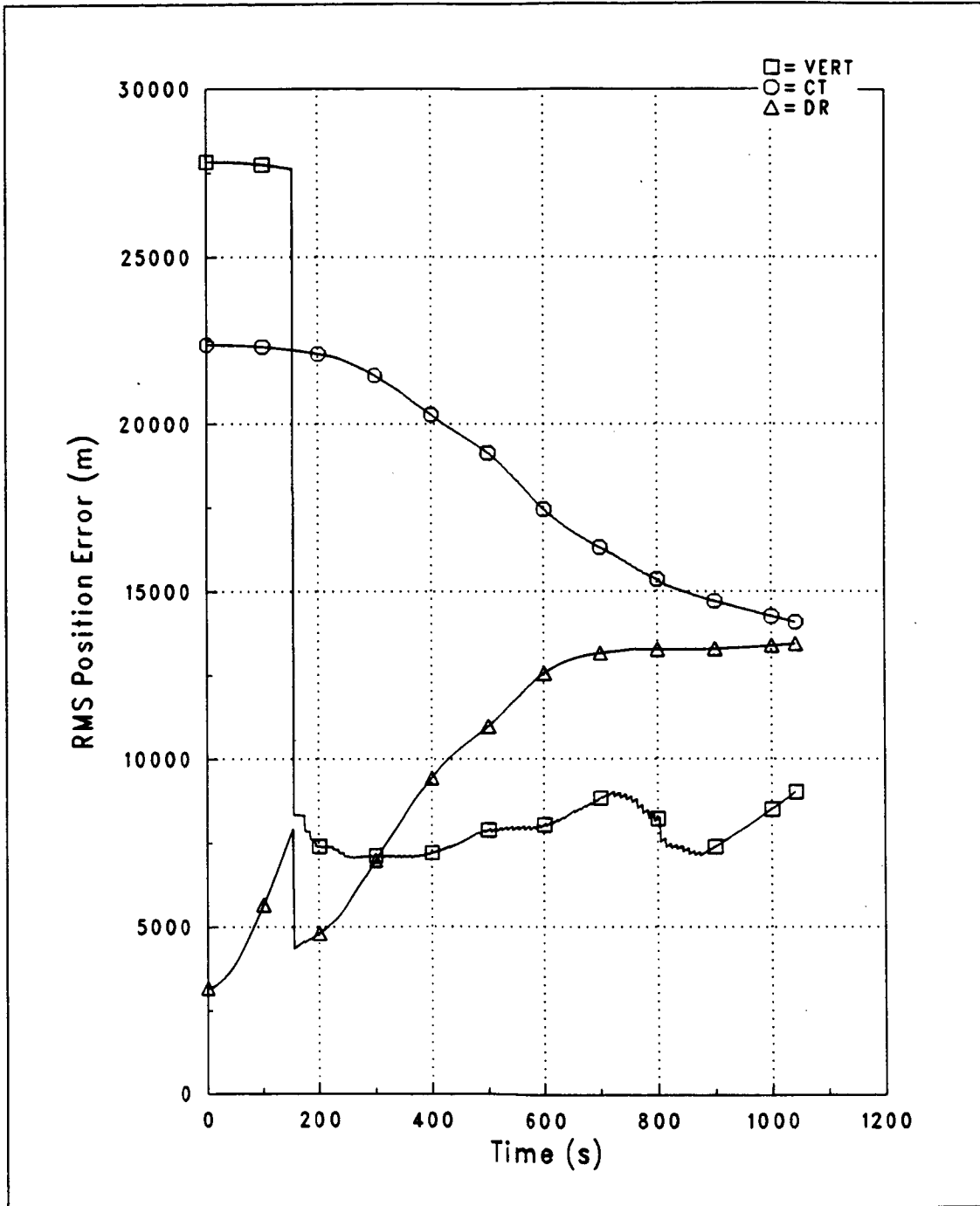


Figure 5-39. Case # 288500D (Diag. Covariance): RMS Position Errors

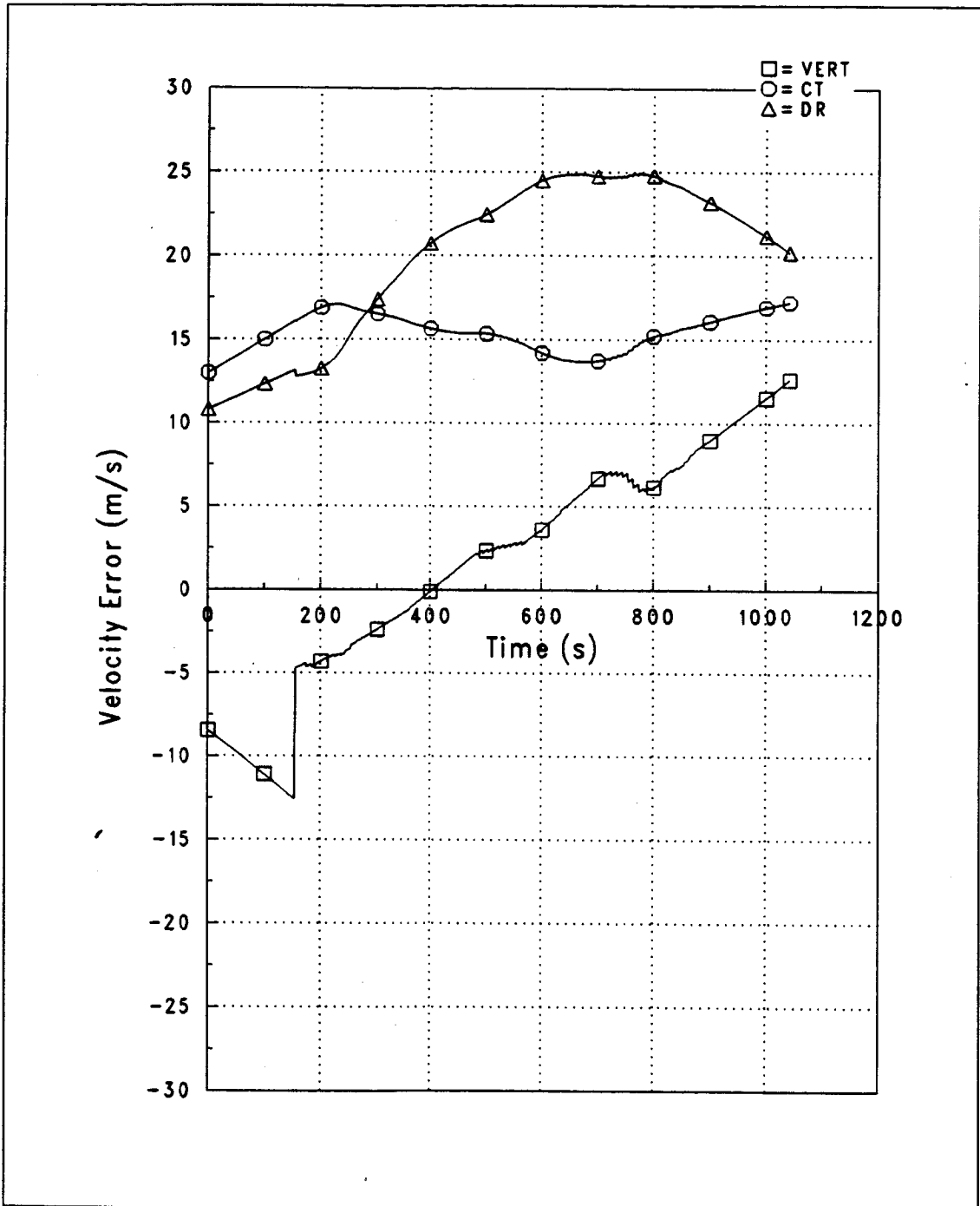


Figure 5-40. Case # 288500D (Diag. Covariance): Velocity Estimate Errors

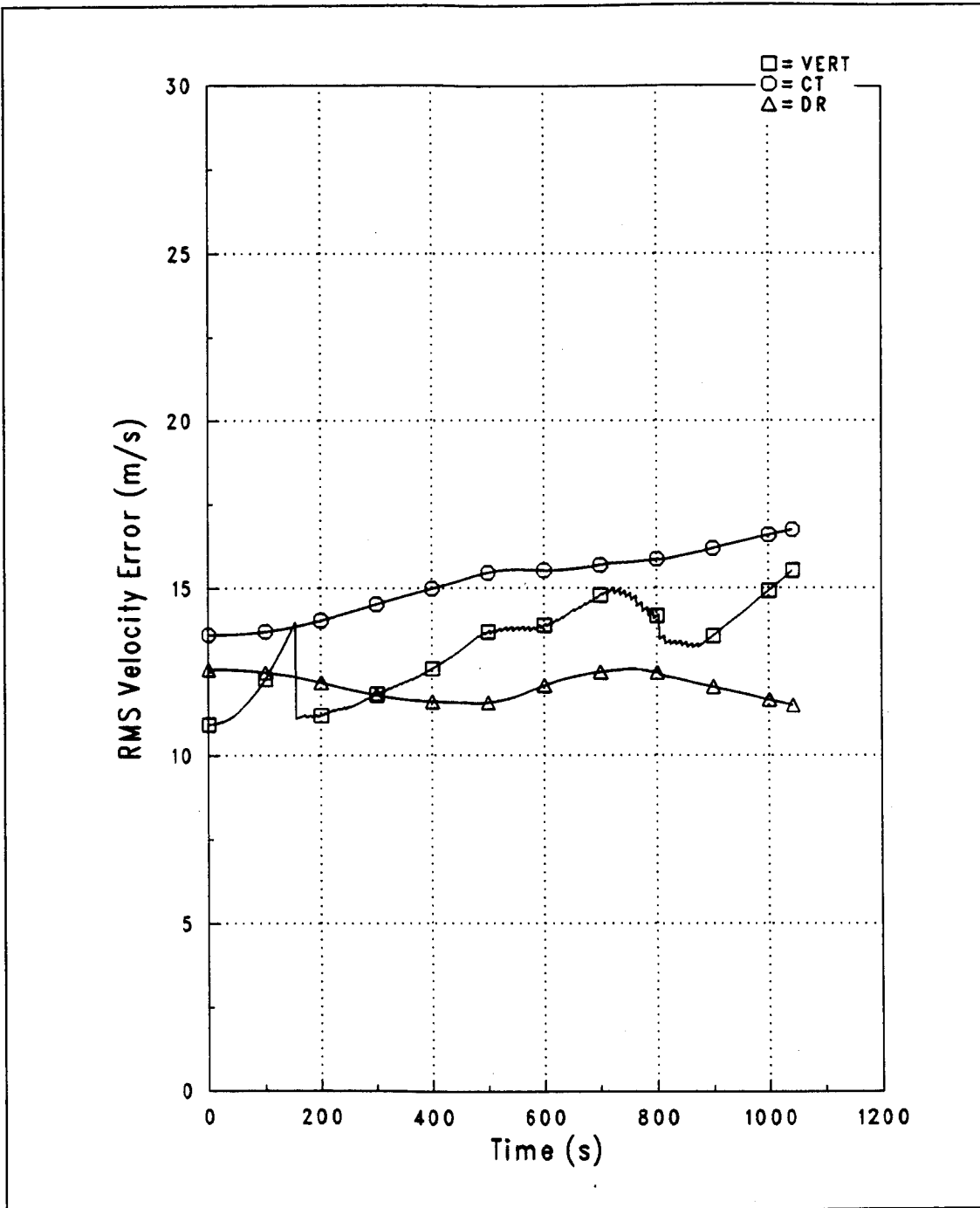


Figure 5-41. Case # 288500D (Diag. Covariance): RMS Velocity Errors

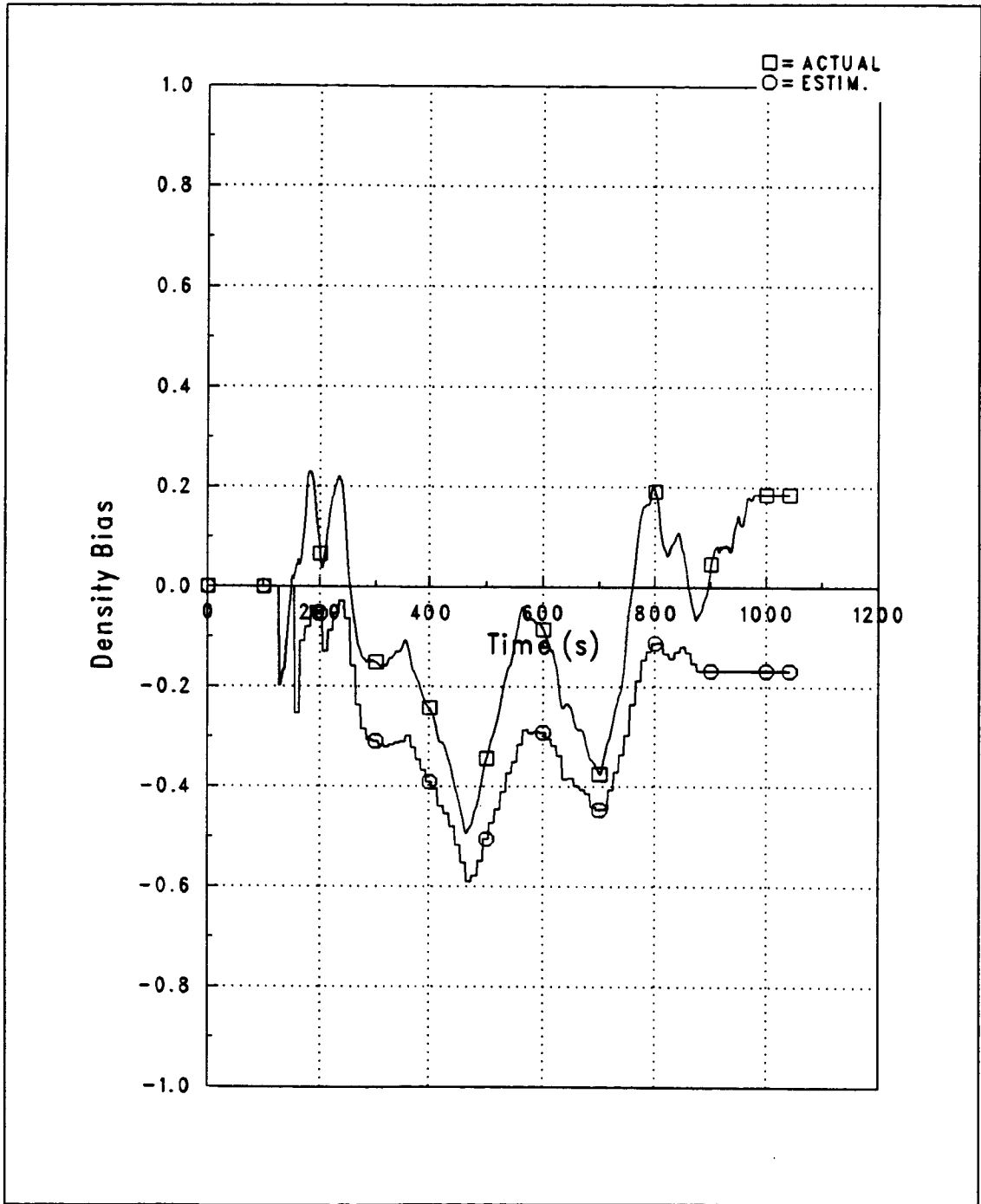


Figure 5-42. Case # 288500D (Diag. Covariance): Density Bias

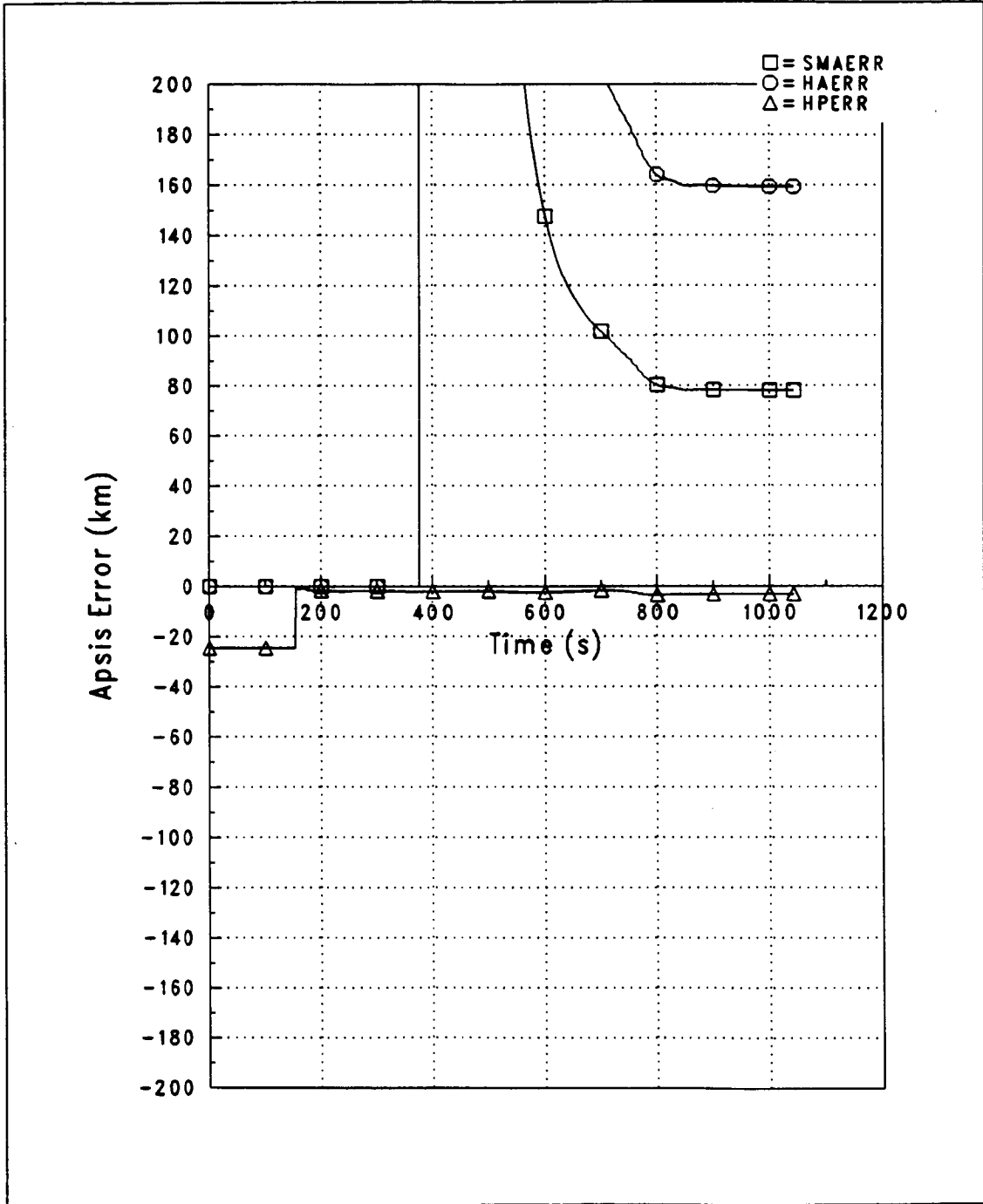


Figure 5-43. Case # 288500D (Diag. Covariance): Orbital Apis Est. Errors

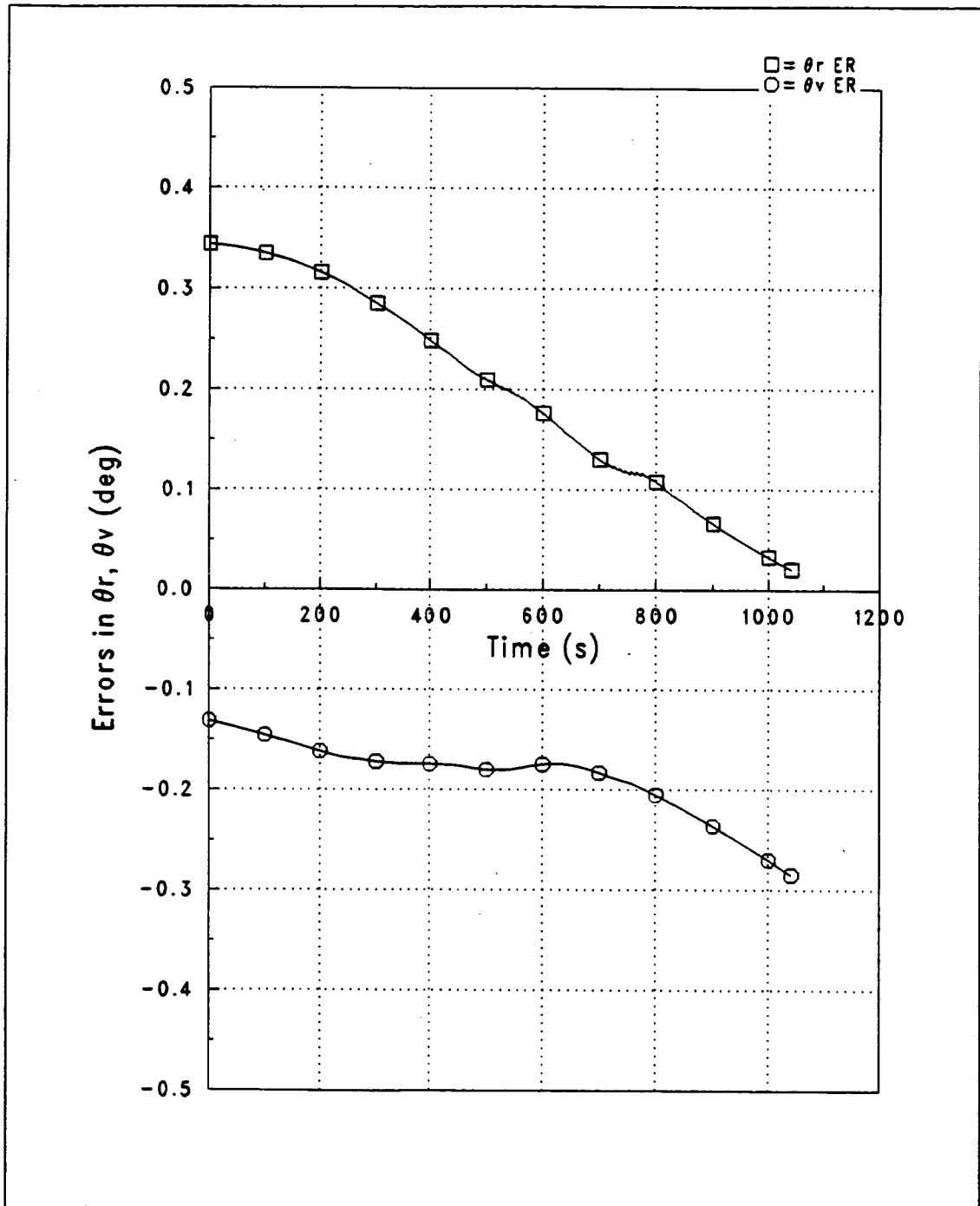


Figure 5-44. Case # 288500D (Diag. Covariance):  $\theta_r$ ,  $\theta_v$  Est. Errors

## 5.4 COMBINED GUIDANCE AND NAVIGATION SYSTEMS PERFORMANCE

### 5.4.1 INTRODUCTION

This section contains a discussion of combined navigation and guidance systems performance, with emphasis on guidance system response to navigation system-provided inputs. The test cases presented can be divided under two headings: those with a constant percentage atmospheric density bias and those with dynamically varying density bias (shear) profiles. Two constant density bias values, +100% and -50%, were flown for the high/shallow and low/steep initial trajectory errors used in the navigation test cases in the previous section. These bias values are considered to be  $3\sigma$  thick and thin cases, respectively. The results of five aerocapture cases flown with different density shear profiles are presented for each of the two sets of initial trajectory errors. These profiles range from mild variations having little impact on performance to severe variations causing large target miss values. All trajectories presented were flown without the inclusion of radar altimeter measurements. Under each bias-type heading, one particular case is described in detail to facilitate interpretation of the data presented.

### 5.4.2 PRESENTATION OF RESULTS

Important performance data for the cases included here are summarized in a set of four tables for each of the density bias types. The first table sums up total aerocapture performance in terms of post-aerocapture  $\Delta V$  requirements for insertion into the target orbit. Included in this table are the values of parameters used in the calculation of these fuel requirements. The propulsive  $\Delta V$  required for insertion into the desired 2000 km by 350 km ellipse,  $\Delta V_{ORBIT}$ , is a function of the apoapsis target miss and the exit periapsis altitude. The  $\Delta V$  required to rotate the orbit plane into its desired orientation,  $\Delta V_{PLANE}$ , is a function of the angular position and velocity plane errors,  $\theta$ ,

and  $\theta_v$ . The orbit plane orientation error may also be expressed as a single angle, the wedge angle, which is defined as

$$\delta = \arccos(\hat{i}_h \cdot \hat{i}_{hd}) \quad (5-5)$$

where  $\hat{i}_h$  and  $\hat{i}_{hd}$  are unit vectors in the direction of the angular momentum vectors of the actual and desired orbits, respectively. All  $\Delta V$  values are computed using the true values of the required parameters, so that the orbit insertion fuel requirements given are for transfer from the actual post-aerocapture orbit to the desired orbit. The equations used for calculation of  $\Delta V$  requirements are derived in "Appendix B. DERIVATION OF ORBIT INSERTION  $\Delta V$  EQUATIONS" on page 199.

The second and third tables show the portions of the total errors in controlled parameters ( $h_{a,m}$  and  $\theta_v$ ) which are attributable to guidance errors (the difference between estimated and target values) and estimation errors (the difference between estimated and true values), respectively. The third table also lists the estimation errors in the other parameters used for  $\Delta V$  calculation.

The fourth table presents values of parameters which directly impact vehicle and trajectory design constraints. These include the minimum altitude ( $h_{min}$ , in units of kilometers), the maximum aerodynamic load factor ( $g_{max}$ , expressed in Earth g's), the maximum convective heating rate ( $\dot{Q}_{max}$ , in units of watts per square centimeter), and the total aerodynamic heat load ( $Q$ , in units of joules per square centimeter). The values of the latter two parameters will help to dictate the type and thickness of vehicle heat shielding material required.

In addition to the tabular data, five figures illustrating important guidance, navigation, and trajectory quantities during aerocapture are included for each case. The first figure is a combination of density bias, orbit plane error, and bank angle time history plots. This combination allows examination of the bank angle control response to density bias variations (if present) and

plane control bank reversal commands. The second figure is a plot of the cosine of the current bank angle command, which can be thought of as the fraction of total lift required in the vertical direction for orbital energy control. The third figure is a plot of the actual and estimated altitude time histories, and the last two plots show navigation results in the form of position and velocity estimation errors.

### 5.4.3 *CONSTANT DENSITY BIAS CASES*

Performance data for the four constant density bias cases are presented in Tables 5-3 on page 144 through 5-6 on page 145 and Figures 5-45 on page 146 through 5-64 on page 157. Data for the nominal case has also been included in the tables, and trajectory plots for the nominal case were given previously in Figures 5-1 on page 82 through 5-7 on page 88.

The results of Table 5-3 indicate that the total  $\Delta V$  required for post-aerocapture orbit correction varied from 65.7 m/s to 74.4 m/s (the minimum achievable  $\Delta V$  (given nominal atmospheric density conditions and no plane errors) is approximately 62 m/s, corresponding to a full lift-down exit phase which hits the apoapsis target while maximizing the final periapsis altitude). It is seen in Table 5-5 that the maximum aerodynamic load experienced was 3.87 g's, a reasonably low value. The minimum altitude constraint was violated in one case (# 031000D, -50% Density). The inability of the vehicle to pull up before reaching the minimum altitude in this case is due to the unfavorable combination of a steep entry trajectory with an extremely thin atmosphere.

Within the control capabilities of the vehicle, a uniform atmospheric density bias will have little effect on guidance performance. As explained in the navigation results, the estimated density will be very accurate even if density bias and altitude estimates are in error. Thus, vehicle aerodynamic control capability will be known very well and the guidance predictions of the capture

and exit phases will be accurate since the predicted density multiplier of Eq. (3-9) is unchanging. Apoapsis target misses in the nominal and all four of the constant density bias cases are the result of bank reversals executed during the exit phase which perturb the trajectory beyond the capabilities of the vehicle to correct. This is discussed further for a specific case in the next section.

#### 5.4.3.1 DETAILED DESCRIPTION: CASE # 031000D, +100% DENSITY

Figures 5-45 on page 146 through 5-49 on page 148 contain trajectory, control, and navigation plots for the low/steep entry trajectory case with a constant 100% thick atmosphere. The navigation system performance for this case was examined in detail in “5.3.3.1.1 Full Covariance (No Radar Altimeter)” on page 91. Figure 5-45 shows the actual vehicle bank angle response to guidance system commands. Guidance cycling is initiated at  $t = 111$  s and the initial command is to roll full-lift up ( $\phi_c = 15^\circ$ ) due to the steep entry trajectory. This command is held constant throughout the capture guidance phase. The constant-altitude cruise phase is initiated at  $t = 147$  s, when the estimated altitude drops below the cruise altitude (34 km). It is here that the effect of the estimated altitude error discussed in “5.3.3.1.1 Full Covariance (No Radar Altimeter)” on page 91 can most clearly be seen. While the guidance computes bank angle commands to drive the estimated altitude to 34 km, the vehicle is actually flying approximately 4 km higher, as seen in Figure 5-47 on page 147. Since the velocity magnitude is well known, the cruise altitude error will simply cause the exit phase, which is initiated when a given velocity depletion has been achieved, to be started at a later time due to the reduced drag at the true cruise altitude. Thus, the cruise altitude error resulting because of the uncertainty in the estimated altitude has no critical impact on the cruise phase guidance.

The effect of bank angle reversals during the cruise phase can be seen in Figures 5-45 and 5-46. The first bank reversal is commanded at  $t = 170$  s, shortly after initiation of this phase. Since the current bank command at this time is greater than  $90^\circ$ , the vehicle is commanded to roll

through lift-down. The effect of this reversal is to induce a negative altitude rate which drives the vehicle away from the cruise condition. To compensate, it is seen that the guidance commands lift-up after completion of the reversal to drive back towards the cruise altitude. This compensating command is seen as the "spike" centered at  $t = 184$  s in Figure 5-46, and the vehicle response to this command is seen in the bank angle history plot. The magnitude and duration of the spike, which determine the time to recover from bank reversal-induced effects, are functions of the constant-altitude guidance gains  $K_h$  and  $K_{\dot{h}}$  discussed in "3.3 CONSTANT ALTITUDE CRUISE PHASE" on page 59.

The exit phase is initiated at  $t = 247$  s when the inertial velocity drops below 4400 m/s. As was discussed in "3.4 EXIT PHASE" on page 61, the initial exit guidance command is to roll full lift-up until the required exit bank angle magnitude becomes greater than  $80^\circ$ . This command is seen as another spike in Figure 5-46 on page 147. After one guidance cycle, the bank angle required to hit the apoapsis target is computed as  $83^\circ$ , so that full lift-up is no longer required. Bank reversals are seen to be the dominant drivers of the bank command during the exit phase for this case. As the altitude of the vehicle increases and atmospheric exit is approached, aerodynamic control authority (i.e. available vertical lift) decreases rapidly. Therefore, larger and larger bank angle command increments will be required to compensate for roll reversal-induced effects. Two reversals are executed during the exit phase. The first, which commands a reversal through lift-up at  $t = 256$  s, causes a shift of approximately  $5^\circ$  in the commanded bank angle toward lift-down. This is most clearly seen as a shift in required vertical lift in Figure 5-46. The second reversal, which commands the vehicle to roll through lift-up at  $t = 304$  s, has a much more significant effect. The bank command is driven to full lift-down by this reversal, leaving no control margin for future dispersions and barely enough negative vertical lift to hit the apoapsis target.

In Table 5-3 on page 144, it is seen that the total apoapsis target miss for this case was 10.1 km. Tables 5-4 on page 144 and Table 5-5 on page 145 show that, while the guidance error was

only 3.9 km, the error of -6.2 km in the apoapsis altitude estimate boosts the total error to 10.1 km. The lift-down commanded during most of the exit phase, while being undesirable in terms of control margin, has a positive effect in that it keeps the periapsis altitude high and reduces orbit correction fuel requirements. The  $\Delta V$  required to correct the apoapsis and periapsis errors is 65.9 m/s. The total out-of-plane velocity error,  $\theta_v$ , is seen to be  $0.045^\circ$ . This is a combination of guidance and estimation errors of  $-0.021^\circ$  and  $-0.066^\circ$ , respectively. The  $\Delta V$  required to correct the resulting plane orientation error is 6.19 m/s, bringing the total propulsive  $\Delta V$  requirement to 72.1 m/s.

Table 5-3. Aerocapture Performance Results (Constant Density Bias Cases)

CASE	$h_{a_m}$ (km)	$h_p$ (km)	$\theta_r$ (deg)	$\theta_v$ (deg)	$\delta$ (deg)	$\Delta V_{ORBIT}$ (m/s)	$\Delta V_{PLANE}$ (m/s)	$\Delta V_{TOT}$ (m/s)
Nominal	-22.4	46.0	0.129	0.015	0.12	67.2	7.17	74.4
031000D (+ 100% $\rho$ )	10.1	43.3	0.106	0.045	0.11	65.9	6.19	72.1
031000D (-50% $\rho$ )	-31.2	25.8	0.020	-0.062	0.06	72.9	3.74	76.7
281000D (+ 100% $\rho$ )	15.4	56.7	0.029	-0.021	0.03	63.7	2.08	65.7
281000D (-50% $\rho$ )	-17.2	36.6	-0.082	0.092	0.12	68.5	7.16	75.6

Table 5-4. Guidance Errors (Constant Density Bias Cases)

CASE	$h_{a_{err}}$ (km)			$\theta_{v_{err}}$ (deg)				
Nominal	-22.4			0.015				
031000D (+ 100% $\rho$ )	3.9			-0.021				
031000D (-50% $\rho$ )	-21.4			-0.003				
281000D (+ 100% $\rho$ )	14.1			-0.168				
281000D (-50% $\rho$ )	-11.7			0.103				

Table 5-5. Estimation Errors (Constant Density Bias Cases)

CASE	$\tilde{h}_a$ (km)	$\tilde{h}_p$ (km)	$\tilde{\theta}_r$ (deg)	$\tilde{\theta}_v$ (deg)	$\tilde{\delta}$ (deg)			
Nominal	-	-	-	-	-			
031000D (+ 100% $\rho$ )	-6.2	-3.6	0.010	-0.066	0.01			
031000D (-50% $\rho$ )	9.8	6.3	-0.037	0.059	-0.05			
281000D (+ 100% $\rho$ )	-1.3	-5.8	0.018	-0.147	0.14			
281000D (-50% $\rho$ )	5.5	5.7	-0.007	0.011	0.02			

Table 5-6. Vehicle and Trajectory Limits (Constant Density Bias Cases)

CASE	$h_{\min}$ (km)	$g_{\max}$	$\dot{Q}_{\max}$ (W/cm <sup>2</sup> )	$Q$ (J/cm <sup>2</sup> )
Nominal	33.4	2.00	166.2	30493
031000D (+ 100% $\rho$ )	33.4	3.87	219.5	24110
031000D (-50% $\rho$ )	22.9	2.85	193.0	28111
281000D (+ 100% $\rho$ )	39.7	1.90	156.1	31342
281000D (-50% $\rho$ )	27.7	1.75	149.3	33436

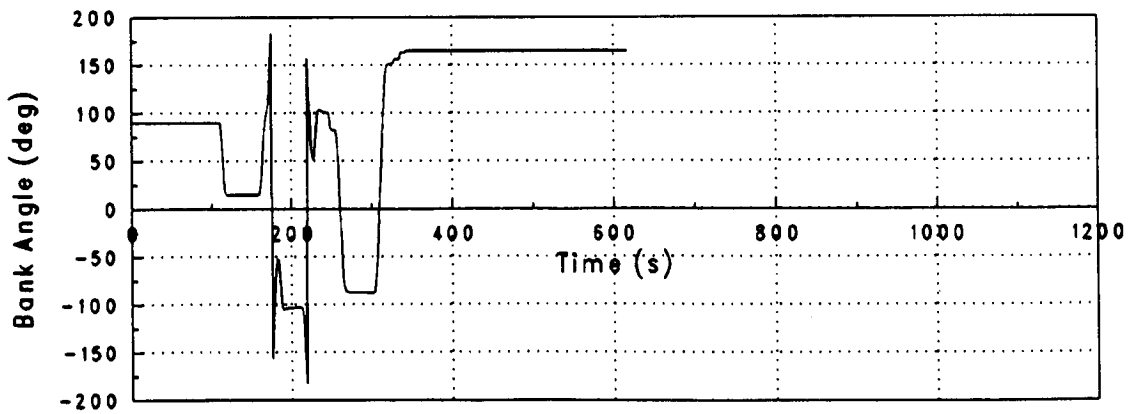
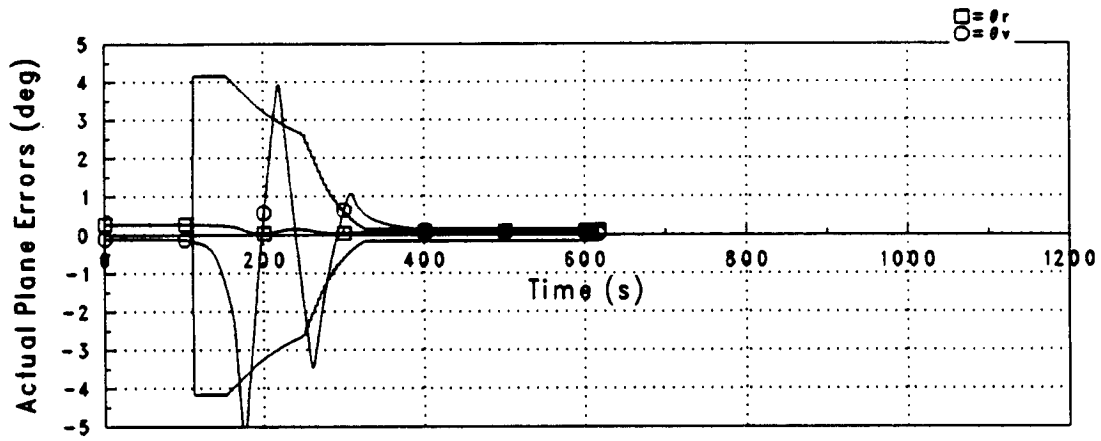
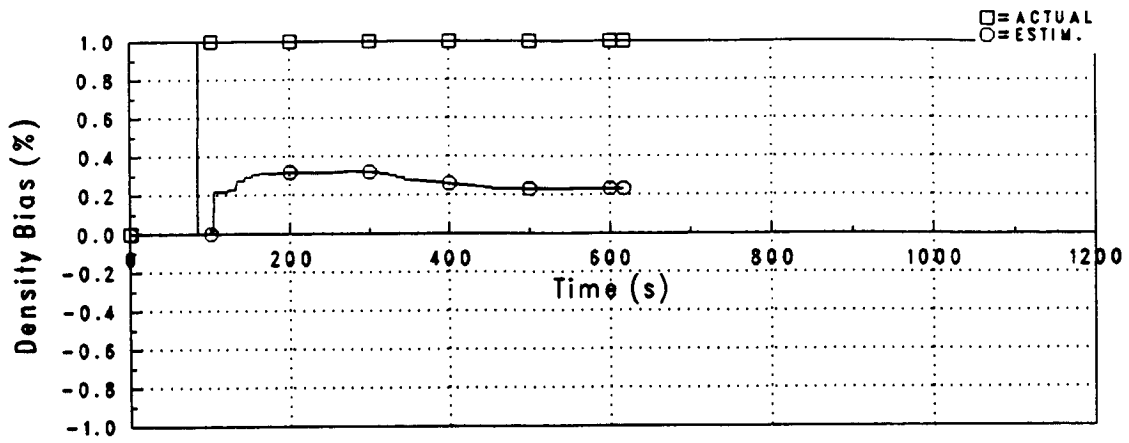


Figure 5-45. Case # 031000D, +100% Density: Bank Angle Control Response

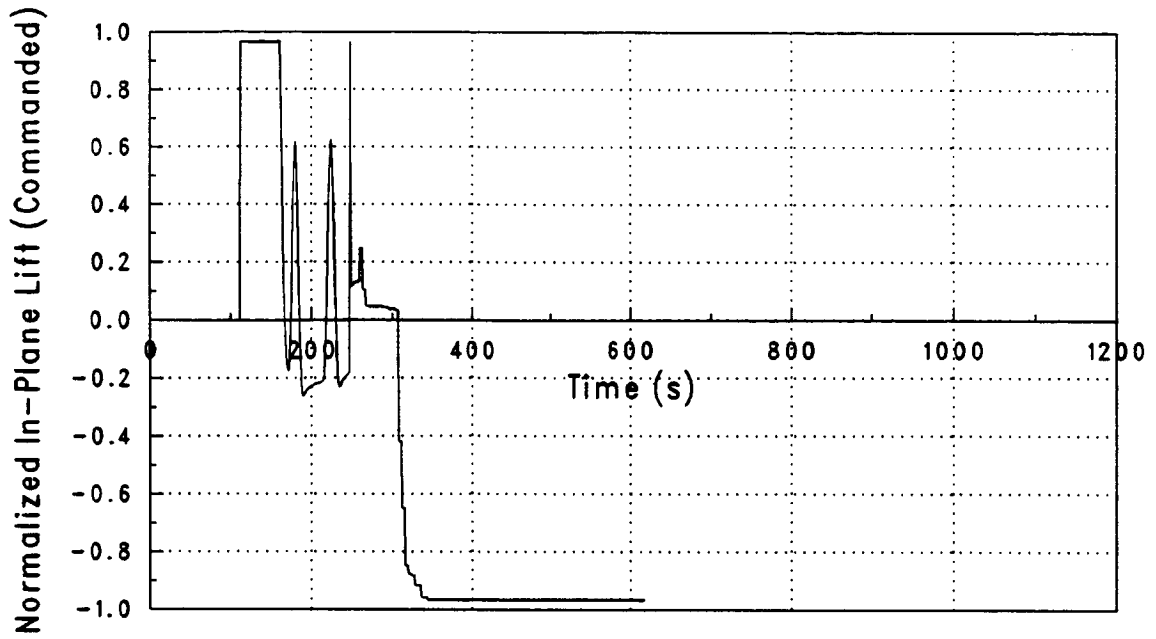


Figure 5-46. Case # 031000D, + 100% Density: Normalized In-Plane Lift

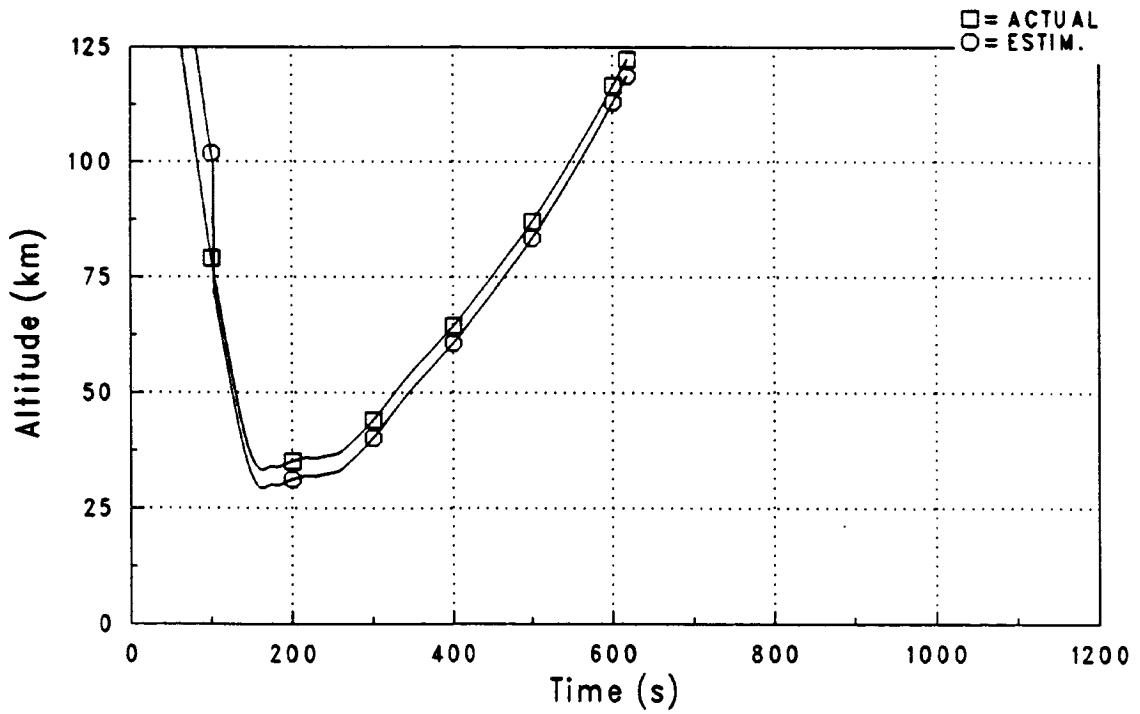


Figure 5-47. Case # 031000D, + 100% Density: Altitude History

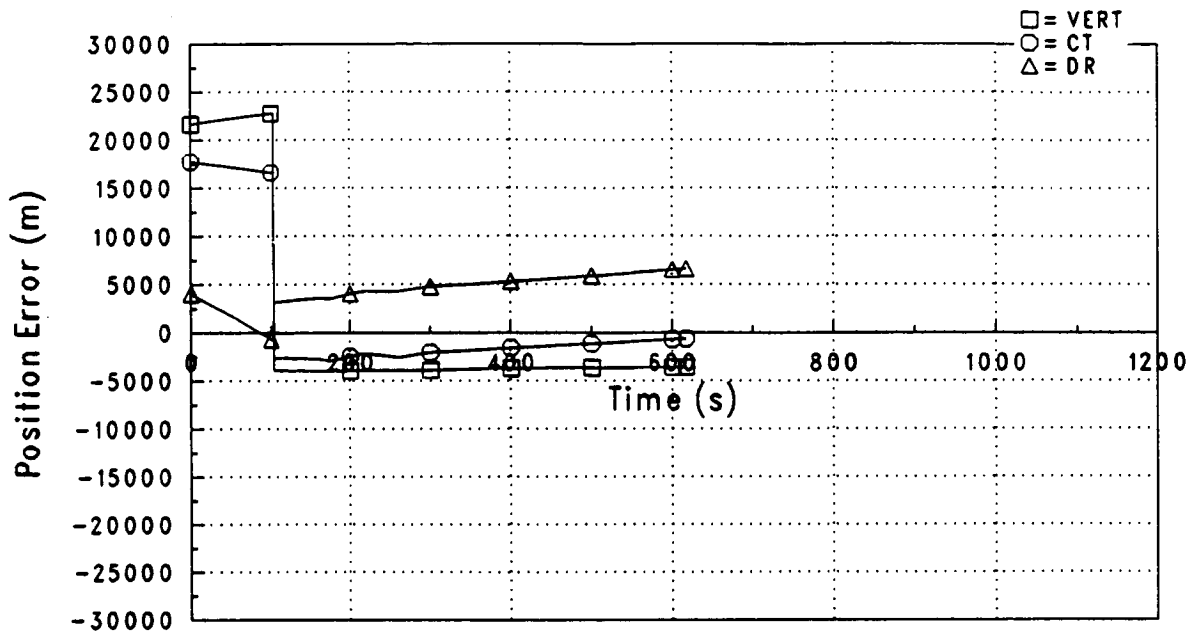


Figure 5-48. Case # 031000D, + 100% Density: Position Estimate Errors

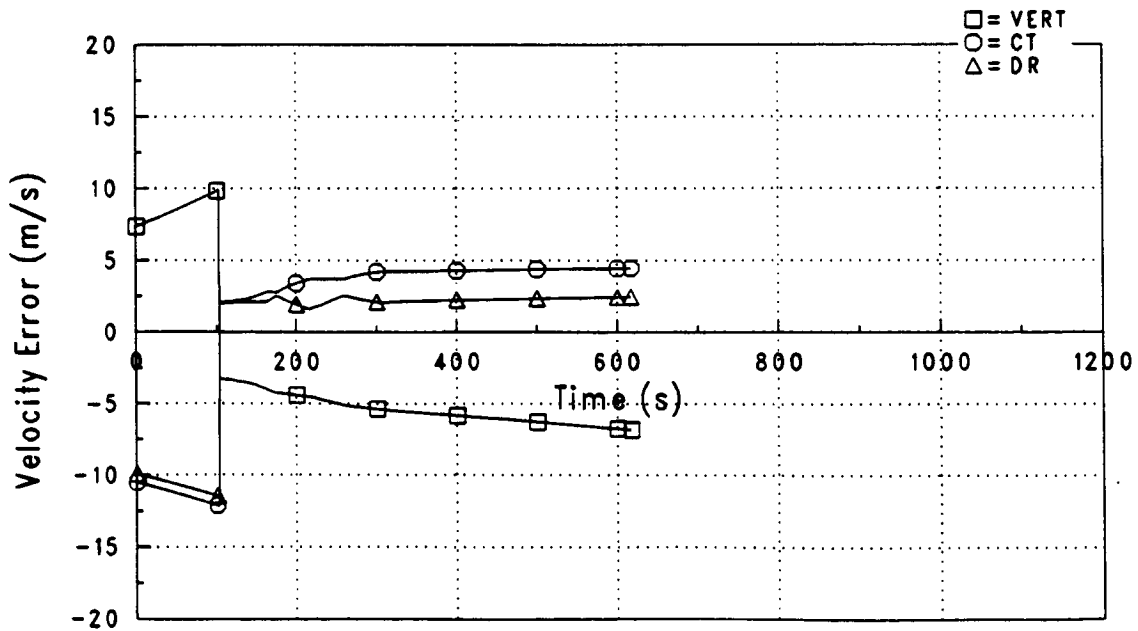


Figure 5-49. Case # 031000D, + 100% Density: Velocity Estimate Errors

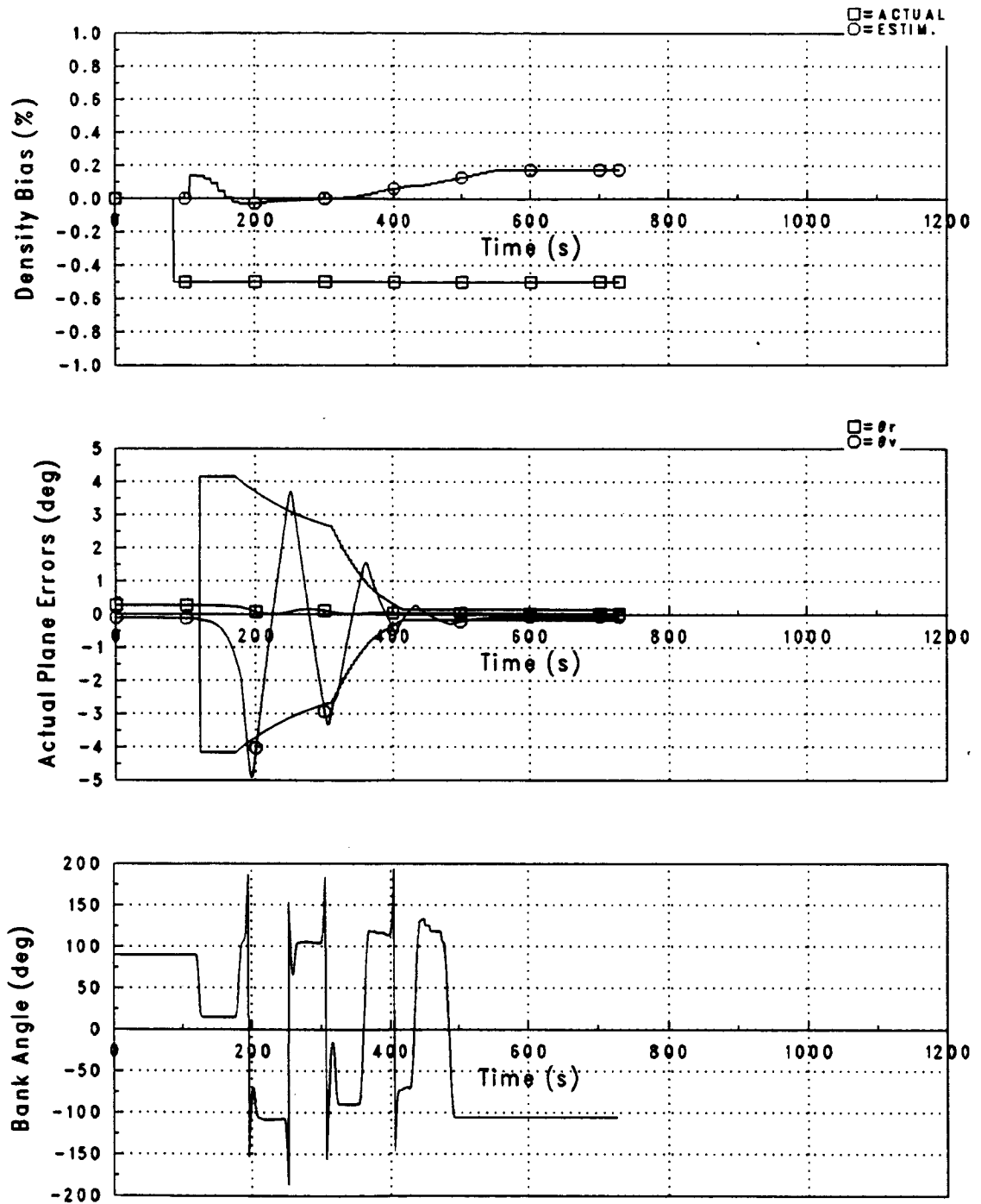


Figure 5-50. Case # 031000D, -50% Density: Bank Angle Control Response

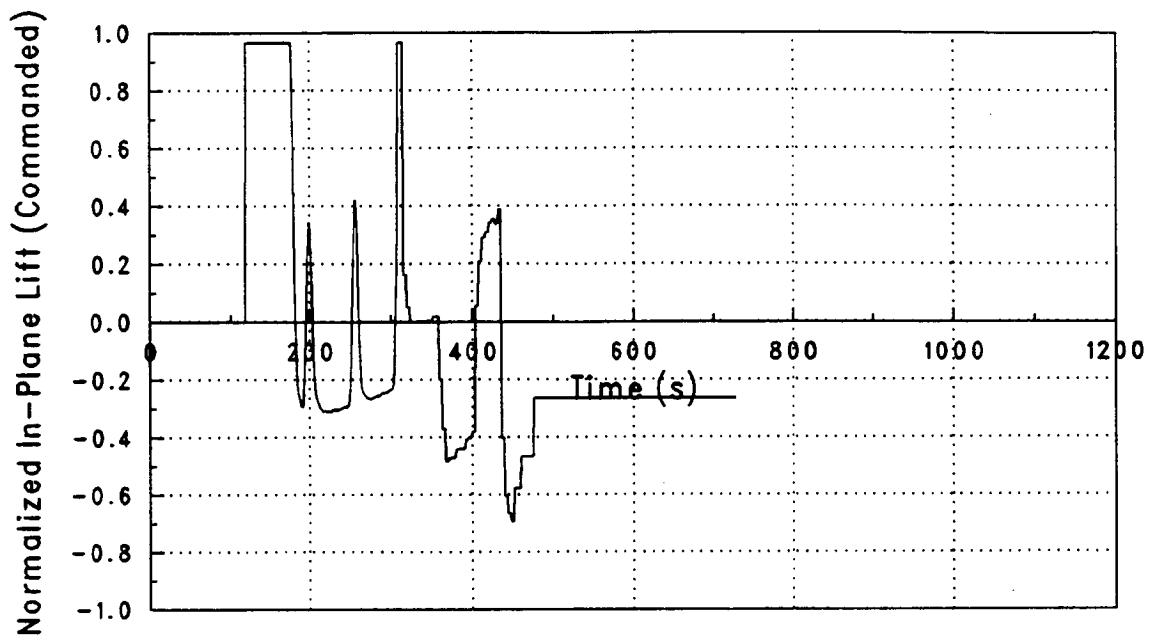


Figure 5-51. Case # 031000D, -50% Density: Normalized In-Plane Lift

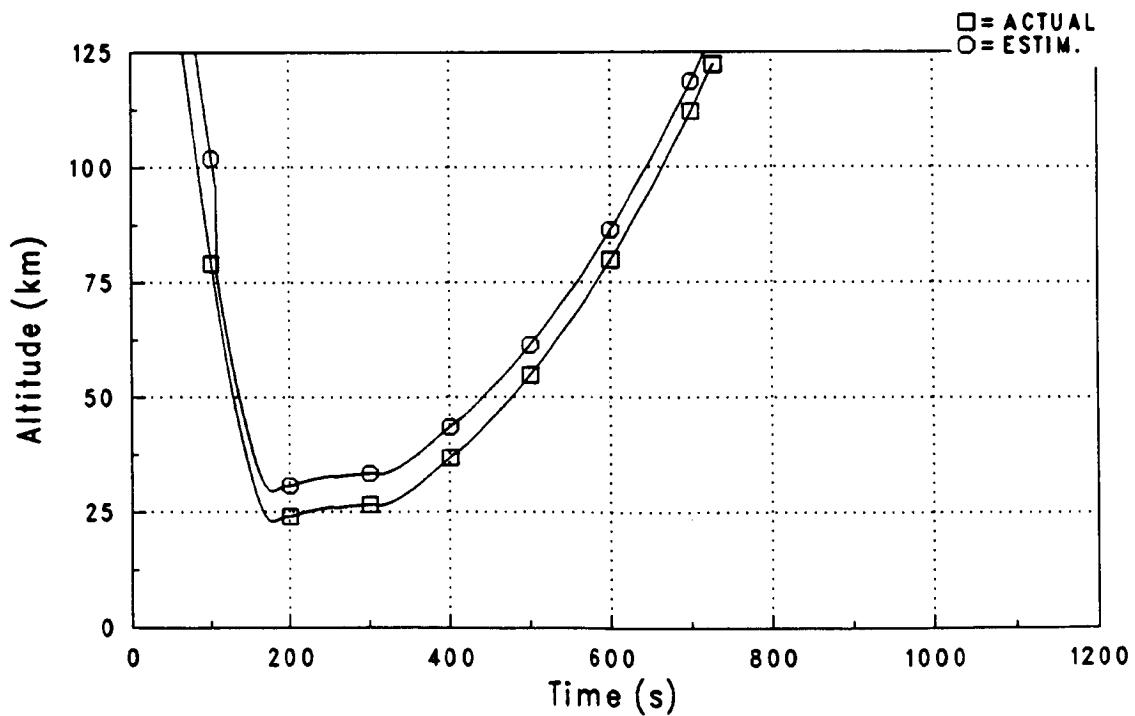


Figure 5-52. Case # 031000D, -50% Density: Altitude History

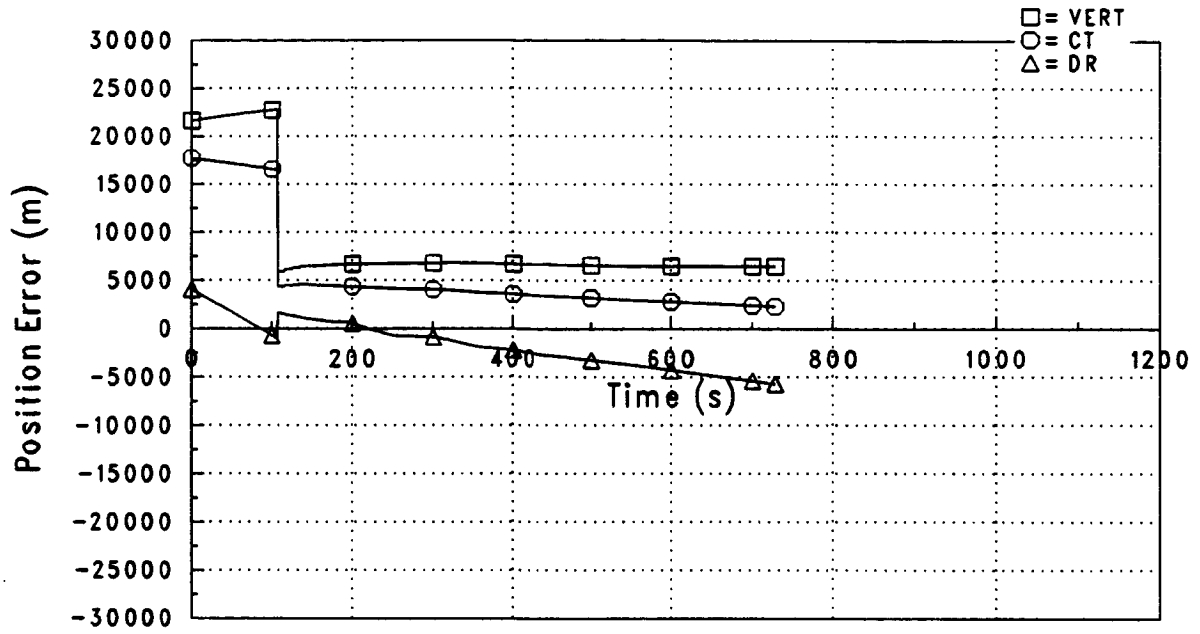


Figure 5-53. Case # 031000D, -50% Density: Position Estimate Errors

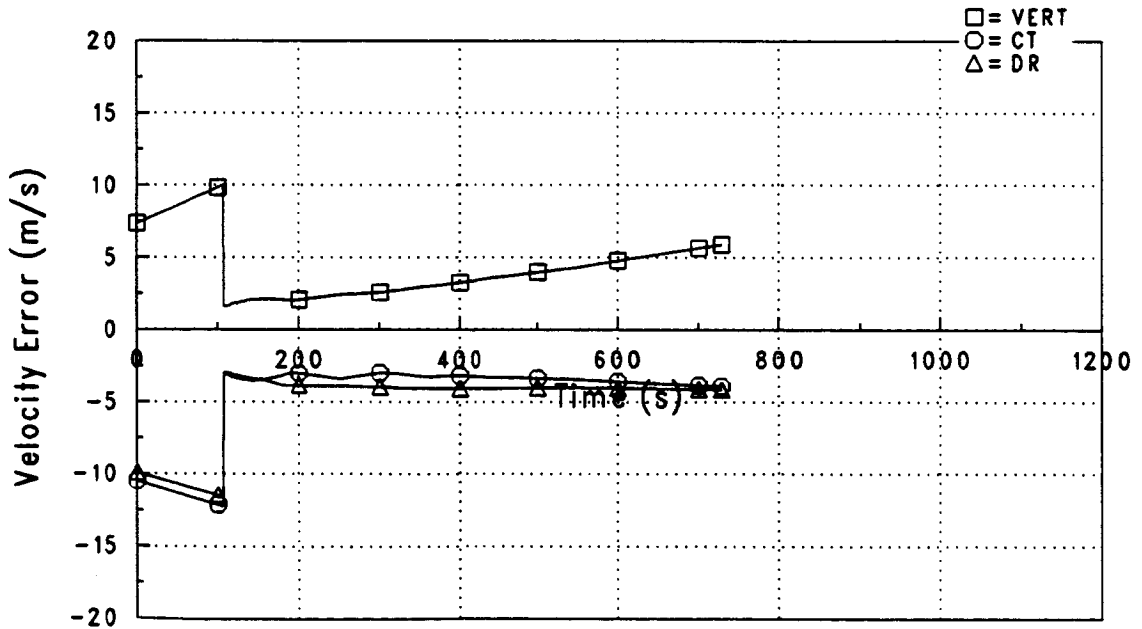


Figure 5-54. Case # 031000D, -50% Density: Velocity Estimate Errors

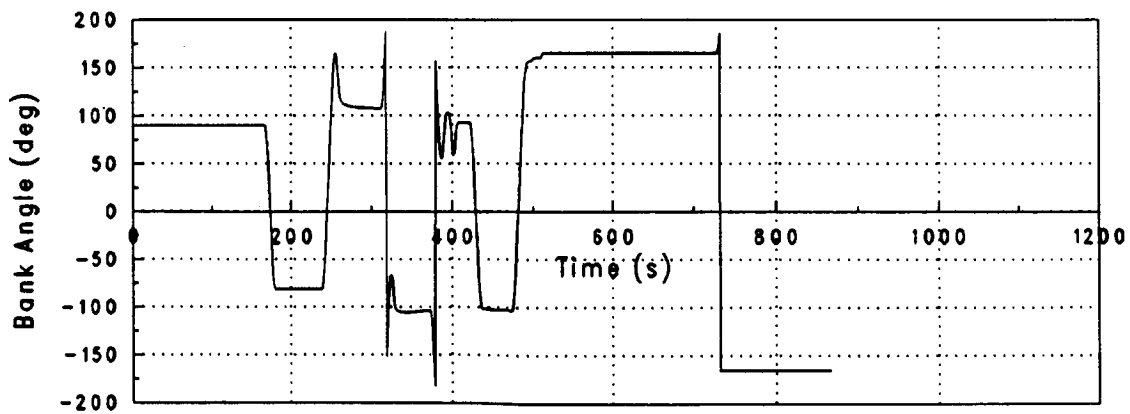
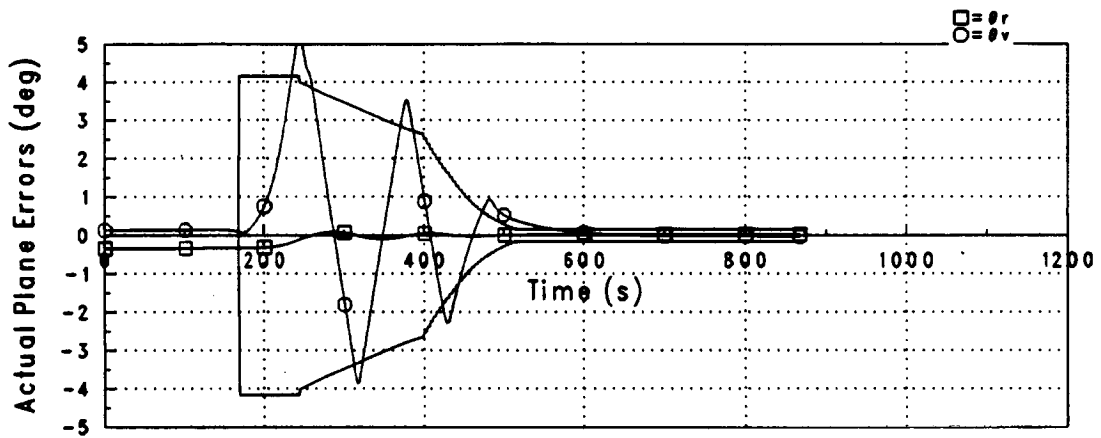
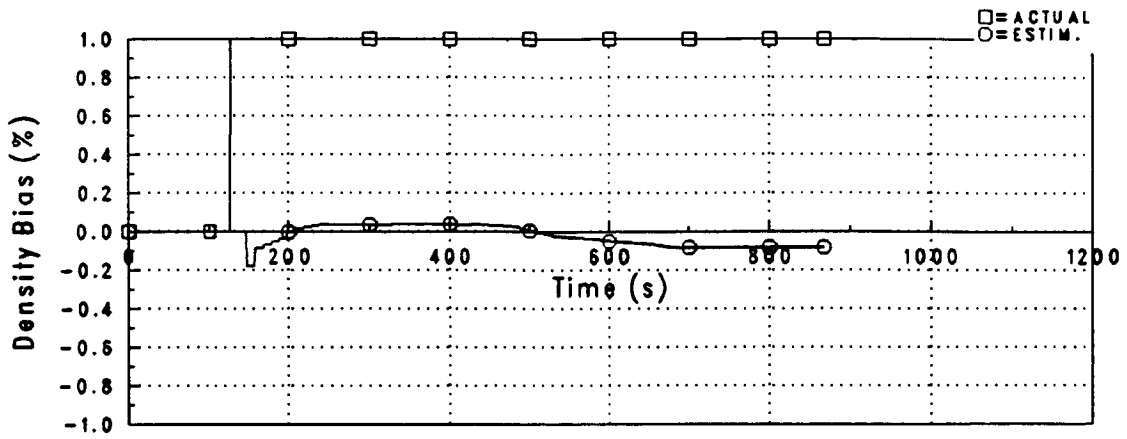


Figure 5-55. Case # 281000D, + 100% Density: Bank Angle Control Response

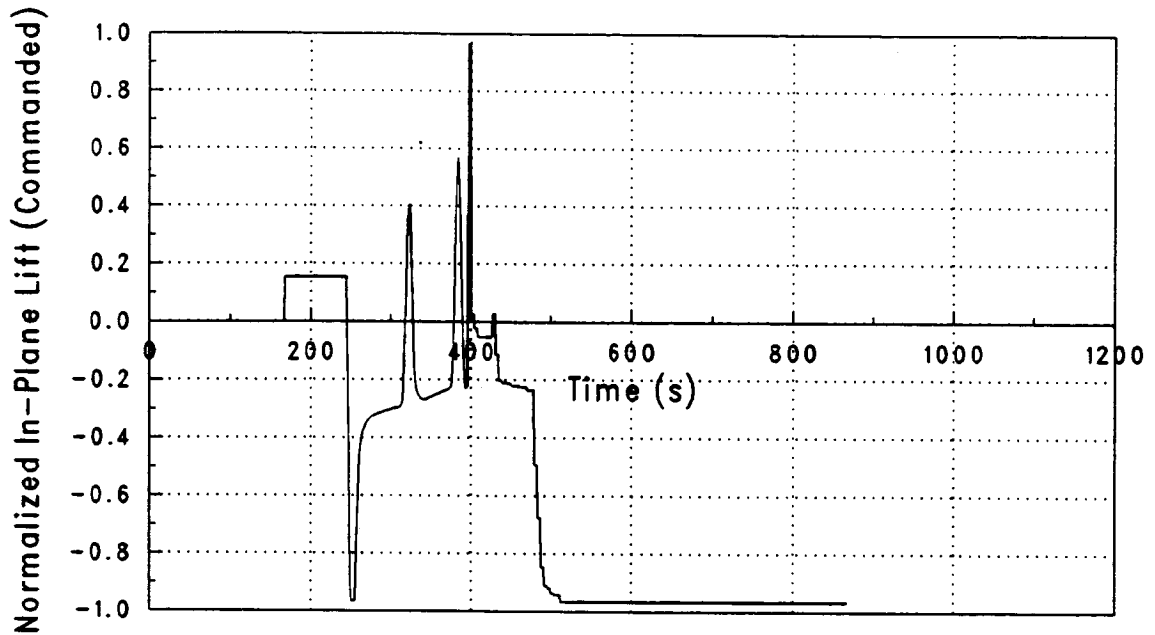


Figure 5-56. Case # 281000D, + 100% Density: Normalized In-Plane Lift

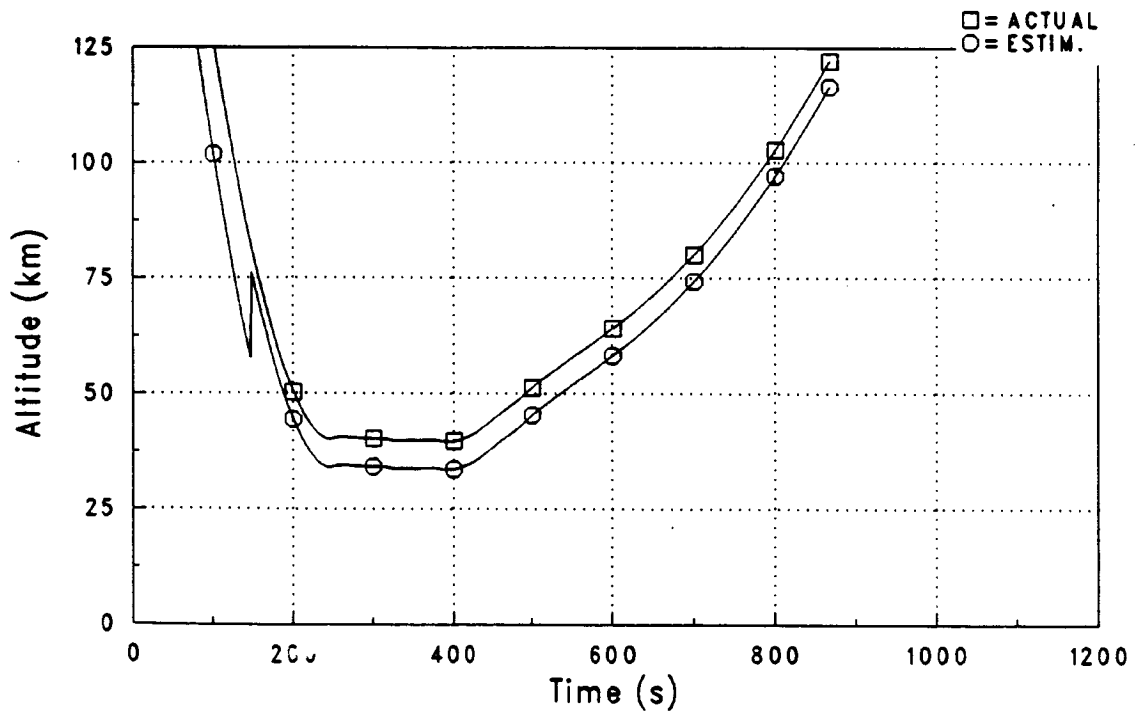


Figure 5-57. Case # 281000D, + 100% Density: Altitude History

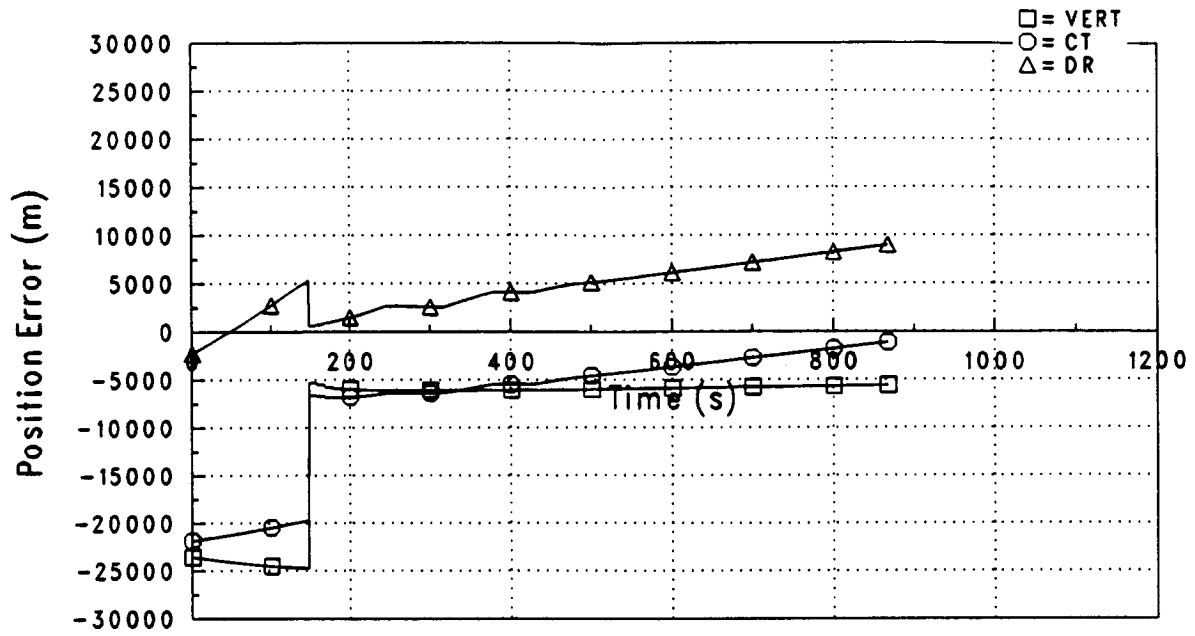


Figure 5-58. Case # 281000D, + 100% Density: Position Estimate Errors

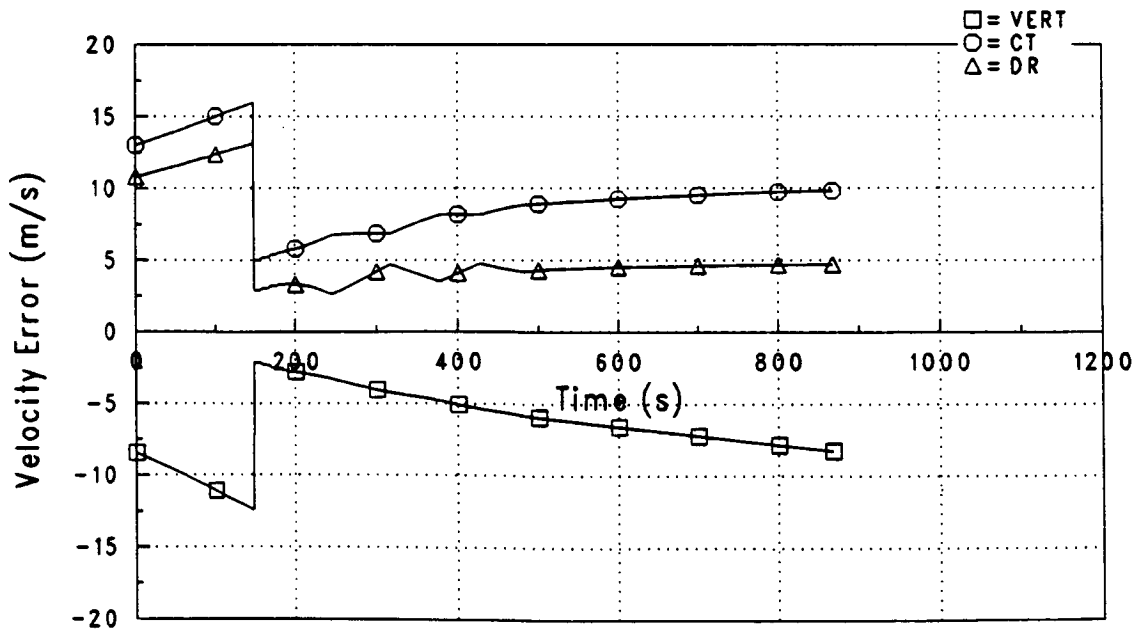


Figure 5-59. Case # 281000D, + 100% Density: Velocity Estimate Errors

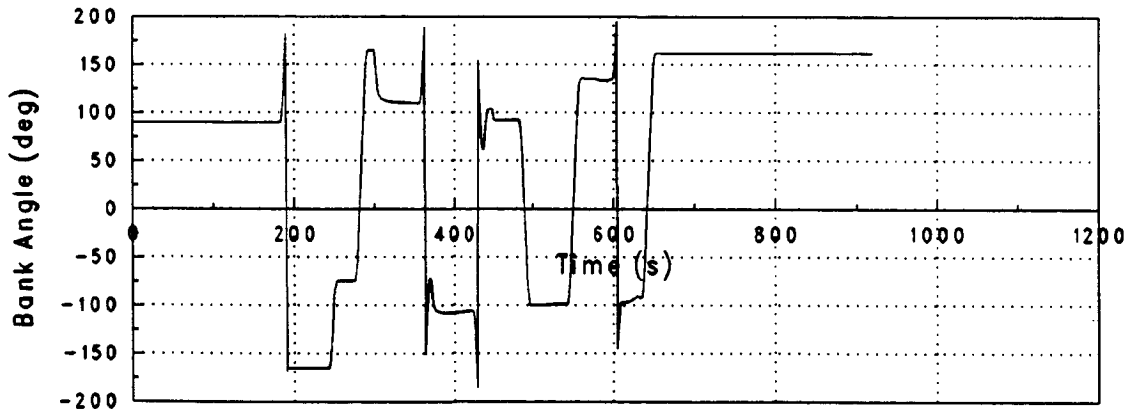
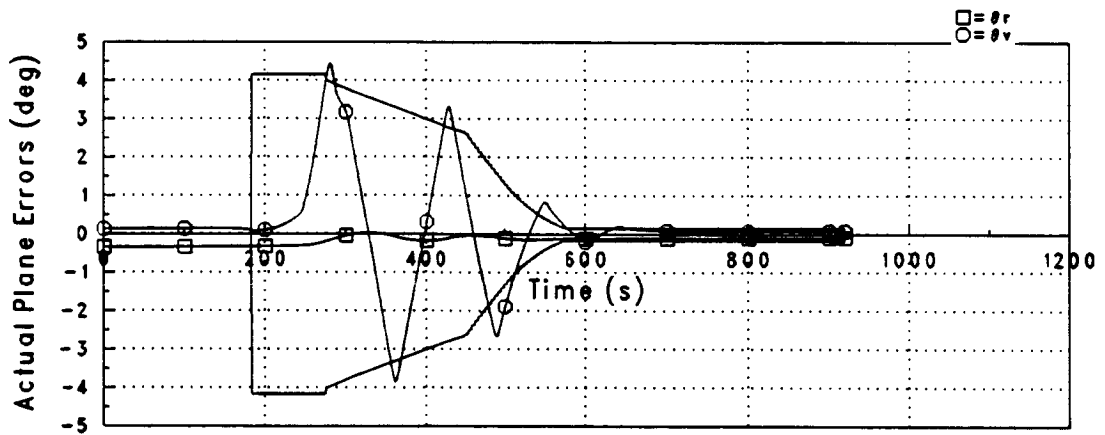
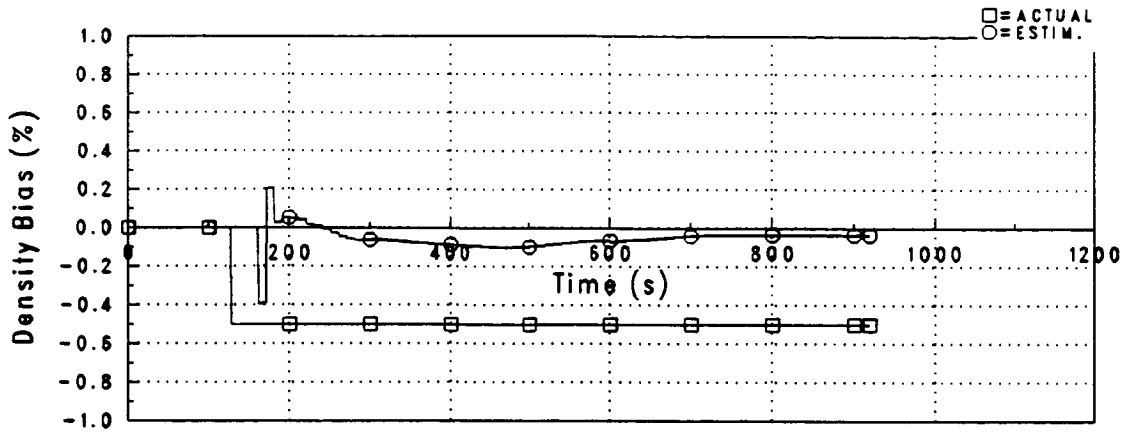


Figure 5-60. Case # 281000D, -50% Density: Bank Angle Control Response

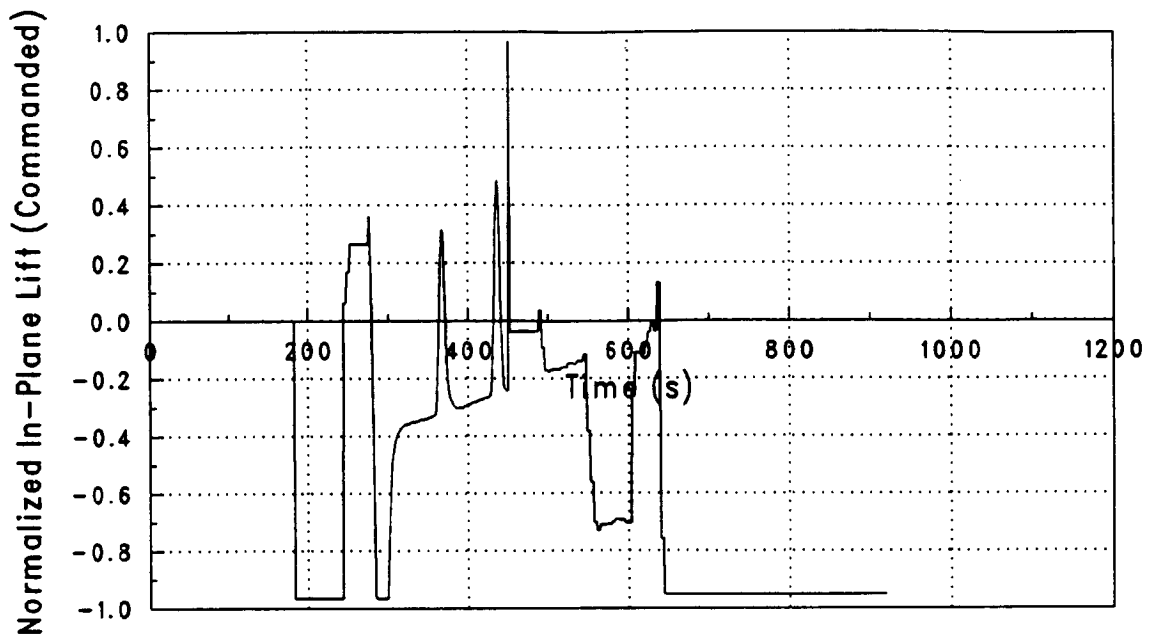


Figure 5-61. Case # 281000D, -50% Density: Normalized In-Plane Lift

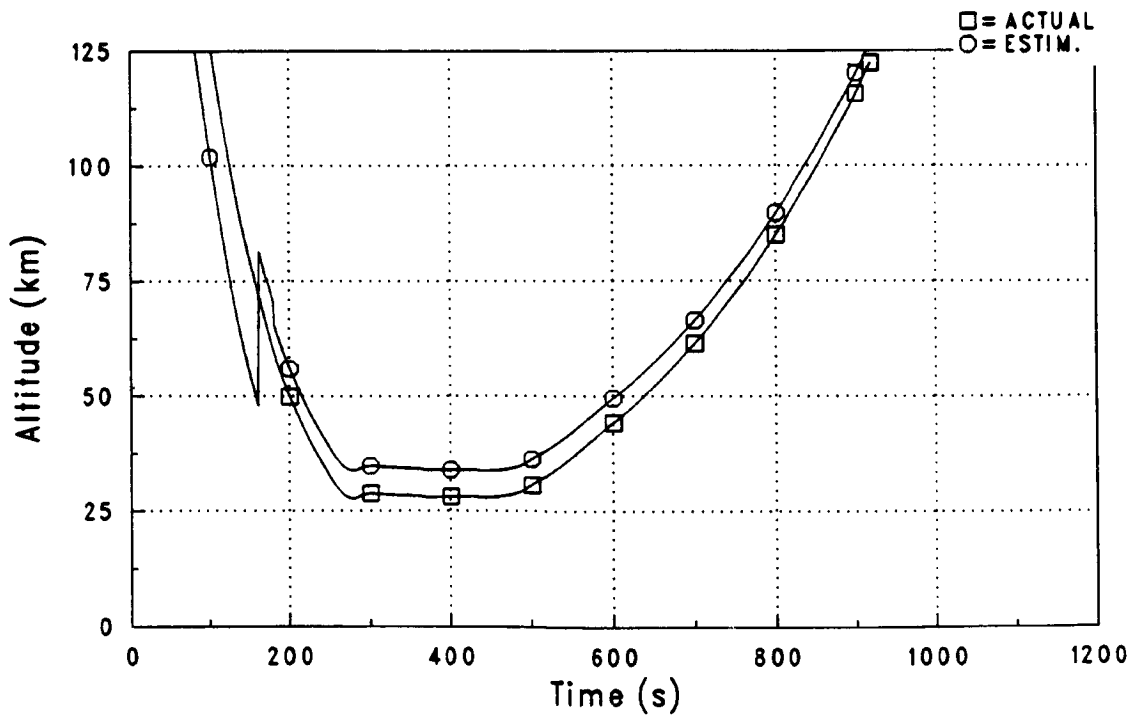


Figure 5-62. Case # 281000D, -50% Density: Altitude History

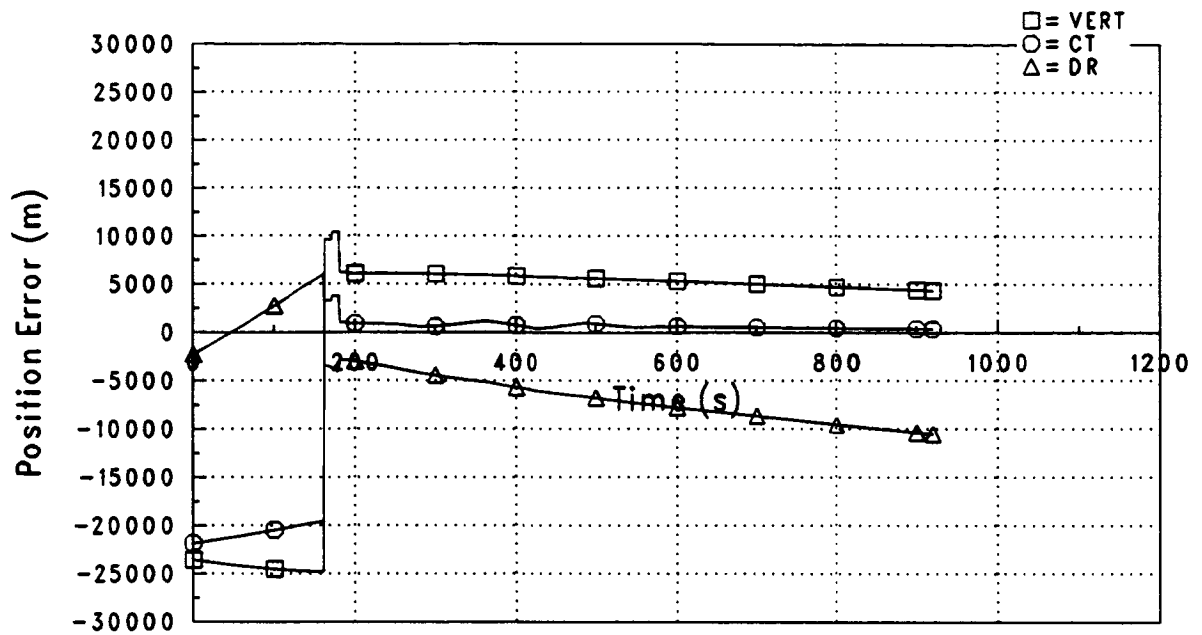


Figure 5-63. Case # 281000D, -50% Density: Position Estimate Errors

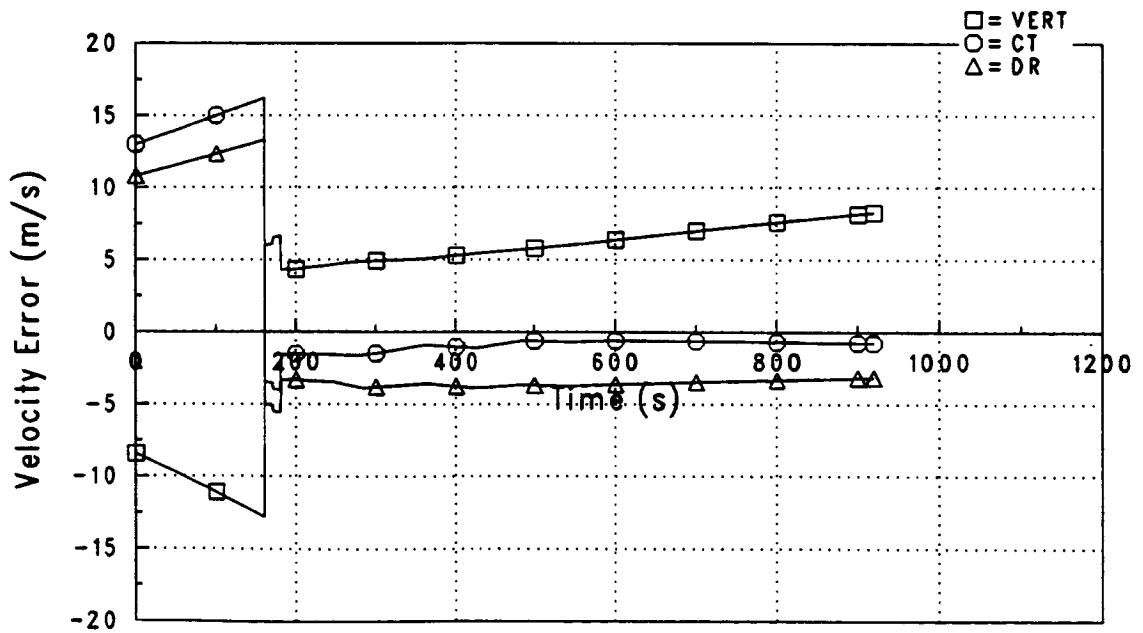


Figure 5-64. Case # 281000D, -50% Density: Velocity Estimate Errors

#### 5.4.4 DENSITY SHEAR CASES

Performance data for the ten variable density bias cases are presented in Tables 5-7 on page 161 through 5-10 on page 162 and Figures 5-65 on page 163 through 5-114 on page 192.

The total required propulsive  $\Delta V$  for orbit correction, listed in Table 5-7, is seen to vary from 67.6 m/s to 98.4 m/s for the cases examined. The large target apoapsis miss values seen in several cases can be attributed mostly to combinations of density shears and bank reversals during the exit phase which deplete control margin by forcing the bank command to full lift-up or full lift-down. Orbit plane control accuracy is also affected in these cases due to the decreased out-of-plane lift component available. The results of Table 5-10 show that the maximum aerodynamic load experienced was only 3.66 g's, and that one case (# 030500D) violated the minimum altitude limit.

Exit phase guidance performance is greatly affected by the presence of unpredictable variations in atmospheric density. Density shears during the capture phase can cause the vehicle to overshoot or undershoot the cruise altitude, but the constant-altitude cruise guidance can quickly correct these errors. Density variations during cruise are immediately compensated for by the guidance and are not a problem unless vehicle control capability is exceeded. Since the exit phase guidance depends on prediction of future vehicle control capability, the presence of density shears, which greatly change this control capability, can cause large target misses and fuel penalties. This problem is compounded by bank reversals which, as seen in the constant density bias results, tend to perturb the trajectory beyond the capability of the vehicle to compensate and reduce the control margin necessary to respond to density shifts. These effects can be seen in the density shear results presented, where all but one of the cases (# 280500D) is driven to control saturation before reaching atmospheric exit.

#### 5.4.4.1 DETAILED DESCRIPTION: CASE # 288500D

Figures 5-110 on page 190 through 5-114 on page 192 contain trajectory, control, and navigation plots for the high/shallow entry trajectory case corresponding to the final entry in the data tables. The navigation system performance for this case was examined in "5.3.3.2.1 Full Covariance (No Radar Altimeter)" on page 113. Cycling of the capture guidance algorithm begins at  $t = 171$  s, approximately 20 s after the initiation of density altitude measurement updates. The initial bank angle command has a magnitude of approximately  $90^\circ$ , as seen in Figure 5-110. It is seen that a bank reversal is commanded immediately after guidance cycling begins. This is due to the negative initial value of  $\theta$ , as seen in the plane error plot. The bank reversal causes  $\theta$  to initially be decreased instead of increased, effectively nulling a large part of the initial error.

The constant-altitude cruise phase is initiated at  $t = 261$  s when the estimated altitude drops below 34 km. Full lift-up is commanded immediately since the vehicle overshoots the target cruise altitude, and the cruise condition is reached approximately 25 s later. The impact of the dynamic density bias profile during cruise can be seen by referring to Figures 5-110 and 5-111. Decreasing density bias requires the vehicle to roll lift-down in order to maintain the vertical lift necessary for constant-altitude flight. This effect is seen between  $t = 360$  s and  $t = 450$  s, where the density bias decreases from -12% to -40%. The lift-down trend caused by the density decrease here is sufficient to offset the natural tendency of the constant-altitude guidance command to drift toward lift-up as aerodynamic control authority decreases, so that the bank command remains nearly constant in this region. The opposite effect is seen between  $t = 470$  s and  $t = 490$  s, where the density bias increases from -49% to -38%. In this case, the increasing density causes a decrease in the magnitude of the bank angle command in order to maintain the necessary level of vertical lift.

Cycling of the exit phase guidance begins at  $t = 495$  s. The most potential for harm from density shears exists during the exit phase, since guidance predictions have no way of accounting for future density variations. The combined effects of bank reversals and unfavorable density shears can be seen over the time period from  $t = 570$  s to  $t = 700$  s. Over this interval, the density bias decreases from 0 to -36%, thereby tending to drive the bank command to lift-down to compensate for the decreasing lifting capability. At  $t = 588$  s, a bank reversal through lift-up is commanded. As explained previously, this drives the vehicle closer to lift-down, compounding the problem caused by decreasing density. It is seen that the bank command is finally driven to full lift-down at  $t = 636$  s, so that no control margin remains to deal with the still decreasing density.

The net effect of density and bank reversal dispersions during the exit phase is seen in the performance results of Table 5-7 on page 161. The apoapsis target is missed by +47.6 km, a value which would have been even higher if not for the negative to positive density shear which occurs after  $t = 700$  s. Table 5-8 shows that the guidance error alone is 50.5 km. The full penalty of the apoapsis error is offset somewhat by the high exit periapsis resulting from flying most of the exit phase full lift-down. The total  $\Delta V$  required to correct the apoapsis and periapsis errors is seen to be 69.1 m/s.

Table 5-7. Aerocapture Performance Results (Density Shear Cases)

CASE	$h_{a_m}$ (km)	$h_p$ (km)	$\theta_r$ (deg)	$\theta_v$ (deg)	$\delta$ (deg)	$\Delta V_{ORBIT}$ (m/s)	$\Delta V_{PLANE}$ (m/s)	$\Delta V_{TOT}$ (m/s)
030500D	10.7	15.8	0.062	0.116	0.12	72.1	6.96	79.0
031000D	-29.4	-33.0	-0.001	-0.190	0.19	85.9	10.5	96.4
031500D	-41.4	-0.80	0.010	-0.234	0.23	80.4	13.0	93.4
035000D	100.4	45.5	0.139	0.144	0.19	77.4	10.6	88.0
038500D	176.9	45.2	0.128	0.145	0.18	87.4	10.2	97.6
280500D	-8.80	42.3	-0.027	0.002	0.02	66.0	1.54	67.6
281000D	14.2	53.9	0.076	0.189	0.19	64.1	10.9	75.0
281500D	133.8	21.4	0.004	0.206	0.20	87.1	11.4	98.4
285000D	48.1	50.3	-0.022	0.009	0.02	69.5	1.40	70.9
288500D	47.6	51.4	0.133	0.041	0.13	69.1	7.57	76.7

Table 5-8. Guidance Errors (Density Shear Cases)

CASE	$h_{a_{err}}$ (km)		$\theta_{v_{err}}$ (deg)				
030500D	11.6		0.102				
031000D	-28.6		-0.204				
031500D	-39.8		-0.241				
035000D	105.0		0.123				
038500D	178.4		0.127				
280500D	-7.3		-0.078				
281000D	17.6		0.098				
281500D	134.5		0.133				
285000D	54.1		-0.089				
288500D	50.5		-0.061				

Table 5-9. Estimation Errors (Density Shear Cases)

CASE	$\tilde{h}_a$ (km)	$\tilde{h}_p$ (km)	$\tilde{\theta}_r$ (deg)	$\tilde{\theta}_v$ (deg)	$\tilde{\delta}$ (deg)			
030500D	0.9	0.7	-0.014	-0.014	-0.02			
031000D	0.8	0.8	-0.015	-0.014	0.01			
031500D	1.6	1.0	-0.017	-0.007	0.01			
035000D	4.6	0.2	-0.013	-0.021	-0.03			
038500D	1.5	0.3	-0.014	-0.018	-0.02			
280500D	1.5	-1.0	0.002	-0.080	0.06			
281000D	3.4	-1.7	-0.008	-0.091	-0.08			
281500D	0.7	-0.3	0.018	-0.073	-0.07			
285000D	6.0	-2.0	0.001	-0.098	0.07			
288500D	2.9	-2.4	-0.006	-0.102	0.01			

Table 5-10. Vehicle and Trajectory Limits (Density Shear Cases)

CASE	$h_{\min}$ (km)	$g_{\max}$	$\dot{Q}_{\max}$ (W/cm <sup>2</sup> )	$Q$ (J/cm <sup>2</sup> )
030500D	26.8	2.74	187.6	27808
031000D	28.5	3.36	205.5	26157
031500D	27.2	3.50	210.0	24112
035000D	28.9	3.66	216.4	25609
038500D	28.8	3.28	200.9	25799
280500D	33.8	1.67	144.1	34307
281000D	34.3	1.21	131.2	35935
281500D	33.4	2.39	169.5	28582
285000D	34.3	1.79	148.9	33596
288500D	34.7	1.56	147.4	35950

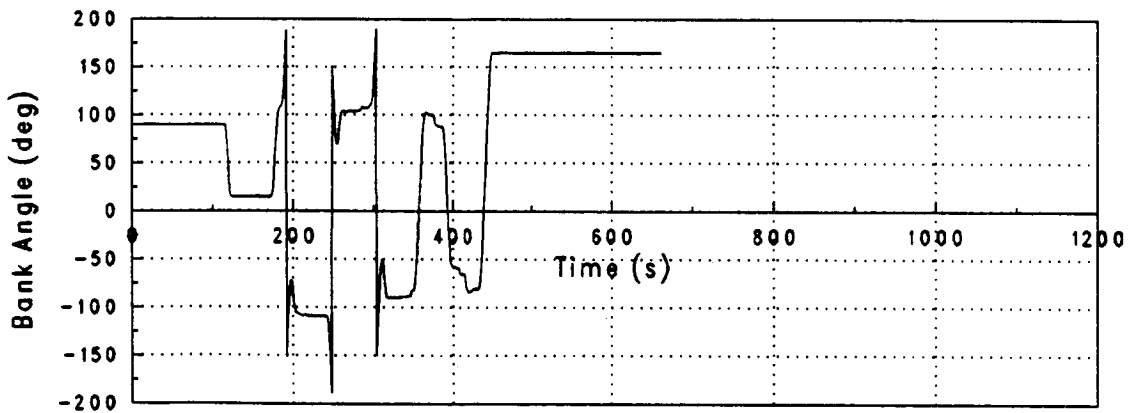
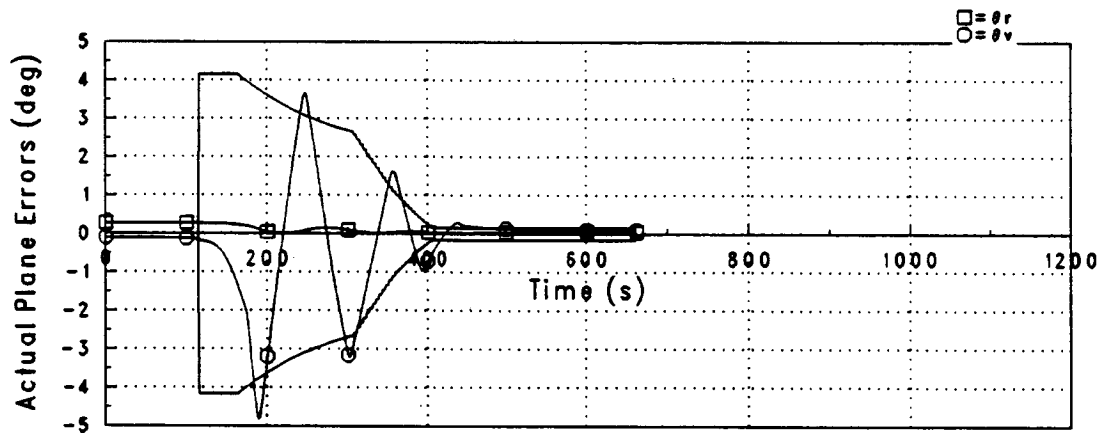
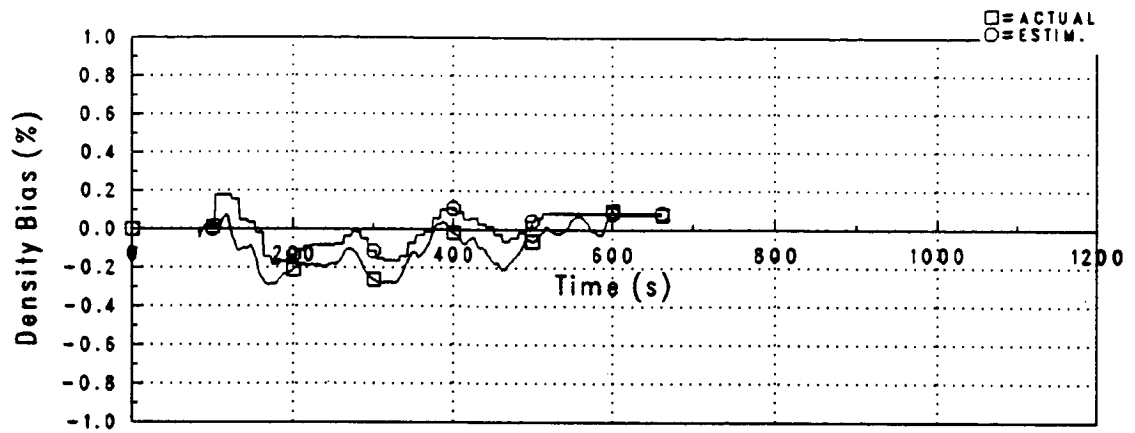


Figure 5-65. Case # 030500D: Bank Angle Control Response

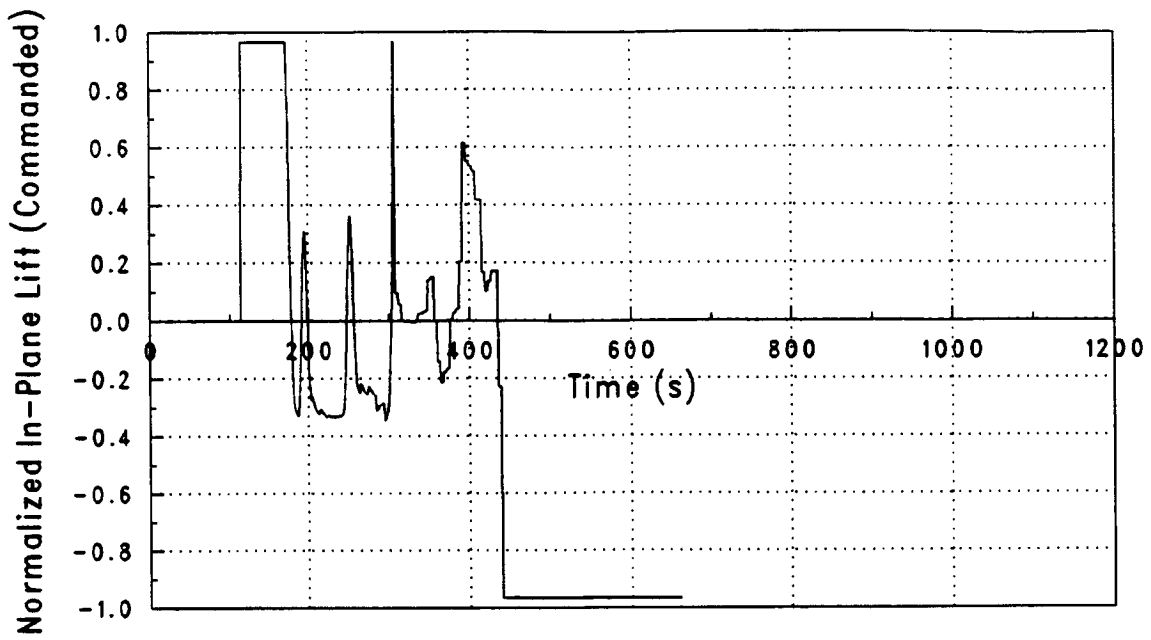


Figure 5-66. Case # 030500D: Normalized In-Plane Lift

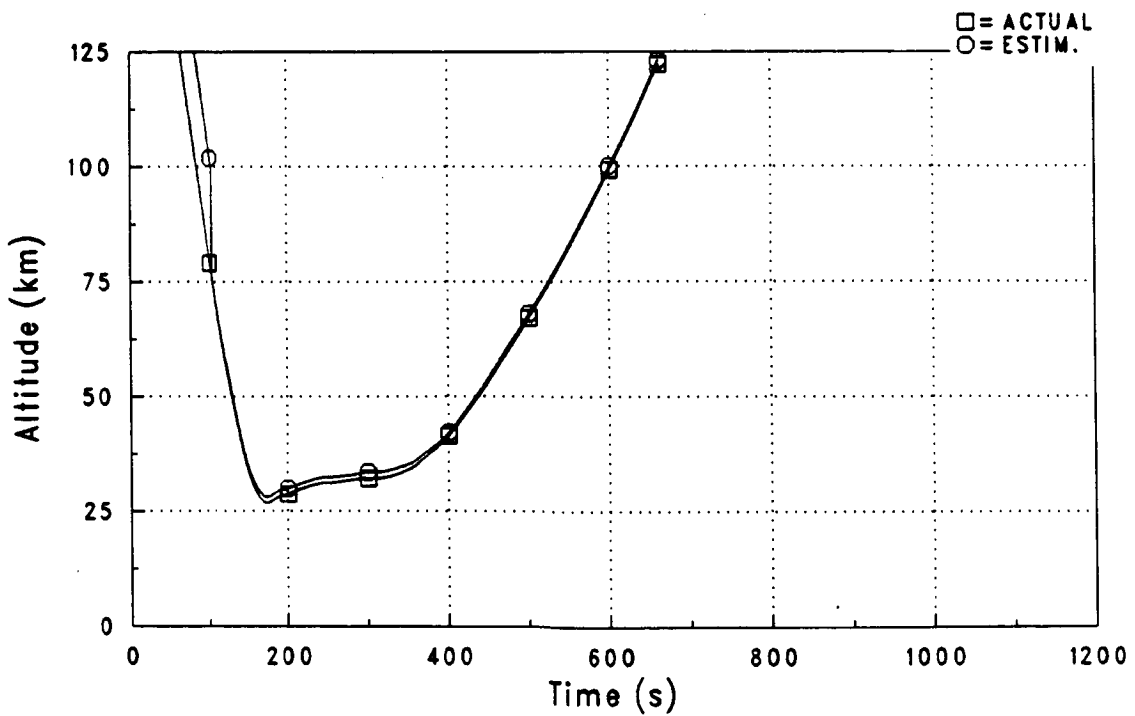


Figure 5-67. Case # 030500D: Altitude History

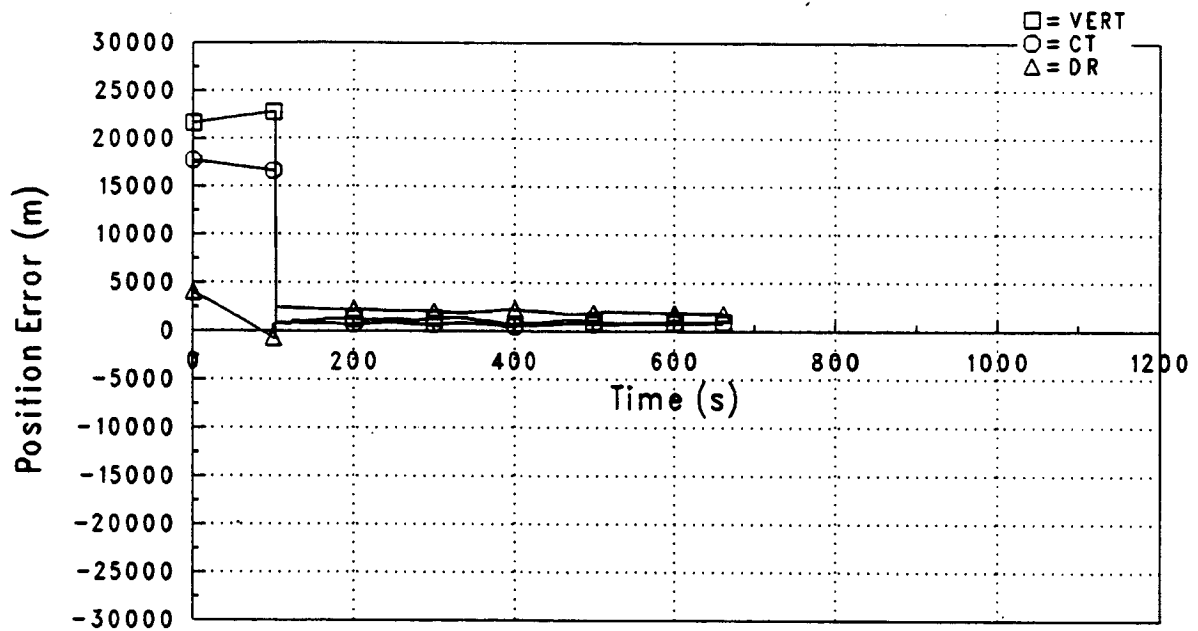


Figure 5-68. Case # 030500D: Position Estimate Errors

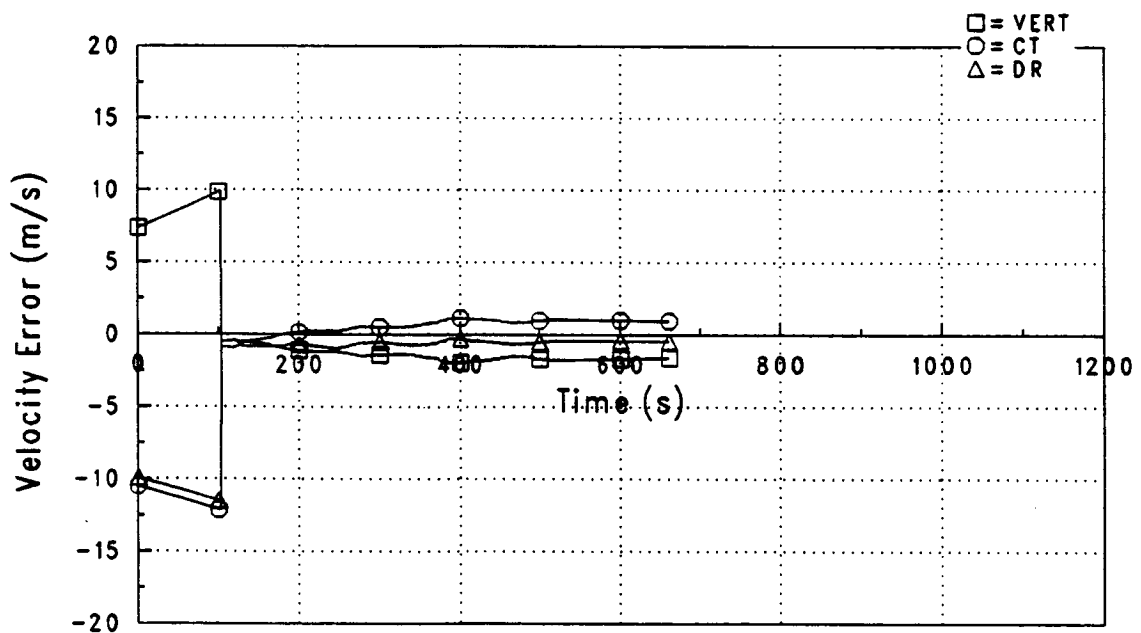


Figure 5-69. Case # 030500D: Velocity Estimate Errors

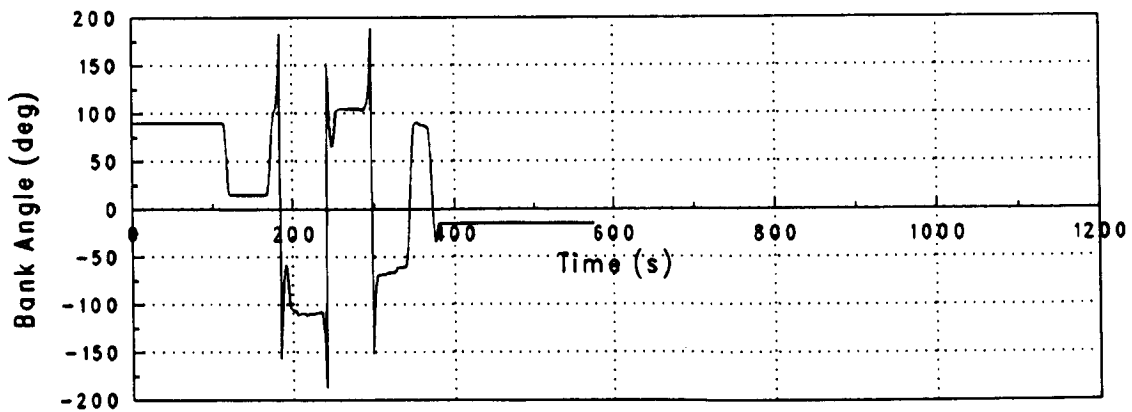
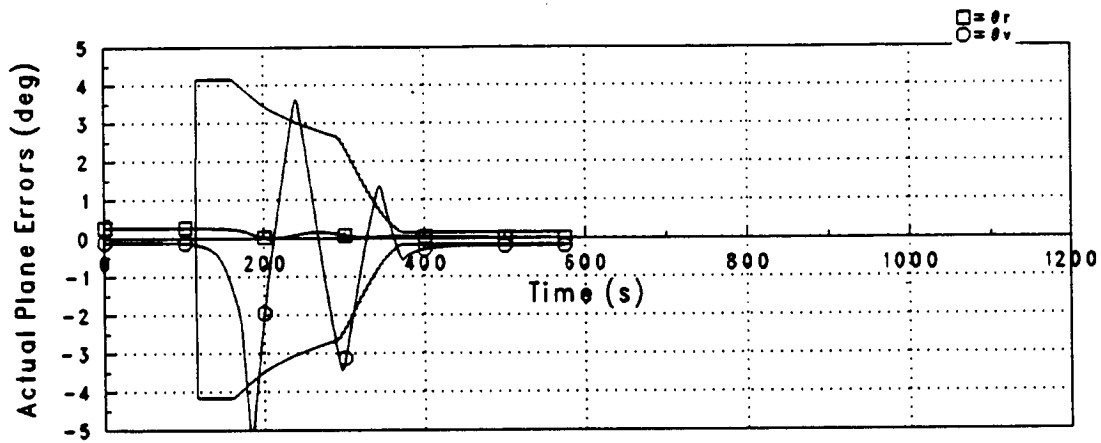
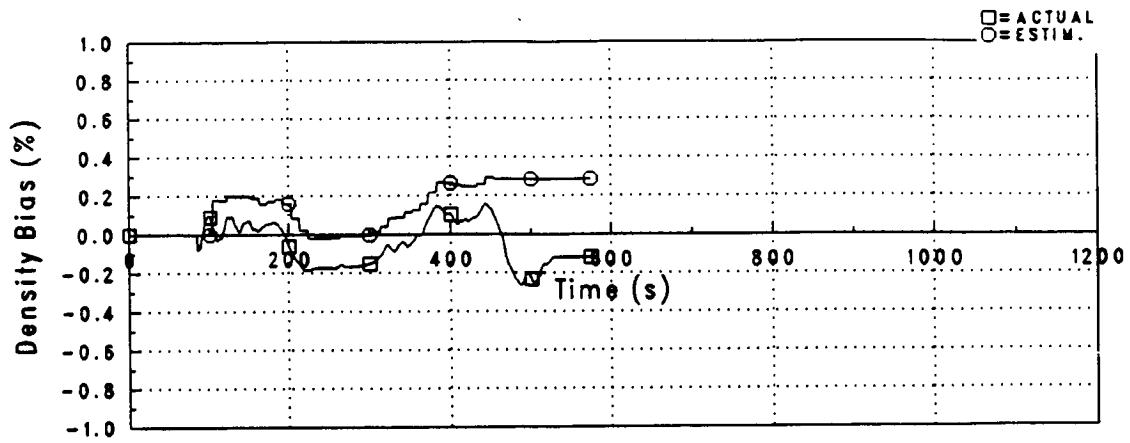


Figure 5-70. Case # 031000D: Bank Angle Control Response

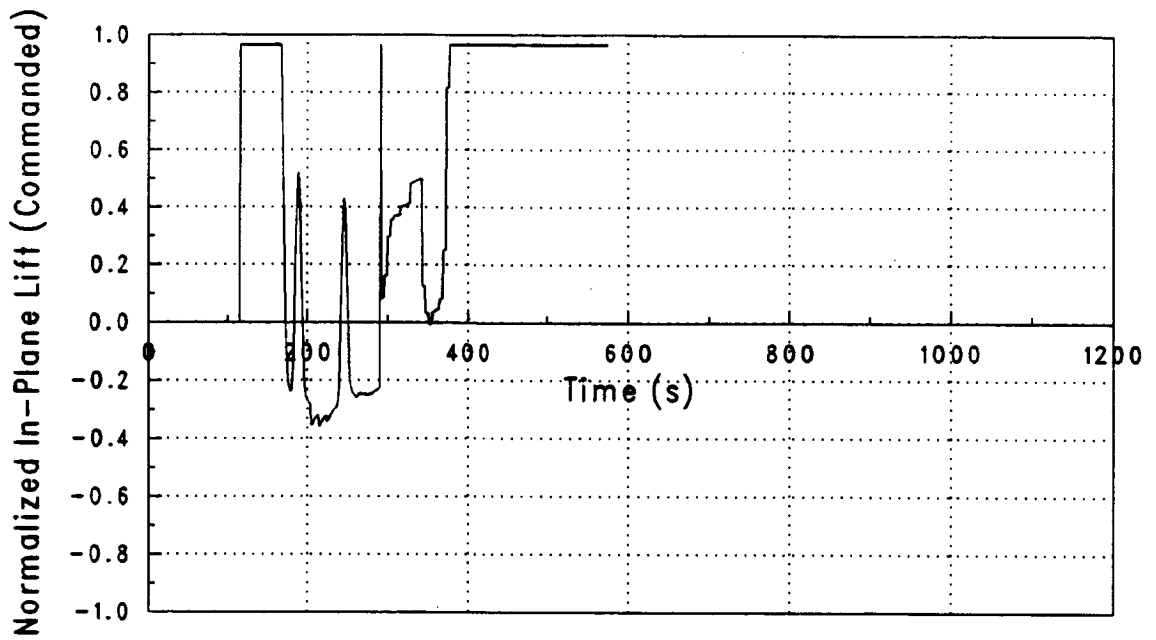


Figure 5-71. Case # 031000D: Normalized In-Plane Lift

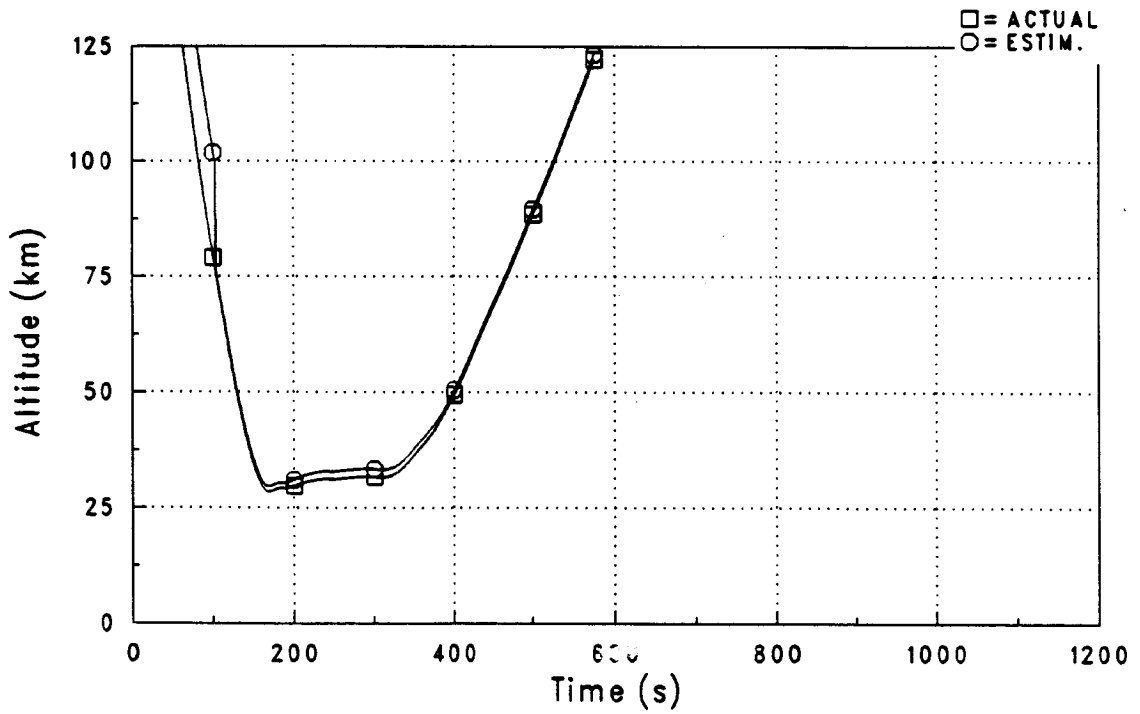


Figure 5-72. Case # 031000D: Altitude History

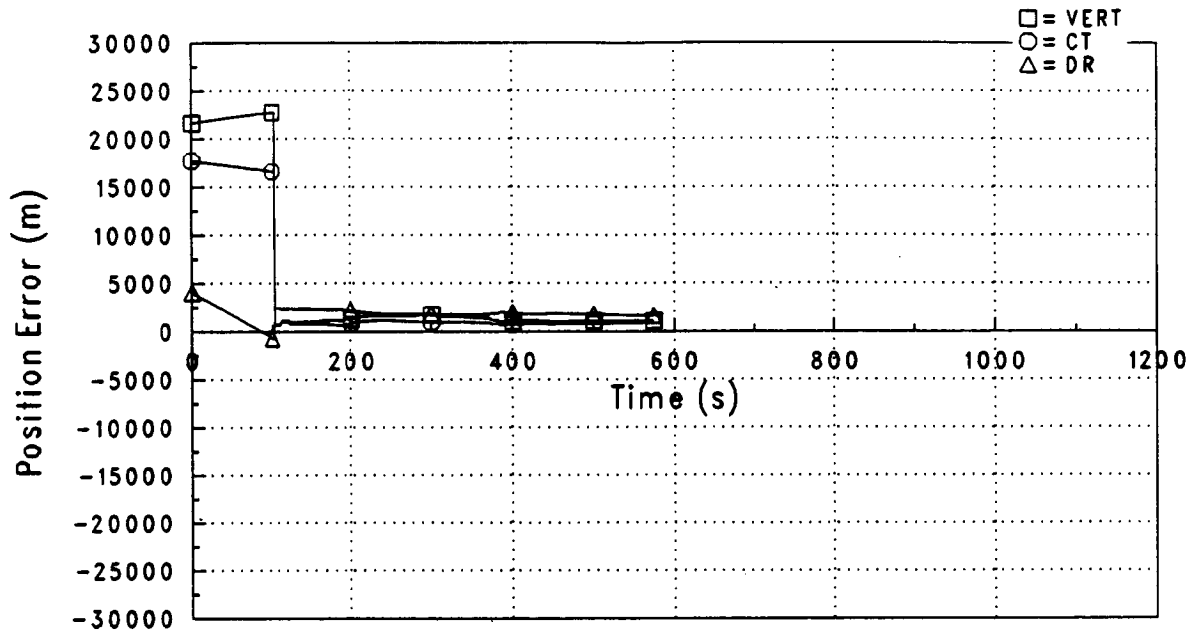


Figure 5-73. Case # 031000D: Position Estimate Errors

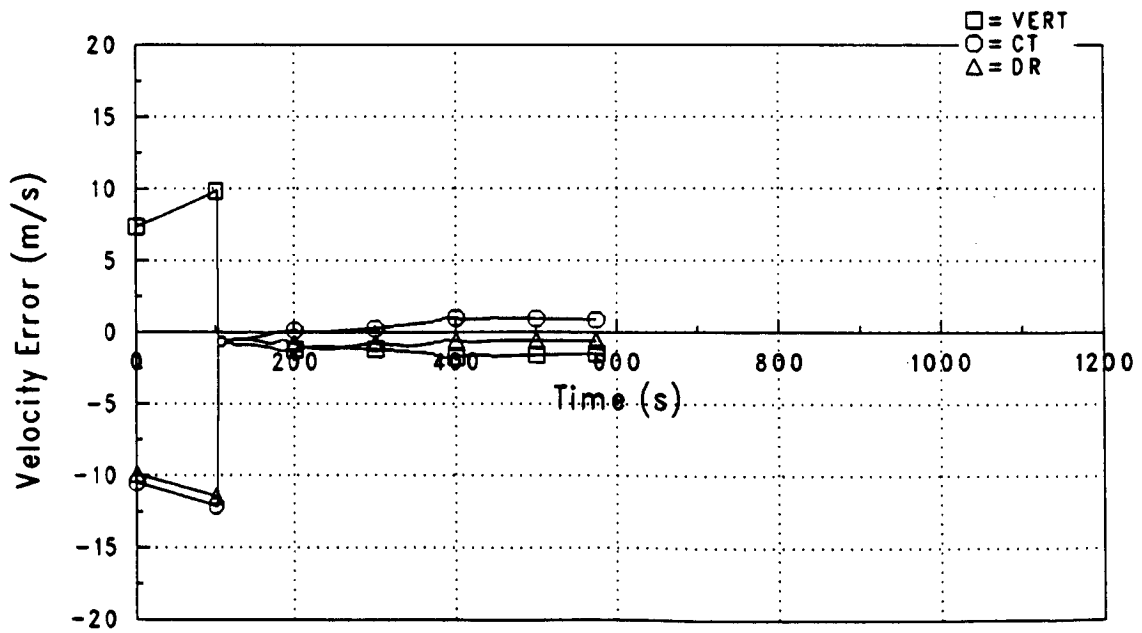


Figure 5-74. Case # 031000D: Velocity Estimate Errors

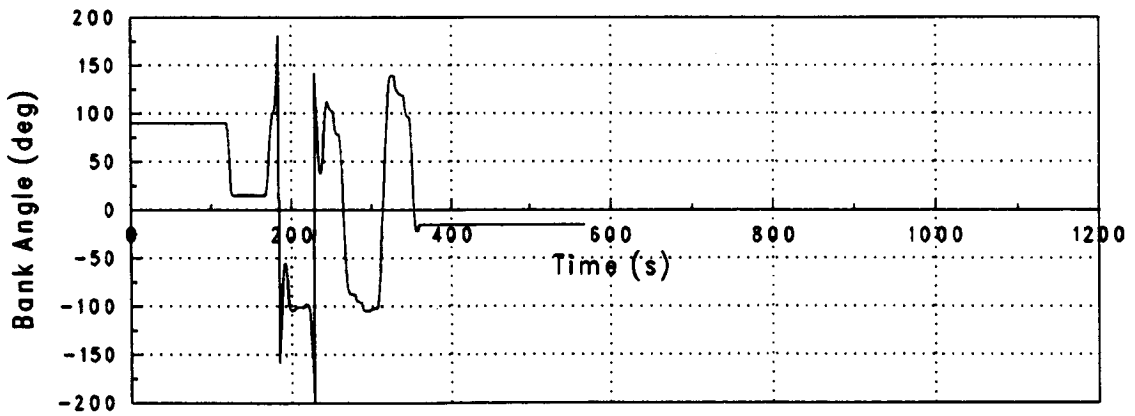
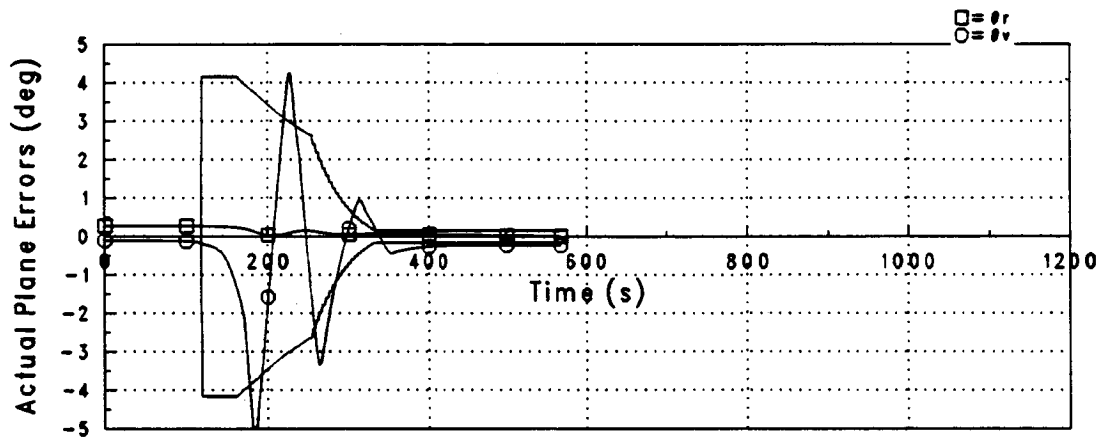
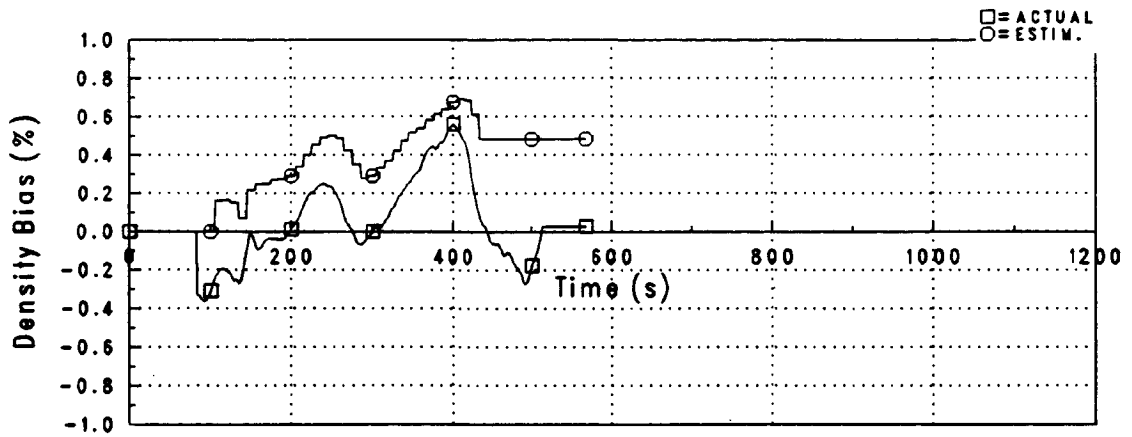


Figure 5-75. Case # 031500D: Bank Angle Control Response

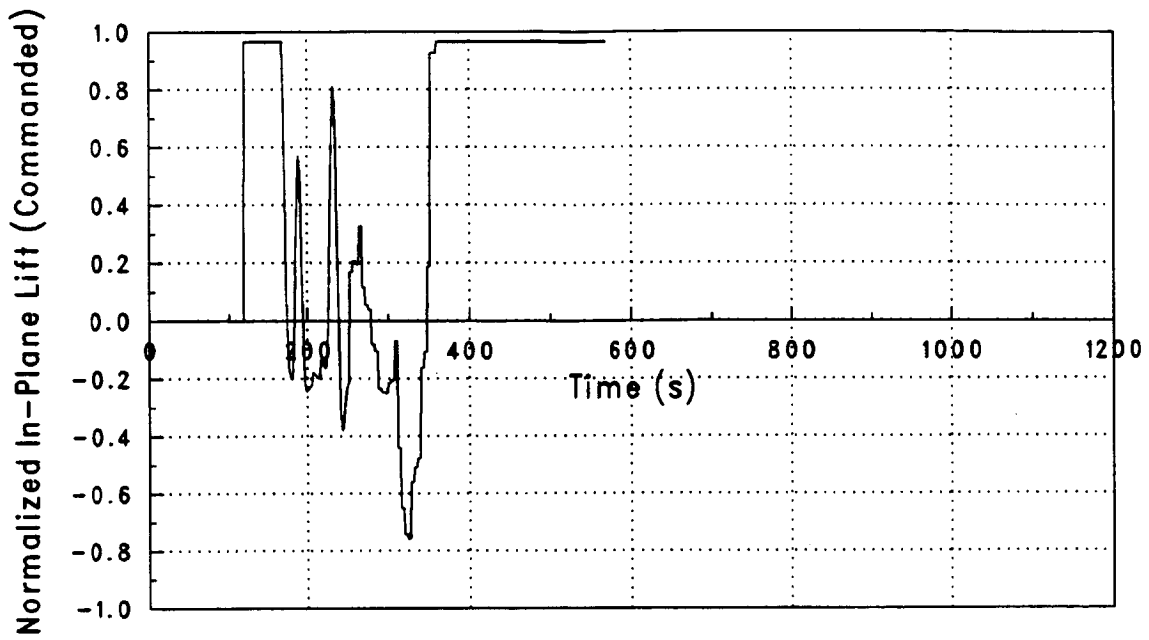


Figure 5-76. Case # 031500D: Normalized In-Plane Lift

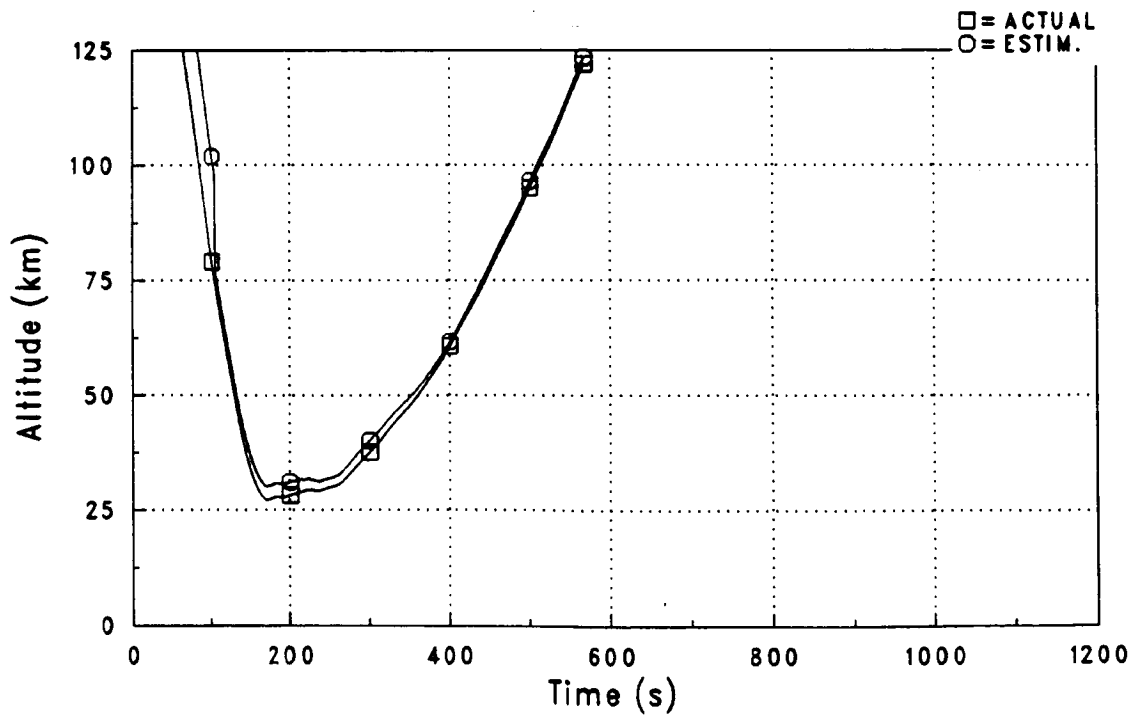


Figure 5-77. Case # 031500D: Altitude History

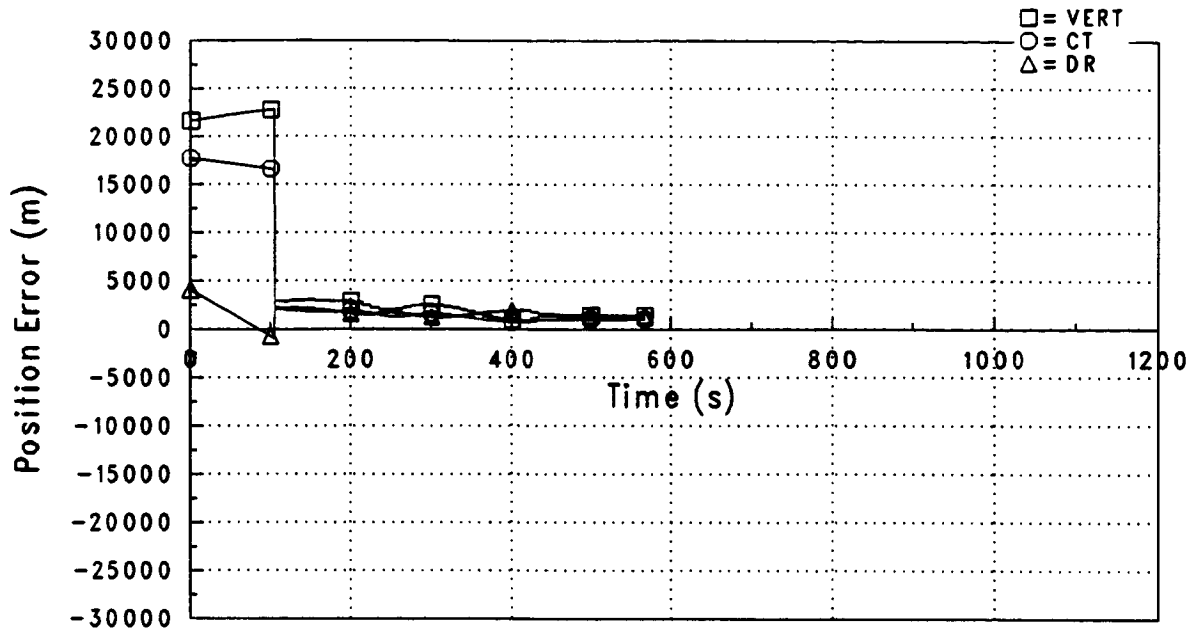


Figure 5-78. Case # 031500D: Position Estimate Errors

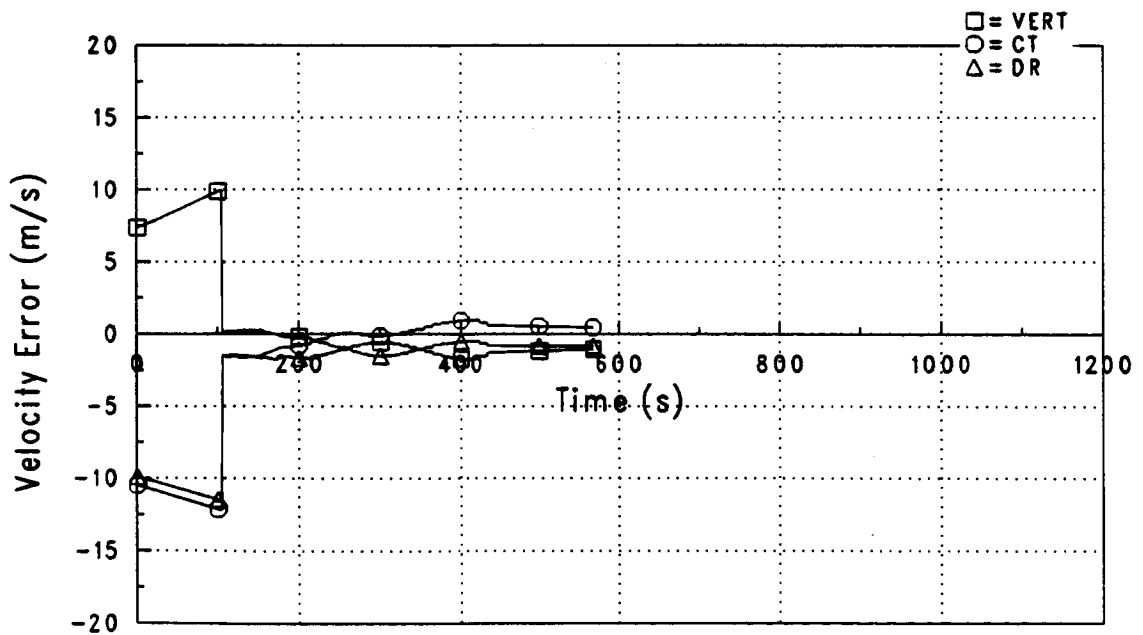


Figure 5-79. Case # 031500D: Velocity Estimate Errors

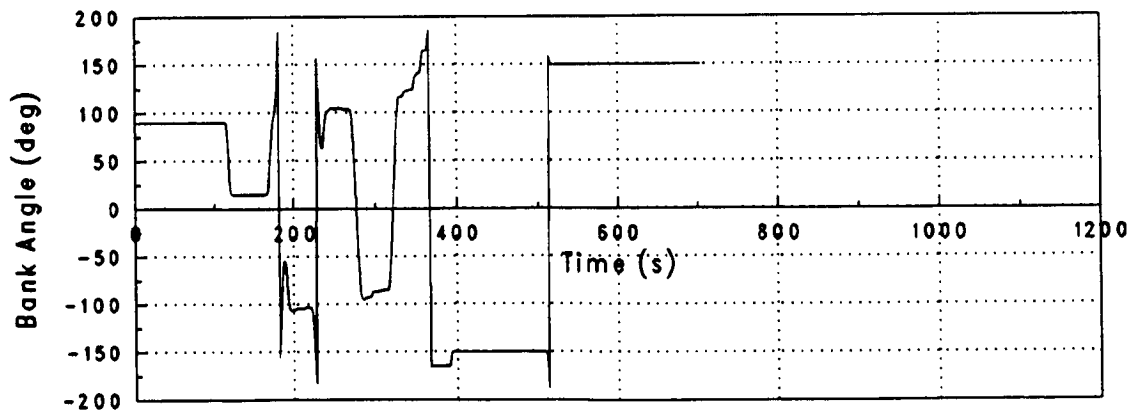
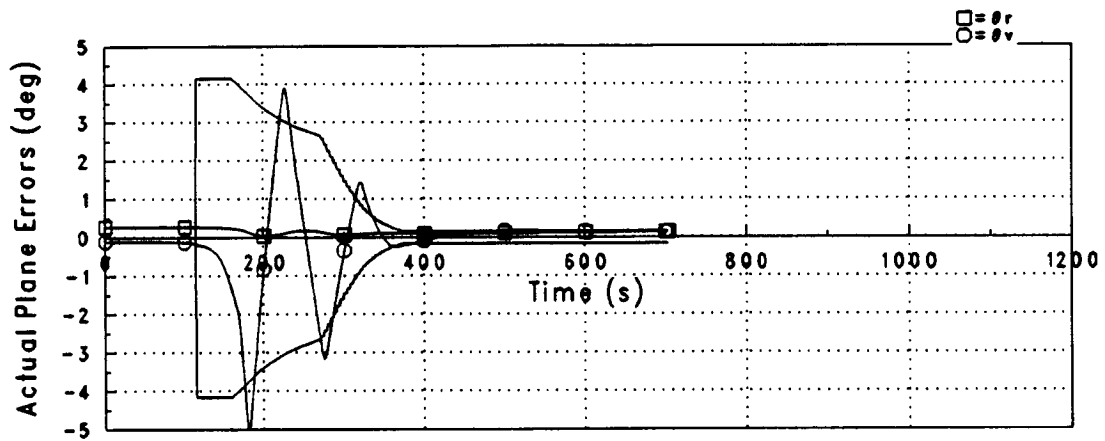
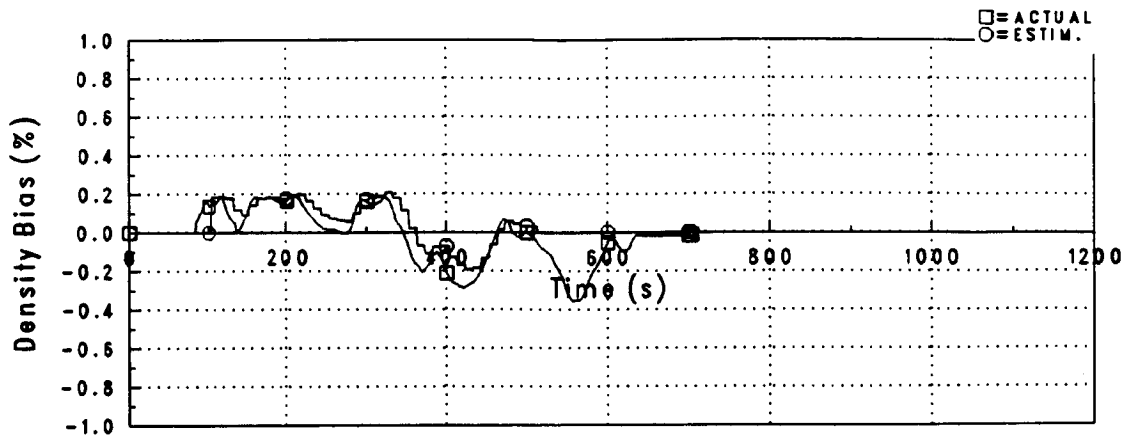


Figure 5-80. Case # 035000D: Bank Angle Control Response

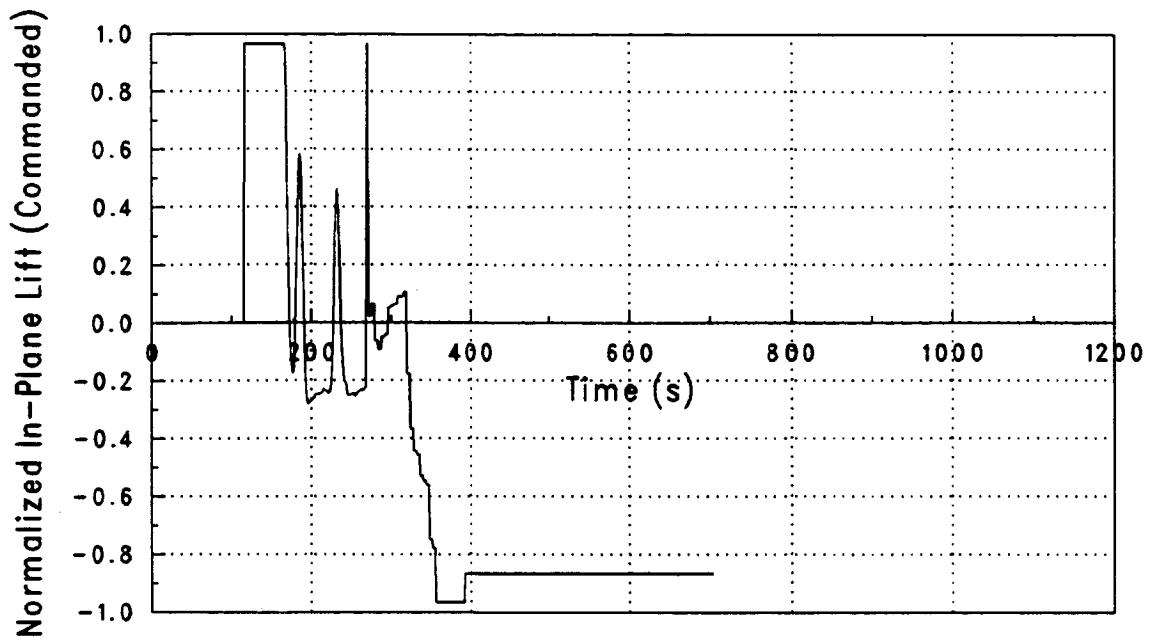


Figure 5-81. Case # 035000D: Normalized In-Plane Lift

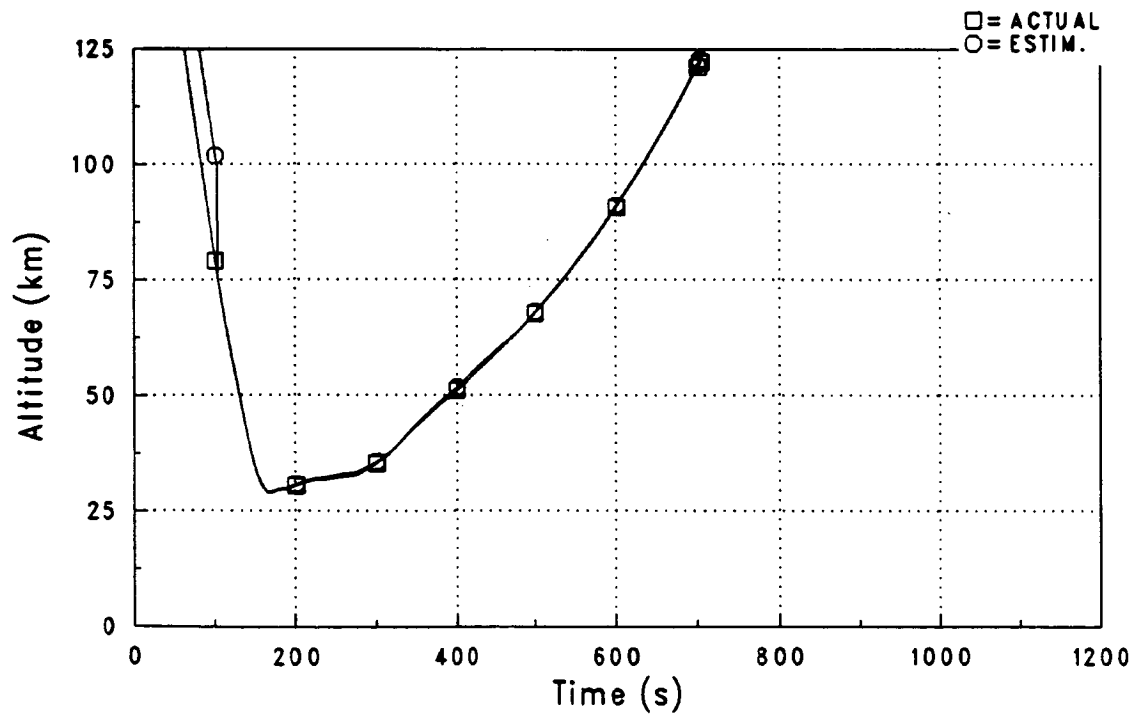


Figure 5-82. Case # 035000D: Altitude History

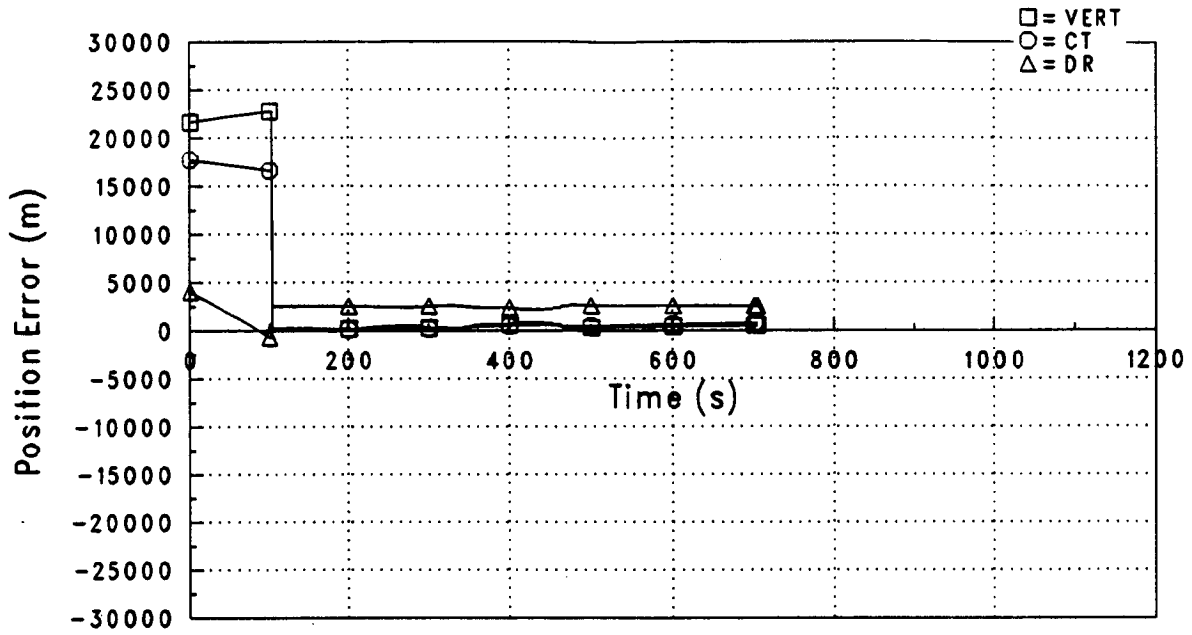


Figure 5-83. Case # 035000D: Position Estimate Errors

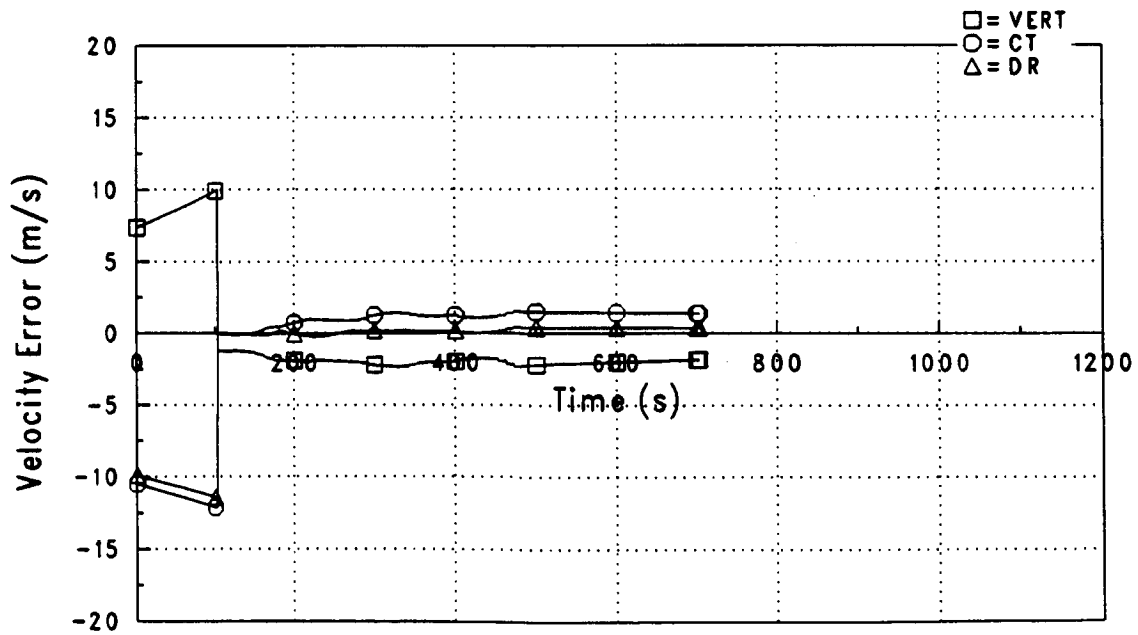


Figure 5-84. Case # 035000D: Velocity Estimate Errors

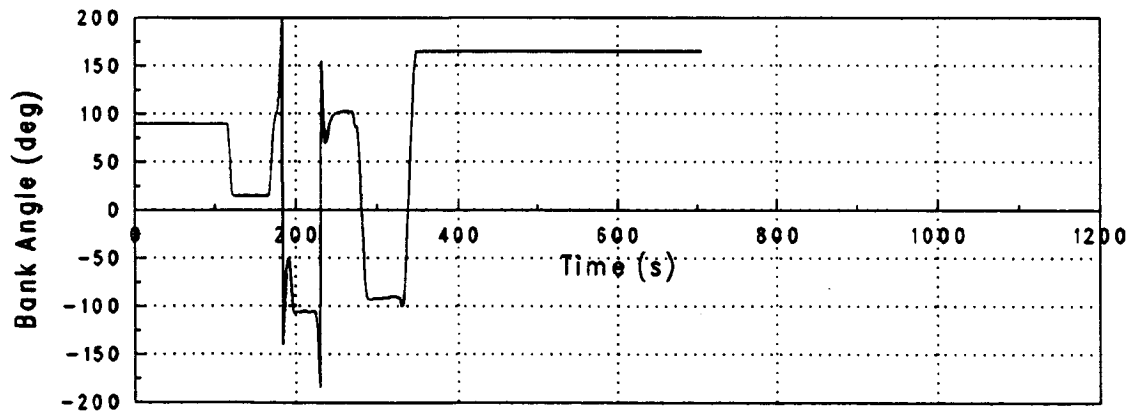
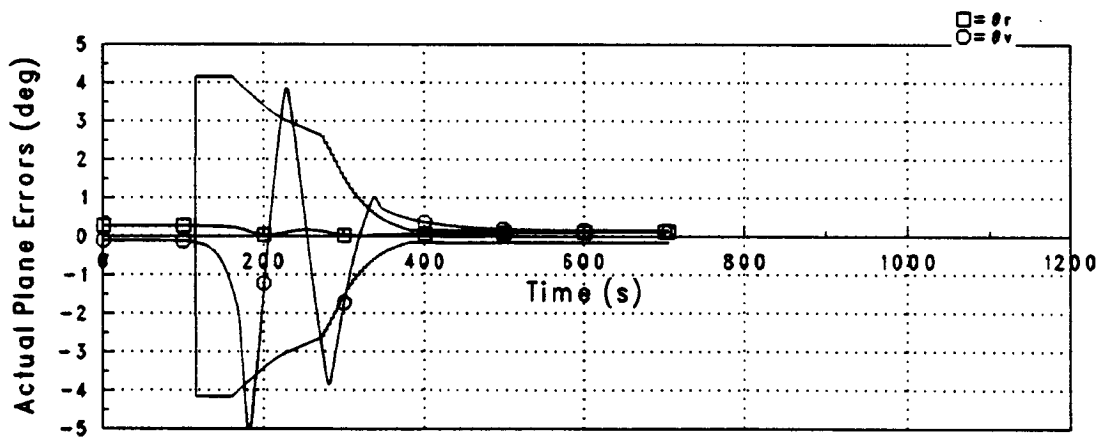
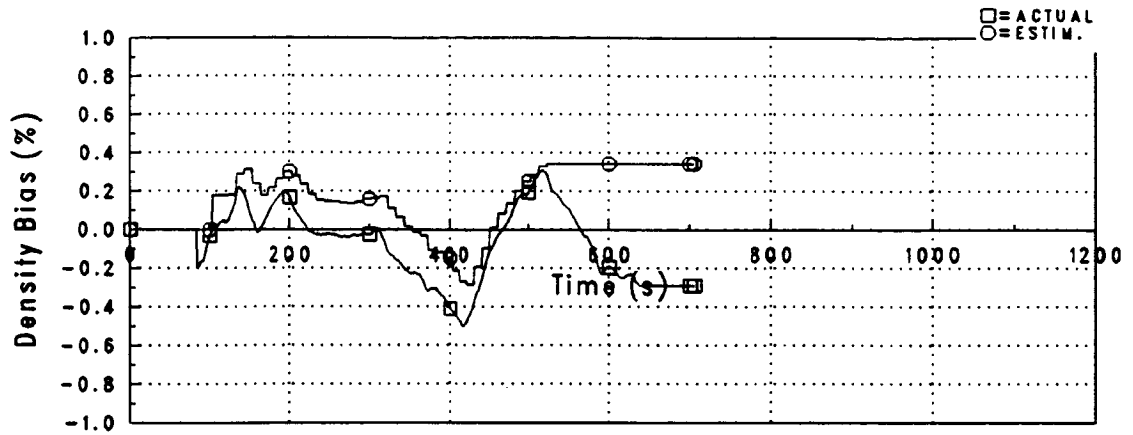


Figure 5-85. Case # 038500D: Bank Angle Control Response

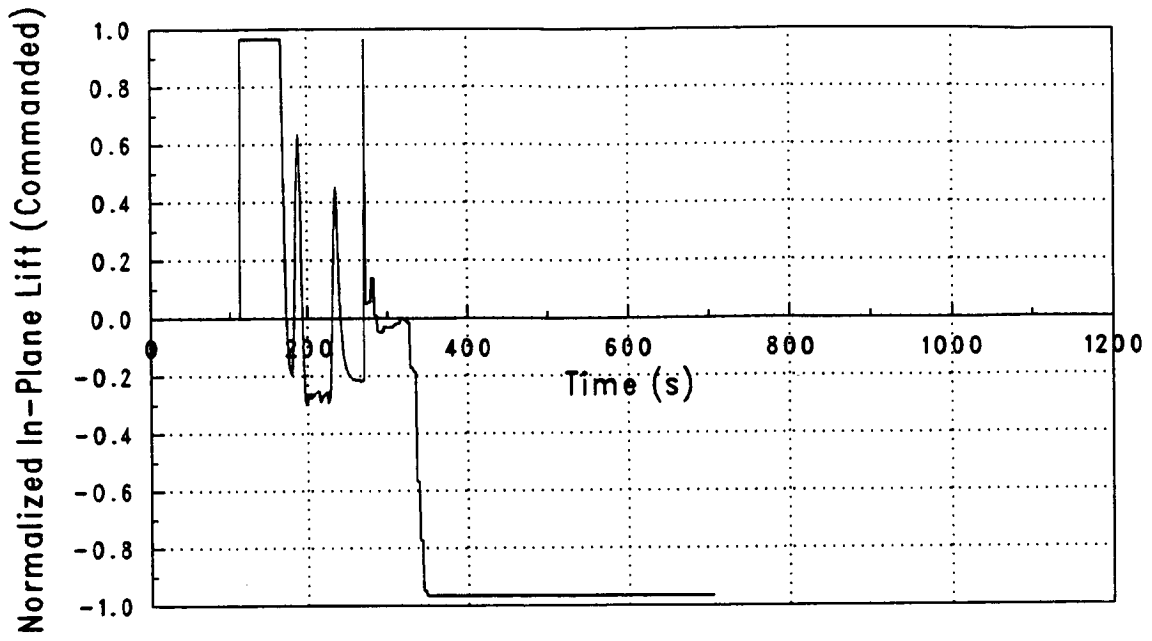


Figure 5-86. Case # 038500D: Normalized In-Plane Lift

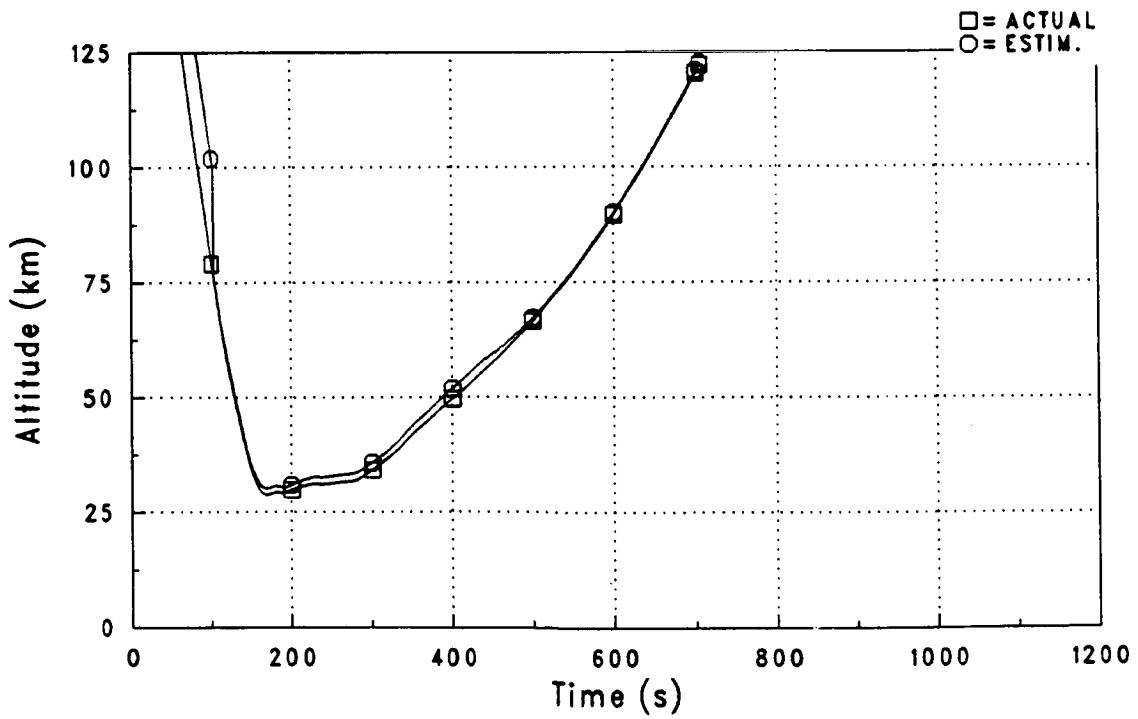


Figure 5-87. Case # 038500D: Altitude History

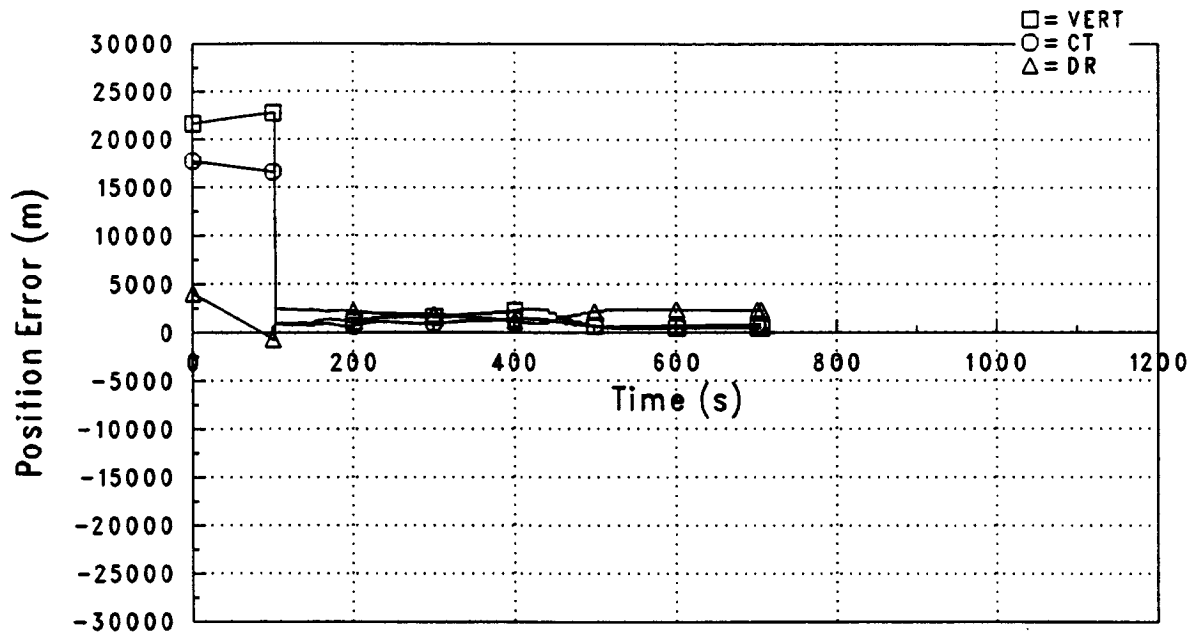


Figure 5-88. Case # 038500D: Position Estimate Errors

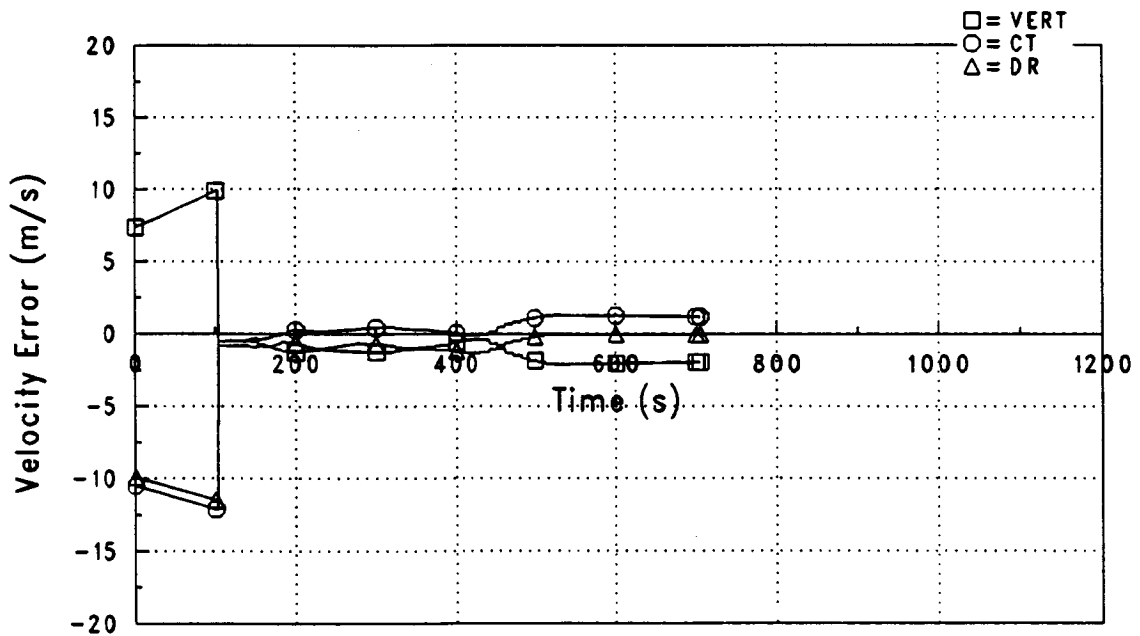


Figure 5-89. Case # 038500D: Velocity Estimate Errors

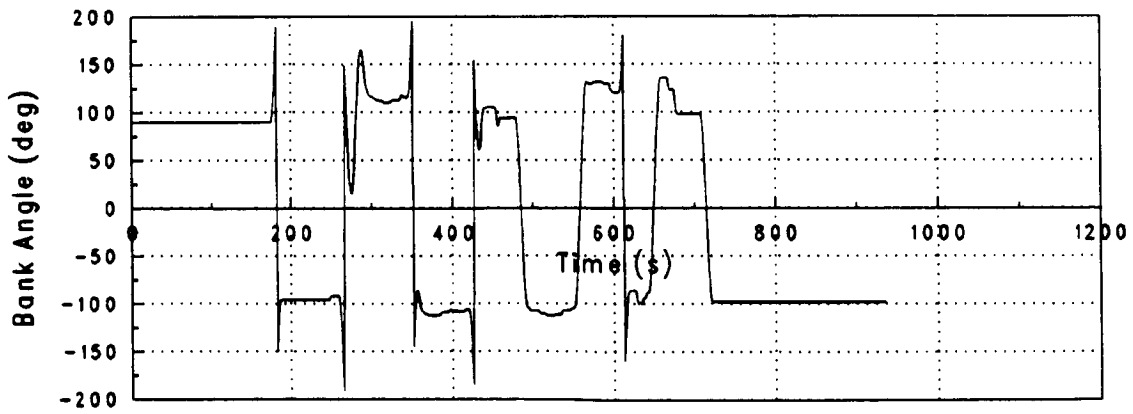
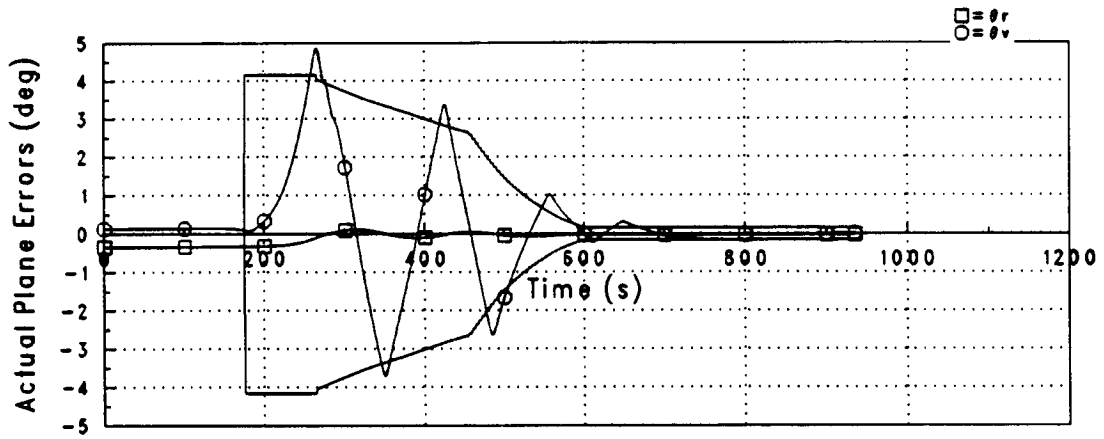
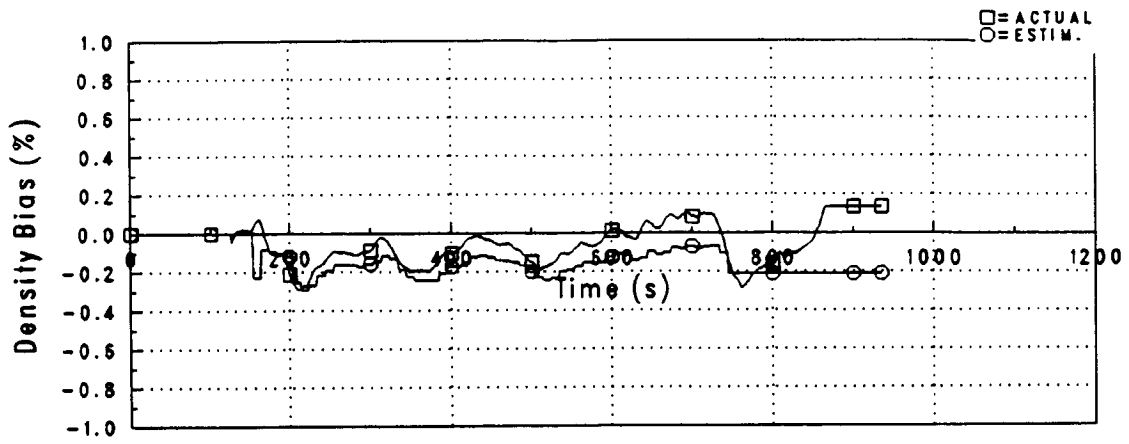


Figure 5-90. Case # 280500D: Bank Angle Control Response

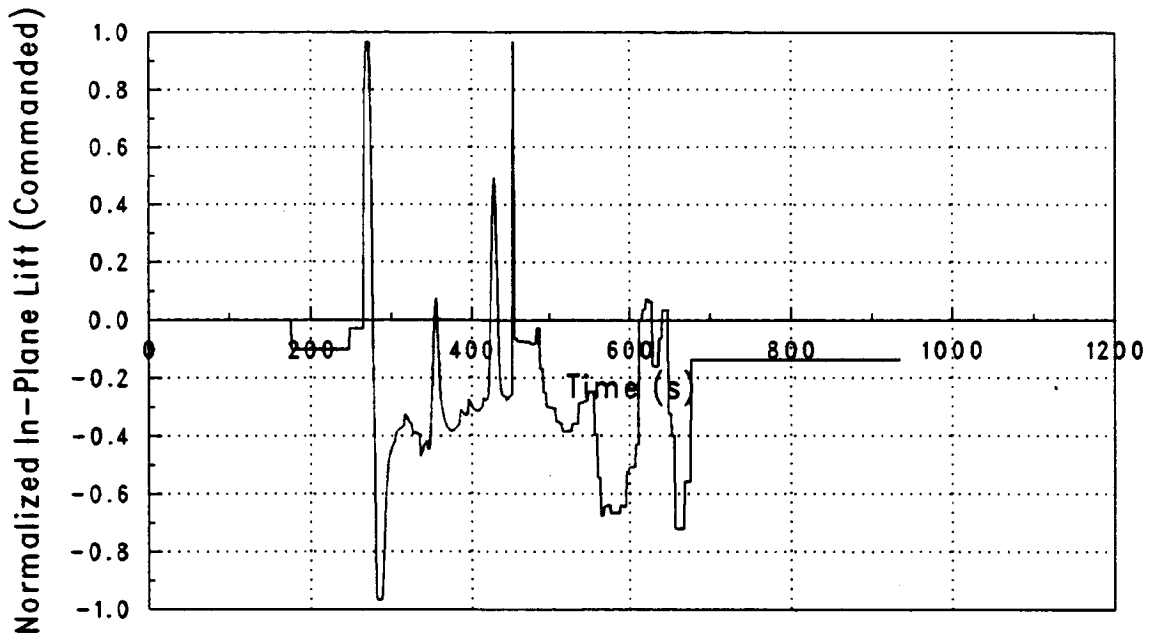


Figure 5-91. Case # 280500D: Normalized In-Plane Lift

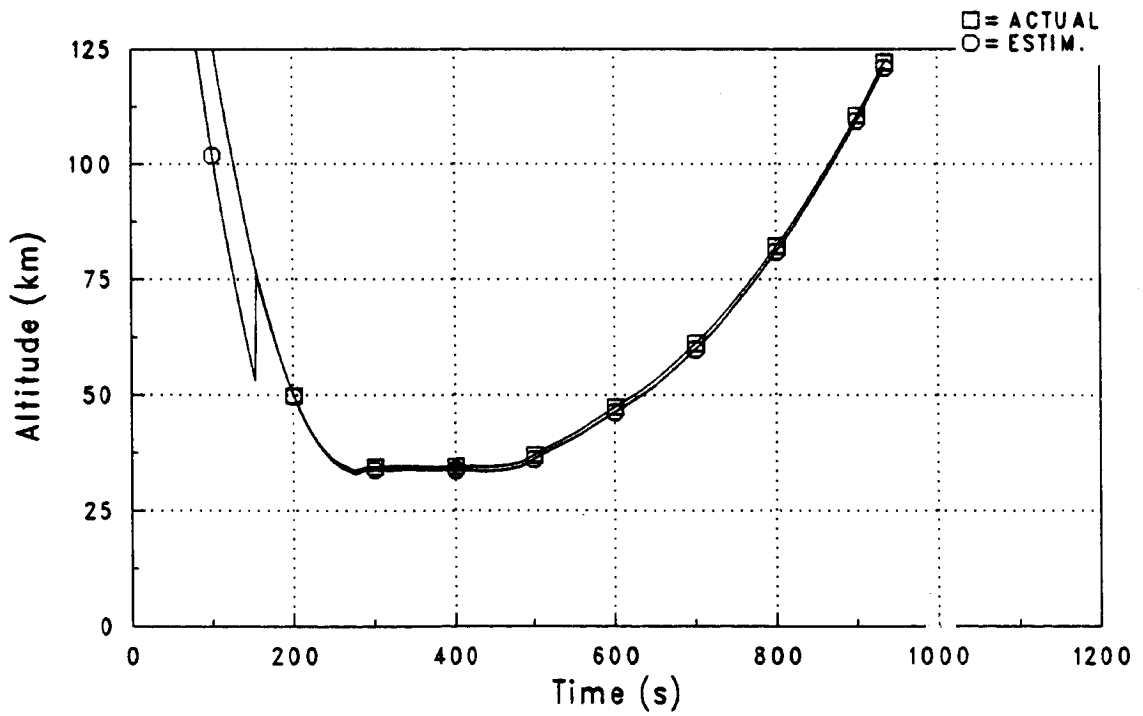


Figure 5-92. Case # 280500D: Altitude History

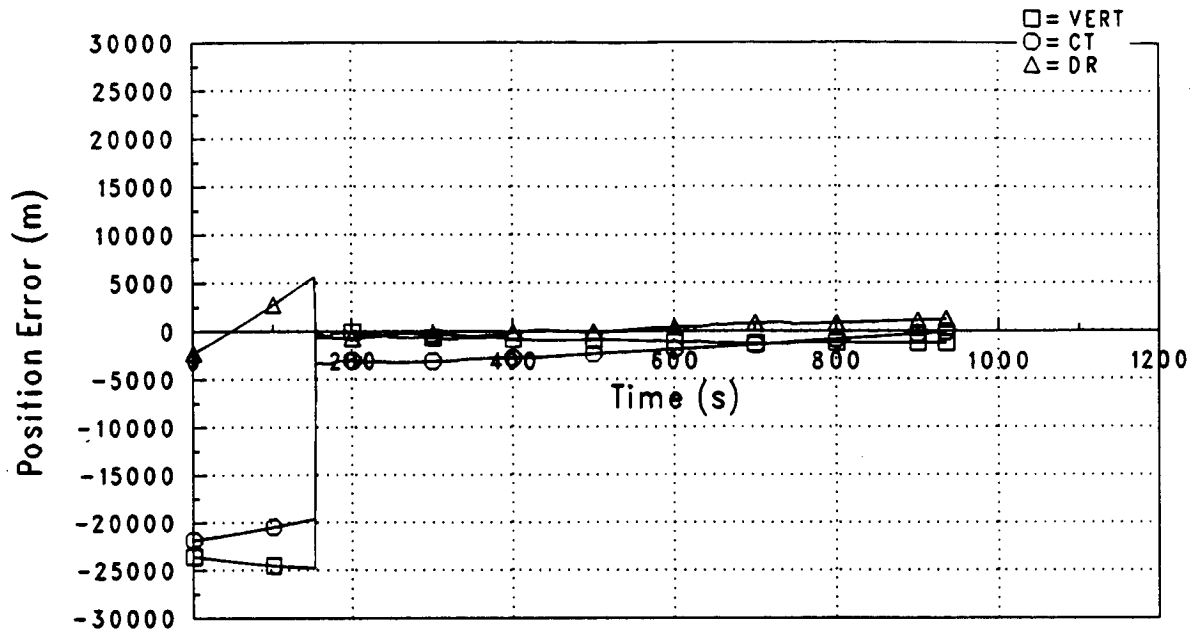


Figure 5-93. Case # 280500D: Position Estimate Errors

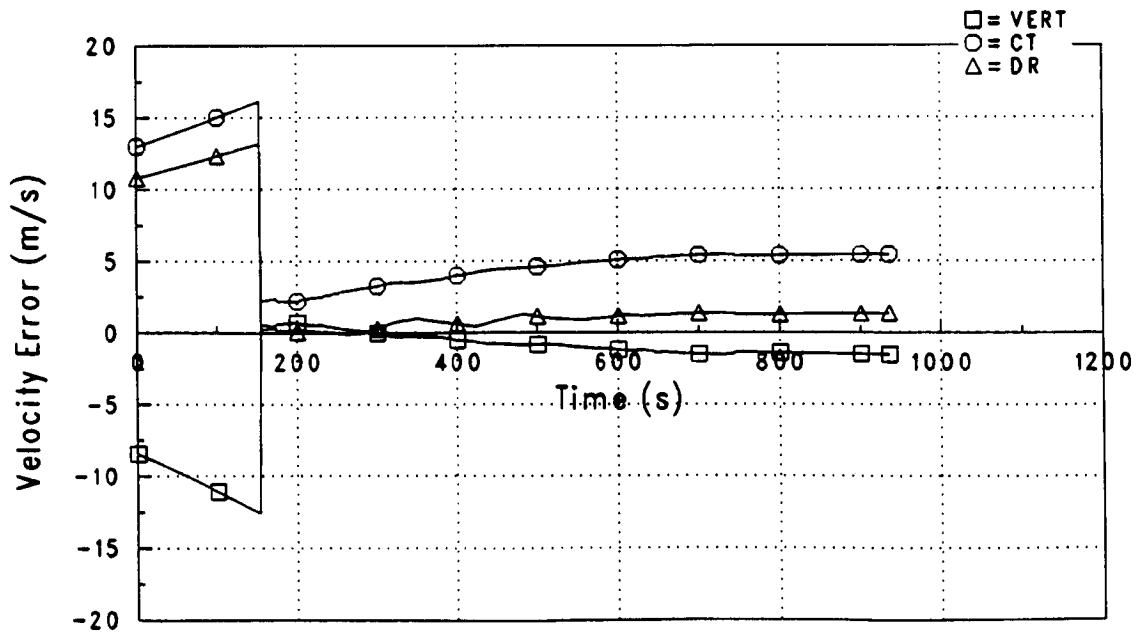


Figure 5-94. Case # 280500D: Velocity Estimate Errors

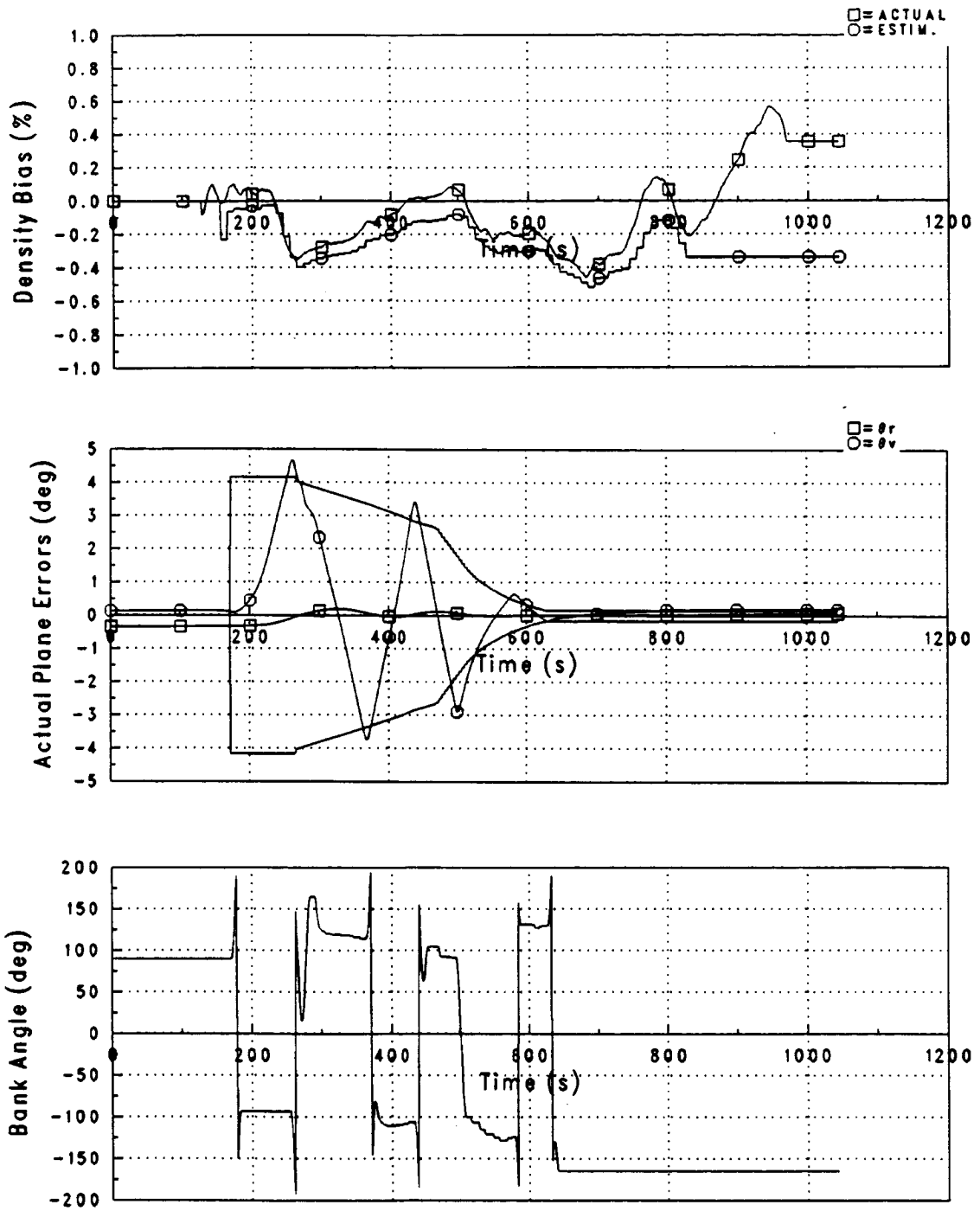


Figure 5-95. Case # 281000D: Bank Angle Control Response

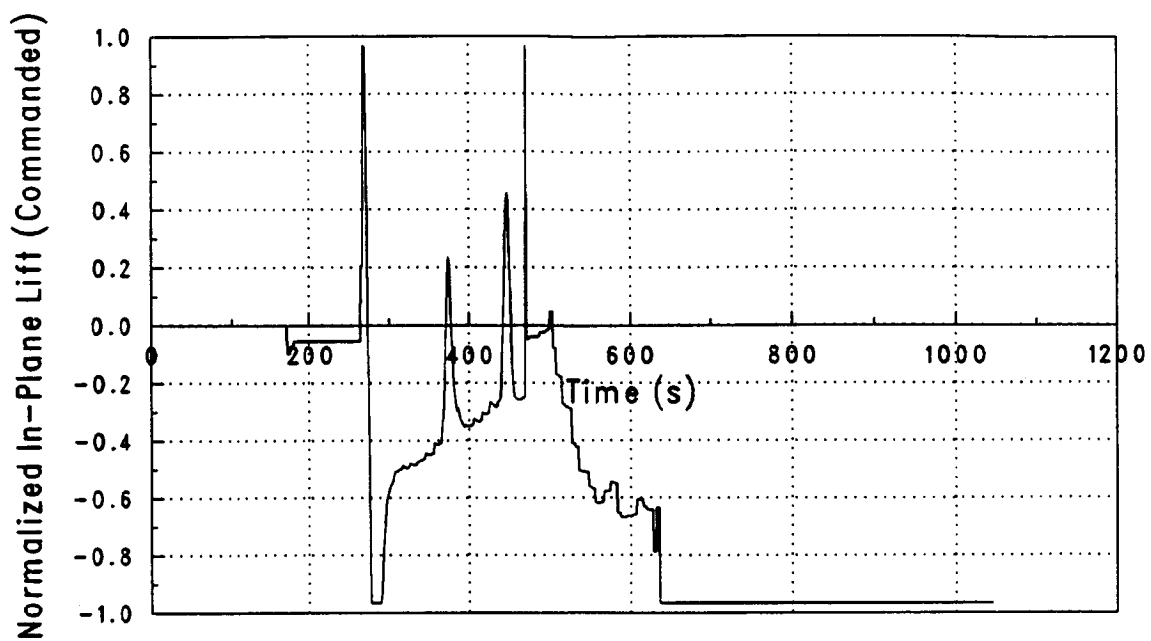


Figure 5-96. Case # 281000D: Normalized In-Plane Lift

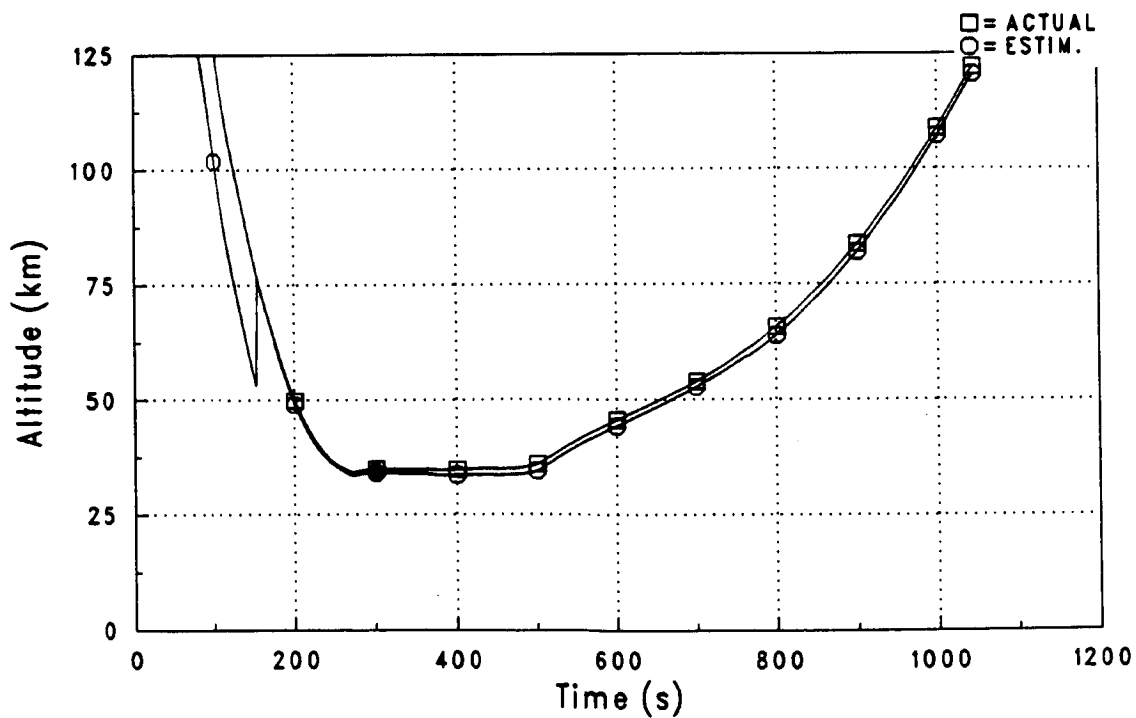


Figure 5-97. Case # 281000D: Altitude History

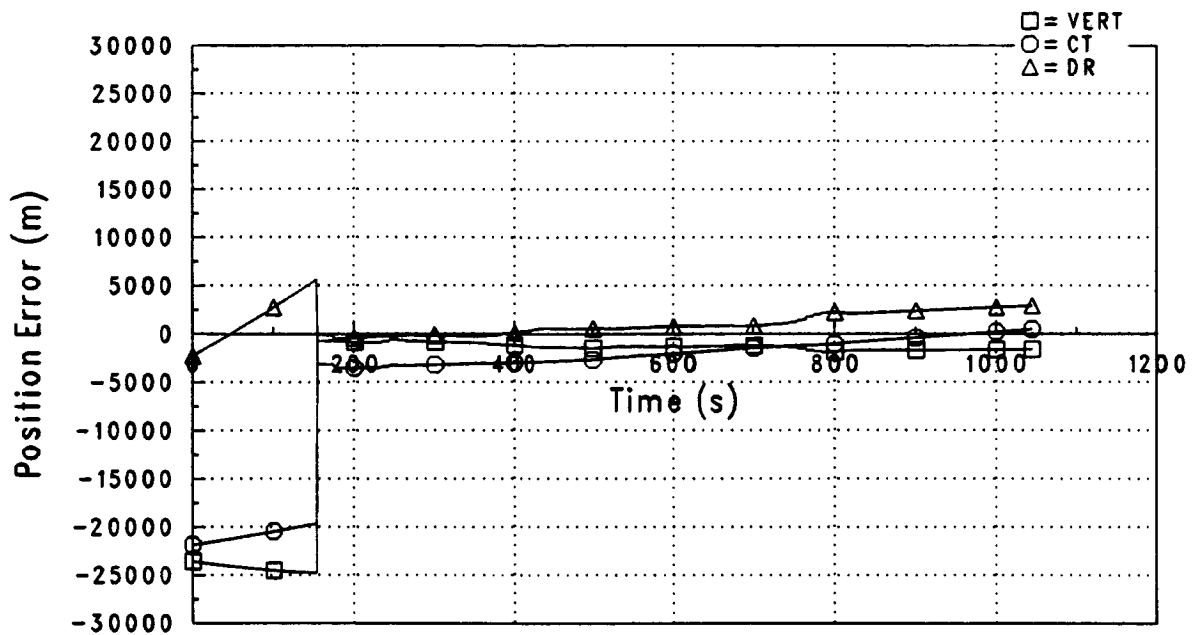


Figure 5-98. Case # 281000D: Position Estimate Errors

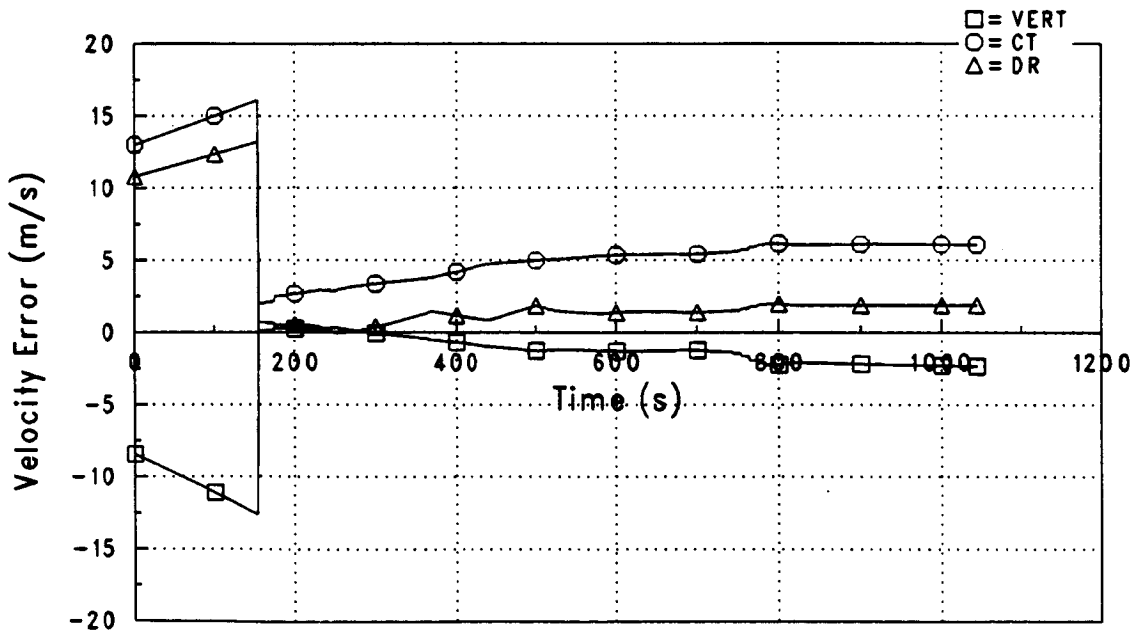


Figure 5-99. Case # 281000D: Velocity Estimate Errors

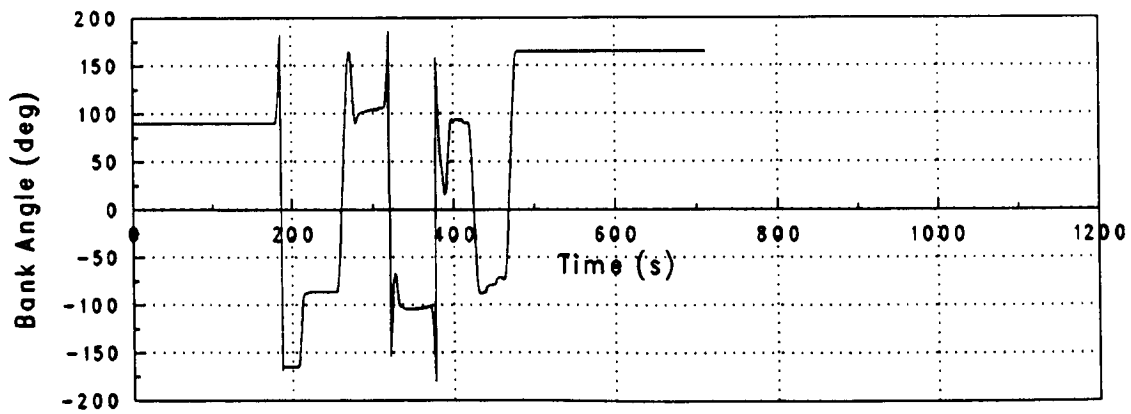
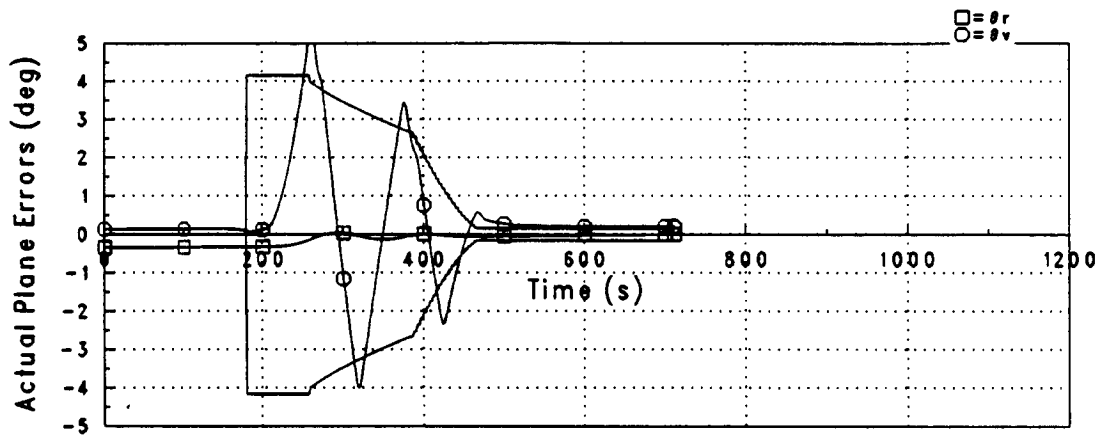
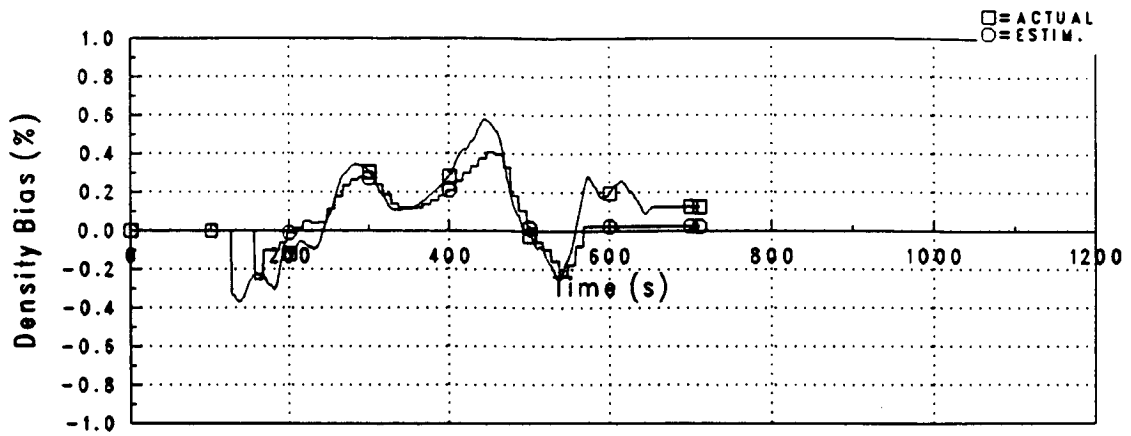


Figure 5-100. Case # 281500D: Bank Angle Control Response

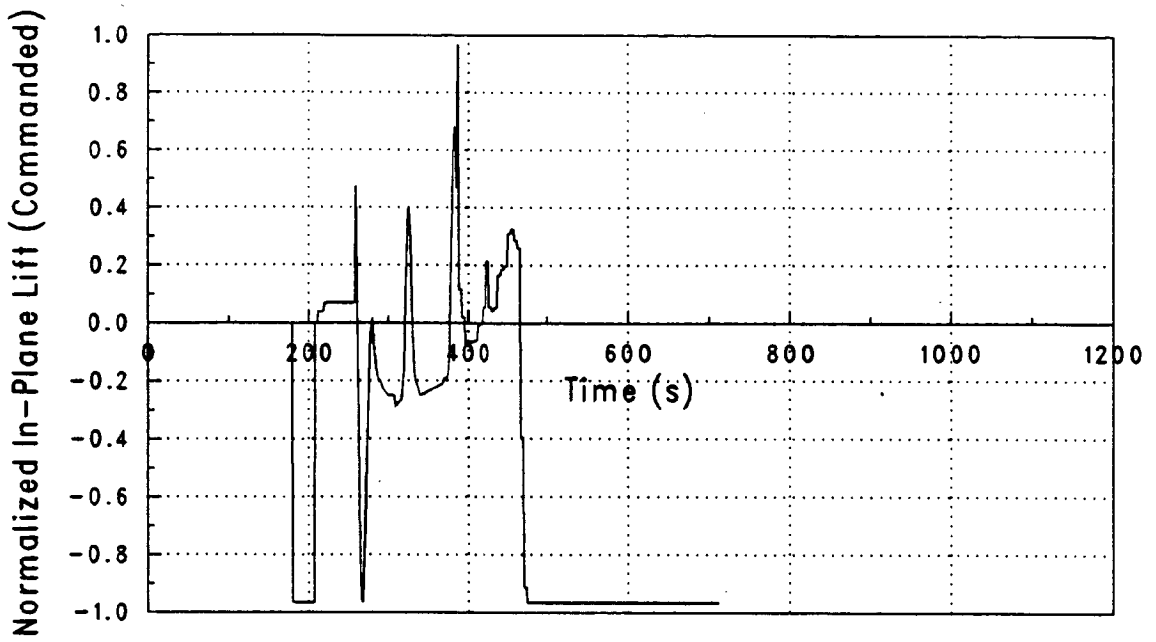


Figure 5-101. Case # 281500D: Normalized In-Plane Lift

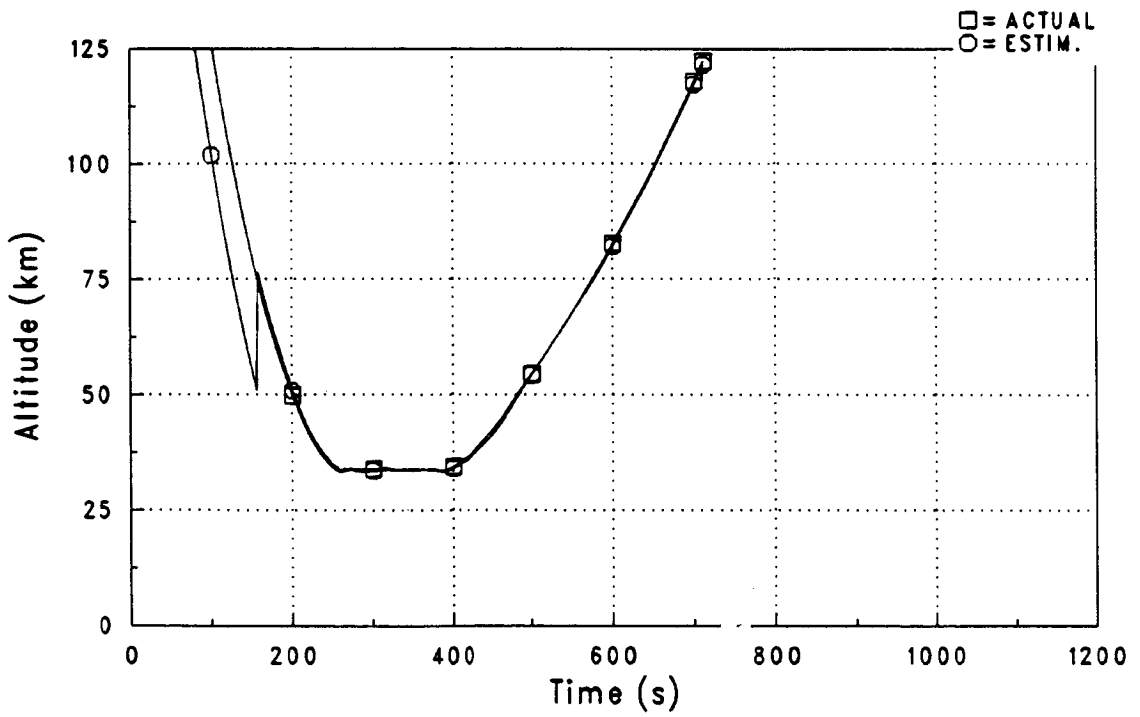


Figure 5-102. Case # 281500D: Altitude History

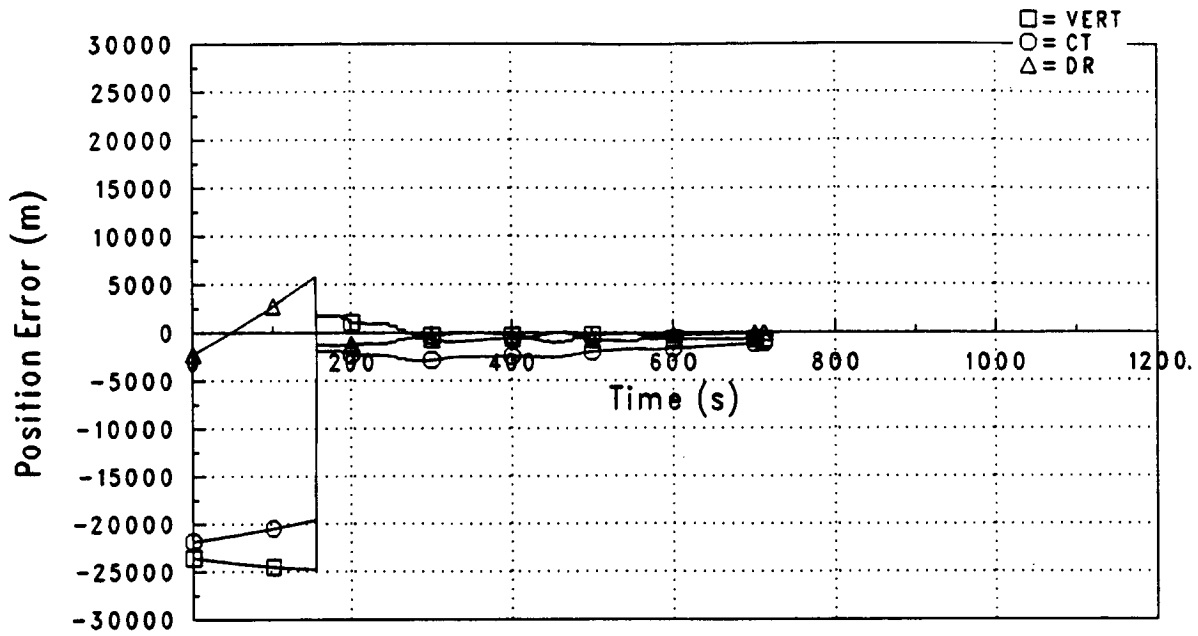


Figure 5-103. Case # 281500D: Position Estimate Errors

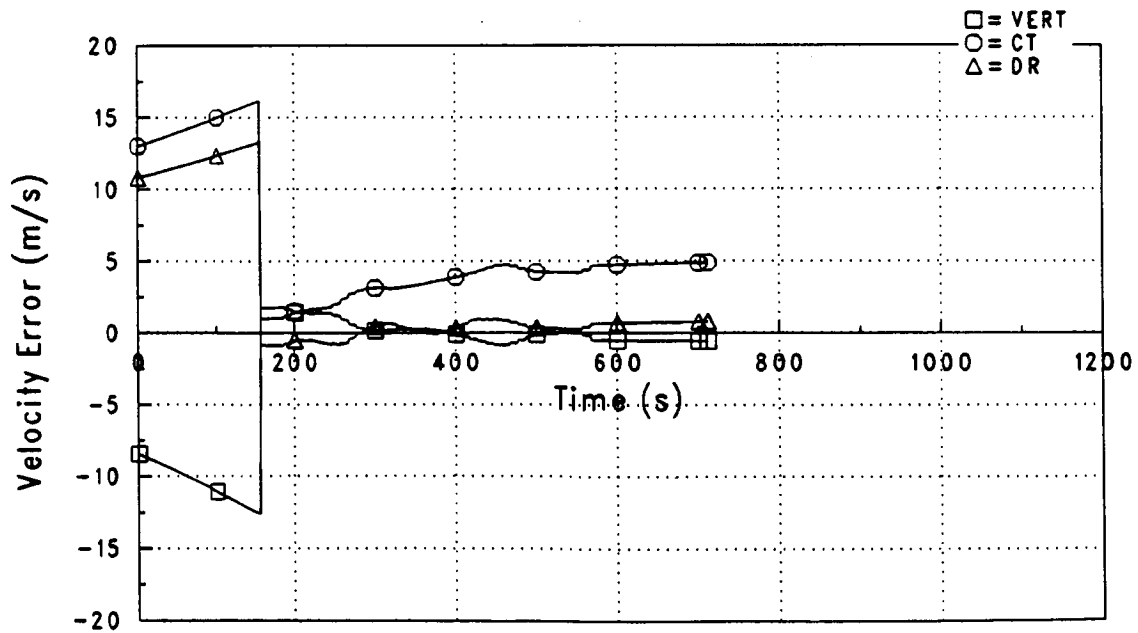


Figure 5-104. Case # 281500D: Velocity Estimate Errors

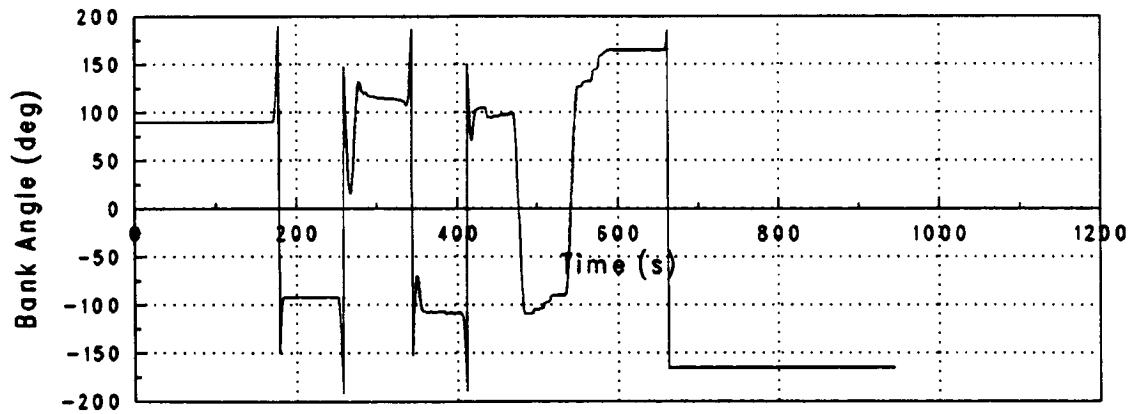
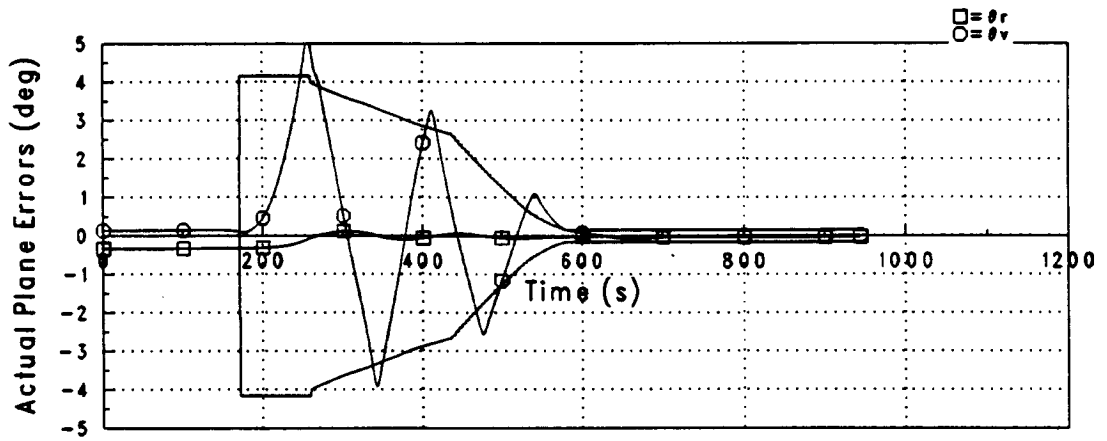
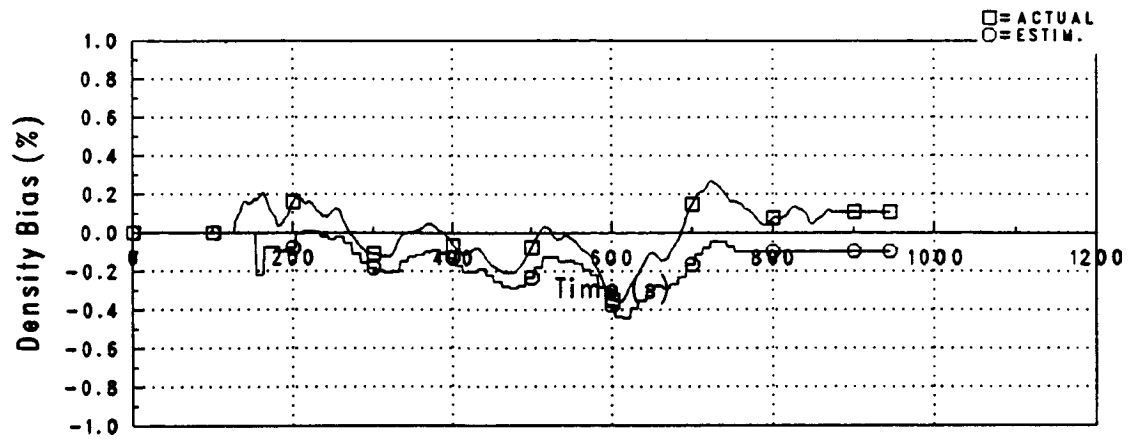


Figure 5-105. Case # 285000D: Bank Angle Control Response

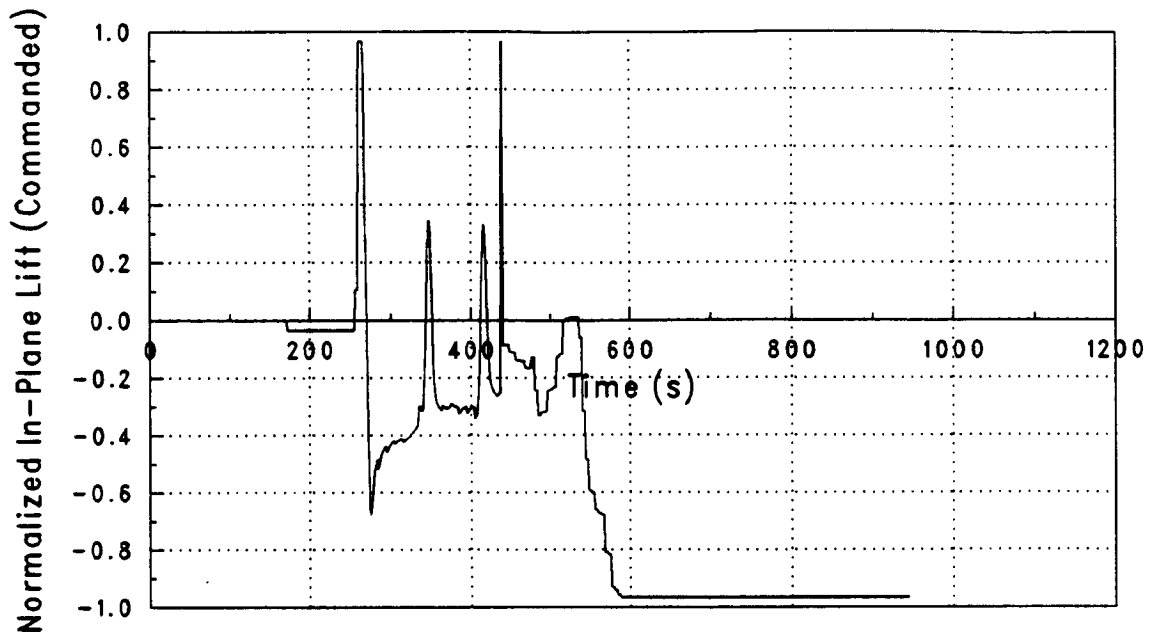


Figure 5-106. Case # 285000D: Normalized In-Plane Lift

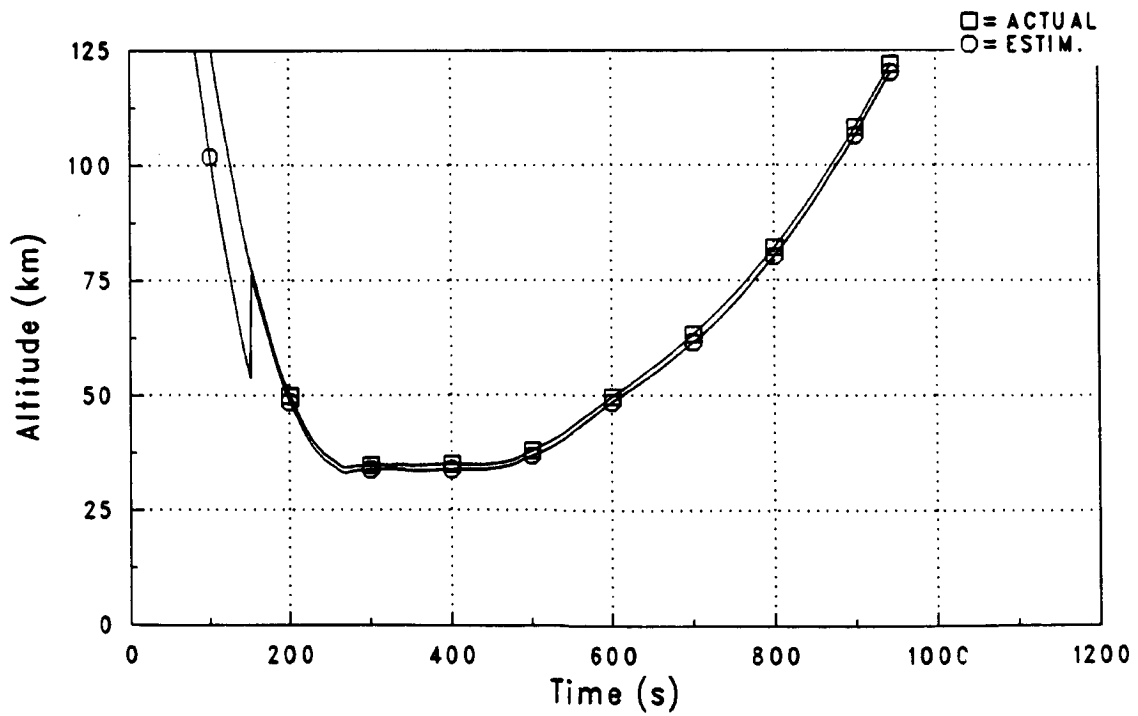


Figure 5-107. Case # 285000D: Altitude History

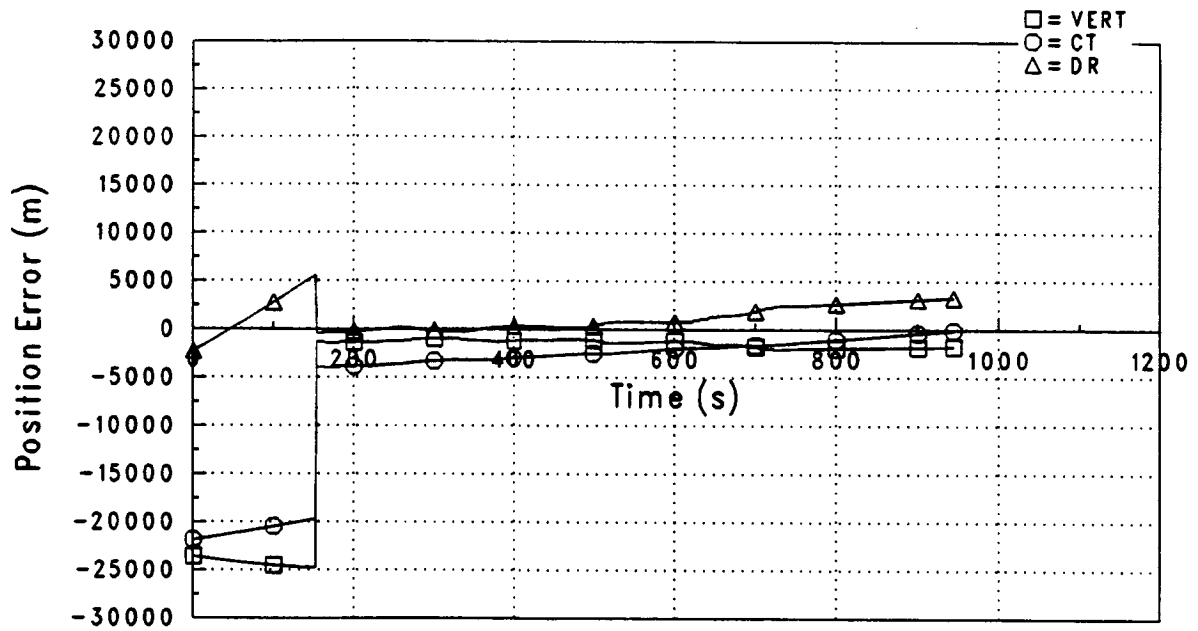


Figure 5-108. Case # 285000D: Position Estimate Errors

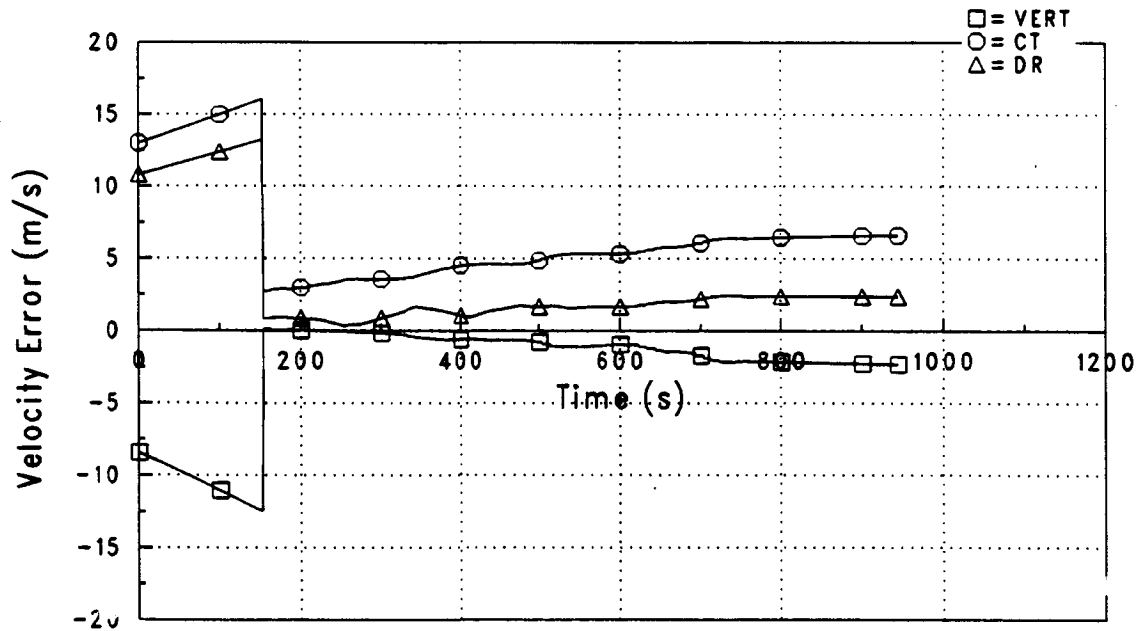


Figure 5-109. Case # 285000D: Velocity Estimate Errors

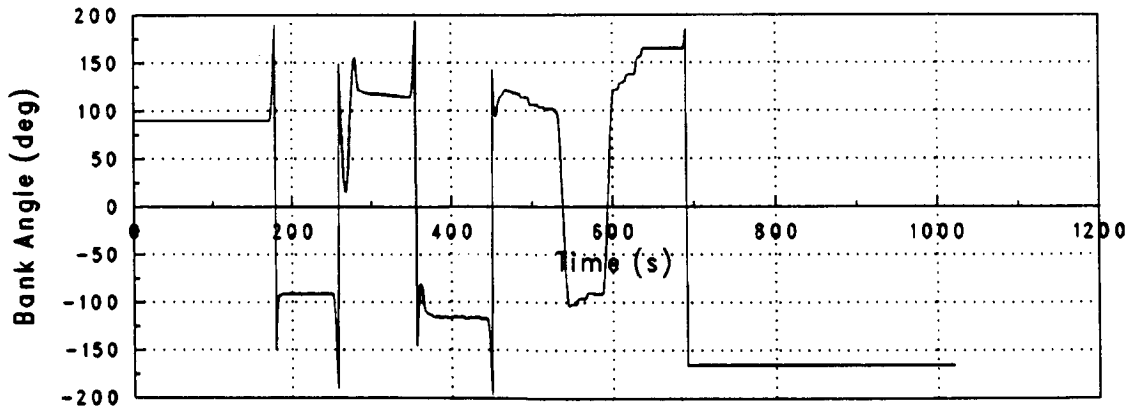
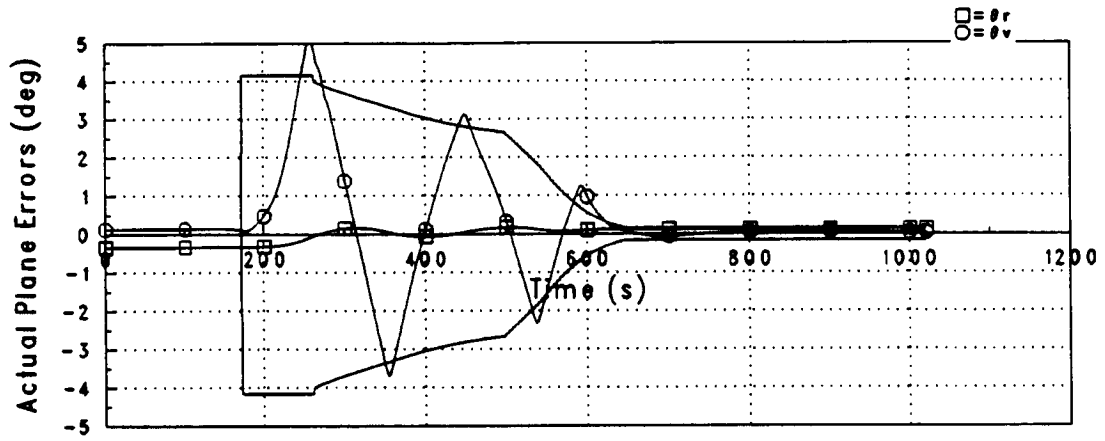
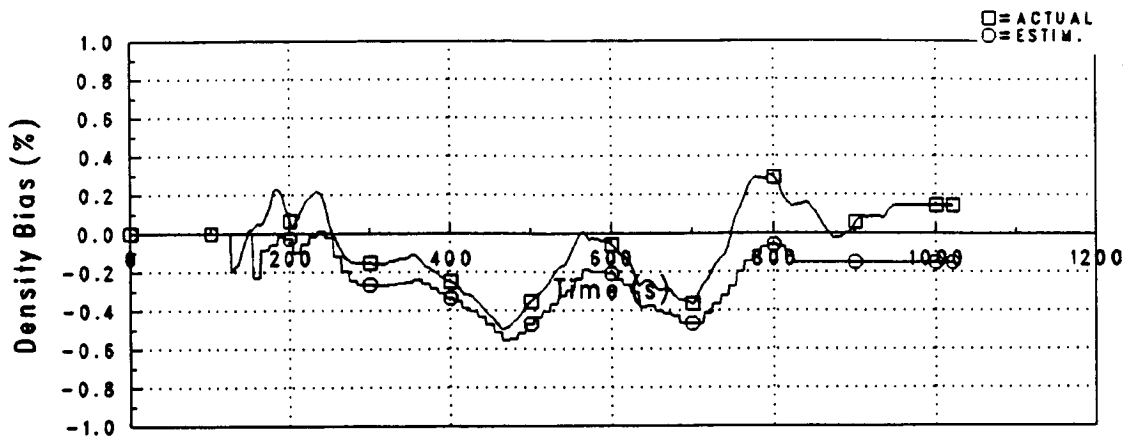


Figure 5-110. Case # 288500D: Bank Angle Control Response

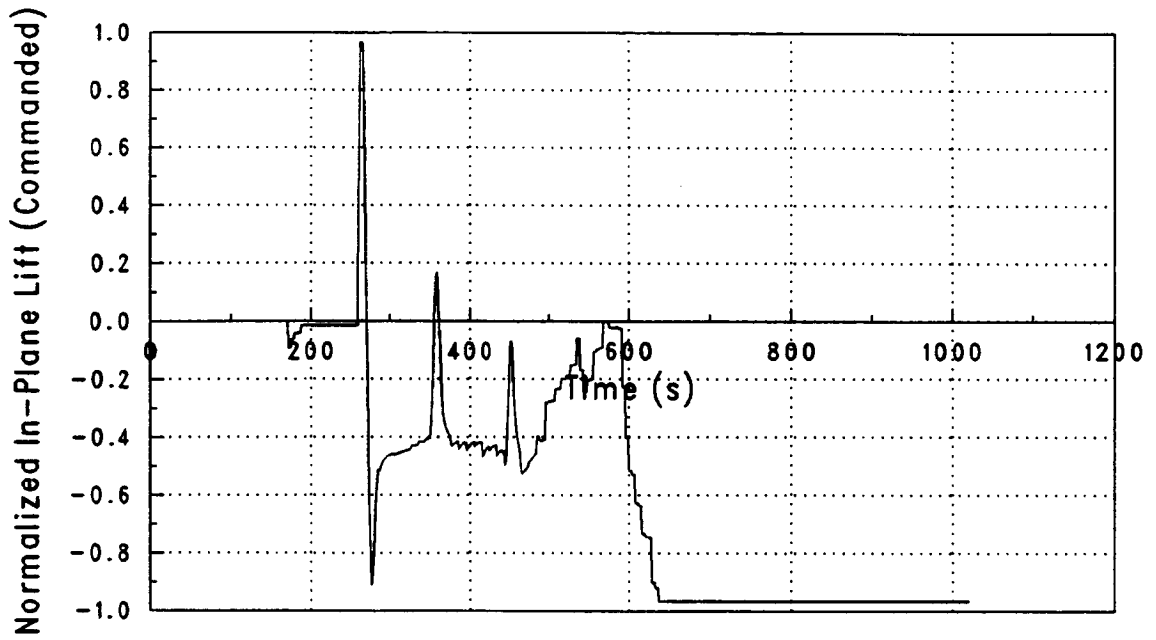


Figure 5-111. Case # 288500D: Normalized In-Plane Lift

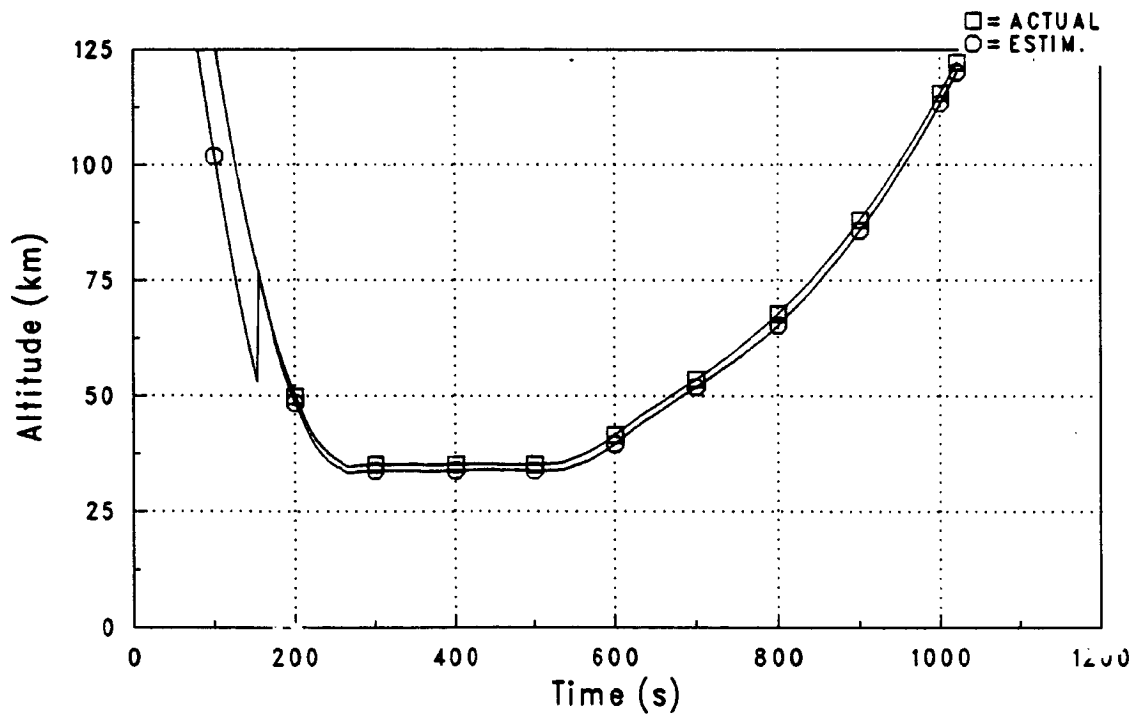


Figure 5-112. Case # 288500D: Altitude History

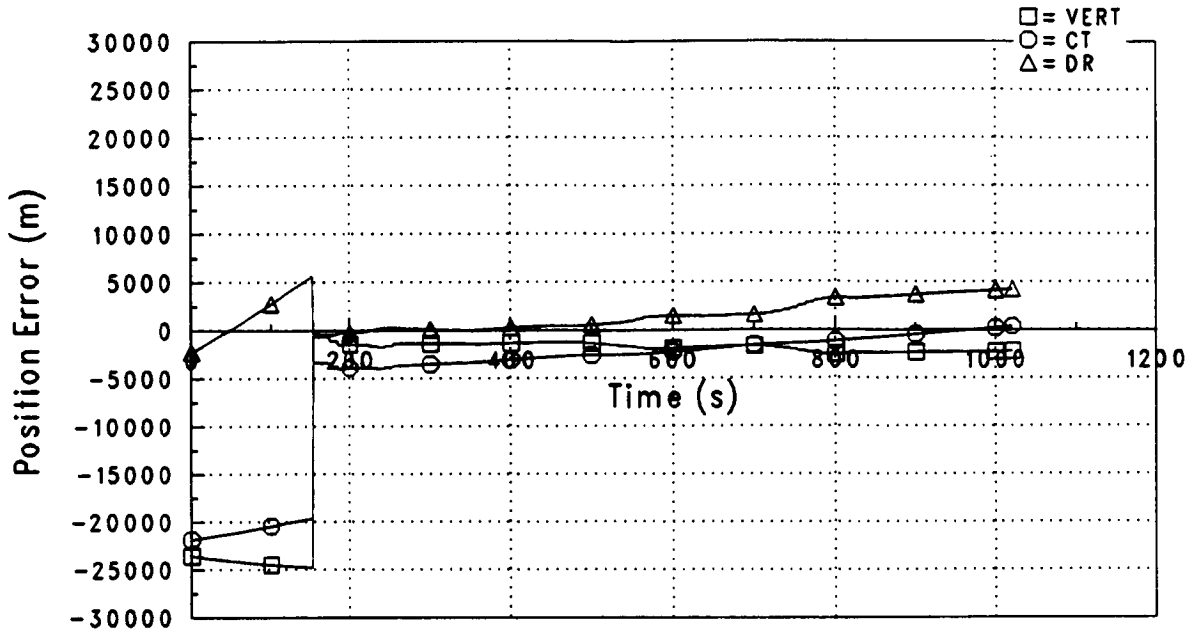


Figure 5-113. Case # 288500D: Position Estimate Errors

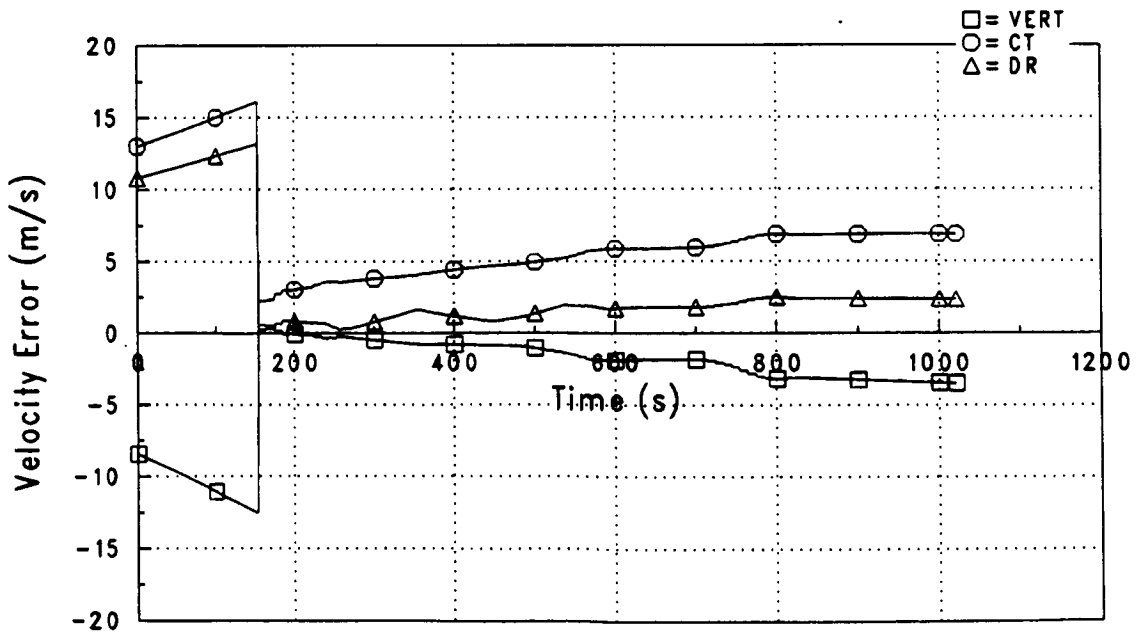


Figure 5-114. Case # 288500D: Velocity Estimate Errors

## CHAPTER 6

### CONCLUSION

The goal of this thesis has been to present the results of a design study of navigation and guidance of an interplanetary transfer vehicle during aerocapture into orbit about Mars. The navigation system presented utilizes a Kalman filter for estimation of vehicle position and velocity components and atmospheric density bias using density altitude information extracted from inertial measurement unit specific force measurements. The addition of radar altimeter measurements was studied in an attempt to allow the filter to better distinguish between altitude estimation errors and density errors. The aerocapture guidance algorithm steers the vehicle to a constant-altitude trajectory for energy dissipation and utilizes bank reversals for control of orbit plane orientation. For guidance purposes, the aerocapture trajectory is divided into three phases: capture, constant-altitude cruise, and exit. The capture and exit phases utilize numerical predictor/corrector guidance to compute constant bank angle commands required to hit specified targets. The constant-altitude cruise guidance utilizes an analytic control law to compute bank commands to null altitude rates induced by dispersions and maintain flight at the desired altitude. Selected test case results have been presented to provide insight into the functioning of the guidance and navigation systems and illustrate their performance.

Navigation results indicate that improvement of pre-aerocapture altitude estimation accuracy is possible using density altitude "measurements" constructed from the specific force measured by the IMU. The difficulty with this measurement is that altitude errors and density errors are indistinguishable; that is, a given measurement residual could be the result of an altitude estimate error, an error between the actual atmospheric density and that predicted by the filter model, or any one of a multitude of combinations of both. However, the altitude error resulting from a  $3\sigma$  density error of +100% was seen to be limited to -5300 m at an estimated measurement altitude of 75 km, so that significant improvements in approach altitude errors ( $1\sigma = 28000$  m) are still possible

even with worst-case density errors. In addition, the nature of the measurement and the mechanics of the Kalman filter allow near perfect estimation of the atmospheric density (which is used directly by the guidance to compute aerodynamic control capability) despite possibly large errors in the estimates of altitude and density bias.

Improved altitude estimate accuracy was seen with the inclusion of radar altimeter measurements prior to density altitude updates; however, the relative improvement will decrease with decreasing radar altimeter measurement accuracy. The inclusion of radar altimeter measurements also allowed the subsequent density altitude measurement residuals to be attributed almost entirely to density bias, allowing more accurate estimation and tracking of this quantity. Future studies should examine possible radar altimeter flight hardware and Mars surface terrain height accuracy knowledge in more detail in an effort to determine actual measurement accuracy levels which might be possible and the potential usefulness of these measurements for filter state vector estimate accuracy improvement.

Although the only measurement information incorporated was in the vertical position channel, improvement in the accuracy of crosstrack and downrange position along with all three components of velocity is possible using the correlations between these components and vertical position which exist due to planetary approach navigation. For the entry state error levels used in this study, it was seen that position and velocity estimate accuracy levels attained without the inclusion of these correlations were insufficient and resulted in large guidance target misses.

Combined navigation and guidance performance was examined for cases with constant and variable atmospheric density bias profiles and large entry position and velocity dispersions. Overall performance of the guidance system (in terms of  $\Delta V$  requirements for orbit correction after atmospheric exit) was found to be good, with penalties ranging from 3.7 m/s to 36.4 m/s over the ideally achievable minimum. The main problem seen in the guidance is sensitivity to dispersions

during the exit phase. Unpredictable density shears during exit can overwhelm decreasing aerodynamic control capability, and bank reversals can reduce control margin and even perturb the exit trajectory beyond the possibility of aerodynamic correction. Dispersions during the capture and constant-altitude cruise phases have very little impact on the accuracy of the final post-aerocapture orbit due to the uniformity and isolation provided by the constant-altitude phase. Cruise altitude target misses caused by density shears during the capture phase are compensated for by the cruise phase guidance, and the effects of perturbations induced by bank reversals and density shears during cruise are immediately sensed and compensated for by the guidance. The true cruise altitude was seen to be offset from the nominal due to altitude estimation errors, but this should not be critical unless the error is large enough to place the vehicle outside of the aerocapture altitude corridor. Future guidance studies should carefully examine the interactions between plane control and energy control since inopportune bank reversals can so greatly impact orbit correction fuel requirements. Possible suggestions include modelling of bank reversal effects in the current exit phase guidance trajectory prediction to allow compensating bank commands to be issued before execution of the reversal or development of a guidance algorithm which completely integrates the energy and plane control functions during aerocapture.

## APPENDIX A

### DERIVATION OF DENSITY ALTITUDE MEASUREMENT EQUATIONS

The drag acceleration is defined as

$$a_d = \frac{1}{2} \rho_{env} \frac{v_{rel}^2}{C_B} \quad (A-1)$$

where  $\rho_{env}$  is the current atmospheric density. Thus, given the measured drag acceleration of equation (2-40), we have an indirect measurement of the true density given by

$$\rho_{env} = \frac{2 C_B}{\hat{v}_{rel}^2} a_{d_m} \quad (A-2)$$

The density altitude,  $h_\rho$ , given the onboard exponential density model in equation (2-37), can be found by solution of

$$\rho_{env} = \rho_0 e^{-\frac{(h_\rho - h_0)}{HS}} \quad (A-3)$$

Equating (A-2) and (A-3) and solving gives the following expression for the "measured" density altitude:

$$h_{h_\rho} = h_0 + HS \ln \left[ \frac{\rho_0 \hat{v}_{rel}^2}{2 C_B a_{d_m}} \right] \quad (A-4)$$

The current estimate of the atmospheric density can be computed as

$$\hat{\rho} = (1 + \hat{K}_\rho) \rho_0 e^{-\frac{(\hat{h} - h_0)}{HS}} \quad (A-5)$$

PRECEDING PAGE BLANK NOT FILMED

using equations (2-17) and (2-37) . This estimate is written in terms of the current geometric altitude estimate. In terms of density altitude, the estimated density is

$$\hat{\rho} = \rho_0 e^{-(\hat{h}_\rho - h_0)/HS} \quad (A-6)$$

Equating (A-5) and (A-6) and solving gives the following expression for the estimate of the density altitude measurement:

$$\hat{q}_{h_\rho} = \hat{h} - HS \ln(1 + \hat{K}_\rho) \quad (A-7)$$

## APPENDIX B

### DERIVATION OF ORBIT INSERTION $\Delta V$ EQUATIONS

Insertion into the desired orbit is accomplished using three maneuvers: a periapsis-raise maneuver executed at the first apoapsis pass after aerocapture, an apoapsis-adjust maneuver executed at the subsequent periapsis pass, and a plane-correction maneuver executed at the line of intersection of the current and desired orbit planes. The  $\Delta V$  requirements for the first two maneuvers are computed using the well-known vis-viva integral [12]

$$v = \sqrt{\mu \left( \frac{2}{r} - \frac{1}{a} \right)} \quad (\text{B-1})$$

At apoapsis on the post-aerocapture orbit, the radius and semi-major axis are given by

$$r = r_a$$
$$a = \frac{r_a + r_p}{2}$$

where  $r_a$  and  $r_p$  are the current apoapsis and periapsis radii, respectively. When these are substituted into (B-1), the velocity at apoapsis is seen to be

$$v_a = \sqrt{\frac{2\mu r_p}{r_a^2 + r_a r_p}} \quad (\text{B-2})$$

In a like manner, the desired velocity at apoapsis, which is the apoapsis velocity on an orbit with apoapsis radius  $r_a$  and periapsis radius  $r_{p_d}$ , is given by

$$v_{a_d} = \sqrt{\frac{2\mu r_{p_d}}{r_a^2 + r_a r_{p_d}}} \quad (\text{B-3})$$

where  $r_{p_d}$  is the desired (target) periapsis radius. The  $\Delta V$  requirement for the periapsis-raise maneuver is therefore given by

C-3

$$\Delta V_{pr} = |v_a - v_{a_d}| \quad (B-4)$$

The apoapsis-adjust maneuver  $\Delta V$  requirement is computed in a similar fashion. The velocity at periapsis on the new orbit after the first maneuver (with apoapsis radius  $r_a$  and periapsis radius  $r_{p_d}$ ) is

$$v_p = \sqrt{\frac{2\mu r_a}{r_{p_d}^2 + r_a r_{p_d}}} \quad (B-5)$$

The desired periapsis velocity, which is the periapsis velocity on an orbit with apoapsis radius  $r_{a_d}$  and periapsis radius  $r_{p_d}$ , is given by

$$v_{p_d} = \sqrt{\frac{2\mu r_{a_d}}{r_{p_d}^2 + r_{a_d} r_{p_d}}} \quad (B-6)$$

The second maneuver  $\Delta V$  is seen to be

$$\Delta V_{aa} = |v_p - v_{p_d}| \quad (B-7)$$

The total  $\Delta V$  required for the periapsis and apoapsis adjustment maneuvers is

$$\Delta V_{ORBIT} = \Delta V_{pr} + \Delta V_{aa} \quad (B-8)$$

The orbit plane orientation correction maneuver is assumed to be simply a rotation of the velocity vector into the desired plane at the line of intersection between the current and desired orbit planes. The angle between the actual and desired velocity vectors at this point is the wedge angle,  $\delta$ . Assuming that the actual and desired velocity magnitudes are the same, the required  $\Delta V$  is given (using the law of cosines) as

$$\Delta V_{PLANE}^2 = v_n^2 + v_n^2 - 2v_n^2 \cos \delta \quad (B-9)$$

where  $v_n$  denotes the velocity magnitude. Simplification of this equation gives

$$\Delta V_{PLANE}^2 = 2 v_n^2 (1 - \cos \delta) \quad (\text{B-10})$$

Using the trigonometric identity

$$1 - \cos \delta = 2 \sin^2 \frac{\delta}{2}$$

gives the final expression for the plane-rotation  $\Delta V$  as

$$\Delta V_{PLANE} = 2 v_n \sin \frac{\delta}{2} \quad (\text{B-11})$$

The total  $\Delta V$  required to correct the post-aerocapture orbit is

$$\Delta V_{TOTAL} = \Delta V_{ORBIT} + \Delta V_{PLANE} \quad (\text{B-12})$$

## LIST OF REFERENCES

1. *A Preliminary Study of Mars Rover/Sample Return Missions*, conducted by the Mars Study Team, Solar System Exploration Division, NASA Headquarters, January 1987.
2. Niehoff, J., *Mars Rover/Sample Return Mission Overview*, Presentation to the Mars Science Working Group, Jet Propulsion Laboratory, Pasadena, California, April 23, 1987.
3. Cruz, M.I., *The Aerocapture Vehicle Mission Design Concept*, AIAA Paper 79-0893, NASA/AIAA Conference on Advanced Technology for Future Space Systems, NASA Langley Research Center, Hampton, Virginia, May 8, 1979.
4. *Space Shuttle Operational Level C FSSR, Part B, Entry Through Landing Navigation*, STS 83-0004A, June 30, 1985.
5. Eckelkamp, R.E., *Shuttle Entry Drag Filter Equations for Guidance*, NASA-JSC Internal Note No. 75-FM-54, July 31, 1975.
6. Levine, G., "Aeroassist Flight Experiment Navigation Study Using Drag Measurements", CSDL OTVJ Memo No. 10E-85-10, April 29, 1985.
7. de Vries, J.P., Norton, H.N., and Blanchard, D.P., *Mars Sample Return Mission 1984 Study Report*, JPL D-1845, September 28, 1984.
8. Cerimele, C.J., and Gamble, J.D., *A Simplified Guidance Algorithm for Lifting Aeroassist Orbital Transfer Vehicles*, AIAA Paper 85-0348, AIAA 23rd Aerospace Sciences Meeting, Reno, Nevada, January 14-17, 1985.

PRECEDING PAGE BLANK NOT FILMED

9. Higgins, J.P., "An Aerobraking Guidance Concept for a Low L/D AOTV", CSDL Memo No. 10E-84-04, May 23, 1984.
10. Mease, K.D., and McCreary, F.A., *Atmospheric Guidance Law for Planar Skip Trajectories*, AIAA Paper No. 85-1818, AIAA Atmospheric Flight Mechanics Conference, Snowmass, Colorado, August, 1985.
11. Kriegsman, B.A., "Recent Information on LINS INS", CSDL Internal Memo, April 25, 1986.
12. Battin, R.H., *An Introduction to the Mathematics and Methods of Astrodynamics*, American Institute of Aeronautics and Astronautics, Inc., New York, N.Y., 1987.
13. Gelb, A., et al., *Applied Optimal Estimation*, The M.I.T. Press, Cambridge, Massachusetts, 1974.
14. Brown, R.G., *Introduction to Random Signal Analysis and Kalman Filtering*, John Wiley & Sons, New York, 1983.
15. *Onboard Navigation Systems Characteristics*, NASA-JSC Internal Note No. 79-FM-5, Rev. 1, December, 1981.
16. Smith, R.E., and West, G.S., *Space and Planetary Environment Criteria for Use in Space Vehicle Development, 1982 Revision (Volume 1)*, NASA Technical Memorandum 82478, January, 1983.

17. Ogata, K., *Modern Control Engineering*, Prentice-Hall Inc., Englewood Cliffs, N.J., 1970.
18. Bond, V., "A Summary of the New System of Astrodynamic Constants", NASA JSC-18829, May, 1983.
19. Kliore, A. (ed.), *The Mars Reference Atmosphere*, COSPAR 1978.
20. Justus, C.G., Woodrum, A.W., Roper, R.G., and Smith, O.E., *Four-D Global Reference Atmosphere Technical Description, Part 1*, NASA TM X-64871, September, 1974.
21. Mahar, K.B., "Atmospheric Density Variations for Aerobraking Studies", CSDL Internal Memo, December 12, 1983.
22. French, J.R., and Blanchard, D.P., *Mars Sample Return Mission 1985 Study Report*, JPL D-3114, July 31, 1986.